Sputtered Metal Oxide Broken Gap Junctions for Tandem Solar Cells

A Dissertation Submitted to the Faculty of the University of Minnesota by

Forrest Johnson

In Partial Fulfillment of the Requirements for the Degree of Doctor of Philosophy

Stephen A. Campbell

May 2015

Acknowledgements

I would like to acknowledge funding from a Department of Energy SunShot grant (#DEEE0005319). This work was conducted in Minnesota Nano Center (MNC), University of Minnesota, an NNIN-supported facility. Part of this work was carried out in the University of Minnesota Characterization Facility, a member of the NSF-funded Materials Research Facilities Network via the MRSEC program. Part of this work was also carried out by the National Renewable Energy Laboratory. I thank Dr. Glenn Teeter and Dr. Joel Pankow for their assistance in characterizing our materials with UPS and XPS. Thank you to my group members: Sreejith Karthikeyan for helping me make the sputter targets and doing the stress measurements, Brian Benton for making some of the films, Sang-Ho Song and Rick Liptak for conceptual help as I began my studies, and the rest of my research group for their support and good times with me. Lastly, I would like to thank my advisor for his invaluable assistance with me making it this far.

Dedication

I dedicate this dissertation to my lovely wife Katie who supported me throughout my degree, as well as to my parents for their guidance and wisdom in my life. I thank God for being my source of perseverance and working through those around me.

Abstract

Broken gap metal oxide junctions have been created for the first time by sputtering using $ZnSnO_3$ for the n-type material and Cu_2O or $CuAlO_2$ for the p-type material. Films were sputtered from either ceramic or metallic targets at room temperature from 10nm to 220nm thick. The band structure of the respective materials have theoretical work functions which line up with the band structure for tandem CIAGS/CIGS solar cell applications. Multiple characterization methods demonstrated consistent ohmic I-V profiles for devices on rough surfaces such as ITO/glass and a CIAGS cell. Devices with total junction specific contact resistance of under 0.001 Ohm-cm^2 have been achieved with optical transmission close to 100% using 10nm films. Devices showed excellent stability up to 600^oC anneals over 1hr using $ZnSnO_3$ and $CuAlO_2$. These films were also amorphous -a great diffusion barrier during top cell growth at high temperatures. Rapid Thermal Anneal (RTA) demonstrated the ability to shift the band structure of the whole device, allowing for tuning it to align with adjacent solar layers. These results remove a key barrier for mass production of multi-junction thin film solar cells.

Table of Contents

List of Tables

List of Figures

Cu_2O ceramic-sputtered film results

$CuAlO_2$ film results

BGJ Devices, metal-sputtered Cu_2O & $ZnSnO_3$ results

BGJ Devices, ceramic-sputtered Cu_2O & $ZnSnO_3$ results

BGJ Devices, $CuAlO_2$ & $ZnSnO_3$ results

Chapter 1: Introduction to the Problem

1. The need for solar energy

Due to depletion of other earth non-renewable energy resources and their effects on the environment, renewable energy is seen as the long-term solution to supply the projected 240 quadrillion-watt power requirements of the world by 2040 (*20*). Solar energy is abundant and renewable and the largest energy resource available. The world experiences a total radiation from the sun of ~174 pentawatts just outside the atmosphere. This is approximately 376,000 times more than the U.S. consumed from all energy forms in the year 2013 (*21*). In comparison, the theoretical maximum potential for geothermal is 160 terawatts and wind harvesting is 21 terawatts (*22*).

As of the end of 2013, the world had a government reported 138.9 gigawatts(*23*) of installed solar capacity. Without government subsidies, the cost of installed solar for

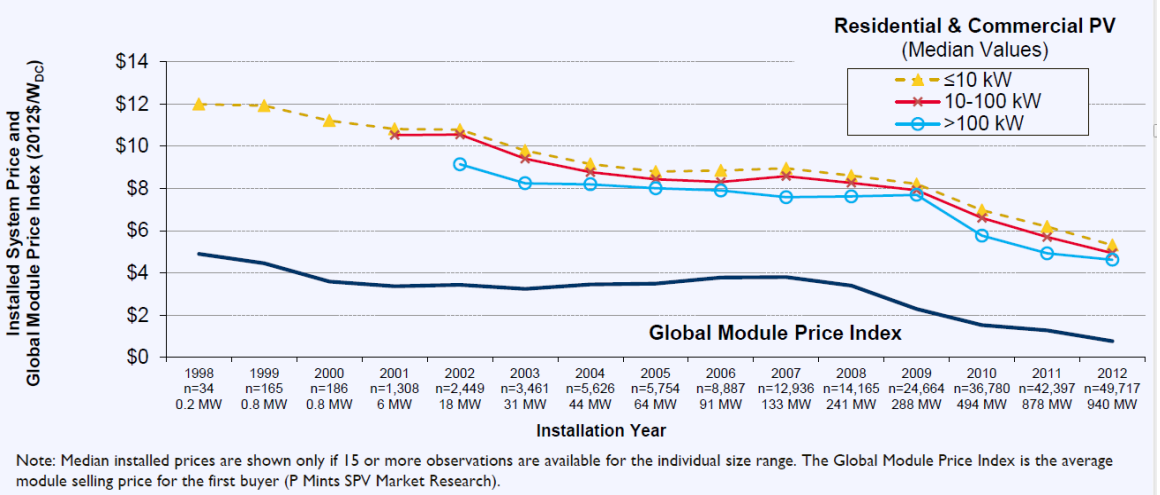

Figure 1.1: reprinted from (5)

residential and commercial installations was around $5/watt in 2012 (figure 1.1) (*24*). Utility scale installations are less somewhat expensive. This is a cost ineffective solution

because the installation costs can't be recuperated within 25 years, the warranted lifetime of installed solar panels. It was predicted in 2012 by the Department of Energy (DOE) (*24*) that solar costs could drop by 75% from 2010 levels to be cost competitive with many nonrenewable sources by the year 2020 at around $1.75. This was the goal of the DOE's Sunshot objective. With recent developments in natural gas extraction methods such as hydraulic fracturing, in order for solar to remain competitive, the cost/watt will likely need to be lowered further by 2020. Since installation and module assembly costs are unlikely to drop appreciably in the foreseeable future, increasing the performance of photovoltaic (PV) devices is extremely important for their widespread use for solar-to-electric energy conversion in order to achieve these objectives.

1.2. Overview of Solar Cell Physics

Harnessing photons for electrical energy directly utilizes the well-known p-n junction diode. The device is referred to as a solar cell when operating under illumination and without a direct applied voltage. As shown in figure 1.2, light enters the junction (typically from the direction opposite the substrate). To maximize photon transport into the junction, the top of the device may be coated with an antireflective layer over an electron-extracting metal grid designed to cover as little area as possible. On the bottom of the device, the hole-extracting contact is typically a metal layer to reflect unabsorbed photons back through the junction to allow further energy conversion. Absorbed photons generate electron-hole pairs which will recombine unless they are extracted within the carrier lifetime. Since the absorption length for a lightly doped ideal semiconductor is extremely long for photons of energy less than the band gap, generally only the higher

energy photons stand a reasonable chance of being absorbed.

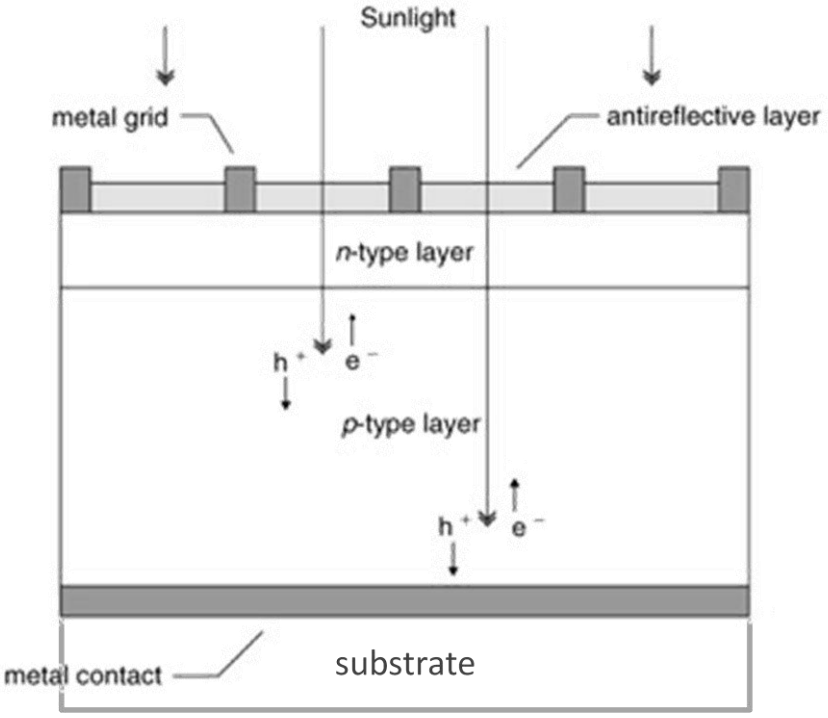

Figure 1.2: Diagram of a typical substrate-based p-n junction solar cell.

Capturing these charges before they recombine can be done in several ways. The most efficient is the use of a built in electric field created by a p-n junction device. Typically the absorbing semiconductor is the p-type side of the junction. The n-type layer may be heavily doped to help with lateral conduction into the collecting grid. It may also be a wider band gap semiconductor to allow most of the incident light to make it through to the depleted region of the light absorbing layer.

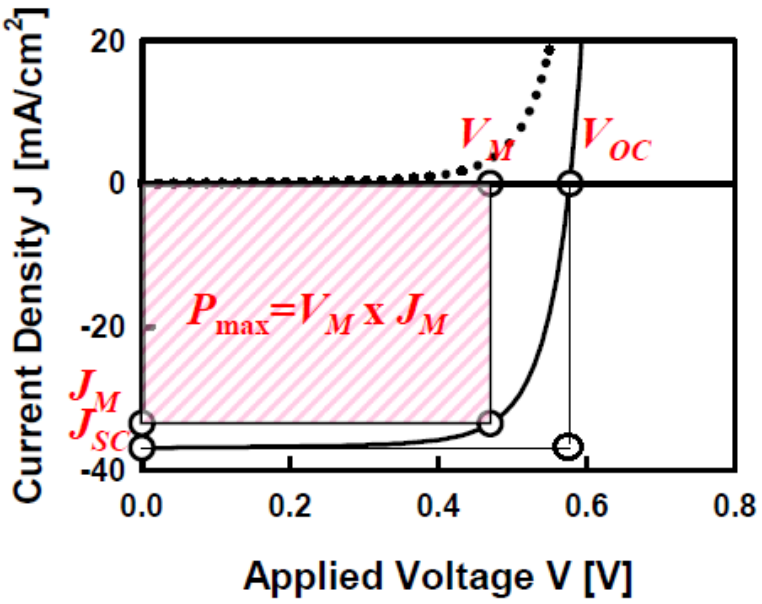

Figure 1.3: The J-V curve for a typical solar cell operating under illumination (solid line), and no illumination (dotted line).

The current—voltage (*I*—*V*) characteristic of a typical solar cell is shown in figure 1.3. The minority-carrier properties determine the solar cell behavior, as indicated by equations 1 to 4 shown below. The primary metric is the power conversion efficiency under the design illumination conditions. This is the product of three properties — the short-circuit current, the open-circuit voltage, and the fill factor. The short-circuit current, I_{SC}, is the maximum current produced by the cell when the ends of the cell are at the same potential, as can be seen when *V* is set to zero in equation 1. It is the sum of the photon-generated current throughout the junction, I_{o1}, and the dark saturation current due to recombination in the quasi-neutral regions, and I_{o2}, the dark saturation current due to recombination in the space-charge region. I_{o2} is typically not significant for a good cell design.

$$I = I_{SC} - I_{o1}\left(e^{qV/kT} - 1\right) - I_{o2}\left(e^{qV/2kT} - 1\right)$$

(1.1)

When the applied voltage to the cell is large enough, the recombination current which is propotional to $e^{qV/kT}$, pulls the total current quickly to zero. The maximum voltage, V_{oc} occurs under open-circuit conditions as shown in equation 2, where I_{o1} is assumed to be much less than I_{SC}.

$$V_{OC} = \frac{kT}{q} ln \frac{I_{SC} + I_{o1}}{I_{o1}} \approx \frac{kT}{q} ln \frac{I_{SC}}{I_{o1}}$$

(1.2)

To get maximum power out of the cell, one looks for the point on the *I*—*V* curve where the IV product is maximized. This is referred to as the *maximum power point* with $V = V_{MP}$ and $I = I_{MP}$. This point defines a rectangle whose area, given by $P_{MP} = V_{MP}I_{MP}$, is the largest rectangle for any point on the *I*—*V* curve. The fill factor, *FF*, is a measure of the *squareness* of the *I*—*V* characteristic and is always less than one (see equation 3). It is the ratio of the areas of the two rectangles shown in figure 1.3.

$$FF = \frac{V_{MP}I_{MP}}{V_{OC}I_{SC}} = \frac{P_{MP}}{V_{OC}I_{SC}}$$

(1.3)

Finally, we get to the solar cell power conversion efficiency, η, which is defined in equation 4 as the ratio of converted electrical powder to the incident optical power, P_{in}, which is determined by the properties of the light spectrum incident on the solar cell. Since the fill factor depends on the series current through the whole device, series resistances in the cell and its connections should be minimized.

$$\eta = \frac{P_{MP}}{P_{in}} = \frac{FFV_{OC}I_{SC}}{P_{in}}$$

(1.4)

Reducing both bulk and surface recombination rates, which are typically related to material and interface defects like grain boundaries, vacancies, antisite defects, and other traps, will increase the open-circuit voltage and the short circuit current if the defect states fall inside the band gap. Thus it is helpful to have large grains in an absorber material and a low defect concentration.

The solar spectral distribution just above the Earth's atmosphere is referred to as the *air mass zero* (AM0) radiation spectrum. The air mass is a measure atmospheric absorption which affects both the spectral content and intensity of radiation. The air mass number is given by $1/(\cos\theta)$ where θ is the angle of incidence ($\theta = 0$ when the sun is directly overhead). The air mass number is always greater than or equal to one at the Earth's surface. The typical standard used for comparing solar cell performance is the AM1.5 ($\theta = 48.2°$) spectrum which is normalized to a total power density of 1 kW/m^2.

Another important property of a solar cell is the collection efficiency, which is defined as the percentage of photons (with energy greater than the gap) which generate electron-hole pairs relative to the maximum possible electron-hole pairs that could be generated. This is influenced by junction material properties such as being a direct or indirect-gap optical absorber as well as the thickness of the junction layers. As quantified by Shockley-Queisser, even when one assumes no carrier recombination or other loss mechanism, there is an power conversion efficiency limit (*25*). This limit comes from the fact that photons less than the band gap of the absorber are not converted to electricity,

and all excess energy for photons greater than the band gap are lost as heat. It is approximately 32 % for a single-junction device constructed with a semiconductor absorber that has the ideal band gap (~1.1 to 1.4 eV).

Optical concentrators, which focus more light into a given cell area, can overcome the 32% limit by increasing open circuit voltage and fill factor, but they introduce other issues such as sun-tracking and heat dissipation. Moreover, when the solar radiation is diffuse, such as on cloudy days, solar concentrators do not improve collection efficiency appreciably. As a result concentrated solar power is most suitable to utility-scale installations sited in low-cloud regions.

1.3. Current State of Single-Junction PV Technology

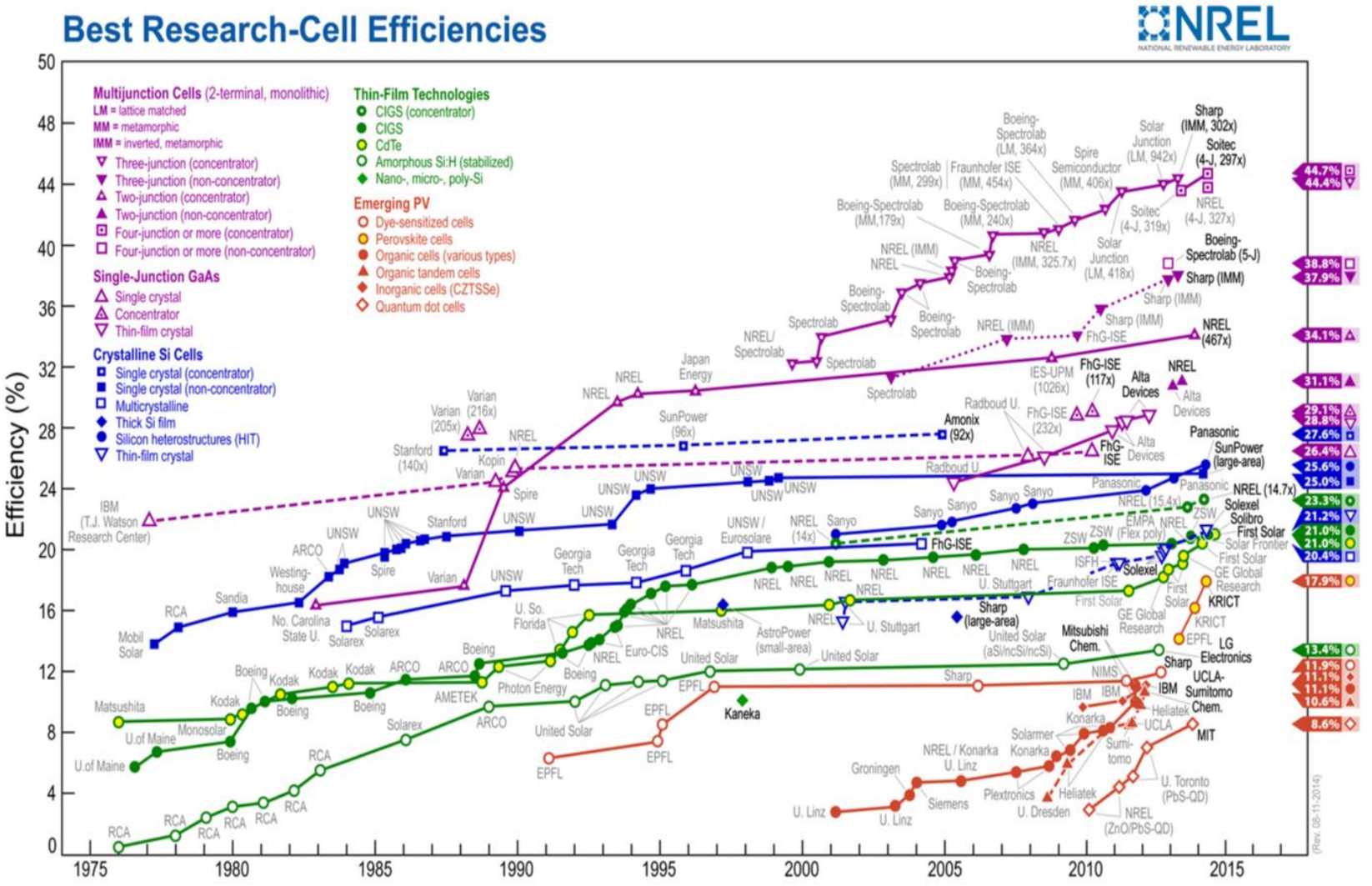

Figure 1.4: NREL Best confirmed research-cell efficiencies as of 8-20-2014.

Of the thin film solar technologies, $Cu(In_{1-x},Ga_x)Se2$ (CIGS) has had the highest unconcentrated demonstrated efficiency for more than 20 years. Currently at 21.0%(*26*) is was only recently tied by CdTe. A direct gap semiconductor, it has a high absorption coefficient that allows all light to be absorbed within a 2-3um thick layer. Device stacks usually consist of TCO/CdS/ CIGS/Mo. The absorber can be grown by thermal coevaporation with deposition rates varying from 20 to 200 nm/min, depending on the effusion rates from the sources (usually over 1000^oC). This method has several drawbacks. It is difficult to control the evaporation source flux and so the stoichiometry of the film. Also, evaporation uses point sources which is problematic for large area manufacturing. The alternative method is a two-step process where metals are deposited first at low-cost and low-temperature, typically by sputtering. This is followed by annealing in a Se and/or S atmosphere, also at 450–600 °C. This method maintains better metal composition, but typically takes longer than coevaporation. In either method Na is incorporated at some point to improve the electrical performance(*27*). Higher temperatures promotes large grain growth of the desired chalcopyrite phase, but are limited by substrates such as soda lime glass, which has a glass transition temperature of ~570 ^oC, and so can warp if the temperature is too high. The absorber band gap can also be graded to improve the operating voltage and current collection (*28, 29*). The ratio of Ga/(Ga+In) in the higher performing cells is between 0.25 to 0.35, which allows for tuning the band gap between 1.1–1.24 eV with higher efficiency over cells lacking Ga(*30*).

Typically the back metal contact is sputtered molybdenum. Some of the Mo is consumed to make a $MoSe_2$ layer during the growth of the CIGS layer. This ends up forming a near-ohmic contact to the CIGS. The Mo deposition chamber pressure must be adjusted to control stress in the film and prevent poor adhesion(*31*). The buffer layer of thin n-type CdS is deposited by chemical bath deposition. The window layer typically consists of an undoped ZnO film and an aluminum-doped ZnO film (*32*). Both are typically deposited in a single sputtering step. This forms a p-i-n structure where the photon collection efficiency is enhanced in the blue energy region by scattering at the p-i and n-i interface(*33*).

Typically cells are manufactured on soda-lime glass substrates, which is inexpensive, has a good thermal expansion match to the absorber layer, provide sodium through indiffusion (*34*). Overall advantages in producing CIGS-based cells include grain boundaries that are primarily passive so even small grain films can be used. Device behavior is also relatively insensitive to defects at the CIGS/CdS junction, allowing some air exposure of the device during processing. Multiple groups have recently achieved efficiencies over 20% (*35-38*) on flexible polyimide foil substrates using thermal co-evaporation, and 19.7% by sputtering, selenization & sulferization(*39*) showing that the gap with soda lime glass-based solar cell performance is narrowing. Current limitations to higher efficiency's for these cells include raising the V_{OC}, which requires a deeper understanding of the chemical and electronic nature of the defects that limit it, and their origin. In addition, the fundamental understanding of the role of sodium and the nature of the grain boundaries and free surface remains incomplete. There are also other issues to its wider commercial adoption such as the availability of indium as a resource and the

continued use (albeit much less) of toxic Cd, removing some of the benefit compared to its closest competitor CdTe.

Other solar cell technologies are discussed in the appendix.

1.4. Exceeding the Shockley-Queisser Limit

a. Overview of Approaches

Historically production-level module efficiency is usually more than a third behind the best-lab efficiencies for most solar cell technologies, and thus it will be some time before a single junction production-level module can reach the current best-lab results. It is obvious from NREL's efficiency chart (figure 1.4) that there have been periods of research, including the past few years, where cell efficiency has increased substantially, however not all of this has translated to production-level module efficiency increases. Overall it can be said that most of the single junction solar cell technologies under industrial production are slowly approaching the Shockley-Queisser efficiency limit.

Several effects have been demonstrated that suggest that it is possible to exceed the Shockley-Queisser limit (*25*). Prominent among these are multi-exciton generation which could convert high energy photons into two electron-hole pairs (*40*), midgap states to permit the collection of photons with energies below the band gap (*41*), photon upconversion in which two photons with sub band gap energy combine to make a single high energy photon (*42*), and thermal upconversion approaches that use low energy photons to heat an object until it reemits higher energy photons (*43*). Hot electron transfer

has also been demonstrated (*44*). Each of these ideas is extremely interesting and could, potentially lead to higher performance devices. However the application of each concept is limited as each imposes significant constraints. Multi-exciton only applies to a small part of the solar spectrum, midgap states can lead to recombination, upconversion processes tend to have low efficiencies except in concentrated light, and hot carrier effects have only been seen in quantum dots where collection efficiencies are problematic. In most cases the effects are real and have been demonstrated, but increases in overall AM1.5 power conversion efficiency have been predicted, but rarely observed. No commercial devices currently use any of these approaches.

One third-generation approach (*45*) has clearly demonstrated an ability to increase efficiency in both research and commercial devices, multijunction (MJ) PV. MJ PV uses multiple devices, typically in a vertical stack, to more efficiently collect different parts of the solar spectrum. In the MJ PV structure, the topmost device uses a wide band gap absorber. It collects the high energy photons while the low energy photons are transmitted to the next device in the stack which has a narrower band gap. In this way, the higher subcells are effectively low-pass photon energy filters. According to models by Martí and Araújo, up to 44 % efficiency is possible from a tandem (i.e. two-junction solar cell) (*46*), and up to 65 % is possible for a cell made of infinite junctions using AM1.5 illumination. Up to four devices in series have been demonstrated. MJ PV has been developed for aerospace applications using the epitaxial growth of compound semiconductors. The current record is 38.8% for a four-junction device. The processing cost of such a device make it orders of magnitude too expensive for terrestrial power

generation. Even in space applications, concentrators are often used to control the cost of the PV devices and increase efficiency (up to 44.7%).

Even in a single crystal material, multijunction cells introduce a number of issues which complicate processing. It is necessary that a photon with a given energy is directed into the appropriate subcell. The photons can be distributed laterally using some sort of prism or vertically by stacking cells with transparent substrates/superstrates. Optical and mechanical complexities make the former much more difficult to be economically competitive.

Subcells can be mechanically stacked on top of each other but electrically isolated, which requires transparent back contact metallizations to allow sub-band gap light to pass through. This approach also increases cost by requiring additional materials. Furthermore the assembly step reduces yield and adds cost. The preferred approach is to monolithically stack all of the cells on top of each other with electrical interconnection. This is the approach we will focus on, and the challenges to overcome will be discussed shortly. The cells can electrically be configured as a 4, 3, or 2-terminal in a tandem (two subcell) device. Four terminal configurations give each subcell its own electrical connections, so they can be fabricated in either p/n or n/p orientation, as well as no restrictions on their current or voltage. This design offers difficulties in electrically isolating the subcells and complexity in routing and connecting subcells externally. Three terminal configurations allow a common electrical connection between adjacent subcells, but otherwise require similar complexity in fabrication. Lastly, 2-terminal configurations offer simplicity for interconnection, however the tradeoff is made with restrictions on the

same polarity in subcells and current matching because the subcell with the least photocurrent limits the overall device current.

The restriction on current matching between subcells results in a relatively narrow restriction in band gaps for the subcells. The relationship of the subcell current to the subcell band gap can be understood through the following two-junction example,

$$J_{SC,1} = e\int_{0}^{\lambda_1} \Phi_S(\lambda)d\lambda, \quad J_{SC,2} = e\int_{\lambda_1}^{\lambda_2} \Phi_S(\lambda)d\lambda \tag{1.5}$$

where $J_{sc,1}$ and $J_{sc,2}$ are the short-circuit current densities for the upper cell and lower cell, respectively, and dependent upon the incident spectrum Φ_s. $J_{sc,2}$ is related to the band gaps of the upper and lower cell, while $J_{sc,1}$ only depends on the band gap of the upper cell. Because of this the lower cell band gap typically must be reduced from the optimum value for a single junction device, while the upper cell band gap is raised until $J_{sc,1} = J_{sc,2}$.

b. Multi-junction III-V Technology

III-V Cells: The III-V multi-junction solar technology is by far the most developed for multi-junction to date, with peak efficiencies reaching 38.8% for a 5 junction(*26*). This is mainly due to the huge advantage of the making a monolithic solar cell using semiconductor compounds with close lattice-matching, making their growth by the well-known process of heteroepitaxy much easier (see figure 1.5 below). Because of this they are almost always made monolithically, and are thus much lighter compared to mechanically-stacked multi-junction cells and so serve well for space applications.

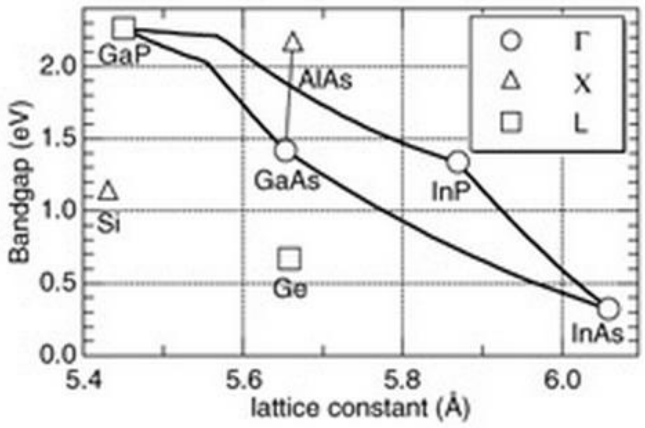

Figure 1.5: Estimated band gap as a function of lattice constant for Si, Ge, and selected III–V binaries and their ternary alloys. The legend indicates the location of the band gaps in the Brillouin zone; band gaps located at the Γ point are direct.

These devices are usually made as a sequence of GaInP(n+-type)/GaInP(p-type)/Ga(In)As(n+-type)/ Ga(In)As(p-type) /Ge(n+-type)/Ge(p-type) junctions or variations thereof, depending upon the number of junctions required. Due to the decrease in current density with band gap due to lower absorption coefficient(*47*) the lower cells are thicker. A key goal in fabrication is the minimization of nucleation centers and propagation of dislocations in concentrations that depend on the amount of mismatch and thickness of the individual layers. These dislocations are often centers for nonradiative recombination, in effect limiting the minority-carrier lifetime or diffusion length, and ultimately the efficiency of the device. It has been shown that the amount of mismatch in lattice constants is correlated to changes in current density between layers, as well as band gap(*48*). It has been observed that critical dislocation formation is associated with layer thickness, growth temperature, and growth rate. In addition, materials can be lattice-

matched at room temperature or lattice-mismatched at growth temperature, however material is usually grown under compression due to higher stability. For epilayers grown on nonsingular or vicinal (100) substrates, the value of lattice mismatch can vary(*49*). Densities of stacking faults and other current shunting defects are around 1 cm^{-2}.

In order to provide a low-resistance connection between the subcells a p^{++}-AlGaAs/n^{++}-GaInP heterojunction tunnel diode is deposited(*50*). It takes advantage of the innate propensity for AlGaAs to incorporate C and for GaInP to incorporate Se to allow high doping levels necessary for tunneling currents. A top-cell back-surface barrier (AlGaInP or AlInP) may be used to passivate the interface between the top-cell base and the tunnel-junction interconnection, as well as reduce outdiffusion of dopants(*51*). Despite the advances of multi-junction III-V cells efficiency and cost reductions, they remain an expensive option for most terrestrial applications. In addition, these devices have a limited projected horizon for use due to diminishing resources of indium and germanium(*52*).

c. Multijunction Non-epitaxial Technologies

The leading multi junction non epitaxial technology is hydrogenated amorphous silicon. Such cells have been made with a stabilized best-lab efficiency of 13.4% for a triple junction (a-Si:H/mc-Si:H/mc-Si:H) cell (*53*), and modules at 11%. Most commercial modules are tandem cells or triple junction cells. A common configuration is the “micromorph” tandem, which pairs an a-Si top cell with a nc-Si bottom cell (*54*). This technology is more easily implemented in MJ form due to the material processing steps operating at lower temperatures so as to inhibit diffusion of necessary dopants. Also, in

amorphous materials because there is no need for lattice matching, as is required for crystalline heterojunctions, Furthermore he band gap is easily adjusted with added Ge or by changing the size of the nanocrystals. Finally, the high trap density in a-Si:H allows one to overcome the connection problem without a tunnel junction through recombination. However, MJ amorphous silicon has not seen meaningful efficiency improvements for years and is expected to lose market share to other thin film cells.

In organic cells a multi junction approach is one of the most promising ways to tackle the main losses in a single junction device. This is due to organic materials' low mobility and the high degree of charge recombination, severely restricting the total cell thickness, which benefits from multiple junctions (*55*). Organic devices are also deposited near room temperature avoiding the thermal problems described below. Furthermore, the absorption range of single organic materials is usually narrow. Recent calculations suggest that tandem organic cells have a 30% higher efficiency potential as compared to single junction organic cells(*56*). While this is promising the technology overall still has to demonstrate that it can overcome the low yield manufacturing and stability issues that prevent it from mass production.

Aside from a-Si:H, multijunction inorganic thin film technology has not been seriously considered for some time, due to investment in single junction showing continuous improvement with the belief that single junction module performance in the high 20%'s will achieve grid parity. Recently, however the company Stion has claimed successful mechanically stacked dual-junction CIGS 'third generation' solar cell with

efficiencies of 23.2% at the lab level(*57*). It remains to be seen whether this can be cost-effectively scaled up to mass production. Mechanically stacked multi-terminal cells have historically been avoided because they introduce new costs in the form of multiple electrical contacts to a cell and possibly focusing optics, additional cell-external electronics, added weight due to multiple substrates, and optical losses if air gaps exist between cells. Stion uses the two glass panes typically used to encapsulate cells as substrates, reducing the impact of the need for multiple substrates. Over the long term, however, it is expected that glass encapsulation will give way to thin film moisture barriers, making the Stion approach uneconomical.

Monolithically integrated inorganic thin film PV has many problems as well. Here we note some of the more pressing.

Optical losses: Photon energies greater than the lower cell, but less than the upper cell can be lost due to free-carrier absorption and nonradiative sub-band gap absorption via impurities or defects, as well as scattering from material interfaces and defects. This makes optimization of intermediate layers essential to get the best possible efficiency.

Thermal budget: A major concern is effect of the temperature required to form the top cell on the behavior of the lower cells. Generally high performance thin-film solar cells require high-temperature processing to get large grain structure. The current assortment of popular thin film technologies using CdTe and CIGS, for example, use a deposition temperature above 500^{o}C. For a given device stack with the lower and upper cells

deposited in sequence, the subsequent temperature processing of the top cell may cause inter diffusion at and bulk or grain boundary diffusion away from interfaces.

Subcell configuration issues: The upper and lower cells must both use a substrate-based design (light comes in through the 'air' side), or superstrate-based design (light comes in through the glass side). At present $Cu(In,Ga)Se_2$ and related thin film technologies only use substrate-based design while CdTe approaches use superstrate design.

Multiple band gaps: Forming the wide band gap subcell (specifically the top cell) is also problematic. The top cell of a two-subcell tandem contributes at least two-thirds of the total power generated. It is essential, therefore, to maximize its efficiency. To achieve an efficiency of 25% for the tandem implies that the top cell must contribute almost 17%. However, the construction of an efficient, wide band gap solar cell is clearly a major challenge. Very high-efficiency, wide-band gap, single-crystal devices have been made. The well-known GaInP/GaAs tandem is one such example, yet little progress has been made in a polycrystalline thin-film form.

Tunnel junctions: The combination of two similar polarity oriented subcells in a 2-terminal device produces a reverse p-n junction, a barrier to carrier transport vertically through the device. A solution to this is a tunnel junction, which typically heavily made by forming a p-n junction that is heavily doped on both sides. This allows a low-resistance contact by tunneling of carriers between the valence band and conduction band

as they move across the depletion region. The films used in these devices a band gap at least as wide as the upper, adjacent subcell and are typically thin (under 40nm) to minimize voltage drop and optical absorption. This solution has been used with success for single crystal GaInP/GaAs tandem junctions, however polycrystalline tandem cells could provide problems. Grain boundaries provide low energy diffusion paths for dopants during upper cell processing, sharply increasing the junction resistance. Conformal coating of the tunnel junction will be difficult due to grain facets. Other possibilities are an extremely thin metal layer with the correct work function although this will impose an optical penalty, or a graded recombination layer (*58*).

Chapter 2: Background on Tunnel Junctions and Related Structures

2. Tunnel junction theory; problems in applying TJ in non epitaxial devices:

A key issue for the fabrication of a monolithic tandem cell is the series electrical connection between the two p-n junctions that allows charge carriers to move across this junction to provide continuous current flow between the two devices. Holes from the top solar cell and electrons from the bottom solar cell flow towards each other and recombine, providing current continuity. Without a tunnel junction carriers would pile up on either side of the junction unless or until the potential was high enough to overcome the built-in voltage of a p-n junction.

We are primarily interested in heterojunctions which are formed when two different n- and p-type materials are joined. There are two basic types of band alignment in such a device. In type I junctions the conduction and the valence bands of the narrow-gap semiconductor are 'nested' within the band gap of the wide-gap material, and the band offsets ΔE_c and ΔE_v have opposite signs (figure 2.1a). Type II junctions can have two different kinds of band alignment. In a staggered type II system, either the conduction or the valence band of one semiconductor lies outside the band gap of the other material, and the band offsets have the same sign (figure 2.1b). At large band offsets a broken gap alignment will be formed in a type II junction, when neither the conduction band nor the valence band of the narrow-gap semiconductor is located within the band gap of the wide-gap material (figure 2.1c).

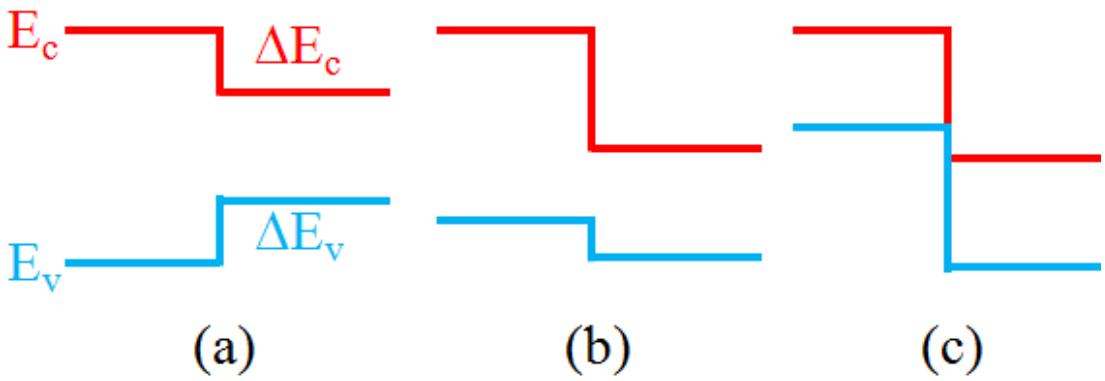

Figure 2.1: Types of junctions prior to equilibrium. (a) Type I –nested band alignment, (b) Type II –staggered band alignment, (c) Type II –broken gap alignment.

A classical tunnel junction utilizes a p-type and n-type material to connect to the rest of the device with the appropriate band alignment, however the band alignment of the tunnel junction layers themselves may be of Type I or II. Typically for solar cell devices however, the tunnel junction is made as a homojunction with similar band structure on either side of the junction, but with opposite doping polarity. This is because homojunctions offer semiconductor growth and processing advantages of similar lattice constants and other material properties important for epitaxial growth. If the doping is moderate to light then at equilibrium a potential barrier exists at the interface and carriers cannot cross the junction without a large applied potential (figure 2.2 –part a, b). The tunnel junction concept heavily dopes both the p-type and the n-type sides, placing the Fermi level outside of the band gap (figure 2.2 –part c). In equilibrium (figure 2.2 –part d) only a very thin barrier exists at the junction and statistically many carriers can pass through the barrier via quantum mechanical tunneling.

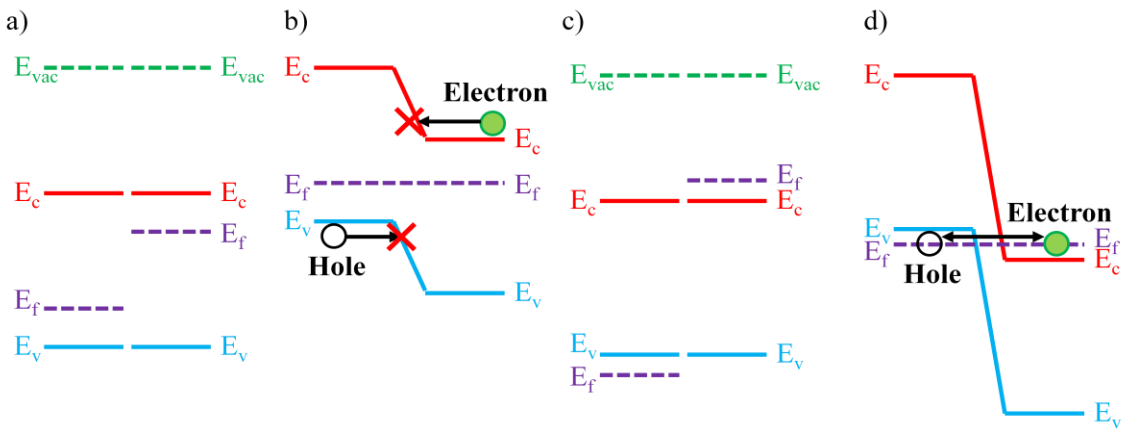

Figure 2.2: band structure for lightly doped before (a) and after (b), and heavily doped p-n junctions before (c) and after (d) equilibrium for typical applications.

The current-voltage (I-V) for the tunnel junction is shown In figure 2.3 (59). When the applied voltage is zero, no current flows (figure 2.3a). When there is a forward bias, the n-type layer is raised relative to the p-type side of the band diagram. Then electrons in the conduction band are directly opposite empty states in the valence band of the p region. There is a finite probability that some of these electrons will tunnel directly into the empty states, producing a forward-bias tunneling current shown in figure 2.3b. With a slightly larger forward-bias voltage (figure 2.3c) the maximum number of electrons in the n region will be opposite the maximum number of empty states in the p region; this will produce the largest tunneling current. As the forward-bias voltage continues to increase, the number of electrons on the n side directly opposite empty states on the p side decreases, shown in figure 2.3d, and the tunneling current will decrease. In figure 2.3e, there are no electrons on the n side directly opposite available empty states on the p side. For this forward-bias voltage, the tunneling current will be zero and the normal ideal diffusion current will exist in the device as shown in the I-V characteristics. The portion

of the curve showing a decrease in current with an increase in voltage is the region of differential negative resistance. When the tunnel junction is under reverse bias (figure 2.3e), electrons in the valence band on the p side are directly opposite empty states in the conduction band on the n side, so electrons can now tunnel directly from the p region into the n region, resulting in a large reverse-bias tunneling current. The reverse-bias current will increase monotonically and rapidly with reverse-bias voltage as shown in figure 2.3e.

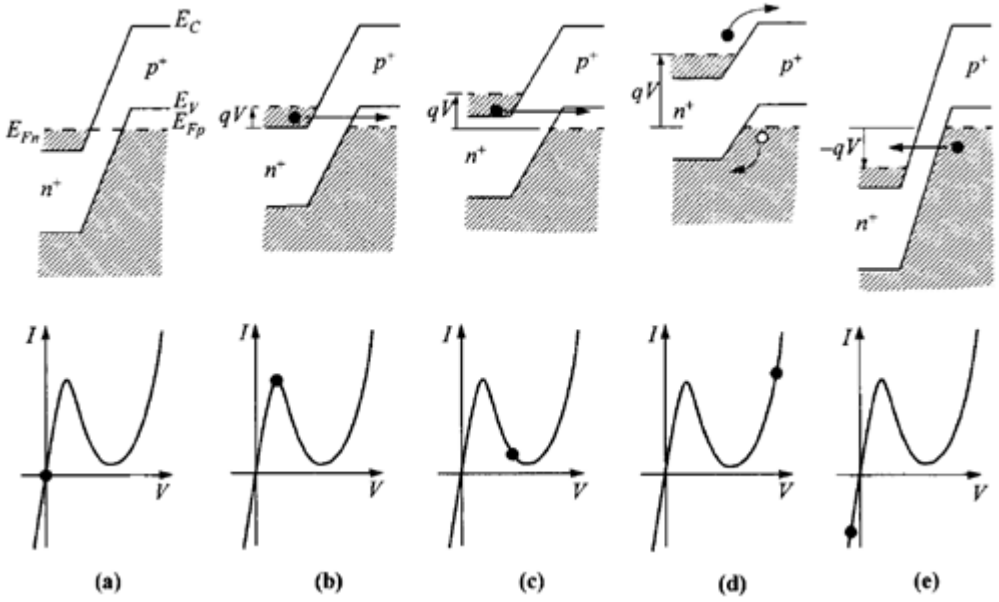

Figure 2.3: The I-V curve for a classic tunnel junction under no-bias (a), forward bias (b, c, d), and reverse bias (e), reprinted from (2).

2.2. Electrical transport across the junction:

Electron transport for a tunnel junction can be divided into three categories. Under reverse bias, and up through the negative differential resistance portion (figure 2.3a, b, c, and e) the dominant method of transport across the junction is by quantum mechanical tunneling (*60*) from band-to-band. The portion in figure 2.3d where the forward bias is

large enough that carriers are excited over the barrier into the p-layer by thermionic emission. Lastly, the region between figure 2.3c and figure 2.3d is influenced by 'excess current', described as an additional tunneling current related to parasitic tunneling via impurities.

When the electric field in a semiconductor is sufficiently high (on the order of 10^6 V/cm), a finite probability exists for quantum tunneling or direct excitation of electrons from the valence band into the conduction band. The tunneling probability is given by the WKB approximation (Wentzel-Kramers-Brillouin) (*61*):

$$P \sim e^{-\int 4\pi\left(\sqrt{2m^*\Delta E}\right)dx/h} \tag{2.1}$$

where ΔE is the energy barrier and the integral is taken over the classically forbidden 'turning points' or boundaries of the barrier. The tunneling of an electron through a forbidden band is formally the same as a particle tunneling through a barrier. Although tunneling can occur between direct and indirect gaps, the later of which requires scattering centers such as phonons or impurities. Direct gap tunneling is much more likely than indirect tunneling typically. In the WKB approximation, the transmission probability can be calculated for arbitrary potential shapes and the carrier energy can be larger or smaller than the potential barrier.

The tunneling time of carriers through the potential energy barrier is not governed by the conventional transit time concept ($\tau = W/\upsilon$, where W is the barrier width and υ is the

carrier velocity), but rather by the quantum transition probability per unit time which is proportional to $\exp[-2\bar{k}(0)W]$, where $\bar{k}(0)$ is the average value of momentum encountered in the tunneling path corresponding to an incident carrier with zero transverse momentum and energy equal to the Fermi energy (*62*). The depletion layer (barrier) width due to degenerate doping is usually on the order of 10 nm or less.

2.3. Other processing considerations

To obtain the narrow depletion widths needed for a successful tunnel junction requires a high doping level, typically above 10^{20} cm^{-3}, with steep doping profiles at the interface (*59*). In conventional crystalline silicon and III-V materials this is done by substitutional doping whereby elements of the lattice are substituted with a different element which either donates an electron or hole. All materials have a limit to the amount of n or p-type substitutional doping they can handle, called the solid solubility. If the limit is crossed the material enters an unstable state where it is prone to segregation and phase change. If the material is polycrystalline than diffusion tends to occur at the grain bounderies. It's also true that at lower temperatures they would precipitate in a grain boundary than in a single crystal material (*63*).

For most modern thin film inorganic solar technology, materials are deposited in poly-crystalline form. Creating a crystalline heavily doped tunnel junction in these layers would be extremely unlikely since subsequent processing temperatures needed for forming the top layers would cause substantial diffusion of dopants between the layers. Thus heavy substitutional doping is not usually performed on poly-crystalline films when high or even moderate post-deposition temperatures are used (*64*, *65*). One possible

replacement for this is the use of stable defect-doped materials. Materials can be doped intrinsically with defects by a slight alteration of their composition such that an element is missing or added to the lattice. However, in practice high concentrations of defects are driven to agglomerate forming extended defects that are both difficult to control and can lead to doping compensation (*66, 67*). As a result, poly crystalline multijunction devices require a different solution to the problem Here we pursue broken gap junctions, as shown in Figure 2.2c.

2.4. Amorphous semiconductors – multijunction silicon PV

When it comes to amorphous PV, the issue of a reverse p-n junction barrier is resolved in a different way. It is understood that dangling bonds are generated when doping is increased in material. It is possible for carriers that are trapped on defects on one side of the interface to move to traps on the other side simply by quantum mechanical tunneling if the trap density is sufficiently high. This process "short-circuits" electrical transport involving the conduction band and valence band states. For this reason, the doped layers in the 'effective' tunnel junction between two solar cells, particularly the sublayers near the interface, are made with very high doping and even intentional defects. The resulting large density of dangling bonds permits the efficient neutralization, by tunneling, of holes from the cell below and electrons from the cell above. Doped nanocrystalline-Si layers or other defective layers have been useful to enhance the recombination without adding optical absorption. Tunnel or shorting junctions have been examined by making *pnip* or *npin* structures (*68*) or by QE measurements in functioning

tandems using red, blue or no bias light (*69*). Amorphous solar cells can handle the higher levels of doping in these junctions because they tend to use very low processing temperatures.

There is a downside to effective tunnel junctions using heavy levels of traps, which is that it places barriers on other device performance metrics, such as optical scattering centers and low mobility, as well as the inability to handle processing temperatures required for higher quality solar cells.

2.5. Broken gap junction theory and Requirements

For a type II Broken Gap Junction (BGJ) device, the fundamental requirement is that the electron affinity of the one layer is equal to or greater than the sum of the electron affinity and the band gap of the other layer (see figure 2.4).

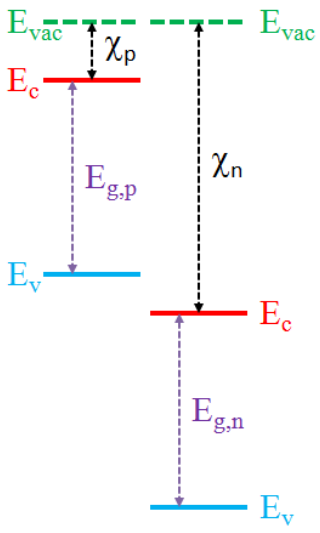

Figure 2.4: p-n band alignment for producing a type II broken gap junction:

$\chi_n > \chi_p + E_{g,p}$

In this scenario electrons in the valence/conduction band of the lower affinity material are at a higher energy than unoccupied states in the valence/conduction band of the high affinity material. At equilibrium these electrons will flow from the low affinity material to the high affinity material, autodoping the junction. This charge transfer creates accumulation or inversion layers on one or both sides of the interface, depending upon polarity, leading to band bending and introducing an energy barrier.

There are four sub-types of type II BGJ devices, as shown in figure 2.5 (*70*). For N-n, N-p, and P-p heterojunctions, the device equilibrium requires extreme band bending to flatten the Fermi level, which typically causes quantum wells to appear near the junction. Carriers cannot move between states on either side of the junction without aligning to a state in a similar quantum well. This phenomenon is useful for detecting or generating mid/far infrared photons for applications such as mid-IR LEDs. In the P-n heterojunction case where the electron affinity of the n-type layer is equal to or greater than the sum of the electron affinity and the band gap of the p-type layer, and the doping is sufficiently above intrinsic level of the necessary polarity, but not necessarily heavily doped – autodoping still occurs however quantum wells do not appear. The p-type material becomes more heavily p-type near the interface and the n-type material becomes more heavily n-type near the interface.

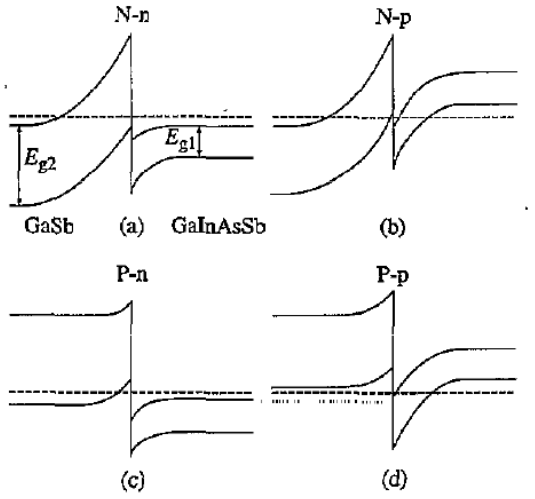

Figure 2.5: Energy band diagrams of four sub-types of narrow-gap GaInAsSb/GaSb heterojunction: (a) N-n, (b) N-p, (c) P-n, and (d) P-p heterojunctions. The capitol later indicates the larger-gap material, however in principle the relative gap sizes don't matter. (reprinted from (1))

Under forward bias, electrons injected into the n-type material recombine with holes injected into the p-type material, giving rise to current through the junction. More importantly, under reverse bias, the electrons in the valence band of the p-type layer are injected into the n-type layer conduction band, while the holes in the valence band of the n-type layer are injected into the valence band of the p-type layer.

The method of carrier transport across the junction interface, as discussed in section 4 is believed to be that of Ballistic transport, which occurs when carriers move between energy bands with high kinetic energy before losing energy by scattering events (*71*). When the electrons move into the accumulation region on either side of the junction, they are accelerated by a strong built-in electric field and reach velocities substantially higher than the saturated or terminal velocity. This is the so called velocity overshoot effect. The electrons eventually scatter and lose the kinetic energy acquired from the field if the accumulation region is wide enough (*71*). Since the scattering rate increases with kinetic

energy, ballistic transport happens within a very short time and within a narrow region that is generally no more than a few tens of nanometers. Electrons can move ballistically across the accumulation region only if the accumulation width is about the distance they travel without scattering and the electric field should be high (*71*). This phenomena is anticipated to produce an ohmic, linear I-V response (*6*). The resistance due to ballistic transport is determined by the transmission coefficient and the transmission coefficient depends only on the barrier shape and not on the profiles of accumulated carriers near the interface.

2.6. Existing work: experimental and modeling

Broken gap junction devices up to this point have been studied almost exclusively using heterojunction III-V materials that are epitaxially grown with good lattice matching. One of the first was Sakaki *et al.* with a junction formed by n-type In_{1-x} Ga_xAs and p-type $GaSb_{1-y}$ As_y by MBE (*72*) where x and y were varied between x=0.62, y=0.64 and x=0.16, y=0.10. The I-V measurements were done at room temperature, and the results showed ohmic behavior when x=0.16 and y=0.10 with a resistance of 6 Ω using a device area of $5x10^{-5}$ cm^2 with power levels up to 100 mA, and a projected energy gap of 0.09 eV assuming literature values for conduction band offsets, and measuring the optical band gaps via optical absorption.

Srivastava *et al.* investigated the n-type GaSb and n-type $lnAs_{0.95}Sb_{0.05}$ junctions (*73*) by MOCVD with an application for mid-IR optoelectronics sources and detectors. The devices were processed at temperatures between 400^o C and 450^o C. They measured the I-V and capacitance–voltage (C-V) characteristics at room temperature and found them to

have a tunnel diode like behavior similar to a metal-(n) GaSb Schottky barrier (device area of $7.7x10^{-4}cm^2$), with both materials having carrier concentrations around 10^{17} cm^3 and a p-n valence band difference measured at 0.67 eV using energy band data from literature.

Gualtieri *et al.* looked at (100) n-type InAs and p-type GaSb junctions grown by MBE (*74*). Samples of both sequences were grown. They performed X-ray photoemission core level spectroscopy (XPS). Carrier concentrations for both materials were around $10^{16}cm^3$. XPS showed a p-n valence band difference of ~0.51 eV for either growth order. They did not provide any electrical measurements or device area.

Collins *et al.* studied the I-V characteristics of n-type InAs and p-type GaSb junctions deposited on (100) GaAs by MBE with temperatures used up to 485^o C (*75*), and found negative differential resistance (NDR) both at room temperature and at 77^o K with current density in the $10^4A/cm^2$ range using devices with an area around $2x10^{-7}$ cm^2. The nearly identical performance at 77^o K shows that thermionic current plays a very small role in the device operation. They note that the valley after the NDR still has a higher current than is typically observed for conventional tunnel diodes but claim there is not a true barrier between the InAs conduction band and the GaSb valence band, so there is little to suppress inelastic processes from scattering electrons in the InAs conduction band into the GaSb valence band.

Mikhailova *et al.* reviewed different type II GaInAsSb/InAs and GaInAsSb/GaSb broken gap junctions grown by LPE in 1994 (*70*) and 2004 (*76*). In 1994 they found that conditions of the band overlapping at the interface are strongly influenced by light intensity and external electric and magnetic fields and determine their transport and

recombination properties. I-V measurements between 4.2^{o} and 300^{o} K for p-type GaSb and n-type GaInAsSb show ohmic profiles with resistance of 6.25 Ω (device area not specified, currents up to 100mA), while the other 3 junctions studied were rectifying. Moreover, the ohmic behavior of the p-n structure was insensitive to the doping level. They claim these devices can be useful as mid-IR detectors as well as showing ohmic I-V characteristics of an n-type GaSb / n-type GalnAsSb structure which only shows ohmic behavior under white light illumination of around 10^{-5} Ω. For the 2004 study in p-type $GaIn_{0.16}As_{0.22}Sb$ and n-type InAs they found a junction gap of 0.08 eV. I-V measurements showed ohmic behavior between 77 and 300^{o} K with a resistance of 7 Ω (device area not specified), while the other three junctions studied were rectifying with large space-charge regions. It was found with p-type GaInAsSb / p-type InAs junctions that an electron channel with a high carrier mobility was created at the interface. Both P-p and P-n devices demonstrated electroluminescence. Both a laser and a photodiode was created using these materials.

More recently, Mattias Borg *et al.* studied GaSb / InAsSb broken gap junction nanowires (*77*) deposited by MOVPE with processing temperatures reaching 470^{o} C. I-V measurements made at room temperature on a single wire (junction diameter of 56nm) show as-deposited wires are ohmic, while wires annealed at 490^{o} C in a H_2 ambient show NDR features (peak currents at 8.1 kA/cm^2) . However, they believe the un-annealed performance is due to current shorting through a nanowire InAsSb overgrowth (which is removed during the anneal) and not through the GaSb/InAsSb junction.

Kristijonas *et al.* also recently measured high performance p+-GaSb/n+-InAs junctions with specific resistivity under 2.8×10^{-7}Ω-cm^2 (*78*) grown by MBE at

temperatures up to 550^{o} C. The device area was 400 × 400 μm and the carrier concentrations in both layers were 10^{19}cm^{-3}. They attribute the increased performance to an optimized MBE growth technique, which allowed the reduction of excess arsenic on the InAs surface and the creation of InSb-like and GaSb-like bonds at the heterointerface.

There has only been one published BGJ device made of metal oxides that we know of, made by Tanaka *et al.* (*79*) using n-type In_2O_3 deposited by pulsed laser deposition on a 200 um thick p-type Cu_2O sheet made by oxidizing a copper sheet. They report ohmic I-V room temperature results down to 192 Ω (device area of $3.1x10^{-2}$ cm^2) but do not test the device further. They also report n-type ITO with Cu_2O giving a slightly more rectifying I-V curve. In_2O_3 has a band structure with a ~5eV electron affinity (*8, 80*), and band gap of 2.9 eV (*81*). Thus it could potentially form a broken gap at the junction with Cu_2O which has an electron affinity around 3.2 eV (*82*) and a theoretical band gap of 2.1 eV. They used In_2O_3 with resistivities under 2 Ω-cm and carrier concentrations above 10^{18} cm^3 and Cu_2O sheets were a polycrystalline p-type semiconductor with a hole concentration of approximately $4x10^{14}$ cm^{-3} and a Hall mobility of approximately 90cm^2/V s. Information such as grain properties, independently-measured band alignment, optical absorption spectra, etc. are not measured. The (important) thickness of the indium oxide layer is also not known. This demonstrates feasibility of a metal oxide broken gap junction however no realistic multi-junction solar cell would utilize BGJ layers in the micrometer regime due to enhanced indirect gap absorption and added series resistance. They measured ohmic specific resistivity of ~6Ω-cm^2 for In_2O_3 doping level at

$2.7x10^{18}cm^3$ or $1.1x10^{20}cm^3$. This is somewhat higher than desired for a multi-junction solar cell.

Simulations were done recently by Sang Ho. *et al.* on a BGJ device made of In_2O_3/Cu_2O (*6*) to confirm the junction would perform as expected and determine the method of transport across the junction. Numerical simulation for the BGJ required simultaneous solution of current continuity and the Poisson equation (*83, 84*), as well as a self consistent treatment of quantum mechanical transport in the tunnel junction. For this they used DESSIS – a commercially available multi physics device simulation tool for numerical simulation. Quantum transport at broken-gap junction is solved by the WKB approximation. Maximum performance conditions (i.e. trap-free absorber materials) were used. Two models were compared for carrier transport through the accumulation region: Nonlocal interband transition and ballistic transport, with both assuming an in-series mechanism of drift-diffusion of carriers from the charge neutral region to the accumulation region. After carriers move across the interface they recombine quickly and contribute current. Interband tunneling current from the valence band to the conduction band (J_{CV}) is given by

$$J_{CV} = -q \int_{0^+}^{\infty} [R_{CV}(x) - G_{CV}(x)]dx \tag{2.2}$$

where the difference between the recombination (R_{CV}) and generation rates (G_{CV}) is given as

$$R_{CV}(x) - G_{CV}(x)$$

$$= \frac{A_{CV}{}^{*}}{qk}\left(\frac{dE_V(x)}{dx}\right)\Gamma_{CV}(\varepsilon,x)\left[T_p(x)log\left\{1 + Exp\left(\frac{E_{F_p}(x) - \varepsilon}{kT(x)}\right)\right\} - T_n(0^-)log\left\{1 + Exp\left(\frac{E_{F_n}(0^-) - \varepsilon}{kT(0^-)}\right)\right\}\right]$$

(2.3)

In Eq. 3, $A_{CV}{}^{*}$ is the Richardson constant, $E_{Fp,n}$ is quasi Fermi level of the hole and electron, ε is the carrier energy, E_V is the valence band edge energy, q is the unit charge, k is the Boltzmann constant, T is temperature and T_n and T_p are the transmission coefficients at the interface which is due to velocity mismatch for electrons and holes, respectively (*85*). x=0$^-$ refers to the position where tunneling begins. They assumed that the transmission coefficients are unity since the carriers that move across the junction recombine quickly with the majority carriers. The tunneling probability (Γ_{CV}) is given by

$$\Gamma_{CV}(\varepsilon,x) = exp\left[-2\int_0^r k(x',\varepsilon)dx'\right]$$

(2.4)

where, k, ε and x are the wave vector, the energy of carriers and position respectively. The wave vector, k, is

$$k = \frac{k_C k_V}{\sqrt{k_C^2 + k_V^2}}$$

(2.5)

where,

$$k_{C,V} = \frac{\sqrt{2m_0 m_{e,h}{}^* \pm \left(E_{C,V}(x) - \varepsilon\right)}}{\hbar}$$

(2.6)

$\hbar, m_e, , m_h$, E_C and E_V are the reduced Planck constant, the effective masses of the electron and the hole and the conduction band edge energy of n-type material and the valence band edge energy of the p-type material, respectively (*85*).

For one test they varied the junction band overlap from 0.0 eV to 0.2 eV with the doping concentrations for p and n layers at 1.5×10^{19} cm^{-3} and the thickness of each layer was set to 200 nm. For the second test they used the ballistic transport model and fixed the n-layer doping at 5×10^{19} cm^{-3} and varied the p-layer from 1×10^{16} cm^{-3} to 1×10^{18} cm^{-3} the thickness of each layer set to 200 nm.

Figure 2.6 compares the I-V characteristics of the p-Cu_2O/n-In_2O_3 junction calculated using the interface interband transition model (Figure 2.6a) and the ballistic transport model (Figure 2.6b) with junction band overlap varied. Under near flat-band conditions where the band overlap is zero, both tunneling models predict linear I-V characteristics in the reverse bias region. However significant differences exist between the two model predictions when there is band overlap. Specifically, a cutoff voltage (V_C) appears for the interface interband transition model in reverse bias (negative voltage) when the band overlap is wider than 0.1 eV. Current stops flowing above this cutoff value. There is no cutoff voltage predicted with the ballistic transport model. Instead the junction is ohmic

over the calculated range, with current flowing both in forward and reverse bias. According the simulation results shown in Figure 2.6a, even if a small bias is applied, when carriers are accumulated at the interface the diffusion current by accumulated carriers cancels the drift current and thus no significant current flows. It is found that the interband transition model does not match the linear I-V characteristics observed for existing BGJ devices made to date (*70, 72-78*) however the ballistic transport model matches the I-V profile.

In the second test, the results from varied doping concentration in the p-layer show (figure 2.6c) when doping concentration is low, a peak voltage (V_P) or cutoff voltage (V_C) is observed in I-V characteristics. The peak voltage (V_P) is the voltage at which current is drops abruptly in forward bias as in a tunnel diode and the cutoff voltage (V_C) is the voltage at which the current begins to flow under reverse bias. These results show that broken-gap junctions can provide low resistance ohmic junctions, even with a relatively low dopant concentration on one side of the junction.

According to the simulation results, when the transmission coefficient is unity, the resistance of ballistic transport at the interface is lower than the series resistance of the charge neutral region. As a result, the series resistance of junction does not determine the I-V characteristics. Thus, the I-V characteristics do not depend on the width of the band overlap since the transmission coefficient is unity due to narrow accumulation width. This is the reason that a broken band-gap junction can achieve a resistance as low as $10^{-7}\Omega\text{-cm}^2$ in InAs/GaSb junctions.

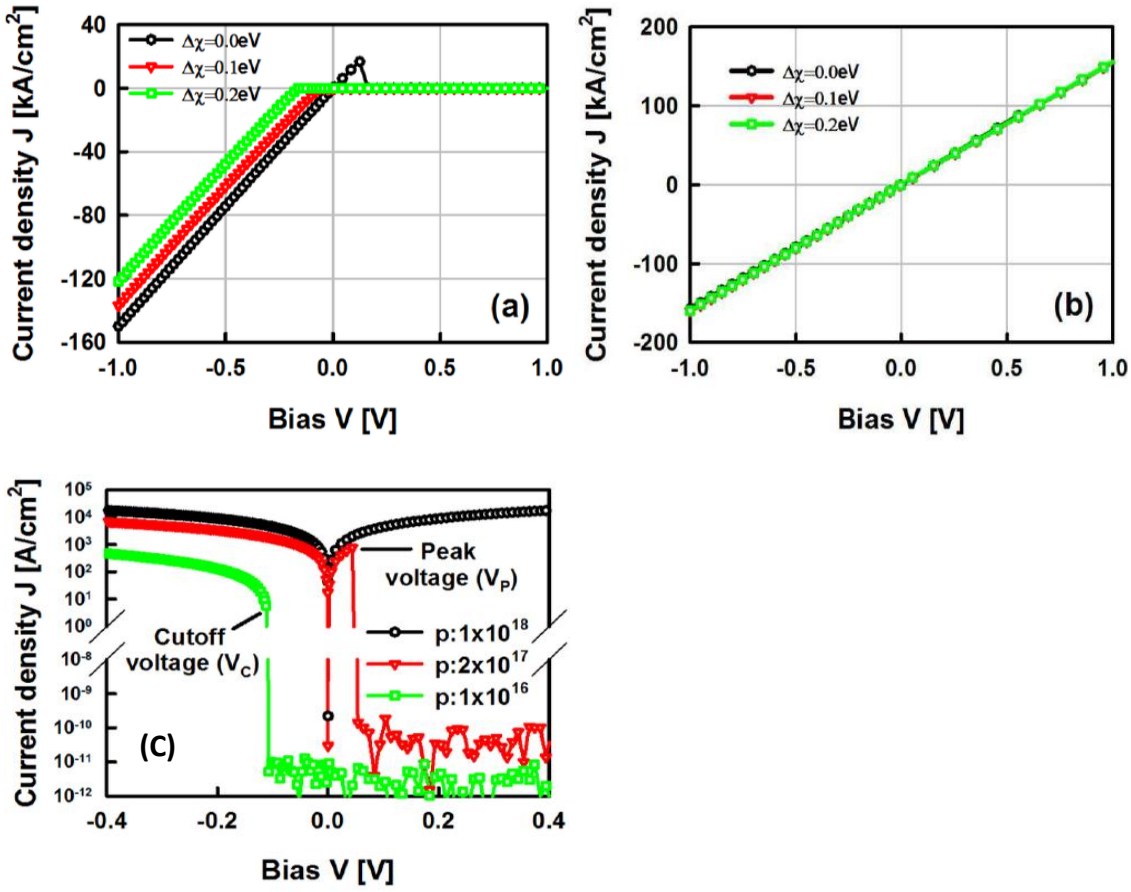

Figure 2.6: A p-Cu_2O/n-In_2O_3 junction J-V characteristics using (a) interband transition model and (b) ballistic transport model for different values of the band overlap $\Delta\chi$ between 0.0 eV and 0.2 eV. The charge accumulation widths on both sides of the junction are less than 4 nm and the maximum electric field is 1 MV/cm. (reprinted from Song *et al*. (*6*))

Chapter 3: Material Selection

3. Metal Oxides

Metal oxides are the material of choice when it comes to transparent semiconductors. They have band gaps ranging from infrared into ultraviolet and conductivity close to some metals at one end, and highly insulating glasses at the other. They can have ferroelectric and magnetic properties useful for modern magnetic media. Common applications are transparent conducting layers for LEDs, LCDs, and solar, as well as gas sensors. Many kinds of metal oxides have been studied in the last few decades, including binary oxides (i.e. ZnO, SnO_2, In_2O_3, TiO_2 , CdO, NiO, Ga_2O_3), doped binary oxides (i.e. Al-doped ZnO (AZO), Sn-doped In_2O_3 (ITO), Sn-doped Ga_2O_3, F-doped SnO_2, Nb-doped TiO_2), ternary oxides ($CdIn_2O_4$, Cd_2SnO_4, $CdSnO_3$, Y-doped $Cd_2Sb_2O_7$, $GaInO_3$, $MgIn_2O_4$, $ZnSnO_3$, Zn_2SnO_4, Cd_2GeO_4, $Zn_2In_2O_5$, $Zn_3In_2O_6$, $CuAlO_2$, $CuGaO_2$, $SrCu_2O_2$, LaCuOS, $ZnInGaO_4$), and more complex materials.

When it comes to producing oxides for practical applications, a small degree of nonstoichiometry usually exist. In many cases this composition is preferred. In nonstoichiometric oxides, the average number of atoms per unit cell is not equal to the number of sites; in the anion or the cation sublattice, there is a deficiency or an excess of the species. Nonstoichiometric oxides are generally mixed valence with nonintergral electron/atom ratios, and their electronic, optical, and other properties depend on the nature and magnitude of nonstoichiometry (*86*).

In the case of nonstoichiometric metal oxides, it is understood that defects cannot be considered to be point defects in the ordinary sense because they are assimilated into the host lattice as structural elements. One way by which anion-deficient nonstoichiometry is accommodated in some metal oxides is by eliminating point defects by the so-called crystallographic shear (*86*). A consequence of crystallographic shear is a decrease in the number of anion sites, compared to the parent structure.

The presence of extended two-dimensional defects, a common feature in transition metal oxides, is at the root of the wide ranges of stoichiometry found in many of the oxides. When one of the two participating structures in the intergrowth is proportionally smaller than the other one, it forms isolated layers distributed in the matrix of the second structure in a statistical manner. Such layers are identified as intergrowth defects (*87*).

Correlation of the structure and physical properties of metal oxides requires a description of the valence electrons that bind the atoms in the solid state (*88-90*). The two limiting descriptions of atomic outer electrons in solids are the localized electron theory (or the ligand field theory) and the band theory. Localized electron theory is applicable when interatomic interactions are weak and the electrons are tightly bound to the atomic core. Localized electrons are characterized by a large value of the energy U required to transfer a valence electron from one site to an occupied orbital on another equivalent site (of the order of the atomic ionization energy minus the electron affinity in the zero-order approximation) and a small band width W ($U >> W$). When there is appreciable overlap between orbitals of neighboring atoms, the band theory of Bloch and Wilson becomes applicable. That is, we assume that valence electrons are shared equally by all the like

atoms in the solid. In this model, U << W; in the extreme case, U=0. When U ~ W, we have the third possibility of strongly correlated electrons in solids. Outer s and p electrons that are weakly bound to the atomic core and interact strongly with neighboring atoms are described by the band model. On the other hand, 4f electrons of the rare earths, which are screened from the neighboring atoms by the $5s^2 5p^6$ electrons, are always localized in solid and are described by ligand field theory. In coordination complexes of transition metals, the d electrons are localized, being described by ligand field theory. In transition metals, the d electrons are itinerant, being in narrow d bands that overlap the broad s-p bands. In post transition metals this is not well understood yet. In transition metal oxides, we come across both localized and itinerant d-electron behavior.

3.2. Transparent Conducting Oxides (TCOs)

TCOs, which we investigated for this application, are typically made in thin film form (~<10um) for electrical applications such as wires and p-n diodes. This is due to material and deposition costs, as well the reality that for the vast majority of applications thicker films are unnecessary. For applications in which the TCO is chosen for its transparency, one must often choose a thickness that represents a good compromise between conductivity and transparency. For many of the applications of TCOs, desired material properties are carrier concentrations on the order of 10^{20}-10^{21} cm^{-3} and a band gap energy above 3 eV, however this can vary. Films for practical use have polycrystalline or amorphous structure and exhibit a resistivity on the order of 10^{-3} Ω or less and an average transmittance above 80 % in the visible. It is well known that the properties of TCOs are

generally more dependent on film thickness (*91*) than most materials. This is usually due to the effect of grain size. Large grains increase carrier mobility through reduced grain boundary scattering, and can dope the material through defect creation in certain circumstances.

It is known that the obtainable resistivity and its thickness dependence in TCO thin films are considerably dependant on the host material used and the kind and content of doped impurity as well as the deposition method and conditions.

Some films, such as AZO and ITO can be made at moderate processing temperatures with very high doping (10^{21} cm^{-3}) and large grain sizes. In these films the mobility tends to be limited by defect and impurity scattering (*92*), meaning that decreasing the carrier concentration increases the mobility. In addition to electrical properties, optical properties are also influenced by film thickness for heavily doped TCOs (*93-95*).

3.2.1. Doping

Most TCOs are n-type semiconductors. They are attractive candidates for transparent conductors (*96*), transparent transistors (*97*), and photodetectors (*98*). Other properties, such as large exciton binding energies and the availability of large substrates, give them potential advantages over other materials such as nitride semiconductors. A first-principles description of optical absorption in metal oxides has recently been put forth (*99*). This work suggests that absorption is also influenced by defect states and impurities.

The electrical conductivity of oxide semiconductors is often difficult to control. Unlike more traditional semiconductors such as Si, Ge, or GaAs, oxides are often grown

or deposited with less sophisticated growth techniques, leading to lower crystal quality and higher concentrations of unintentional impurities (*100*). It has been found that background impurities often play a dominant role in conductivity (*101-105*), however oxide semiconductor conductivity usually occurs through manipulation of the large level of native point defects, such as vacancies and interstitials.

For most oxides, several states are suitably shallow to act as donors. However, achieving high electron concentrations may be inhibited by the formation of native acceptor defects or incorporation of impurities that act as compensating acceptors. In addition, the filling of the conduction band with free carriers leads to a shift of the absorption edge (*106*), band-gap renormalization (and possible deviations from the rigid-band model (*107*)), and free-carrier absorption (*99*).

Most semiconducting oxides are naturally n-type, and have proven difficult to reliably dope p-type. Very few oxides are naturally p-type (i.e. Cu_2O, NiO, and derivatives thereof) (*108-110*). Most of the nontransition metal-based oxides have valence bands that form from filled oxygen 2p orbitals and conduction bands that form from metal s orbitals. In transition metal-based oxides the valence band oxygen relationship is the same but the conduction band is determined by the nature of the metal d states, (i.e., localized or itinerant) (*111*).

The difficulty lies in the fact that the valence band energies are far from the vacuum level, which makes it difficult to introduce holes into the valence band via acceptor dopants, and because various compensation mechanisms will be activated to lower the energy of the system by filling the holes with electrons. In addition, valence bands composed of highly localized oxygen 2p orbitals give rise to bands that have small

dispersion and heavy hole masses. Even if holes can be introduced, small polaron formation may thwart attempts at achieving p-type conductivity (*112*). In comparison the native p-type oxides have valence band maximums that are significantly closer to the vacuum level.

3.2.2. Other characteristics

Nontransition metal oxides are diamagnetic insulators under ordinary conditions. Since the intrinsic activation energy for electronic conduction is higher than the energy required for the creation and migration of point defects, ionic conduction predominates over electronic conduction in many of these oxides at moderately high temperatures. Pure transition metal oxides with the metal ion in a d^0 electronic configuration exhibit intrinsic electronic conduction only at high temperatures. They may also show spontaneous ferroelectric distortions and lose oxygen at higher temperatures. The nature of electron conduction depends on the strength of electron-phonon coupling and the width of the conduction band derived from metal d states. Transition metal oxides with partially filled d bands can be metallic or insulating, can exhibit temperature-induced nonmetal-to-metal transitions, and can vary magnetically from Curie-Weiss to Pauli paramagnetism.

3.2.3. Binary vs. Ternary or higher Oxides

One advantage of using binary compounds as TCO materials is the easier control of the chemical composition in film depositions than found when using multicomponent oxides. In addition, it is well known that TCO thin films with high transparency and conductivity can be prepared using binary compounds without the use of any intentional

impurity doping (*113, 114*). The resulting films are n-type degenerate semiconductors with free electron concentrations on the order of 10^{20} cm^{-3} provided by native donors such as oxygen vacancies and/or interstitial metal atoms. However, since TCO films without intentional impurity doping were found to be unstable when used at a high temperature in oxidizing atmospheres, binary compounds without impurity doping have proved unusable as practical transparent electrodes (*115, 116*). Ternary oxides have also shown a diverse range of electrical and magnetic properties.

3.2.4. Theoretical Calculations

Density Functional Theory (DFT) (*117, 118*) is now commonly employed to study the electronic nature of semiconductors. Traditionally, functionals such as the local density approximation (LDA) or the generalized gradient approximation (GGA) have been used, producing accurate results for many structural and energetic properties not only of bulk materials but also of surfaces, interfaces, and point defects (*119, 120*) however they typically fail when it comes to wide band gap semiconductors. Calculated band gaps are frequently significantly less than experimental values (i.e. 1 eV vs. 3 eV) and this problem makes it difficult to calculate defect energy levels and their formation energies. Attempts have been made to correct these calculations (*120-124*), however many have missed the mark, with the exception of hybrid functionals (*125*). The general idea of this class of functional is to mix in a portion of exact exchange with the exchange-correlation functional of a standard DFT-GGA functional. This approach is capable of producing structural properties as good as or superior to those obtained with LDA or GGA, but in addition the electronic structure is significantly improved, including the

band gap, reproducing the experimental transition levels of a number of defects and impurities in conventional semiconductors (*126-131*).

3.2.5. Amorphous materials

Since the deposited oxides may be amorphous, nano crystalline, or poly crystalline, it is important to understand the effects of crystal structure. In crystalline solids the atoms are arranged with both long range order and short range order. Amorphous materials have only short range order, however atoms are not distributed 'randomly' (*132*). Because of this, amorphous materials tend to be less dense than crystalline ones, giving rise to unique properties such as the direct band gap and high optical absorption coefficient seen in amorphous silicon while crystalline silicon has an indirect band gap and a low optical absorption coefficient.

Typically most metal oxides qualify as ionic-bonding solids however this assumes perfect nucleation during growth. In most thin film metal oxide growth techniques, some amount of long range van der Waals bonding occurs. Because of this they also tend to have a larger density of defects. The knowledge of most materials is derived from their calculated perfect crystal structure and reinforced by comparing parameters derived experimentally through near-perfect crystalline material. Unfortunately, the methods used to understand and manipulate the behavior of crystalline solids don't work well with amorphous solids. While knowledge of the later lags the former, much has been learned. Random Close Packing theory (*133-136*) is typically used to describe atoms with ionic

like bonding and Continuous Random Network (*137*) is used to describe covalent bonded solids.

When it comes to modeling amorphous material, a reasonable structural model must be obtained however no currently conceivable set of experiments implies a unique model (*138*). Many authors cite correlation of their results with a single experiment such as diffraction, but typically ignore other experiments. For this reason the results of amorphous material modeling are treated with skepticism.

3.2.6. Band Conduction and Variable Range Hopping

A more common issue that has become important in disordered/amorphous solids is that of Anderson localization. In the classical band theory electrons in a solid are assumed to be distributed among a set of available stationary states following the Fermi-Dirac statistics. The states are given by solutions of the Schrödinger equation which utilize the crystal potential. The latter reflects the translational periodicity of the structure. The electronic structure of highly disordered or doped oxides (with high impurity concentration) cannot be described in terms of the normal band structure because disorder can localize electron states. The criterion for localization is that the energy difference between localized sites be greater than the bandwidth. Mott pointed out that the boundary between localized and extended states (the mobility edge) is sharp and that electrons in localized states move by a phenomenon known as variable-range hopping. Some metal oxides have been known to exhibit Anderson localization and variable-range hopping when produced at low temperature in the amorphous state.

In the localized electron model the insulating ground state of solids is predicted. At finite temperatures, electron-phonon and electron-electron interactions become important, especially when the bands are narrow, as in the case of d bands. Considerable work has been carried out on the effect of electron-phonon interactions on the transport properties of oxide materials. The strength of the electron-phonon interaction (the polaron) is represented by Frohlich's coupling constant. If the interaction is sufficiently large, charge carriers move along with the associated polarization (small polaron) which produces a small thermally activated mobility.

Electrical transport properties of oxides provide useful criteria for distinguishing localized and itinerant electrons in solids. Thus, the temperature dependence of drift mobility μ for collective electrons is different from the behavior for small polarons. For collective electrons, μ goes as $T^{-3/2}$. When the bands are narrow, mobility becomes thermally activated $\mu \sim e^{-Ea/kT}$ where E_a is the activation energy for hopping. The mobility is small (<0.1 cm^2/Vs) for localized semiconductors exhibiting hopping conduction and large (>1 cm^2/Vs) in band conduction.

3.2.7. Picking the materials:

When it comes to picking the specific type of metal oxide materials to use, the principle question is identifying the material pair whose band structures produce a broken gap, and also align with the devices that the broken gap device is intended to couple. As identified in section 2.3, a p-type material must have a valence band with a higher energy

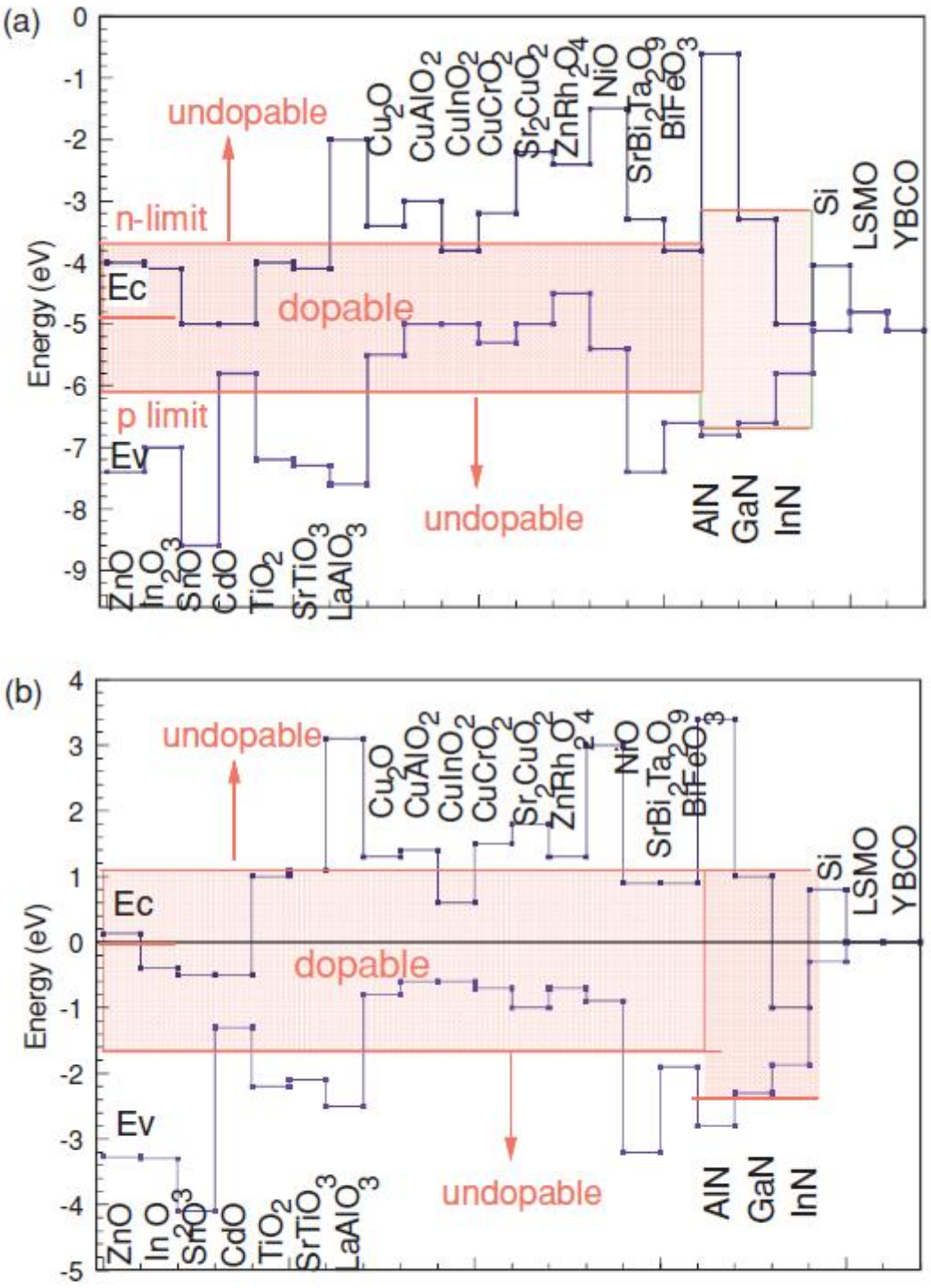

Figure 3.1 from ref (*9, 10*). (a) Valence and conduction band energies of various oxides vs vacuum level, with the doping limits, showing the dopable and undopable cases. (b) Similar plot, with the oxide bands aligned using their charge neutrality levels (CNLs).

than the conduction band of the n-type material (or perhaps less than .3 eV overlap), which for nearly all confirmed metal oxides is no higher than ~5.5 eV (*8*). In addition, the work function of the nondegenerate oxide should be within +/- .3 eV of the adjoining upper cell layer work function, and since CIAGS solar absorber has a work function around 4.0 eV this restricts the type of p-type material to 3.7 – 4.3 eV. Robertson and Clark found that oxides that could potentially be doped p-type (*10*) (figure 3.1). Only Cu_2O, $CuAlO_2$, $CuInO_2$, $CuCrO_2$, $SrCu_2O_2$, $ZnRh_2O_4$, and NiO are candidates with a valence band less than ~5.3 eV. All of these materials can be theoretically doped within the necessary range, however Cu_2O and $CuAlO_2$ have experimentally and theoretically confirmed these values while NiO shows high electrical instability (*139*). To minimize optical absorption, the material should have direct band gaps ideally above the visible spectrum of 3 eV, but lower band gap materials could be utilized for multi-junction solar cells where the high energy photon energy flux through the cell is reduced due to higher cell absorption. With these considerations $CuInO_2$ with a gap of 1.4 eV is not going to be useful. NiO has a high work function, over 5.2 eV (*140*), eliminating it from consideration for a broken gap device. As of this writing, little is known about $SrCu_2O_2$ other than it is polycrystalline at growth temperatures over 400^{o}C and shows mixed phase growth by PLD (*141*), both undesirable qualities for our application. $CuCrO_2$ is polycrystalline at higher growth temperatures of 500^{o}C and Mg doping worsens this (*142*). Little is also known of $ZnRh_2O_4$, but it has a less than optimal band gap of ~2.2 eV (*143*). In contrast, thin film $CuAlO_2$ and Cu_2O have been studied by many groups in the last decade. Both have reasonable band structure for this application. $CuAlO_2$ has shown an amorphous structure with high thermal stability up to 700 ^{o}C (*144*), making it the most

attractive candidate for resisting the high temperature needed for the top cell growth in a tandem solar device. Thus we will focus $CuAlO_2$ as the optimal p-type material while also considering Cu_2O due to its ease of fabrication and reproducibility.

Minami *et al.* (*8*) reviewed the major electrical and optical properties of the n-type metal oxides. Because of the p-type materials we chose, with valence bands of 5 to 5.3 eV we are restricted, as stated in section 2.3, to picking an n-type material with a conduction band at least 5 eV in order to create a low resistance BGJ device, and allowing for up to 0.3 eV overlap. As can be seen in figure 3.2, meeting the electron affinity requirement restricts the functional materials to $ZnSnO_3$ and $GaInO_2$, which also have a band gap larger than the visible spectrum (note in the figure shown, the work

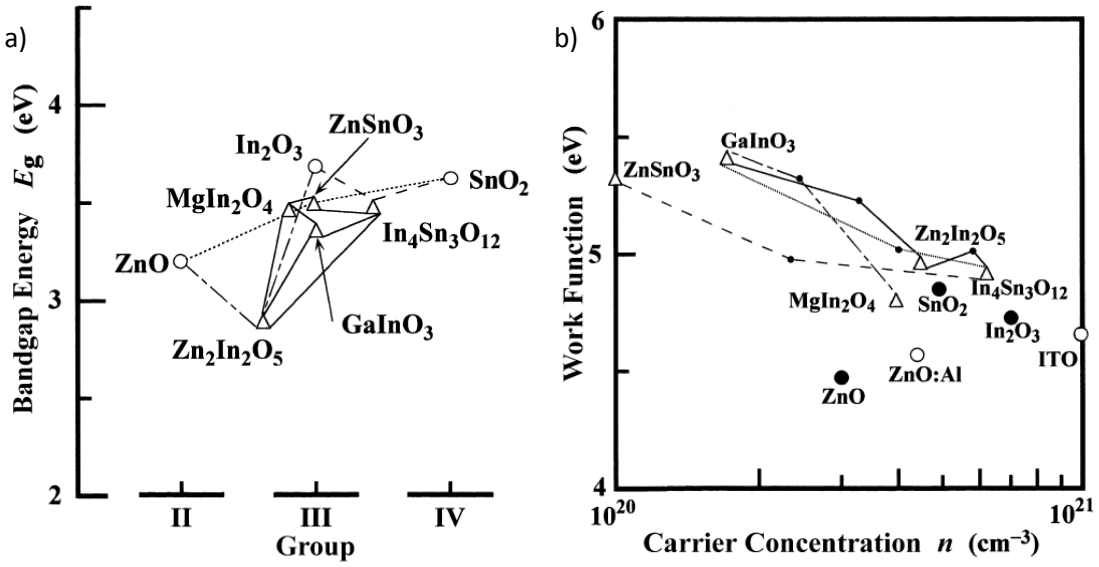

Figure 3.2 from ref (*8, 9*). (a) shows the bandgap energy of TCO materials: binary (○) and ternary compounds (Δ) and multicomponent oxides (lines), while (b) shows the relationship between work function and carrier concentration of TCO films: binary (○ , ●) and ternary (Δ) compounds and multicomponent oxides (•) prepared with a composition of 50 wt%.

function approximately equals the electron affinity since the materials are heavily doped).

In addition to energy band requirements, there is the very important issue of manufacturing reproducibility and stability of materials with the former often being dependent upon trace elements in the material. For example, it is well known that nominally undoped ZnO bulk crystals exhibit native n-type conductivity. In spite of intensive research over the past decade, however, there is still no consensus on whether the native n-type conductivity originates from intrinsic or extrinsic defects. It was initially assumed that oxygen vacancies affected conductivity, due to experiments involving oxygen partial pressure adjustment (*145-148*), however it has more recently been shown by a number of approaches that oxygen vacancies in ZnO are actually deep donors (*149-151*). Nominally undoped SnO_2 thin films and bulk crystals typically exhibit n-type conductivity as well, claimed to be due to Sn interstitials or oxygen vacancies (*152, 153*) with the later based on conductivity changes correlating to annealing oxygen pressure (*154*). First-principle calculations (*154*) show oxygen vacancies are deep donors, and that Sn interstitials have high formation energies, all of which point to native defects not being the dominant source of conductivity. By focusing on oxides with intentional extrinisic doping we can marginalize these issues.

Additionally one must consider the stability of materials in different environments. TCO films such as ZnO, ITO, and SnO_2 tend to have limited applications because they are unstable chemically and/or thermally in certain environments. ZnO films are more stable in activated hydrogen environments than other TCO films (*115, 155, 156*) however, they are not stable in high-temp oxidizing environments and chemically

unstable in acidic and basic solutions (*157*). SnO_2 films show high stability in acidic and basic solutions and in high-temp oxidizing environments, but they are easily reduced by hydrogen activated in plasma or at high temperatures (*155, 158-160*). These problems are exacerbated when the materials lack impurity doping (*115, 161*). $ZnSnO_3$ films, as will be shown more in section 3.2 have the advantages of both ZnO and SnO_2 in stability.

Finally when it comes to making a thin film suitable for large area mass production applications, such as solar technology one must also consider the types of elements used. In this case $ZnSnO_3$ stands out over $GaInO_3$, which uses the rare-earth element indium and thus is subject to the anticipated large price increases over the coming decades. For these reasons $ZnSnO_3$ is the material of choice for our BGJ devices.

3.3. N-type materials: Zinc-Tin-Oxide

Zinc stannate ($ZnSnO_3$ or ZTO) is a multifunctional material, which typically has a structure of perovskite oxides, however it has been produced in other structural forms. Its related compounds have attracted considerable attention due to application in various fields, such as gas sensors, moisture detectors, electronics materials (*162-166*) and plating additives (*167*).

Zinc-stannate can be made with a trigonal $LiNbO_3$-type structure (*3*), or in ilmenite (IL)-type structures (*5*), or hexagonal and cubic perovskite-type structures (*163, 164, 168-172*). Kovacheva and Petrov et al. (*5*) argue that from a general crystallochemical point of view $ZnSnO_3$ cannot adopt a perovskite structure under normal conditions since the ionic radius of Zn^{2+} (0.74 Å) (*173*) is too small, however non-equilibrium film

deposition conditions such as sputtering would be exempt from this restriction. They claim an ilmenite structure is more plausible however, and go on to demonstrate one by an ion exchange reaction. Their XRD data is shown in figure 3.3.

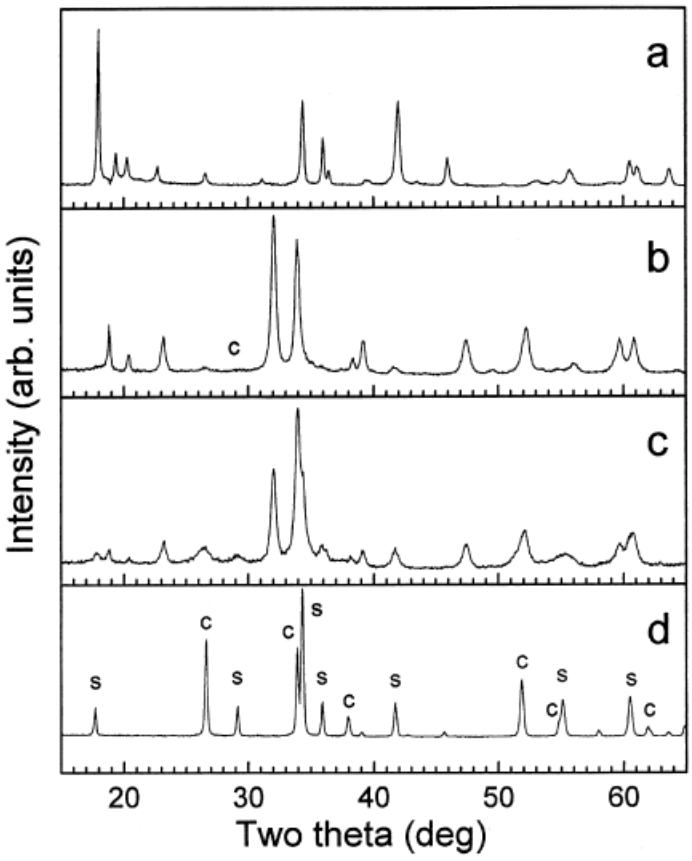

Figure 3.3 from ref (*5*). XRD spectra of (a) Li_2SnO_3 (LT). (b) $ZnSnO_3$ obtained at 350 ^oC, (c) $ZnSnO_3$ partly decomposed at 600 ^oC; (d) two-phase mixture of Zn_2SnO_4 and SnO_2 obtained from $ZnSnO_3$ after heating at 1000 ^oC for 3 h. Phase notation: c – cassiterite SnO_2; s – spinel $ZnSnO_4$.

Gou et al. (*15*) calculated the total energies of all known theoretical structures of $ZnSnO_3$ (see Table 1) and found them to be in good agreement with experimental results (*3, 5*). They found the LN-type structure has the lowest total energy at T=0 K followed by

the IL-type; whereas total energy of the cubic perovskite structure is much larger than that of LN-type structure. The larger energy difference suggests that the cubic perovskite phase of $ZnSnO_3$ is difficult to form under ambient conditions where as LN-type or even mixed LN/IL-type should be the easiest. The crystal structure of $ZnSnO_3$ (shown in figure 3.4) forms an octahedral framework, with Sn and Zn octahedral sharing both faces and edges with one another, each Sn octahedron sharing corners with other Sn octahedral, and each Zn octahedron sharing corners with other Zn octahedral. The cation sequence along the c-axis is Sn-Zn-(Vacancy)-Sn-Zn-(Vacancy)-Sn…The selected interatomic distances and the bond angles of $ZnSnO_3$ are listed in Table 1 … This compound contains only the cations with the electronic configuration of $(n-1)d^{10}ns^0$, Zn^{2+}, and Sn^{4+}.

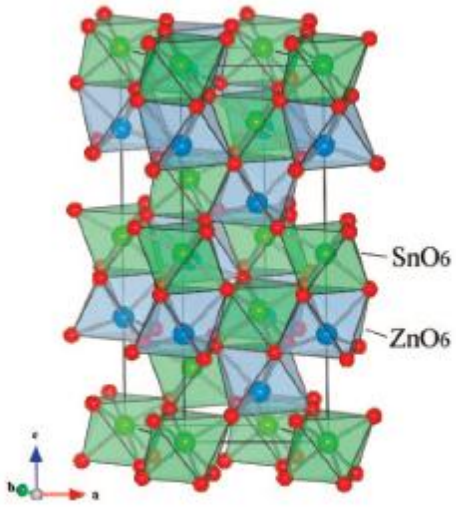

Figure 3.4. Crystal structure of $ZnSnO_3$ in the Hexagonal space group R3c. Reprinted from (*3*).

Phases	Space group	Lattice parameters	ΔE	ΔH_f
$ZnSnO_3$	*R*3*c*	a=5.387(5.262),[a] c=14.344(14.003) [a]	0	0.15
	R-3	a=5.419(5.284),[b] c=14.348(14.091) [b]	0.09	0.23
	Pm-3*m*	a=4.086	3.76	3.90
	R-3*c*	a=5.429, c=14.387	0.11	0.25
	Pnma	a=5.422, b=7.994, c=5.428	0.22	0.36
	Cmcm	a=3.082, b=9.934, c=7.653	0.85	1.00

Table 1. Calculated lattice parameters, a(Å), b(Å), and c(Å), difference in total energy, ΔE (eV/f.u.), and heat of formation ΔH (eV/f.u.) of $ZnSnO_3$ with all the hypothetical structures and compared with experimental data. Reprinted from ref (*15*).

[a]Reference (*3*)

[b]Reference (*5*)

It has been shown by petrographical and chemical analyses (*174*) that the only stable phases in the ZnO–SnO_2 system at high temperature (>1000°C) are Zn_2SnO_4, ZnO and SnO_2, and that if crystalline $ZnSnO_3$ exists, it should appear and be stable at relatively low temperature – below 600°C (*5*). However the preparation of $ZnSnO_3$ by the thermal decomposition of $ZnSn(OH)_6$ demonstrated that amorphous $ZnSnO_3$ is stable within the temperature range 350–750°C (*175*). The density of $ZnSnO_3$ is 5.32 g/cm^3 in the amorphous state and 6.76 g/cm^3 in the crystalline state (*176*). The latter is closer to the density of pure SnO_2 of 6.9 g/cm^3. ZTO films tend to be amorphous when there is more than 20% of each metal present (*14*, *177-179*). When the amorphous films are annealed to the point of crystallization, mixtures of ZnO, SnO_2, and Zn_2SnO_4 are seen (*14*, *179*). The intermediary binary phases influence the electrical properties of ZTO films, as seen by the fluctuations of ZTO films as a function of composition. But, the trends observed from

the various reports are not consistent with one another, so the influence of the bulk phases is unclear. Of all the sputtered films studied, the highest reported conductivity of a ZTO films with approximately stoichiometric $ZnSnO_3$ composition has been 250 S/cm (*177*), which is much higher than needed for a thin BGJ device. The conductivities of ZTO films are typically an order of magnitude less than the most conductive TCOs such as ITO and ZITO. The band gap for crystalline $ZnSnO_3$ devices has been found to be above 3.35 eV (*180*).

a) Vacuum-deposited properties of zinc-stannate films: (ceramic sputtering)

Minami *et al*. developed a process for the deposition of zinc-stannate by RF magnetron sputtering in a mixture of argon and oxygen with 50W power utilizing a custom made target made from a mixture of ZnO and SnO_2 powders (99.99% purity) to form compositionally correct $ZnSnO_3$, however they characterized it as being mixed phase (*177*). The total sputter gas pressure and the partial pressure of the oxygen were varied from 0.4 Pa to 1.2 Pa and from 0 to $5x10^{-3}$ Pa, respectively. Most of the depositions were done with the substrates not intentionally heated but reaching about 140^{o} C during material deposition, although some depositions were done at a substrate temperature of 300^{o} C. All films deposited below 300^{o} C were found amorphous with film thicknesses between 300 and 500 nm. The electrical and optical properties of the films depend strongly on sputter gas pressure, oxygen partial pressure, and substrate temperature. The best overall performing films had resistivity down to $4x10^{-3}$ Ω-cm and an average transmission over 80 % in the visible range. Band gap not measured but likely over 3 eV to get this optical performance. General trends demonstrated oxygen partial

pressure improving transmittance. Resistivity also increased with oxygen partial pressure, however room temperature-deposited films showed it decreased when adding oxygen initially, while later at higher levels it increases resistivity. They also confirmed that zinc-stannate films had almost no change in resistance when heated up to 400^{o} C in air, unlike SnO_2 (*161*) or ZnO (*115*) films, and performed etching experiments to confirm chemical stability.

The oxygen partial pressure trend was confirmed by Jin *et al.* (*13*) (Figure 3.6), who also used RF magnetron sputtering with a ceramic target sintered at 1400^{o}C with 1:1 ZnO : SnO_2 with a diameter of 8.5 cm. The substrate-to-target distance was 5 cm. The Ar pressure was kept at 1 Pa and the oxygen pressure ranged from 0 to 6 mPa. All films were deposited at room temperature onto glass and Polypropylene adipate thin film substrates. The film growth rate increased linearly with applied target power, however resistivity increased exponentially below 120W. They claimed this was due to insufficient kinetic energy for adatoms to be incorporated effectively. At higher pressure the mobility is sufficient but there are fewer oxygen vacancies and so the carrier concentration decreases, however film thicknesses where not given and mobility and carrier concentration were not quantified. The optimal film was found to be 400nm thick and amorphous.

In their next paper Minami *et al.* (*181*) deposited films using substrate deposition temperatures up to 500^{o}C. The oxygen partial pressure was varied from 0 to 8 mPa. They found that the films were still amorphous, and that films were relatively unaffected by post-deposition anneals in inert gas or vacuum up to 700^{o}C. The best film properties were similar to the previous attempt. They also confirmed Jin *et al.*'s (*13*) finding that

increasing the oxygen partial pressure increases mobility, likely through decreased oxygen vacancies and so films had less scattering. The carrier concentration overall had a slight decrease. They also showed that increasing oxygen partial pressure with films deposited at 300^{o} C had little impact. This points to the easier ability of oxygen to be incorporated into metal films at higher temperatures. Lateral variation in film resistivity was a factor of 5 or less, depending on the deposition gas pressure parameters.

b) Co-sputtering from ceramic targets

Moriga et al. (*182*) investigated the deposition of ZTO films using co-sputtering of ceramic targets using parallel opposed magnetron targets where the substrate is held to the side (the SnO_2 target was doped 3 wt% with Sb_2O_5 to improve electrical conductivity during sputtering), which they claim confines energetic electrons and the off-axis perpendicularly-placed substrate does not get bombarded by energetic oxygen ions resulting in damage-free film growth. The resulting composition vs. resistivity had a similar overall trend to Minami's work, but with a higher offset, excluding the zinc-poor data, which was substantially lower here. The former lends credence to the idea that energetic oxygen and/or electrons are actually useful in creating defects.

c) Reactive sputtering metallic targets

In contrast to the ZTO films Minami made by ceramic sputtering, reactive sputtering of metallic zinc/tin targets offers different manufacturing opportunities, and was investigated by Hong *et al.* (*183*) using an alloy target to make films for transistors. He found the optimal oxygen partial pressure to be 0.8 mTorr and total pressure of 30 mTorr with RF or DC power at 50 W (2 inch diameter target), target-to-substrate distance 7.5

cm, giving a film about 50 nm thick. After a 500^{o} C anneal the films had peak mobilities around 31 cm^{2}/Vs. Optical properties were not reported.

d) Material stability

Wang *et al.* (*180*) studied the effects of post-deposition annealing on ZTO films deposited under 1.33 Pa pressure argon and 125W from a 2inch diameter target at room temperature. The films were about 210nm thick. Annealing conditions were a 5% H_2-N_2 forming gas, O_2, and O_2 followed by H_2-N_2 forming gas for 1hr. He found almost no change of film morphology after anneals, however transmission and band gap increased slightly. The forming gas dropped the resistivity by about an order of magnitude while the oxygen increased it by an order of magnitude. Using X-ray Photoelectron Spectroscopy (XPS) measurements they show the two-stage O_2/forming gas treatment causes the reduction of Zn^{2+} to Zn, which not only suppresses the reduction of Sn^{4+} to Sn^{2+} but also results in the oxidation of Sn^{2+} to Sn^{4+}. Choi et al. (*184*) looked at the affect of rapid thermal anneal using films made by RF magnetron sputtering at room temperature at 100W power, Ar at 20 sccm and pressure of 2 mTorr on glass substrates. The films were RTA at 10^{-3} Torr for 10min at temperature between 300 and 600^{o} C. He used a ZnO (50 atomic%) target. Although the composition of his films was not reported, Minami showed that the film stoichiometry is very similar to target composition, with only a slight reduction in tin. His results show resistivity decreasing with RTA by over an order of magnitude at 600^{o}C mostly due to a carrier concentration increase, but the mobility improved as well. Optical properties did not change appreciably. RMS roughness smoothed from ~2nm to ~.6nm (which they claim increased film density). XRD showed that the films remained amorphous. The Ultraviolet Photoelectron

Spectroscopy (UPS)-measured work function shifted from 3.81 eV to 4.68 eV. Films overall did not reach the electrical performance that others had achieved.

Ko *et al.* (*14*) characterized the XPS binding information of ZTO films made by co-sputtering ZnO and SnO_2 targets with varying Sn concentration (RF power 40W and 38W respectively with 0.13 Pa argon and oxygen mixture) onto glass substrates. As-deposited (amorphous) and annealed films show very little difference from thermal treatment (Figure 3.5). From XRD measurements, only films above Sn = 50 atomic % displayed $ZnSnO_3$ peaks. For comparison, the reference zinc $2p_{3/2}$-peak energy is at 1022.4 eV for ZnO, pure zinc at 1021.5 eV, and zinc-hydroxides at 1023.4 eV, while for tin $3d_{5/2}$-peak energy is at 486.1 eV for SnO, 487 eV for SnO_2, and 484.8 eV for pure tin

(*185*).

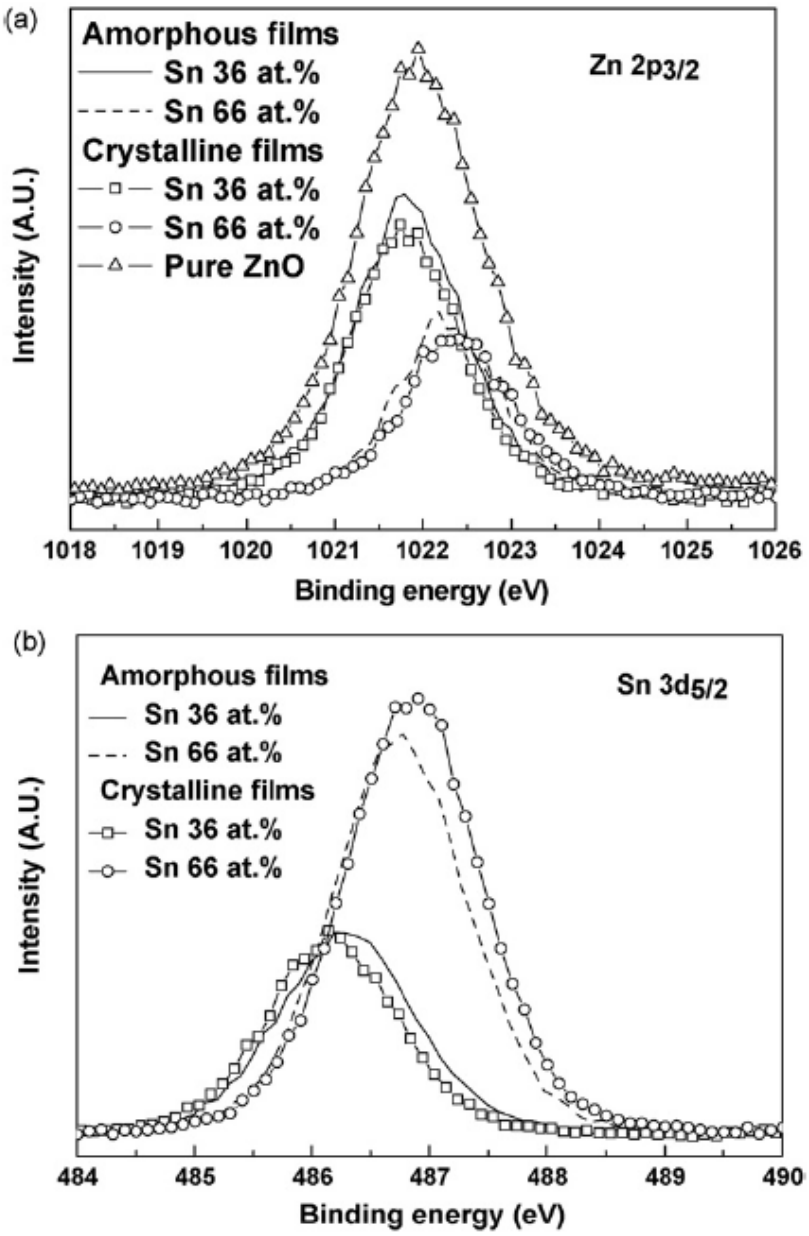

Figure 3.5. XPS spectra of (a) Zn $2p_{3/2}$ and (b) Sn $3d_{5/2}$ core shells obtained from the amorphous (as-prepared) and the crystallized (annealed at 650 ^{o}C) films containing 36 and 66 Sn at. %. For comparison, the spectrum from pure ZnO is also included in the Zn $2p_{3/2}$ spectra. Reprinted from (*14*).

Ko et al. (*186*) studied amorphous ZnO-SnO_2 films (overall zinc-deficient composition) using under 42 W of RF power to each ceramic target, with 0.133 Pa pressure with 1% O_2 with resulting films 200 nm thick. Post-annealing was carried out in vacuum and air up to 600^o C for 1h. Results for as-deposited films showed extremely smooth surfaces with rms surface roughness under 0.3 nm typically, and annealed films increasing to 0.5 nm. XRD revealed increasingly high crystallization temperatures with more zinc composition. Prior to crystallization the mobility increased marginally and carrier concentration increased substantially up to 300 or 400^o C, but both declined substantially with higher temperature annealing. They claim the decrease is due to poor crystallinity and free carrier trapping at grain boundaries forming a double-Schottky potential barrier (*187*).

Satoh *et al.* looked into the affect of doping Zn_2SnO_4 with small levels of Al, which could be important for our research because of the possibility of aluminum diffusion into the zinc-stannate layer. They used RF magnetron sputtering at 200W, 2 Pa argon with a 400^{o}C substrate temperature to deposit 370 to 510 nm thick films onto silica substrates. The results show that while aluminum has a somewhat moderate affect on optical properties, the electrical properties change drastically, reducing conductivity by six orders of magnitude when doped at 5.3 atomic % Al, with both mobility and carrier concentration dropping. No data on copper doping exists at present.

Moon *et al.* (*188*) investigated the doping of CuO into varied SnO_2–ZnO fabricated in the form of a pellet by sintering at 800^{o}C for 3 h, subsequently coating them with CuO, and heating them multiple times up to 750^{o}C for up to 3hrs. This also has bearing on our

work due to the copper oxide present in the p-type material. The electrical conductivity was lowered with CuO doping by roughly one to two orders of magnitude at room temperature for ZnO and SnO_2 pure films, and can be extrapolated to be at least an order of magnitude reduction for films closer to $ZnSnO_3$ composition based upon results from others.

Kim *et al.* (*189*) studied the effects of hydrogen doping on electrical properties of ZTO films made by co-sputtering, and found that with a moderate addition of H_2 in the sputtering gas, the carrier concentration increased in the films 57 % and resistivity dropped by 27 % but at the price of decreasing the optical transmittance. This they claim is from the presence of shallow hydrogen donors and oxygen vacancies causing SnO localized states.

Kulczyk-Malecka *et al.* looked at the possible diffusion of silver coatings into zinc stannate (*190*) by reactively sputtering a zinc/tin alloy target (using either DC or pulsed DC magnetrons) onto glass substrates, varying chamber pressure, oxygen level, and magnetron configuration. Some samples were first annealed at 650^{o}C and analyzed, and then coated with silver and then all samples annealed at 250^{o}C. Results show silver had a diffusivity in the range of 10^{-21}-10^{-20} m^2/s annealed and as-deposited samples while sodium (from the glass substrate) diffused 1 to 2 orders magnitude faster through 650^{o}C annealed coatings and is influenced by temperature.

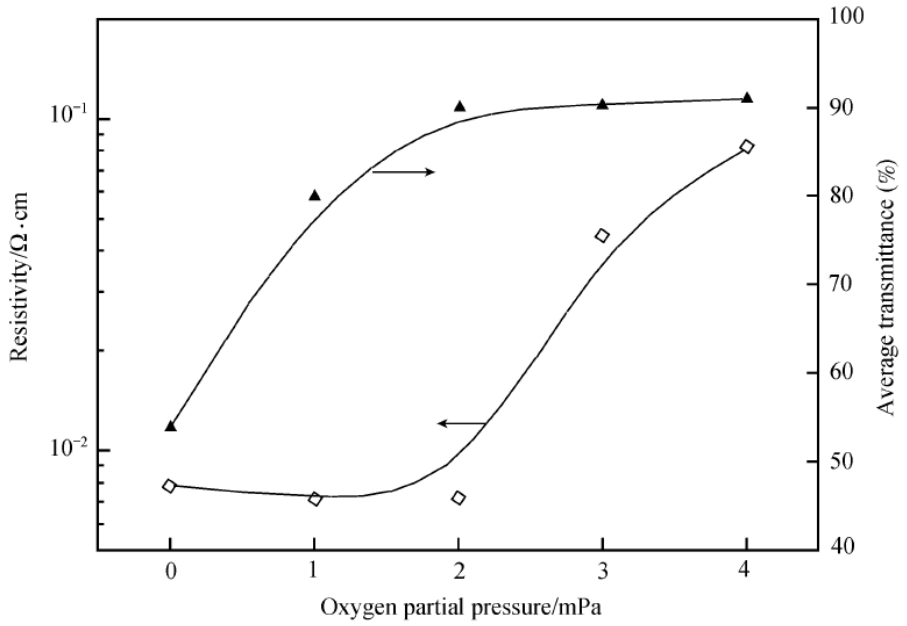

Figure 3.6. The resistivity and average transmittance as functions of the oxygen partial pressure for the Zn-Sn-O films. Reprinted from (*13*).

e) Theoretical calculations

Multiple groups have performed first-principle calculations on $ZnSnO_3$ (*17, 191-193*). Wang *et al.* performed the first study using DFT Full-potential linearized augmented plane-wave method with generalized gradient approximation for the hexagonal R3c structure. The structure parameters obtained agree well with the experimental results for synthesized polycrystalline $ZnSnO_3$, however the electronic structures point to a 1.0 eV direct band gap, which is far below the experimental 2.8 – 3.9 eV reported (*180, 194-196*). They attributed the calculated optical spectra to be due to transitions from valence band O 2p levels to conduction band Sn 5s levels or higher conduction band Zn 3d levels in the low-energy region, and from O 2p to Sn 5p or Zn 4p conduction band in the high-energy region.

Zhang et al. (*192*) also looked at the LN-type structure using plane-wave pseudopotential DFT code to simulate ground-state calculations, linear-response computations of phonon frequencies, Born effective charges, spontaneous electric polarization, and dielectric and piezoelectric tensors. Their results show hybridization between Zn 3d and O 2p states from DOS data, while the Mulliken charge population shows this compound is mixed ionic–covalent. They found that the Z* of Zn and O atoms show relatively large anomalous behavior and the large spontaneous polarization is mainly attributed to the large displacement of Zn atoms because of the mixed ionic–covalent character between the Zn–O bonds. The optical dielectric tensor is nearly the same; however, the static dielectric tensor along and perpendicular to the polarization direction shows strong anisotropy. The large dielectric constants and nonlinear optical susceptibilities indicate that the LN-type $ZnSnO_3$ would be a candidate as a high-performance dielectric and nonlinear optical material.

Nakayama et al. (*193*) reproduced the crystal structure of LN-type $ZnSnO_3$ using first-principles computations utilizing the generalized gradient approximation with the projector-augmented wave method, spin polarization calculation, relaxation and the final energies of the optimized geometries were recalculated so as to correct for changes in the plane-wave basis during relaxation. Results confirmed the qualitative accordance of the pressure driven phase-transition from Zn_2SnO_4+SnO_2 mixed phases to the LN-type $ZnSnO_3$ phase. The electronic structure analysis and calculations confirmed the strong ionic character of Zn and Sn ions observed by Zhang et al.

Most recently Körner et al. (*17*) did first-principle studies of stoichiometric and nonstoichiometric crystalline and amorphous Zn–Sn–O systems (c-ZTO, a-ZTO) using the self-interaction correction-based LDA and the computational mixed-basis pseudopotential method. A 60 atom super cell of crystalline $ZnSnO_3$ was used giving an integrated total of 36 states in the conduction band. The structure was the hexagonal Bravis lattice (space group R3c) with a unit cell volume of 342 $Å^3$. They were able connect structural features with electronic properties and found that defect levels originating from oxygen vacancies are too high in energy to be responsible for levels above the valence band edge. The reported a more reasonable band gap for crystalline ZTO of about 3 eV, which is in the range of experimentally reported values. Their data shows from the energetic stability of c- and a-ZTO compounds with different Zn/Sn ratios show that the decomposition of $ZnSnO_3$ into Zn_2SnO_4 and SnO_2 at sufficiently high temperatures is conceivable, confirming experimental data by others. Their DOS results point to a lowering of the mass density of an a-ZTO sample leads to an increase of the conduction band edge (Figure 3.7).

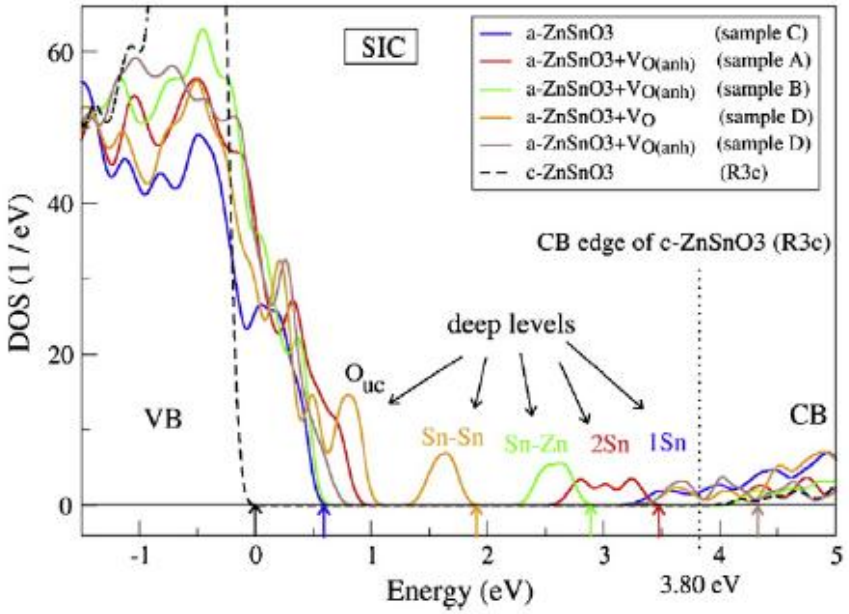

Figure 3.7. Total density of states of c-$ZnSnO_3$ and amorphous supercells which partially contain oxygen vacancies (V_O). The tails of about 0.5 eV width above VB originate from the O 2p disorder. Partially higher levels stem from undercoordinated oxygen atoms (O_{UC}). The deep levels lying higher in the gap originate from defects related to oxygen holes. Sn-Sn and Sn-Zn denote levels caused by two Sn atoms or a Sn and a Zn atom respectively. 1Sn and 2Sn denote levels of isolated Sn atoms surrounded by O atoms which stongly deviate from the perfect octahedral. The little arrows at the bottom mark the highest occupied levels of the DOS. Reprinted from (*17*).

.

3.4. P-type materials: Copper Oxide

The various compounds of copper oxide (CuO, Cu_2O, Cu_4O_3, and Cu_3O_2 (*197*)) are well known and have been studied since before the 19th century, although typically only CuO and Cu_2O are found in nature. Cu_2O crystallizes in a centrosymmetric simple cubic Bravais lattice (*4, 198, 199*) with space group 224 (Pn3m). Its unit cell contains six atoms (Figure 3.8). The four copper atoms are positioned in a face-centered cubic lattice (black balls), the two oxygen atoms are at tetrahedral sites forming a body-centered cubic

sublattice (white balls). As a consequence, oxygen atoms are fourfold coordinated with copper atoms as nearest neighbors, and copper atoms are linearly coordinated with two oxygen atoms as nearest neighbors. X-ray diffraction reveals dominant peaks/intensity at 36.45^{o}/100 (111), 42.33^{o}/37 (200), and 61.4^{o}/27 (220) (*200*). Other lattice properties are shown in Table 2 below. It is also possible for Cu_2O to transform from the cuprite to a hexagonal structure if the pressure reaches 10GPa (*201*).

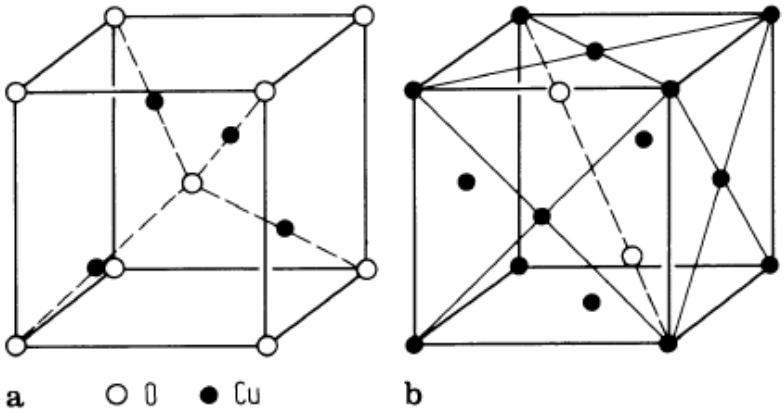

Figure 3.8. Unit cell of cuprous oxide lattice: (a) origin on a oxygen site; (b) origin on a copper site. Dashed lines represent the bonds whereas solid lines are only a guide for the eyes. This structure contains two Cu_2O formula per unit cell.

Young's modulus	30.12 GPa
shear modulus	10.35 GPa
c_{11}	116.5–126.1 GPa
c_{12}	105.3–108.6 GPa
c_{44}	12.1–13.6 GPa
thermal expansion coefficient	$2.3 \times 10^{-7}\,K^{-1}$ (283 K)
Fröhlich coupling constant α	0.21*
$\varepsilon(0)$	7.11
$\varepsilon(\infty)$	6.46
electron affinity χ	≈3.1 eV (300 K)
work function Φ	≈4.84 eV (300 K)
deformation potentials**	$D_e = 2.4$ eV, $D_h = 2.2$ eV

lattice constant	4.2696 ± 0.0010 Å
space group	$Pn\bar{3}m$ (224)
bond length Cu–O	1.849 Å
separation O–O	3.68 Å
separation Cu–Cu	3.012 Å
cell volume	$(77.833 \pm 0.055) \times 10^{-24}\,cm^3$
formula weight	143.14
density	5.749–6.140 g/cm^3
melting point	1235 °C

Table 2. General & Crystallographic properties of Cu_2O (*1*) (*4*). Reprinted from (*16*)

* After ref. (*18*).

** After ref (*19*) .

It is important to note that the given values are almost independent of the temperature, because the Cu_2O has a very small expansion coefficient (the lattice constant changes less than 0.5% from 0 to 600K). When the temperature is below 300K, it's thermal expansion becomes negative (*202*). The thermal conductivity of Cu_2O is 4.5W/(K m), the specific heat capacity is 70 J/(K mol) and therefore the thermal diffusivity is 0.015 cm^2/s (*203*).

The Cu^+ ion electronic structure ends $3d_{10}4s_0$, with the 4*s* orbitals only slightly higher in energy than the 3*d* levels. The Cu 3*d* levels form the valence band of Cu_2O and the empty Cu 4*s* levels form the conduction band (*204*), which also means that the bands

have the same parity. Cu_2O is a semiconductor with a direct gap at the center of the Brillouin zone (Γ−point) of ~2.1 eV. Other inter-band transition energies have been studied at 4.2K giving 2.304 eV, 2.624 eV, and 2.755 eV (*205, 206*).

a) Intrinsic and Extrinsic doping

The role of intrinsic doping in Cu_2O has been investigated by many groups. The possible intrinsic point defects in Cu_2O are vacancies V_{Cu} and V_O, interstitials Cu_i and O_i, Frenkel defects (V_{Cu} −Cu_i) and (V_O −O_i), Schottky defect ($2V_{Cu}$ −V_O), and antisites Cu_O and O_{Cu}. Frenkel and Schottky defects are stoichiometric defects (their presence does not change the stoichiometry). Early on it was determined by Brattain (*207*) that cuprous oxide is a compensated material with both donors and acceptors present, and this is due to native defects in the structure, primarily copper vacancies, which are higher in concentration than donors and makes the material naturally p-type. Theoretical studies were performed by a number of groups which all suggest that copper vacancy and copper split configurations have the lowest formation energies in essentially all conditions (*208-214*). The carrier concentration was found by Carel *et al*. to depend on the amount of cation deficiency (*215*). Temperature-dependent Hall effect measurements on oxidized copper sheets and sputtered thin films have given activation energies of 0.19 to 0.4 eV (*207, 216-220*).

One question still be debated is whether Cu_2O can be rendered n-type via intrinsic defects or by extrinsic impurities. Scanlon *et al*. looked at this recently (*221*), and determined by first-principles calculations that it is impossible for intrinsic defects such

as proposed oxygen vacancies to do this. Biccari et al. (*222*) demonstrated extrinsic n-type doping using chlorine. The carrier concentration as a function of temperature results suggesting that chlorine in amphoteric. It acts as a donor when substituting the oxygen, and as an acceptor when occupying an interstitial position. Nitrogen doping of Cu_2O has shown more progress, finding it was possible to change the hole density by up two orders of magnitude (*223-225*). Scanlon *et al.* (*226*) have used screen hybrid DFT to study the theoretical doping of hydrogen into Cu_2O. The formation energies for hydrogen on the tetrahedral interstitial site were found unexpectedly to be the low unlike many nitrides and oxides, and also found hydrogen on oxygen sites turns from a donor state into an acceptor state for Fermi energies very close to the conduction band. The lowest-formation hydrogen is 0.17 eV. It is an amphoteric defect that changes from donor to acceptor when the Fermi energy is located in the middle of the bandgap and should passivate the intrinsic Cu vacancy acceptors and thus pin the Fermi level to midgap.

Akimoto *et al*. (*223*) studied nitrogen-doped Cu_2O thin films with hydrogen plasma or cyanide treatment for use as Cu_2O/ZnO solar cells. Luminescence properties were improved and the hole density increased by an order of magnitude with cyanide treatment indicating the passivation of nonradiative centers and hole traps attributed to the termination of Cu-dangling bonds by the formation of Cu–CN bonds. The magnitudes of the improvements in the optical and electrical properties caused by the cyanide treatment were found to be comparable to those of the hydrogen treatment. However, the cyanide treatment has an advantage in that its passivation effect is more thermally stable than that of the hydrogen treatment.

b) Copper inclusions

Meyer *et al*. (*16*) observed metallic copper inclusions (as identified by XRD) for films deposited with low oxygen flows (<3 sccm) at 400C. Weichman *et al.* studied the role of copper crystals or 'inclusions' in copper oxide films for over a decade (*227-234*). He found they were present in Cu_2O films processed under certain conditions. They claim the inclusions form natural Schottky barriers with the surrounding material, depleting carriers within the film and raising the resistivity, however their formation assists in creating copper vacancies which help dope the material p-type. It is possible for larger concentrations of precipitates to form effective metal/insulator boundaries that make the device perform like a diode. They also show data demonstrating that heating this material causes a sharp increase in conductivity by three orders of magnitude at a certain transition point.

As a downside, the inclusions also result in increased carrier scattering centers and optical scattering, with increased absorption at some wavelengths. They were found to influence the dielectric constant in the high frequency limit. Based upon calculations, they concluded that the depletion region around each copper inclusion correlates to the low frequency and temperature variations in the dielectric constant. They were able to track and quantify the level of these inclusions via NMR. They propose a model demonstrating the relationship between defect concentration and activation energy in the material in contrast to the standard semiconductor model of the conductivity proportional to defect concentration only and activation energy is related to the ionization energy of

the specified impurity. For low conductivity materials like Cu_2O the activation energy increases as conductivity increases but it's the opposite for high conductivity materials.

c) Depositing copper oxide thin films

Bulk synthetic crystals of Cu_2O (referred to as cuprite) can be prepared by several methods such as oxidizing copper sheets, by melt growth, by floating zone growth, and by hydrothermal growth (*235*). Thin films can be grown by almost any kind of deposition technique, such as electrodeposition, sol–gel, spray, and sputtering (*236-241*). For vacuum deposition many substrates such as sapphire, glass, have been used, typically giving textured films with grain sizes varying from 40 to 100 nm. Epitaxial growth of cubic Cu_2O can be done on cubic MgO substrates as they provide the best lattice match. Since the amount of literature on Cu_2O is vast, we will only focus on information relevant to the sputtering of thin films, which has only been studied in the past couple of decades.

i) Deposition Conditions

In the table below is known critical information for successful sputtering of Cu_2O films. When information was not given 'N/A' appears.

Target Type	Power Density (W/cm^2)	Chamber pressure	O_2	Intentional heating (^oC)	Dep. Time (min)	Sub.-Target distance (mm)	Sub.	Ref
RF Mag. Cu	1.65	N/A	0-9sccm	0-700	N/A	N/A	glass, sapphire, GaN on sapphire	(*16*)
RF Mag.	60W/(cm	0.13 Pa	150 – 350	0-500	39.4	N/A	glass	(*242*)

Cu	$^{2}_{N/A}$)		sccm					
DC Mag. Cu	2.47	0.53 Pa	26-28%	0-797	N/A	N/A	fused quartz	(*216*)
RF Mag. Cu	~1.91	0.96 - 1.25 Pa	0-32%	0	30	60	glass	(*238*)
RF Mag. Cu	60W/(cm $^{2}_{N/A}$)	0.13 Pa	200 sccm	400-500	39.6	N/A	glass	(*223*)
RF Mag. Cu	($W_{N/A}$)/ 44.12cm^2	0.069 – 0.637 Pa	.037 - .021 Pa	0-500	~9.8	60, 70	glass	(*243*)
DC Mag. Cu	2.83	1 Pa	2.4-29%	0	10	70	quartz	(*244*)
HiTUS Cu	RF 9.86-22.2, DC 5.55-18.5	> 5×10^{-3} mbar	5-90 sccm	0	N/A	250	Si(100), Corning 7059 glass	(*245*)
DC Mag. Cu	2.97	0.84 Pa	0.067-0.32 Pa	200	N/A	65	glass	(*246*)
RF Mag. Cu	3.54	0.1 Pa	7-11.1%	300	300	N/A	glass	(*247*)
DC Mag. Cu	1.15-0.57	4 Pa	$6x10^{-4}$ to $5x10^{-2}$ Pa	29.85, 375	N/A	65	glass	(*241*)
DC Mag. Cu	1.02-1.2	1.5-8 Pa	.02 Pa	200	N/A	65	glass	(*248*)
DC Mag. Cu	0.38 – 1.5	4 Pa	3sccm	200	62.5-7	65	glass	(*249*)
Mag. Cu	N/A	N/A	0-0.9 Pa	0	N/A	N/A	glass	(*250*)
DC Mag. Cu	~.22-2.2	0.7 Pa	5%	0	N/A	150	N/A	(*251*)
RF Mag. Cu_2O	0.41-1.63	0.9 Pa	0	0-200	N/A	N/A	TiN/SiO_2/Si	(*237*)
RF Mag.	3.8	0.5 Pa	0-20	0	N/A	N/A	SiO_2/Si, Pt/SiO_2/	(*252*)

Cu_2O			%				Si, quartz	
RF Mag. Cu	3.14	0.56-1.56 Pa	0-64%	90	60	70	Si<100>	(*239*)

Table 3. Cu_2O sputter conditions

ii) Deposition properties:

Most of the work on producing Cu_2O has been with target power in the 0.5-3W/cm^2 range. Growth rates for reactively sputtered copper targets have generally been in the 140nm/min range (*16, 243*) while ceramic sputtered targets were an order of magnitude lower (*237*). Lower values reported by Ishizuka (*242*) may be due to larger substrate-target separation (not mentioned). Ricardo *et al.* (*243*) observed a 17% increase in growth rate with heating, while Reddy *et al.* (*241*) saw a drop of 20%, possibility pointing to influence of the heated plasma on reactive DC vs. RF sputtering.

Yang focused on sputtering where oxygen was provided by the ceramic target (*237*), observed no film growth below power density's of 0.82W/cm^2, which then increased at a decreasing rate up to 1.63W/cm^2 at about 14nm/min. In terms of reactive sputtering from a copper target, Paretta (*250*) found sputtering rate decreased by factor of ~5 above ~0 .08 Pa oxygen partial pressure and leveled off thereafter. This steep drop off was confirmed by Li (*245*), who also found that the energy of the sputtered copper species must be kept low as higher reaction energy tends to favour the formation of CuO. Ohwaki (*251*) found the deposition rates of copper oxide increased monotonically with increasing DC power while composition analysis revealed a plataeuing effect producing Cu_2O

composition in the range ~15W to ~80W. For Lu (*246*) the deposition rate went down by a factor of two with increasing oxygen, while cathode potential went up by a similar proportion. This points to higher potential required to sputter a poisoned target, and that this has a large share of influence on deposition rate at the specified chamber pressure vs. sputtered atom gas-collisions. However, Reddy showed (*248*) that within 1.5 Pa to 8 Pa the deposition rate still dropped by a factor of two.

A number of groups have found that single phase Cu_2O exists (identified by XRD) within a narrow range of oxygen partial pressure for reactive sputtered copper targets. Meyer (*16*) found a limited range of 3–5 sccm oxygen where pure Cu_2O phase was produced. The variance by about a factor of 1.5 was also seen by others (*238, 245, 246, 252*). With Ishizuka (*242*) using much higher flow rates at no intentional heating, however heating above 400^oC introduced the copper phase on the low end of the oxygen flow rate, compressing the usable range to 210-225 sccm. However, some have shown the range of oxygen to be much narrower (*243, 244, 247*) (*250*).

iii) Optical properties:

Many groups did not report the optical transmission of their films, while band gaps range around 2.0–2.7 eV, which correlate with transitions described previously. Most of the films with band gaps towards the higher end have transmission under 70% (*16*) (*238*) (*245*) and films with lower band gaps gave improved transmission (*247*) (*248, 249*). Li found that the larger band gap films were produced with higher target power (*245*) and also that increasing oxygen during deposition led to decrease in the band gap (*247*).

Heated films by Ishizuka (*242*) at 400^{o}C had optical absorption below the gap averaging 20% for phase pure Cu_2O compared to room temperature absorption over 70%. Reddy also found an improvement with heating (*241, 248, 249*), which may be attributed to an increase in the packing density and the crystallinity in the films and causing a reduction in optical scattering defect centers, however their large drop in mobility is somewhat inconsistent with this.

Zhu (*244*) found as-deposited optimal films had a very high optical absorption in the visible spectra, and the transmittance decreased with the increase of the thickness of the film.

iv) Electrical properties:

Generally films with nominal Cu_2O composition had resistivity's in the range 10^1 to 10^3 Ω-cm, with mobility's around 1-60 cm^2/Vs and carrier concentration from the high 10^{14} cm^{-3} to low 10^{16} cm^{-3} range, with Lu (*246*) getting the best films with resistivity of 1.76 Ω-cm. Parretta (*250*) did temperature-dependant resistivity measurements pointing to thermally activated carriers. Activation energies were measured by a few groups between 0.16 and 0.42 eV (*218, 224, 253*), while higher growth temperatures tended to result in lower activation energies (*216*).

Meyer et al. (*16*) did some revealing measurements for carrier concentration and mobility vs. oxygen flow (in Figure 3.9), which show the carrier concentration increases by over 3 orders of magnitude for films with roughly Cu_2O concentration and excess oxygen, with similar trends for the other orders of oxide. A similar trend was confirmed for ceramic-sputtered films by Noda (*252*). The Cu_2O films with excess oxygen likely

formed excess copper vacancies, known to be the primary acceptor, causing the carrier concentration increase. As oxygen levels increased further deep level oxygen interstitials likely formed, while mobility reduced substantially due to impurity scattering, causing an increase in overall resistance.

For films deposited at higher substrate temperatures, hall measurements showed mobility increased by between one to over two orders of magnitude from room-temperature deposited films at 375^{o}C (*241*) to 500^{o}C films (*242*), while in the same span carrier concentration had less change (although variation between samples went down substantially) resulting in overall large decreases in resisitivity with higher temps. Reddy found with increasing sputter pressure (*248*), mobility and carrier concentration dropped by an order of magnitude down to 2.4 cm^2/Vs and $8.13x10^{14}cm^{-3}$. Yang found (*237*) that the resistivity of 100 Ω-cm for cuprous oxide thin films did not change with film thickness.

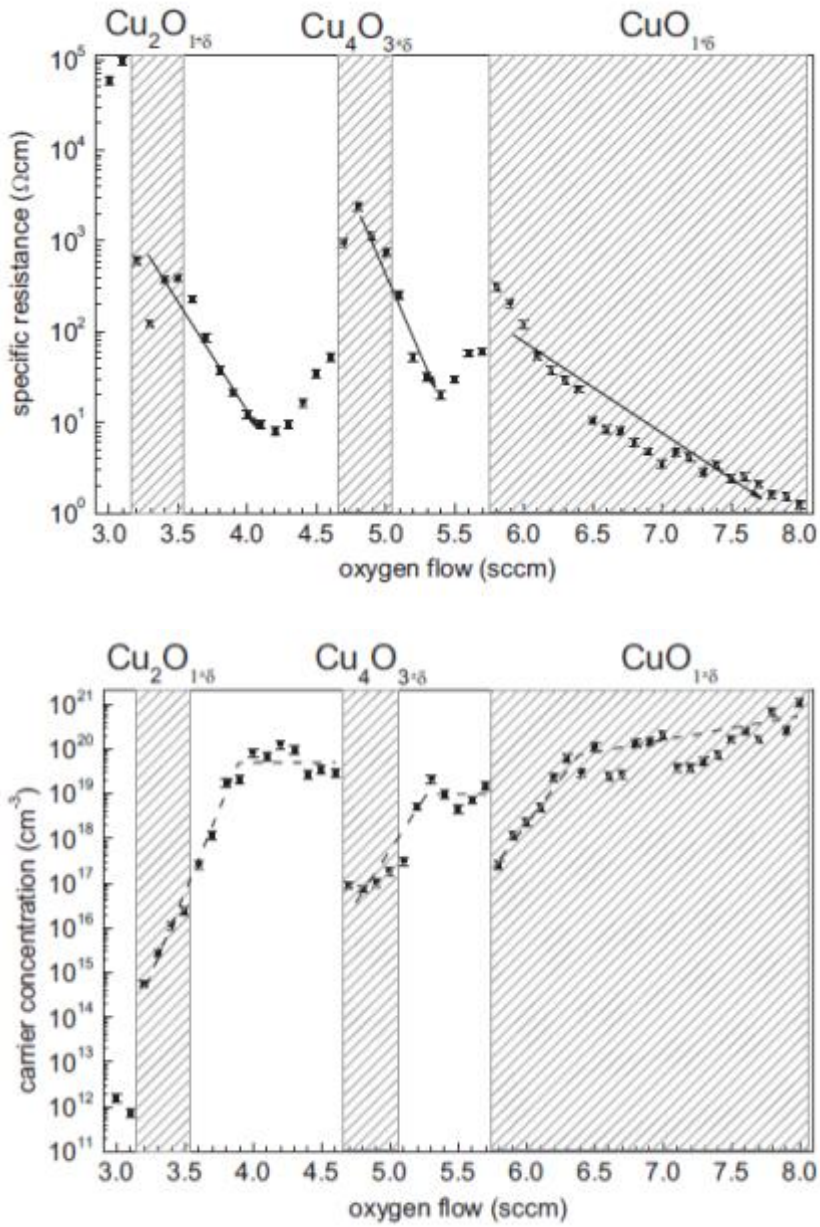

Figure 3.9. Specific resistance (a) and carrier concentration (b) vs. sputtering oxygen flow for Cu_2O films. The shaded phase regions are approximate stochiometry determined by XRD. Reprinted from (*16*).

v) Structural properties:

It was found by Akimoto (*223*) that crystallographic orientation, which relates to the continuous atomic arrangement and surface defect density (related to grain size), seems to be important in getting high electrical performance in Cu_2O-TCO devices. Many films have been produced with mixed orientation composed of primarily (111) and (200) peaks with dominant (200) peaks (*16, 238, 239, 246*) while only Yang (*237*) produced films with dominant (111) peaks. A few groups managed to make single-orientation (200) films (*242*) (*216*) (*243, 244*) and the common parameters to achieving this appear to be minimizing the substrate temperature, as well as high ad-atom energy through a combination of higher sputtering power and sufficiently low chamber pressure, while there is no clear correlation with substrate type. Zhu observed that (*244*) when the oxygen partial pressure and chamber pressure were fixed while argon flow was varied between 20 and 70 sccm, pure Cu_2O phase was formed in all cases, however at 20 sccm there is single (200) orientation, while at 60 sccm there is single (111) orientation and at 70 sccm mixed-orientation occurred, suggesting the difference between achieving (111) vs. (200) orientation is fine tuning ad-atom energy. They observed that fully (111)-oriented films have a distinctive quadrangular surface morphology with clear grain boundary.

Meyer *et al*. (*16*) studied the influence of substrate heating on the lattice constant, and observed it to vary from 0.444 nm for an unheated substrate, decreasing to the lattice constant of bulk Cu_2O with increasing growth temperature of which a similar trend was seen between the as-grown and subsequently annealed films.

Ricardo *et al*. observed (*243*) found that deposition under temperature increase leads to a weaker texture and to an increased amount of polycrystalline domains, with domain

size larger for textured fraction on samples produced at room temperature with the opposite at high temperature. High compressive stress was seen in samples deposited at room temperature while it was much smaller for high temp deposition. Yang (*237*) showed XPS binding energy with shake-up peaks around 945 eV which are indictave of CuO bonding (*254*) for films confirmed to be phase-pure Cu_2O by XRD , which they found was due to an existing CuO layer down to the depth of 3 nm and the bulk of copper oxide below that consisting of pure cuprous oxide. UPS measurements gave a work function of 4.84 eV.

d) Thermal/chemical stability issues:

The temperature / oxygen partial pressure phase diagram of the binary Cu–O system has been mapped by a compilation of experimental data (*255-258*) from (*7*) (Figure 3.10). It is clear that Cu_2O is unstable in air at room temperature, and will tend to convert to CuO, however the kinetics for this to happen are slow-enough that it can be considered stable for most practical applications (*259, 260*).

Yang (*237*) found that stoichiometric Cu_2O films annealed at 250–450°C for 1 min in N_2 remained stable up to 250^{o}C, but at 350^{o}C or higher showed the introduction of small copper and CuO peaks in XRD. The former is expected in a reducing atmosphere, but the later is unexpected, unless viewed in light of copper inclusion formation processes described by Weichman. Pierson (*238*) had phase-pure Cu_2O films at 4 sccm of oxygen and an applied bias of -50V. These demonstrated better stability showing no change for anneals up to 300^{o}C in air for 4hrs, confirming slow kinetics of Cu_2O->CuO conversion

at these temperatures. Post-deposition anneals of Cu_2O+Cu films in air resulted in a conversion of more Cu to Cu_2O, also in agreement with Figure 3.10.

In Cu_2O, the self-diffusion of copper atoms was confirmed to take place on a face centered cubic sub-lattice by a vacancy diffusion mechanism (*261*). Self-diffusion of copper and oxygen in Cu_2O by radioactive tracers $_{64}Cu$ and $_{18}O$ were performed by Moore (*262, 263*), Perinet (*264-266*) and Peterson (*267*). In Cu_2O the chemical diffusion was measured by conductivity at high temperature and by microthermogravimetric reequilibration. The results show a dependence of copper atom self-diffusion on the oxygen partial pressure correlated to $p^{1/4}O_2$ confirming the fact that the copper ions migrate through the copper vacancies (*268*). The results for oxygen diffusion show a dependence on the oxygen partial pressure as $p^{0.4}O_2$ and point to oxygen ion diffusion proceeding by an interstitial mechanism/singly negatively charged oxygen interstitials, while other types of defects have much less influence.

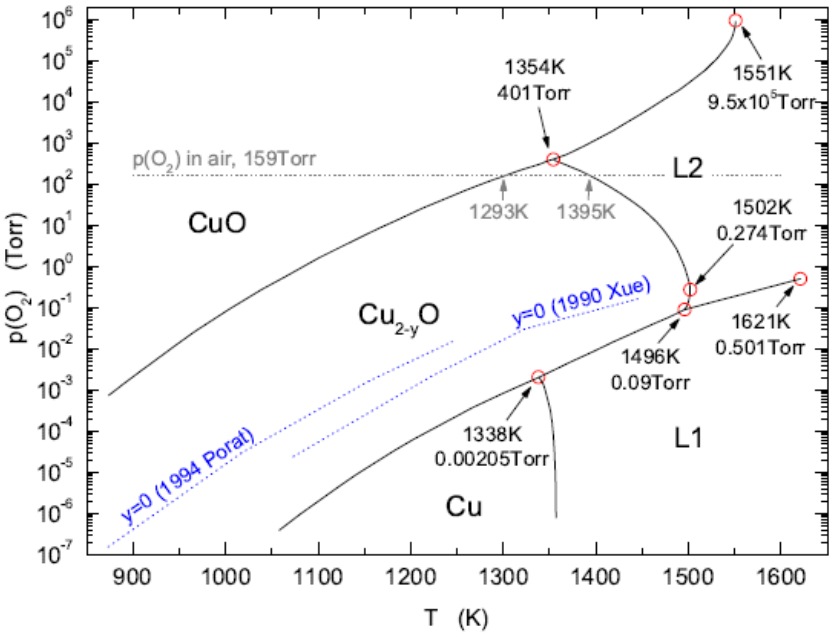

Figure 3.10. Phase diagram for partial pressure oxygen of Cu_2O. L1 represents pure liquid copper and L2 corresponds to the composition ranging from pure liquid copper to the oxidic melt CuO. Reprinted from (*4*, *7*).

Data by Li (*245*) for high rate DC reactive sputtered optimal 40nm-thick Cu_2O films with post-deposition anneals for 1 hour up to 225°C in air resulted in little change optically, while mobility went up by an order of magnitude. Noda *et al*. (*252*) studied the effects of post-deposition RTA on sputtered Cu_2O films for 30s in argon up to 600°C. Results showed grains began to grow at 400°C, and grew much larger at 600° C (by AFM and XRD). Hall measurements showed mobility increased by an order of magnitude and carrier density decreased by more after anneal at 600°C for films with 1.6% oxygen causing an overall slight increase in resistivity. For films made with 0.8% oxygen the resistivity dropped by over 2 orders of magnitude. In a more recent work done by Chen et al. (*269*) for solar cell applications, Cu_2O films were produced by RF magnetron sputtering from a copper target onto a ZnO/ITO-coated glass substrate at 50W at

4.3mTorr with argon at 50 sccm and oxygen between 1-3 sccm, followed by 300 to 500^{o}C anneal (film thickness between 800-1000 nm). They found that by adjusting anneal time above 400^{o}C, porous, thin oxides formed, particularly developed in the grain boundary regions, implying that they were produced by fast diffusion processes (grain sizes between 30 to 50nm). After annealing at 500^{o}C, copper-rich nanoclusters form on top of copper oxide grains. XRD showed all films had mixed orientation Cu_2O with dominant (111) orientation. Resistivity went down by a factor of five with annealing temperatures increasing to 500^{o}C while mobility tracks it in essentially the same pattern. Optical transmission increases below 800nm while the band gap shifts from 2.1 to 2.55 eV.

e) Theoretical calculations

The effective mass was investigated by Hodby (*18*) and Nie (*270*), as many first-principles calculations and experiments have been done by others (*19, 214, 271-284*). The effective hole masses are labeled with LH (Light Hole) for the Γ+ 7 and HH (Heavy Hole) and SPH (spin-orbit Split-off Hole) for the Γ+ 8 (an explanation of the acronyms can be found in (*270*)). The effective masses of the free carriers were measured by cyclotronic resonance. For symmetry reasons m_e and m_{LH} have to be isotropic whereas m_{HH} and m_{SPH} have to be anisotropic. With Cu_2O being partly ionic, the free carriers are surrounded in their motion by a cloud of phonons which increases their mass. Using the experimental values of m_e and m_{LH} h the effective density of states, $N_c(300\ K) = 2.47 \times 10^{19}\ cm^{-3}$ and $N_v(300\ K) = 1.11 \times 10^{19}\ cm^{-3}$ can be found.

Calculations of the Cu_2O electronic structure have been performed by several different techniques. Self-consistent techniques based on Local Density Approximation (LDA) or Generalized Gradient Approximation (GGA) underestimate the energy of the band gap by 1.5 eV (*16, 271, 275, 276*) due to inaccuracy in predicting the position of the conduction bands, whereas those based on the Hartree-Fock approximation overestimate it. However the shape of the conduction bands are qualitatively correct and therefore they can give an idea of the real conduction bands simply shifting them in the energy. Hybrid functional, pseudo-self-interaction methods, and self-consistent GW calculations yield very good agreement of the bandgap with experimental data (*214, 278-282*). For the latter, a standard single-shot GW calculation is not enough to obtain a correct bandgap. The drawback of GW is the high demand for computation time. However, the accuracy (e.g., of optical properties match with experiment) is much better than with hybrid functional (*283*).

The correctness of band calculations was investigated by several kinds of spectroscopic experiments (x-ray photo-emission (XPS), x-ray absorption (XAS), x-ray emission (XES), ultraviolet photo-emission (UPS), resonant photo-emission (RPES), angle resolved photo-electron (ARPES) Auger electron (AES) and bremsstrahlung isochromat spectroscopy (BIS, also called inverse photo-emission); low-energy electron-diffraction (LEED); and predictions on absorption coefficient) (*271, 272, 276, 277*). Cu_2O shows an unusual linear coordination O−Cu−O of copper atoms that cannot be explained by simple ionic forces which, instead, predict an unstable structure. The cited experiments found that the hybridization between orbitals O2*p*–Cu4*sp* exists, confirming a long time hypothesis for cuprite stability.

f) Other interesting notes about this material:

The temperature dependence of the hole mobility was studied by Le *et al.* (*216*) and others on large grain polycrystal or monocrystalline Cu_2O (grown by similar techniques), and it was claimed that the dominant limitations to the mobility are phonon scattering at higher temperatures and carrier scattering from ionized centers at temperatures below 200 K.

Biccari (*7*) counters that the mobility versus the temperature would have the opposite trend at higher temperatures, increasing instead of decreasing, and moreover an improbably high concentration of impurities, greater than 10^{18} cm^{-3}, would be needed. Another hypothesis, suggested also for other materials (AgBr, TlBr), to explain the rapidly decreasing mobility with temperature is based on auto-trapping of the holes in metastable states which originate only at temperature above 200K (*220*). Another issue is the effect of the surface on Hall mobility measurements, claimed to influence mobility by up to an order of magnitude for more resistive films (*285*).

Greiner *et al.* (*286*) studied the influence of oxidation state on the work function of common metal oxides, including copper oxide. They found that the increase of oxygen deficiencies lowers the work function in general of a transmission metal with the correlation being attributed to the change in cation electronegativity with oxidation state. A model is presented that relates the work function to the oxygen deficiency for d^0 oxides in the limit of dilute oxygen vacancies. It is proposed that the rapid initial decrease in

work function, observed for d^0 oxides, is caused by an increase in the density of donor-like defect states. It is also shown that oxides tend to have decreased work functions near a metal/metal-oxide interface as a consequence of the relationship between defects and work function and that metal oxides also tend to have higher work functions than their elemental metals. Most importantly they provide insights for tuning the transition metal oxide work function in materials. This allows us the advantage of adjusting band alignment in our Cu_2O film to form better devices.

More recently studies have been done on the influence of interface morphology on copper oxide-based device performance. Wei *et al*. (*287*) looked at the efficiency of Cu_2O-based solar cells and found that the crystal orientation & microstructure of Cu_2O films can modify device performance due to easier formation of interface states. The epitaxial growth of the Cu2O homojunction with n/p films of the same crystal orientation (preferably single (111)) reduces the interface states and the formation of a textured structure on the surface helps the photons to be absorbed more effectively, which both enhance the photovoltaic conversion efficiency of Cu2O film solar cell. McShane *et al*. (*288*) investigated the affect of surface morphology of p-type Cu2O on p-n junction interface in homojunction solar cells. The results showed that the junction quality and the cell efficiency varied significantly depending on the crystals faces exposed at the p-n junction, although the resistivity of the p- and n-layers remained comparable. They suggest that the coordination of atoms on (111)-terminated p-Cu2O crystal surfaces may deviate significantly from the ideal coordination of atoms on (111) planes in the bulk

crystal structure, preventing well-aligned epitaxial growth and generating many interface states.

Some groups have looked at the affect of film thickness on Cu_2O properties. A dependence of the band gap was observed upon film thickness has been studied by Poulopoulos *et al.* (*289*) on Cu_2O films prepared by sputtering and subsequent oxidation in a furnace with thickness between .75 and 230nm onto different substrates. Resutls show a blue shift of the energy between the top valence and the first excited conduction sub bands, which increases smoothly as film thickness decreases. This points to intense quantum confinement effects. This was correlated to the influence of stress in the films by Zhu *et al*. (*290*) for sub-11nm films.

3.5. P-type materials: Copper-Aluminum-Oxide

$CuAlO_2$ (copper aluminum oxide or CAO) has been a material of great interest ever since Kawazoe *et al*. (*291*) proved the first p-type thin film by PLD. This is first and formost due to it's wider bandgap compared to other similar p-type metal oxides. Structurally, $CuAlO_2$ belongs to the family of delafossite compounds, named after the mineral $CuFeO_2$ (*292*). Delafossite compounds are ternary oxides which have the general formula $A^{(I)}B^{(III)}O_2$, where $A^{(I)}$ represents a univalent noble metal cation (i.e. Cu^+, Ag^+, Pd^+, etc.) linearly two-fold coordinated to two oxygen ions; and $B^{(III)}$ represents a cation (Al^{3+}, Ga^{3+},Co^{3+}, etc.) nominally in the +3 oxidation sate, octahedrally coordinated by oxides. These structures are usually described as two alternating planar layers stacked along the c-axis: a layer of A cations in triangular array with no oxygen and a layer of edge sharing BO_6 octahedra originating layer of $[BO_2]$. According to stacking sequence,

two polytypes are possible: hexagonal 2H type with P63/mmc space group symmetry and the rhombohedral 3R type with space group symmetry of $R3\bar{m}$ (*293-295*). Although $CuAlO_2$ is usually referred as a 3R type delafossite with rhombohedral symmetry, 2H type $CuAlO_2$ could occur when planar defects are introduced in the crystal structure (*294*). As part of delafossite family, $CuAlO_2$ is composed of alternating stacking layers of O–Cu–O dumbbells and edge-sharing AlO_6 octahedral (Al occupying the octahedral interstices) layers. The Cu and Al atoms form alternating layers perpendicular to the c axis. Cu atoms are linearly coordinated by O and the Al atoms are six fold-coordinated with O atoms. The Cu and Al sites in $CuAlO_2$ are surrounded by different local neighborhoods from the large aspect ratio of the c/a axis' of $CuAlO_2$, and as a consequence have unique physics properties, such as negative thermal expansion (*296*), as well as anisotropic electronic conduction characteristic (*297*) (known to be with delafossite compounds) and therefore the crystal orientation of the films is a factor in optimizing the electrical properties.

Reported lattice parameters for 3R-type $CuAlO_2$ are: a= 2.858 Å, c=16.958 Å and with main bond-lengths: Cu-O=1.861 Å, Al-O: 1.912 Å, Cu-Cu = 2.860 Å (*298*). The stacking sequence for delafossite structure of ABO_2 oxides in the 3-D projection for 3R polytype is shown in figure 3.11. In 1984, Benko *et al*. reported (*299*) $CuAlO_2$ first as a wide band gap p-type oxide and measured the band gap at 1.65 eV (indirect), 2.3 eV (direct forbidden), and 3.5 eV (direct) by photoelectrochemical measurements. The theoretical density of $CuAlO_2$ is 5.097 g/cm^3 and has been sintered in the range 2.6 – 4.1 g/cm^3 by Liou *et al.* (*300, 301*), which is similar to that of Al_2O_3 density = 3.95 – 4.1

g/cm^3, but much less than that of the copper oxides of Cu_2O density = 6.0 g/cm^3 and CuO density = 6.31 g/cm^3.

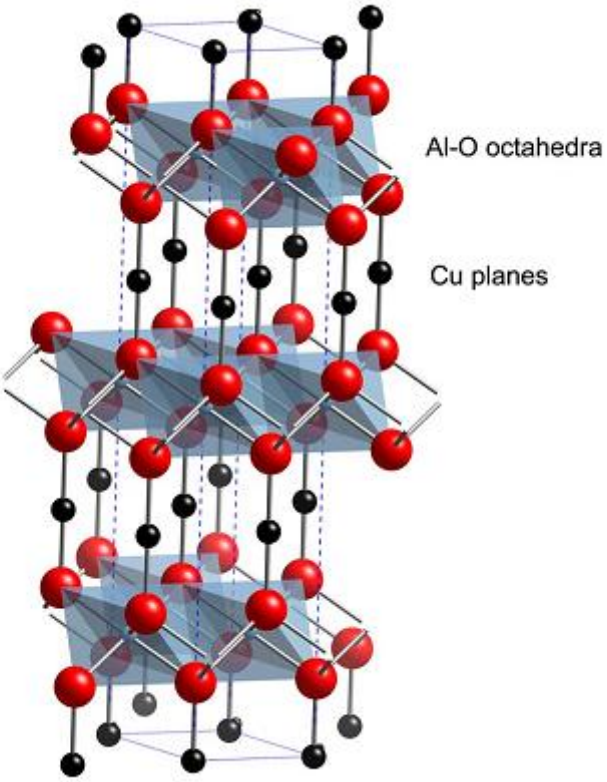

Figure 3.11. The crystal structure of the 3R polytype of $CuAlO_2$. Alternating layers of Cu atoms (black) and AlO_6 (red) octahedra stacked along the c axis give the structure its anisotropic character.

The Phase diagram of $CuAlO_2$ was investigated first by Misra *et al*. (*302*) using a solid-state reaction of mixed CuO-Al_2O_3 powder. The formation of copper aluminum oxides $CuAlO_2$ and $CuAl_2O_4$ and phase equilibria in the system Cu_2O-CuO-Al_2O_3 was investigated by Jacob *et al.* (*303*) and later by Neumann-Spallart (*11*) (see figure 3.12). It shows that $CuAlO_2$ is a metastable phase, i.e. $CuAlO_2$ is thermodynamically stable in air ($p(O_2)$=21.3 kPa) only between 1003 °C and 1250 °C. Below 1003 °C a mixture of

$CuAl_2O_4$ and CuO is formed instead of $CuAlO_2$. In the PLD films the working point (filled circle labeled "PLD" in the phase diagram, figure 3.12, representing the oxygen pressure used in their work) can be positioned such that $CuAlO_2$ can exist, as its lower phase boundary is shifted to lower temperatures due to reduced oxygen pressure. The phase boundary is very sensitive however, and it is theorized that in each case, the sample will find itself outside the $CuAlO_2$ existence range and may decompose. They claim this is the reason for the fact that a phase pure $CuAlO_2$ cannot be detected in as-deposited PLD films.

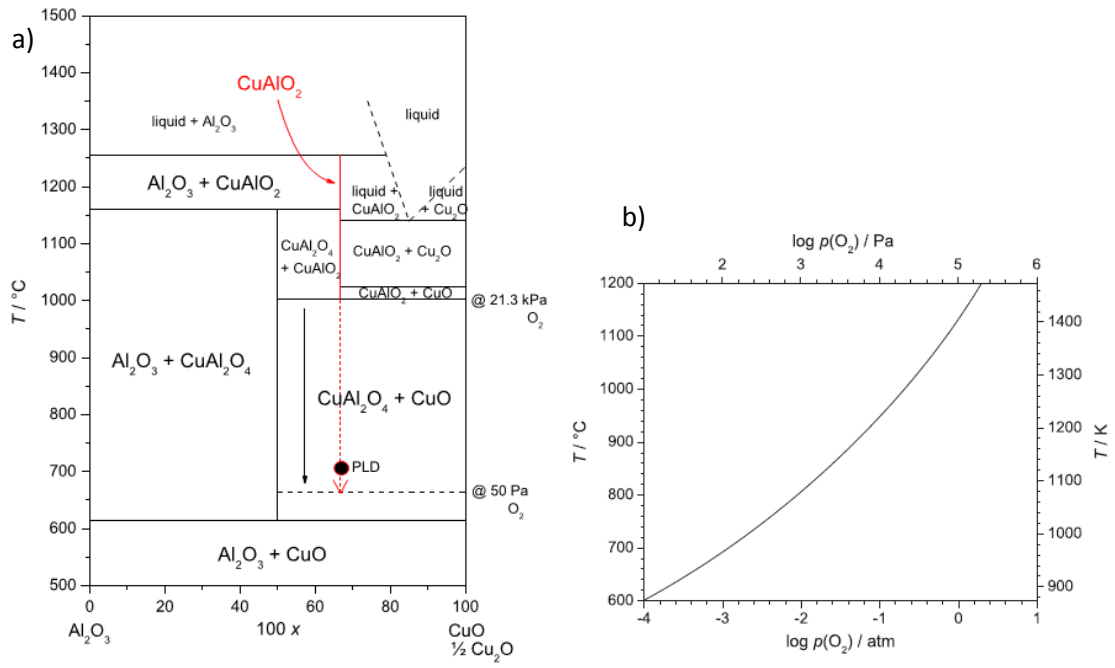

Figure 3.12. (a) shows the quasi-binary phase diagram of the system CuO/Al_2O_3 at 0.21 atm O_2, and the red line of $CuAlO_2$ is Neumann-Spallart and Pinto's correlation of stoichiometric $CuAlO_2$ with the oxygen partial pressure, which allows it to form at lower temperatures according to (b). Reprinted from (*11*).

3.5.1. Intrinsic & Extrinsic doping

The theory of p-type conduction in intrinsic $CuAlO_2$ has been explained by a few different models. Benko *et al*. (*299*) were the first to identify the sign of the charge carrier for bulk $CuAlO_2$, in which they proposed hole transport by hopping mechanism through the laminar structure. Most of the reports (*299, 304, 305*) claim that the p-type conductivity is due to excess interstitial oxygen which they justify experimentally from increased conductivity with higher oxygen partial pressure during deposition. Thomas (*306*) claims that ions are trapped in interstitial sites and bind electrons, leaving behind empty states in the valence band which act as positive holes. Due to the high band gap of $CuAlO_2$, visible light photons are not energetic enough to excite electrons into the conduction band, making the oxide transparent. However, due to electron trapping by the oxygen ions, the material is also electrically conducting.

Hosono *et al.* (*291*) explained the p-type nature of the material by the detailed theory of "Chemical Modulation of the Valence Band (CMVB)", in which they found that localization of metallic oxides is reduced by the cations with closed shells, such as Cu^+, Ag^+, and Au^+ with a $d^{10}s^0$ electronic configuration and gave the following explanation: The delafossite $CuAlO_2$ can be treated as a linear arrangement of O—Cu—O dumbbells, which locally are exactly the same as found in Cu_2O. The delafossite on the other hand, is not a three dimensional web of dumbbells, but are instead stacked in series (along the c-axis), alternating with Al_3O_6 octahedral layers, which are highly insulating. This reduces the Cu crosslinking from 3-dimensional in Cu_2O, down to 2-dimensional. Now the only Cu interactions are perpendicular to the c-axis in $CuAlO_2$. This limitation in the dispersion of the valence band results in enough widening of the band gap for successful

optical transparency. An important side effect is that conductivity will then be inevitably anisotropic. This was confirmed experimentally by Lee *et. al.* (*307*) with electrical conductivity along the *ab* plane (σ_{ab}) being much higher than that along the c-axis (σ_c) by a ratio of 25, and Nagarajan *et al*. reported (*308*) that some of the delafossites have anisotropy up to 1000 times higher along the *ab* plane.

Others have reported $CuAlO_2$ films with variable-range hopping (*307*), band-conduction (*291, 309*), and small polaron transport (*293*). Tate *et al.* (*295*) did a study on the conduction and found a large *ab*-plane room-temperature hole mobility (3.0 $cm^2 V^{-1}s^{-1}$) and a resistivity anisotropy of 40-25 in the temperature range of 180-350 K with carrier-density temperature dependence being consistent with band conductivity resulting from the ionization of a likely Cu vacancy defect about 700 meV above the valence band. They observed a low-temperature paramagnetic moment consistent with a density of about 10^{20} cm^{-3} spins that may be related to this defect.

Some work on extrinsic doping of $CuAlO_2$ with Mg has been studied by Jiang *et al*. (*310*) and XRD results confirmed Mg substitution on Al sites is lower than 2 atomic %. Also due to substitution the surface roughness of the films was reduced and the c-axis orientation of the films, as well as optical and electrical properties improved. Dong *et al.* (*311*) looked at the affect of doping $CuAlO_2$ with up to 2 atomic % zinc and suspect the zinc is substituting the aluminum sites. For intermediate levels of zinc the transmittance goes down, however an increased transmittance of about 80% is achieved for 2% zinc. The electrical conductivity increases rapidly with the increase in doping concentration. At

room temperature, the electrical conductivity for the doped sample with 0.5% zinc is about 2 orders of magnitude higher than that of the undoped sample and higher levels of doping are believed to cause a large increase in impurity & defect scattering thereby decreasing conductivity.

i) Deposition Conditions

In the table below is known critical information for successful sputtering of $CuAlO_2$ films. When information was not given 'N/A' appears.

Target Type	Power Density (W/cm^2)	Chamber pressure	O_2	Intentional heating (^oC)	Dep. Time (min)	Sub.-Target distance (mm)	Sub.	Ref
RF Mag. $CuAlO_2$	100W/ cm^2 N/A	1Pa	20%	500	120	40	Quartz	(*312*)
RF Mag. $CuAlO_2$	100W/ cm^2 N/A	1Pa	20%	500	N/A	40	Quartz	(*313*)
RF Mag. $CuAlO_2$	100W/ cm^2 N/A	1Pa	10-60%	500	120	40	Quartz	(*314*)
DC Mag. 2Cu+2Al	0.88 Cu, 2.46 Al	0.53Pa	20%	300	240	N/A	Quartz	(*315*)
DC Mag. 2Cu+2Al	0.88 Cu, 2.46 Al	0.53Pa	5 – 20%	500-700	240	N/A	Quartz	(*316*)
DC Mag. 2Cu+2Al	0.88 Cu, 2.46 Al	0.53Pa	20%	500-680	240	N/A	sapphire	(*317*)
DC Mag. Al/Cu=3	0.66-1.59	4Pa	0.25% –7.7%	250	N/A	65	glass	(*12*)
DC Mag. Al/Cu=3	0.78-1.06	5Pa	1.2%	30–375	N/A	65	glass	(*318*)
DC Mag.	10	20Pa	40%	180	240	18	Glass,	(*319*)

$CuAlO_2$							Si	
DC Mag. Cu/Al =1 pellets	12	20Pa	40%	202	240	18	Glass, Si	(*320*)
DC Mag. Cu/Al =1 pellets	12	20Pa	40%	100	3-150	15	Glass, Si	(*321*)
DC Mag. CuAl	12	20Pa	40%	202	3-150	18	Glass, Si	(*322*)
DC Mag. CuAl	100W/ cm^2 N/A	0.67Pa	10%, 40%	0,300,600	N/A	140	*c*-plane sapphire	(*323*)
RF Mag. $CuAlO_2$	2.65	0.67Pa	10%	0-700	60	30	*c*-plane sapphire	(*324*)
RF Mag. Cu+Al	Cu:30W/ cm^2 N/A, Al:60-110W/ cm^2 N/A	N/A	5%	100	N/A	N/A	glass	(*325*)
RF Mag. CuAl	6.66 W/cm^2	1.33Pa	5%	N/A	N/A	60	glass	(*326*)
RF Mag. $CuAlO_2$	6.28	N/A	0-20sccm	0-600	30-45	N/A	quartz, polished sapphire	(*327*)
Helicon-wave-excited RF $CuAlO_2$	500W RF power with −400 V bias ,2inch-diameter	0.083Pa	0-40%	600-800	N/A	N/A	(0001) Al_2O_3	(*328*)
RF Mag. $CuAlO_2$	80W/ cm^2 N/A	0.71Pa	40%	0	90	60	Glass, quartz	(*329*)
Pulsed Mag. Cu_2O/Al_2	N/A	0.2-0.27Pa	0-40%	N/A	10,60	N/A	glass	(*330*)

O_3 powder								
DC Mag. CuAl	120W/ cm^2 N/A	0.31-1.2Pa	5-100%	940	N/A	N/A	n-Si, SiO_2/n-Si	(*331*)

Table 4. $CuAlO_2$ sputter conditions

3.5.2. Deposition properties:

Generally, films deposited under generic RF or DC sputtering systems resulted in deposition rates equal to, or lower than those of aluminum, at between 0.3nm/min and 6.8nm/min (*323*) (*12*) (*324*) (*330*) for forming films with sufficient oxygen content. High deposition rates have been reached with high power (*327*) at 9nm/min or custom systems such as Tsuboi *et al.* using dual opposed targets with programmatic sputtering (*315*) (*316*) (*317*) giving 3.33um/min. Lu found films with a sufficient level of oxygen content had the right copper & aluminum content as well as good depth homogeneity examined by (RBS) and (SIMS) (*327*), while Tsuboi *et al.* and others (*316*) (*317*) characterized better performing films as oxygen-rich. Reddy *et al.* (*12*) found that adjusting the oxygen partial pressure above $3x10^{-3}$ mbar led to a deposition rate drop by a factor of 4 while cathode potential dropped by 25 %, attributed to oxidation of the target, while Stevens saw an even higher drop (*323*). At low oxygen partial pressure Reddy observed mixed phase of Cu_2O along with $CuAlO_2$ and at higher pressure Al_2O_3 was introduced in the films. They also noted (*318*) the cathode potential linearly increasing with substrate temperature, while deposition rate increased from 21 to 26nm/min.

Yao *et al.* (*331*) observed films grown at a low pressure of $5.0x10^{-3}$ and $8.0x10^{-3}$ mbar being composed of pure $CuAlO_2$ without crystalline CuO impurity phase detectable even for a oxygen partial pressure of 100%. However, increasing working pressure to $1.2x10^{-2}$ mbar led to the formation of crystalline CuO clusters for a wide oxygen partial pressure range from 10 to 90%, peaking at 50%, suggesting the adatom energy having some bearing on film phase formation.

The work done by Tsuboi & Banerjee suggests influence of ionized species and/or the plasma on deposited films is crucial to getting simultaneously good optical & electrical properties. Unfortunately in this work we were restricted to using a sputter system with substrate-target distances of 12.5 cm nominal. Because of such large distances high pressure sputtering is not feasible without extremely low deposition rates. The AJA 2000 is a sputter-down system, restricting the type of targets used to solid 3-inch disc targets and not powder targets such as those used by Alkoy. The power systems are also restricted to DC or RF mode, not pulsed DC power supplies such as those used by Alkoy. The two exceptions to this are Lan and Reddy, however they don't describe key sputtering system dimensions and Reddy's system operates at a still relatively high pressure of 30mTorr with medium target-substrate distance.

3.5.3. Optical properties:

Direct band gaps for films with nominal $CuAlO_2$ composition have been between 3.1 eV and 3.9 eV (*12*) (*319*) (*320*) (*321*) (*322*) (*325*) (*327*) (*329*) and indirect gaps around 1.86 eV - 2.1 eV (*314*) (*319*) (*320*) (*322*), with many groups reporting direct gaps at 3.5

eV using oxygen pressures roughly 1mTorr and sputter powers around 1W/cm^2 (*314*) (*315*) (*316*) (*317*) (*12*). Transmittance was typically 60-90% for optimal films (*314*) (*12*) (*319*) (*321*) (*322*) (*326*) (*330*) (*329*) with higher oxygen deposition conditions, however achieving the higher values generally went hand in hand with a steep falloff in conductivity, reported in the following section.

Some groups (*325, 326*) (*315*) (*316*) (*317*) found that by adjusting aluminum content, films with thicknesses usually above 100 nm give transmission between 20–80%, while the optical direct band gaps of the films shifted higher with more aluminum content, confirming theory.

Comparing the results of groups with films made at different substrate temperatures (but still well below the crystallization point) suggests they have marginal influence on the optical properties. Banerjee (*321*) investigated the affect of film thickness, and found band gaps shrink and visible transmittance decreases from 3.94 eV and 99% at 3min and 30nm thickness to 3.34 eV and 75% after 150min and 400nm thickness.

3.5.4. Electrical properties:

Thin film deposition of copper aluminum oxide delafossite films have been sputtered by many groups since Kawazoe *et al.* found good optical and electrical properties in PLD sputtered films. Despite this in most of the publications we reviewed here electrical properties are either highly insolating or else they are not studied when it comes to films deposited at temperatures under 300^{o}C, an important parameter for our application.

Disregarding deposition temperature, room temperature conductivity for the better performing films with nominal $CuAlO_2$ composition are in the range of 3.1 Ω–cm to 7.2×10^3 Ω-cm (*312*) (*12*) (*319*) (*320*) (*322*) (*330*) (*331*), however some of the groups reported substantially higher at 10^5 Ω-cm or more (*315*) (*325*) (*326*), and many don't report any value. Reported mobilities are 8 $cm^2\ V^{-1}\ s^{-1}$ to 39.5 cm^2/Vs, and carrier concentrations of $4.25x10^{15}$ cm^{-3} to $2x10^{18}$ cm^{-3} (*322*) (*12*) (*331*).

Reddy *et al.* (*12*) obtained the best conductivity (see Figure 3.13) at an oxygen partial pressure of $6x10^{-4}$ mbar, showing that mobility improvement is primarily responsible while higher oxygen content reduces carrier concentration. At low oxygen partial pressure of $1x10^{-4}$ mbar the films showed a resistivity of 15.2 Ω–cm due to the presence of mixed phase of Cu_2O along with $CuAlO_2$ and at $1x10^{-3}$ mbar Al_2O_3 was introduced in the films leading to dielectric behavior and amorphous nature hence of high electrical resistivity, confirmed by others. Reddy (*318*) and Lan (*314*) both observed mobility and optical band gap and transmission to follow an inversely related trend with oxygen pressure. Yao et al. (*331*) observed the opposite trend when depositing at 940°C.

Hsieh *et al.* (*326*) and Tsuboi (*316*) (*317*) found that resistivity increased immensely with levels of aluminum close to 25%, which they attribute to the incorporated Al^{3+} ions substituting the Cu^{2+} ions, thus decreasing the hole concentration.

Lan (*314*) found Ohmic contact measurements giving a 4.26 eV work function. In the temperature range of 250–310 K, the films show thermal-activation type conductivity, found by Banerjee (*319*) to be 0.26 eV. Banerjee also measured a room temperature Seebeck coefficient of +128 μVK^{-1}.

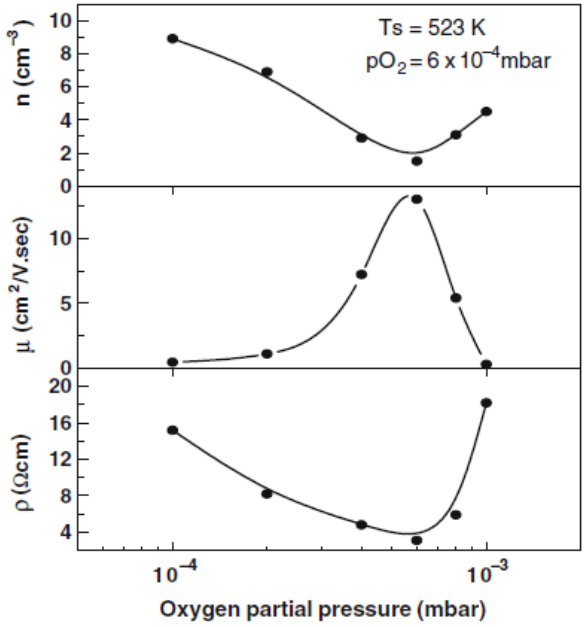

Fig. 4 Variation of electrical resistivity (ρ), Hall mobility (μ), carrier concentration (n) of $CuAlO_2$ films

Figure 3.13 from ref (*12*).

3.5.5. Structural properties:

Many reported films deposited at room temperature up to around 500-600^{o}C were reported to be amorphous (*316*) (*323*) (*327*) (*315*) (*329*), while some have found films deposited between 500 and 700^{o} C have been polycrystalline having $CuAl_2O_4$ and CuO/Cu_2O phases (*316*) (*317*), but Li still found them amorphous (*324*).

Exceptions to this were Reddy et al. (*12*) (*318*), who achieved polycrystalline films for temperatures above 250^{o}C using higher sputter pressure, known to be necessary

parameter for making some multicomponent metal oxides (*332*). Banerjee used high power-high pressure, and close target-substrate distance (*319*) to get phase pure (identified by XRD) polyctrystalline $CuAlO_2$ and ~32 nm grain size (*320*), while fourier transform infrared spectra showed Cu–O, Al–O, and O–Cu–O bonding, and EDX analysis revealed 4 atomic % excess oxygen (*322*). In 2005 Banerjee looked at the influence of film thickness (*321*), and results by TEM revealed the formation of $CuAlO_2$ nanoparticles around 10, 20, and 30 nm for the films deposited in 3, 9, and 15 min.

Crystal orientation for polycrystalline films has been observed at (015) orientation with a surface roughness 0.5 nm(*313*), c-axis normal to the substrate surface (*317*), (006) orientation (*319*) (*328*), Alkoy et al. (*330*) As-deposited samples showed a strong XRD peak around 36^o.

3.5.6. Theoretical calculations

Density Functional Theory calculations have been undertaken by many groups in an attempt to better understand the p-type nature of $CuAlO_2$ and related delafossites. Yanagi *et al*. (*309*) in 2000 performed energy band calculations by using full-potential linearized augmented plane wave method with experimentally determined lattice parameters, revealing the upper valence band is primarily composed of admixed state of Cu 3d and O2p orbitals. This was confirmed by Aston *et al*. (*333*) using high resolution x-ray photoemission/emission/absorption spectroscopy. Pellicer-Porres *et al*. (*334*) produce single crystals and thin films, combined with electronic structure calculations confirmed the lowest energy direct allowed transition at 3.53 eV however, Robertson *et al*. (*335*) calculated higher bandgaps and suggested that the 1.8 eV excitation relates to defects of

some sort. Nolan (*336*) in 2008 used the Vienna ab initio Simulation package to show the origin of the p-type nature of $CuAlO_2$ is due to the facile formation of copper vacancies, which can be tuned so that under oxidizing conditions formation of Cu vacancies is promoted while formation of compensating defects is unfavourable. Laskowski *et al*. (*337*) calculated that electron-hole pairs are very strongly localized at a single Cu plane and confined within only a few neighboring shells.

In 2010 a host of studies were made to advance the understanding of intrinsic defects in $CuAlO_2$. Huang *et al*. (*338*) investigated the formation energies of intrinsic defects in $CuAlO_2$ using GGA+U calculations and their results support previous studies showing that p-type defects (V_{Cu},V_{Al},Cu_{Al}, and O_i) invariably have lower formation energies than their n-type counterparts, with V_{Cu} and Cu_{Al} the lowest. However, the transition levels of the V_{Cu} and Cu_{Al} defects are deep, which are responsible for the poor p-type conductivity in $CuAlO_2$. Scanlon and Watson (*339*) in addition found V_{Cu} and Cu_{Al} will dominate under Cu-poor/Al-poor conditions and confirm deep defect levels as being likely mistaken as indirect band gaps. Christensen *et al*. (*340*) found using QSGW yields reasonable values for both structural and band gap properties, with LDA+U giving the most accurate band gap fit but with other inconsistencies.

Liu *et al*. (*341*) obtained band structure results revealing that Cu and O are mainly covalent whereas Al and O is mainly ionic as well as a significant optical anisotropy in the components of polarization directions (100) and (001). Trani *et al*. (*342*) used self-consistent Coulomb hole plus screened exchange calculations, which predicts direct band gaps that are compatible with experimental optical gaps only after including the strong

polaronic and excitonic effects present in these materials but were not in agreement with the small indirect gaps observed.

Poopanya *et al*. (*343*) used the constant scattering time (s) approximation and achieved a direct gap of 3.31 eV, and observed that the Seebeck coefficient S(T) increases with increasing acceptor doping level corresponding to a level of 0.262 eV, which is identified as the Fermi level of $CuAlO_2$.

3.5.7. Annealing affects and stability:

Banerjee *et al.* did anneals (*305*) at 473 K in an O_2 atmosphere (at chamber pressure 0.2 mbar) between 30 to 150 min, and found that excess oxygen was incorporated with increasing annealing time. Electrical conductivity increases to a maximum after 90min and thereafter decreases, likely due to excess oxygen scattering. Alkoy *et al*. (*330*) tried higher temperatures of 350–550^{o} C for 1–4 h in air, which further increased transmittance up to a peak value of 95% at a wavelength of 600 nm, however resistivity did not change appreciably. For high temperature annealing at 1100°C in air for 3 h, films tend to be mostly delafossite-type $CuAlO_2$ or a phase mixture of $CuAlO_2$ and $CuAl_2O_4$ (*327*) while also obtaining higher bandgaps up to 3.80 eV and transmission increases to over 80%. Su *et al*. (*324*) focused on post-annealing with temperatures of 1050^{o}C in air ambient for 20min with a ramping rate of 50^{o} C/min on sapphire substrates. Only the film deposited at 700 °C showed the highly preferred c-oriented crystalline $CuAlO_2$, with electric conductivity of 1.01 Scm^{-1} and at temperatures below 190 K, conductivity indicates variable range hopping is dominant as proposed by Kawazoe *et al.* Others saw mixed

phase $CuAlO_2$ and Al_2O_3 under similar conditions (*329*) along with increased surface roughness, an average drop of 40% in transmittance and direct band gap dropping to 3.5 eV (conductivity values were not reported).

Kumekawa *et al.* (*344*) used thermogravimetry and thermodynamic calculations, pointing to $CuAlO_2$ thermodynamic instability in air below 800^o C and that the oxidation reaction, $4CuAlO_2 + O_2 \rightarrow 2CuO + 2CuAl_2O_4$ should occur if the reaction kinetics are high enough. However, rate constants and activation energies indicated slow kinetics of the oxidation reaction, showing kinetic stability of $CuAlO_2$ even under some thermodynamically unstable temperatures and atmospheres. This has been confirmed by Brahimi for very strong acidic electrolyetes such as HCl, $HClO_4$ or aqua regia and then for long periods of time (*345*). Upon post-annealing cool down there is not a complete loss of the $CuAlO_2$ phase, once formed. Therefore, it can be concluded that the rate of the decomposition reaction is slow enough and/or decreases rapidly as the temperature is decreased and the crystallites are sufficiently large.

Focusing on oxygen reducing anneals, Lan *et al*. (*313*) used sputter-deposited (015) orientation films and achieved the preferred growth along (001) c-orientation using postannealing in N_2 ambient at 900 °C for 5 h. Using the *ab* plane as a conduction path with high conductivity, the resistivity of film was reduced by 3 orders of magnitude to 37 Ω-cm. The activation energy is evaluated to be around 0.088 eV. The surface roughness of the film increased from 0.5 nm for as-deposited film to 2.1 nm. La *et al.* (*312*) and others (*311, 346*) had similar results and attributed conductivity increase to Cu vacancy

and interstitial oxygen formation. Four optical bandgaps estimated at the energies 3.00, 3.15, 3.50, and 3.75 eV change appreciably by anneal, however transmission does not. Tsuboi *et al.* (*317*) had similar conductivity results however they found them independent of substrate material and deposition temperature. Tsuboi *et al.* (*317*) used temperatures of 1050^{o}C which caused a reduction in the molar fraction of oxygen, with composition of predominating $CuAlO_2$ and c -axis preferential orientation. They claim this is due to the small lattice mismatch between the rhombohedral [010] of delafossite-type $CuAlO_2$ and the hexagonal [1100] of the sapphire substrate. The annealed films had poor optical transmission and a band gap of about 3.5 eV. Stevens *et al.* (*323*) found oxygen deficient films formed the delafossite structure after annealing with poor electrical properties. Films deposited with P_{O2}=2 mTorr transformed into the delafossite structure and exhibited p-type conductivity after annealing at temperatures above 750 °C. In general, an anneal temperature near the phase formation boundary led to an increase in conductivity. The results by these authors suggest high temperature annealing in N_2 drives the formation of $CuAlO_2$ conductive phase along with the best overall properties.

Tsuboi *et al.* (*315, 316*) made $CuAlO_2$ films (described previously in sputtering section), which were annealed between 500 and 1050^{o}C for 4 h in N_2 at 1 atm. Results show $CuAlO_2$ peaks appearing at 700^{o}C or higher along with the disappearance of the $CuAl_2O_4$ and CuO phases and Cu- and Al-rich annealed films had in addition a Cu_2O phase and an amorphous Al_2O_3 phase, respectively. In comparison with the optical absorption edge of the $CuAlO_2$ films, those of Cu-rich and Al-rich films shifted to the longer and shorter wavelength regions respectively with overall band gap around 3.5 eV.

The resistivity dropped by three to five orders of magnitude to 10-10^2 Ω-cm independent of Cu/Al ratio.

Chapter 4: Experimental Methods

4. Alternate thin film deposition methods:

Creating high quality thin films for the applications described is typically done in a vacuum environment, especially for metals and metal/non-metal stacks. A vacuum environment, the use of highly pure material sources, and in-situ cleaning of substrates, all allow one to minimize the incorporation of impurities in the film. Of great concern here is the strong reaction that most metals have with oxygen and other hydroxide species present both in the gas and on surfaces in all uncontrolled environments. Also, controlling adatom nucleation is important for minimizing crystal defects and film uniformity,. In a vacuum environment the adatom energy can be controlled by creating a controlled flux of atoms, as well as controlling the substrate temperature and ambient gas conditions. In atmospheric pressure conditions this is difficult. We will briefly consider the deposition methods available for producing TCO materials.

Thermal evaporation is a process whereby source material (typically in solid form) is heated in a vacuum (usually by thermal conduction, electron bombardment, or a laser). Atomic species and sometimes clusters evaporate or sublime and deposit on the

surrounding and much cooler, chamber walls and samples. When depositing single element materials this is straight forward, however evaporating alloys with the correct stoichiometry can be difficult because the different elements can have widely varying vapor pressures. A solution to this is to co-evaporate individual elements from different sources operating at different temperatures. Evaporating metal oxides is more difficult. Metal oxides may decompose at evaporation temperature causing the primary flux from the source to be metal atoms or metal suboxide molecules. In addition, small changes in the chamber partial pressure of oxygen containing species such as water vapor can drastically change the composition of the film. These effects leads to variation in the oxygen content level in the deposited film, which may be acceptable for certain insulators like SiO_2, but in most TCO materials slight changes in oxygen can greatly influence the properties. This issue is compounded for ternary or higher metal oxides. Pulsed Laser Deposition (PLD), which uses a laser pulse to provide a rapid, localized heating of the source, mitigates these problems, however it has other problems that make its industrial use, and even its application to device fabrication, difficult so it was not considered for this project.

Chemical Vapor Deposition (CVD) is another common deposition process where material is deposited by chemically reacting a volatile compound of the desired material with other gases to produce a nonvolatile solid that deposits atomistically on a suitably placed substrate. The basic steps of CVD are the transportation of reactants to the surface of the substrate, reactant adsorption on the surface, heterogeneous chemical reaction on the surface of the substrate, lattice incorporation or film deposition, desorption of reaction

byproducts, and transportation of byproducts outside the deposition zone. CVD can deposit many materials, however much work remains to be done in getting reproducible, quality ternary metal oxides. Also, CVD tends to be more expensive than physical vapor deposition methods. Therefore this method was not considered.

4.2. Sputtering

Sputtering is a well-known technique and one of the most important for making thin films. It is classified as a Physical Vapor Deposition (PVD) process by which the atoms of a solid target are ejected into the gas phase due to the bombardment of high energy ions. These processes have been used for more than 150 years. Initially it was used for making metallic mirrors, however Overbeck *et al.* (*347*) demonstrated substantial progress for compound materials in 1933, observing tin thin films deposited on glass substrates from a circular target in air, oxygen and nitrogen atmospheres. The introduction of magnetic and electric fields in 1936 by Penning was a milestone in sputtering technology, enhancing the plasma confinement and increasing the sputtering rate. The process has been used commercially since the early 1970s. Various types of customized sputtering systems are available for specific applications. Sputtered thin films are used in a variety of fields such as depositing metal layers for CDs and DVDs, semiconducting transparent conducting oxides layers, anti-reflecting and UV protecting layers in the glass industries etc.

Sputtering is the removal of atoms from a solid target by ion bombardment (*348*). The sputtering system consists of a chamber which is maintained at a reduced pressure (typically 1 to 100 mTorr) of an inert gas such as argon, as shown in Figure 4.1.

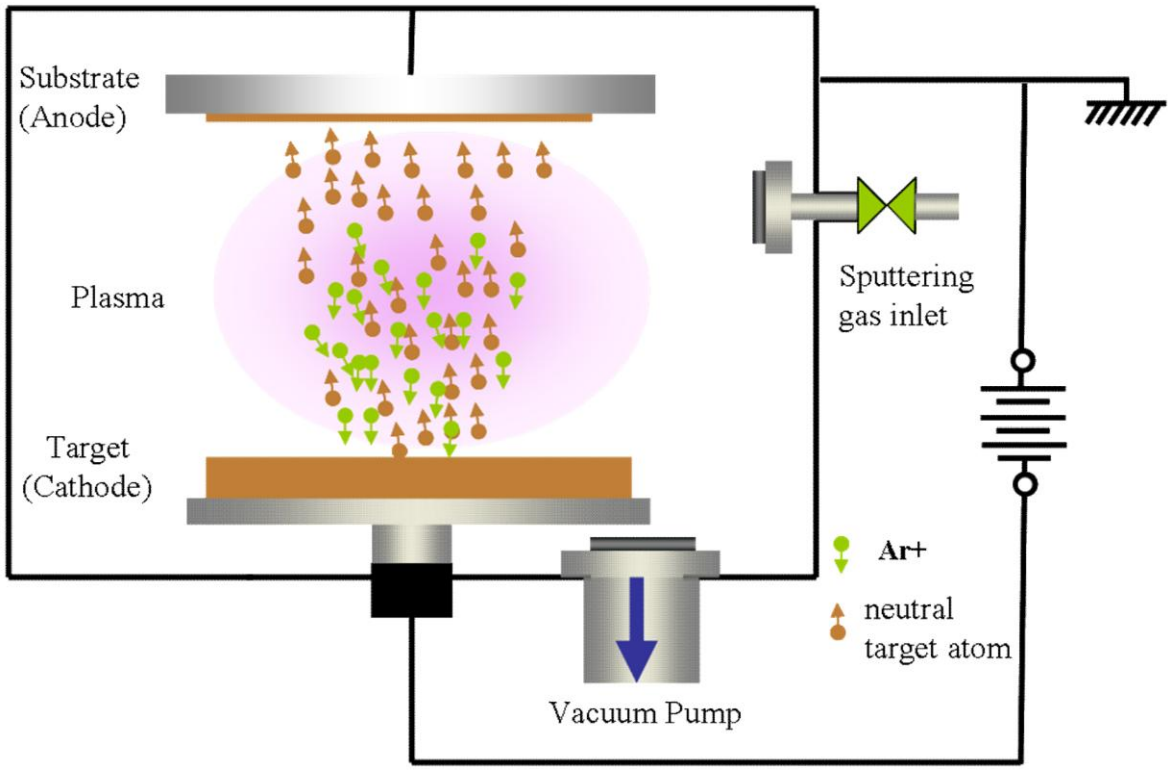

Figure 4.1: Schematic of D.C. sputtering.

For the sputtering process to work, a plasma is generated in between the anode and cathode. At a high-enough applied electrical potential electrons are ripped off the cathode and accelerate towards the anode, as well as secondary electrons due to ion bombardment of the cathode –which is the dominant process in steady state sputtering. Along the way many of them interact with gaseous atoms (*349*). Interactions include: 1) Elastic scattering, in which an electron collides with an atom and the total kinetic energy is conserved. Ionization, resulting in an electron loss from the collision; 2) Excitation,

whereby some energy is transferred to the atom (possibly resulting in the generation of photons); and 3) Two-step ionization, where an intermediate atomic excited state transfers to an ionic state.

The positive ions are accelerated towards the (cathode), which is where the target is placed. The ions impact the target surface. Collisions lead to fast recoil particles which lose their energy by hitting other atoms in the target, starting a collision cascade. The long time (10^{-11} - 10^{-9} s) of this cascade is damped by the energy dissipation, resulting in local heating of the target. When the energy imparted on atoms within the collision cascade is greater than the surface binding energy, then they are ejected from the target if they are close to the surface (*350*). In addition to the ejection of neutral target atoms, sputtering also produces atomic clusters, secondary electrons and ions, and photons. These species will condense on opposing surfaces, including a placed substrate, in the vacuum chamber.

One of the main parameters influencing the sputtered particles energy is the operating pressure. This can be related to the *mean free path* λ_{mean}, the average distance which a particle can travel before colliding or reacting with another particle. This is inversely proportional to pressure as given by:

$$\lambda_{mean} = \frac{RT}{\sqrt{2}\pi d_{gas} N_a p} \tag{4.1}$$

where R is the universal gas constant (8.135 J K^{-1}/mol), d_{gas} is the diameter of a molecule

of the inert gas, N_a is the Avogadro number (6.0221 x 10^{23} mol^{-1}) and p is the pressure. If λ_{mean} is higher than target-substrate distance d, the ejected atoms will travel ballistically, hit the substrate and condense to form thin films. A higher mean free path results from lower pressure, however in order to strike a plasma a minimum number of collisions is required. On the other extreme, a higher pressure reduces the mean free path, causing scattering of sputtering particle and leading to a decreased sputter rate (*351*). As a result of the gas phase collisions, transport in this regime includes a significant diffusive component. These collisions also thermalize the ejected species, reducing the energy that they have as they deposit on the surface of the substrate.

The minimum voltage needed to start a sustainable plasma (known as a glow discharge) is the *breakdown voltage, V_b*. The breakdown voltage relationship to operating pressure and distance is known as Paschen's Law (*352*). The breakdown voltage magnitude depends on various factors such as the operating pressure, the gaseous medium, the electrode geometry, the nature of the electrode material etc. (*353*). It is proportional to the inverse log of pressure at low pressures, reaches a minimum, and increases proportionally to pressure at higher pressures.

The *Sputter yield* is another important sputtering metric which is defined as the number of atoms ejected from the target surface over the number of incident ions. The sputter yield depends on various factors, including the atomic mass of incident ions, their kinetic energy, electronic configuration, and the angle of incidence. On the target it

depends on atomic mass, electronic structure, crystal structure, orientation, surface binding energy, surface roughness and density (*351*).

One of the key technologies that accelerated the sputtering yield has been the invention of magnetically enhanced sputtering (*354*). The magnetron design consists of permanent magnets arranged behind the target holder where the target material is located. As previously stated, during sputtering secondary electrons are created at the target surface and are influenced by a magnetic field, which is typically designed to confine the electrons in a closed loop path on the target surface to further increase ionizing collisions. This results in a highly dense, stable plasma and hence a high sputtering rate, however the downside is that sputtering tends to take place nonuniformly across the target producing a "race track" pattern which reduces target life (*355*). Additionally, the magnetron can be designed such that the plasma takes up a large or small volume, which combined with the substrate position and target-substrate distance determines whether the plasma interacts with the deposited film. In certain films the influence of the plasma is beneficial in producing defects during film growth however a lack of plasma can be compensated for by introducing a negative substrate bias.

A big disadvantage of DC sputtering is that insulating materials will not work as a target due to charge accumulation on the surface. In Radio Frequency (RF) sputtering this is overcome using an alternating high frequency and a large potential voltage. The ions are attracted to the target on the negative half cycle and sputter the surface along with depositing a positive charge. On the positive half cycle the electrons reach the target

surface to neutralize the charge. A frequency of 13.56 MHz is the most common in order to minimize RF interference (*356*), however a wider range can be used. In order for this method to work efficiently an impedance matching circuit is needed between one electrode and the power supply to maximize the power transfer. It also typically results in a deposition rate much lower than DC sputtering. A potential disadvantage for use with insulating materials is that they are commonly brittle, and have poor thermal conductivity along with nonuniform target heating leading to thermal expansion which tends to fracture the target at higher sputter powers (*356*).

Reactive RF sputtering is an extension of RF sputtering ceramic targets except that the target may be electrically conductive however the material processing necessitates added reactive gas elements such as oxygen be inserted in gas form in the chamber to be incorporated in the deposited film rather than sourcing the reactive elements from the target material. Typically in this scenario the reactive gas reacts with the target (even if the target is already ceramic) to form an electrically and thermally insulating layer which is why RF is usually used.

Pulsed DC magnetron sputtering is a newer deposition technique in which the target is driven by DC voltage pulses in the mid frequency region (10 to 350 kHz). This technique has been more recently implemented for the reactive sputtering of dielectric materials because of its improved arc suppression (*357, 358*). Controlling the duty cycle determines how much time is spent moving positive ions towards the target, called *pulse-on* time, and how much time in moving electrons towards the target, called *pulse-off* time.

This mitigates the charging problems associated with continuous DC reactive sputtering of dielectric materials by discharging the charged regions on the target during the reverse voltage phase. Depending upon sputter configuration the peak voltage during *pulse-on* or *pulse-off* can be symmetric or asymmetric.

In the present work we focused on the production of metal oxide films via reactive RF sputtering from metallic or ceramic targets. The system used was an AJA 2000 with 2 RF guns (Power/Plasma Products Model: RF5S, 500 watts max), and two DC guns (Advanced Energy Model: MDX-1K power supplies, 1000 watts max). It uses 3 inch diameter targets of less than .25inch thickness. Solid electrical conduction is made with a copper mesh between the target copper backing plate and the gun. Oxygen feeds through a lateral tube from one side of the main chamber, and argon can be selectively fed through from either gun three or four inside the shield, which also electrically functions as the anode. The oxygen flow controller ranges from 0 to 10 +/- 0.1 sccm . The argon flow controller ranges from 0 to 100 +/- 0.1 sccm.

4.3. Characterization Methods

4.3.1. X-ray / Ultraviolet Photoelectron Spectroscopy

X-ray Photoelectron Spectroscopy (XPS) analyzes the surface by irradiating a sample in vacuum with monoenergetic soft x-rays and analyzing the energies of the emitted photoelectrons. The spectrum is obtained as a plot of intensity (or counts per second) versus the kinetic or binding energy of the electrons. While the kinetic energy (KE) of

the electron is the experimental quantity measured by the spectrometer, it is dependent on the energy of the x-ray source employed and is not an intrinsic material parameter. An energetic x-ray photon incident on the target atom excites it to a higher energy state, from which the target atom relaxes by emitting a photoelectron. Photoelectrons are emitted from all energy levels of the target atom, and the resultant electron energy spectrum is characteristic of the emitting atom type and may be thought as its XPS fingerprint. The measurement is surface-sensitive down to around 10nm due to limited escape depth of electrons. The beam diameter tends to be in the centimeter region.

The binding energy of the electron is the parameter that identifies the electron specifically, both in terms of its parent element and atomic energy level. XPS can be used to identify and determine the concentration of the elements on the surface because each element has a unique set of binding energies (*359*). Variations in the elemental binding energies arise from differences in the chemical potential and polarizability of compounds. In addition to photoelectrons emitted in the photoelectric process, Auger electron may be emitted due to the relaxation of the excited ions after photoemission. In the Auger process, an outer electron falls into the inner orbital vacancy, and a second electron is simultaneously emitted, carrying off the excess energy. The Auger electron possesses kinetic energy equal to the difference between the energy of the initial ion and the doubly charged final ion, and is independent of the mode of the initial ionization. Thus, photo-ionization normally leads to two emitted electrons - a photoelectron and an Auger electron. In this work an Al K_{α} x-ray source was used and the equipment model is a Surface Science SSX-100 with a resolution of 0.8 eV. Sample transfers were made in the

air and the samples were pre-sputtered to remove surface contaminants before being analyzed at room temperature in a UHV environment.

Ultraviolet Photoelectron Spectroscopy (UPS) is a method similar to XPS, except that the focus is on energetic electrons emitted from valence band energies of elements in the samples (*360*). It is able to measure them more accurately than XPS. The system design and sample preparation are similar, except that in UPS ultraviolet light is incident on the sample, emitting electrons down into the valence band of materials, but no lower. A fine resolution energy analyzer is used analyze the emitted electrons. Typically a gold surface is used as a reference for calibrating each measurement. Due to the short range of the emitted photoelectrons the measurement is particularly sensitive to the surface within 10 nm, even more so than XPS. As a result, adsorbed carbon and hydroxide contaminants on the sample surface are much more important in UPS measurements than they are in XPS. UPS measurements are able to extract the valence band of a material, as well as the work function. The work function is achieved by measuring the full width of the photoelectron spectrum (from the highest kinetic energy/lowest binding energy point to the low kinetic energy cutoff) and subtracting from the photon energy of the exciting radiation. The difference is the work function. The top of the valence band is determined by linearly fitting the photoelectron spectrum to get the x-axis intercept.

In our work, measurements were done by the National Renewable Energy Laboratory (NREL) using a Physical Electronics UPS/XPS system with an operating pressure of $5x10^{-8}$Torr, with sputter cleaning done using $5x10^{-7}$ to $1x10^{-6}$ Torr helium using a Kratos ion source at 37mA. Samples were cut to ~1 cmx2cm with the film deposited onto ITO-

coated glass for sufficient conduction, and half of the sample was exposed ITO in order to make grounding contact in the system.

4.3.2. Auger Electron Spectroscopy

Auger Electron Spectroscopy (AES) method is based on the excitation of so-called 'Auger electrons'. This ionization process can be provoked either by electrons – commonly known as the Auger process – or by photons (*361*). The latter is described in the previous section. The machine we used is based on the use of primary electrons with typical energies at 5keV and the possibility to focus and scan the primary electron beam in the nanometer and micrometer range analyzing the top-most atomic layers of the sample. The emitted Auger electrons are part of the secondary electron spectrum obtained under bombardment of electrons with a characteristic energy, allowing one to identify the emitting elements. The experimental setup is very similar to that of a Scanning Electron Microscope – with the difference that the electrons are not only used for imaging but also for chemical identification of the surface atoms. Our system (Physical Electronics Model 545) contains a differentially pumped ion gun for sample cleaning and automated depth-profile thin film analysis.

In the plotted energy signal, the auger peaks are superimposed on the spectrum of the secondary electrons and backscattered electrons, which are typically much larger. For this reason the differentiated electron energy signal is usually used to detect and quantify auger peaks.

4.3.3. Rutherford Backscattering

In Rutherford Backscattering (RBS) the primary ion energy ranges from about 100 keV (for H^+) to several MeV (for He^+ and heavier ions) (*362*). The ion–target atom interaction can be described using the Coulomb potential from which the Rutherford scattering cross-section is derived, which allows absolute quantification of the results. Information in principle arises from a thickness of the order 100nm, but analysis of surface layers is also possible by using channeling/blocking techniques. An ion beam is directed onto a solid surface, a part of the primary projectiles is backscattered from the sample and the energy distribution of these ions is measured. Since the ion–target atom interaction can be described by two-body collisions, the energy spectra can be easily converted into a mass spectra. Structural information is obtained from crystalline samples by varying the angles between beam and sample. A limitation with RBS is that only the individual atoms of an element can be detected and no information on compounds or molecules can be gained. Models are typically used for structure analysis, and usually based on results from XRD, which provide the symmetry of the unit cell but not, directly, the real atomic positions.

In this work we used a MAS 1700 Pelletron tandem ion accelerator (5SDH) equipped with charge exchange RF plasma source by National Electrostatics Corporation (NEC), and an analytical endstation (RBS 400) by Charles Evans & Associates. The ion detector adjustable between 90° and 150° for grazing-angle scattering (enhanced surface sensitivity). For modeling Quark and RUMP (*363*) software were used.

4.3.4. Scanning probe microscopy (AFM/KFM/CFM)

In Atomic Force Microscopy (AFM) a tip, integrated to the end of a spring cantilever, is brought within the interatomic separations of a surface, such that the atoms of the tip and the surface are influenced by interatomic potentials (*364*). In the constant force mode, as the tip is rastered across the surface, it bounces up and down with the contours of the surface. By measuring the displacement of the tip (*i.e*. the deflection of the cantilever), one can theoretically map out the surface topography with atomic resolution. Typical designs bounce a laser off of the cantilever and are able to measure the vertical and lateral deflection using a quadra-photodiode. The AFM is essentially identical in concept to the scanning profilometer, except that the deflection-sensitivity and resolution are improved by several orders of magnitude. The output of the photodiode vertical deflection is connected to a feedback controller that regulates the force between the sample and the tip by moving the sample up or down. The sample is moved by a PZT scanning actuator. There are many modes of AFM operation including contact mode, tapping mode, Kalvin Force Mode (KFM), and Conduction-AFM (CAFM). CAFM requires a conductive tip with a sufficiently low-resistance grounded sample. The probe is operated in constant contact with the sample while applying a DC bias (which may be swept to different levels at each scanning point). This allows for imaging of the conductivity of a sample. For CAFM measurements an Agilent 5500 environmental SPM was used with nitrogen flow and controlled low 0.1 % humidity. The principle limitation in resolution for all of these techniques is usually the tip's diameter and aspect ratio, however sample features including moisture are also a factor. For standard AFM measurements a Veeco Dimension 3000 was used with a standard silicon tip <25nm in radius.

4.3.5. Film thickness

The thicknesses of the thin films prepared for the work presented in this thesis were measured either by ellipsometry or by a stylus profiler.

Ellipsometry reflects a polarized light source off the sample and looks at the change in polarization and intensity using a detector (*365*). This change is dependent on the film thickness and complex refractive index. The data can be fitted to a model typically composed of only a few layers of homogenous and isotropic material to help determine the properties. In this work we used a Variable Angle Spectroscopic (i.e. multi wavelength) Ellipsometry or VASE instrument.

A stylus profiler takes measurements electromechanically by moving the sample beneath a diamond tipped stylus. The high precision stage moves the sample according to a user defined scan length, speed and stylus force. Surface variations cause the stylus to be translated vertically, which can be electrically measured. The film whose thickness has to be measured, is deposited with a region masked. This creates a step on the sample surface whereby the thickness of the sample can be measured accurately by measuring the vertical motion of the stylus over the step. It is also possible to image the surface using 2 dimensional scanning, however this was not employed for our work. In this work a KLA Tencor p-16 was used.

4.3.6. Resistivity measurements

The resistivity of the films is determined by the four-probe Van Der Pauw method (*366*) with the electrodes in square planar geometry (we used samples typically between 5x5 mm^2 and 1x1 cm^2). The Van Der Pauw method sources a current through a pair of adjacent electrodes and samples the voltage difference through the other pair on the opposing side of the sample. In order to obtain accurate measurements the sample must have a flat shape of uniform thickness, relatively homogeneous and isotropic, contacts located at the perimeter of the sample, and the area of contact of any individual contact should be at least an order of magnitude smaller than the area of the entire sample. In our work indium layers were used as the electrodes, and were pressed onto the four corners with a size such that the total indium contact area was less than 10% of the total sample area. The current voltage measurements were carried out using a HP 4156A Semiconductor Precision Parameter Analyzer typically swept from 0 to 5 volts. The average resistivity of a sample is given by $\rho = R_S \cdot t$, where R_s is the sheet resistance given by the slope of the sourced current and measured voltage characteristic curves (if device showed Schottky behavior to low voltage, the slope was determined at high voltages ~5 volts) processed through the Van Der Pauw formula, and t is thickness.

4.3.7. Capacitance Voltage measurements

Capacitance Voltage (C-V) measurements are useful for determining semiconductor parameters. It can be used for many devices but primarily for metal-oxide-semiconductor and metal-semiconductor devices wherein a sufficiently large capacitance can form across the device and leakage current is minimized. The procedure for taking C-V measurements involves the application of DC bias voltages across the (effective)

capacitor while making the measurements with an AC signal. Commonly, AC frequencies from about 10kHz to 10MHz are used for these measurements. Lower frequencies tend to respond to material defects such as traps while higher frequencies do not. The bias is applied as a DC voltage sweep that drives the semiconducting material from its accumulation region into the depletion region, and then into inversion, depending upon band alignment on both sides of the junction. The carrier concentration vs. material position can be derived from the C-V data. Calculating the slope of ($1/C^2$) versus voltage graph, the bulk concentration N_B is found. For these measurements we used a HP 4294A Precision Impedance Analyzer.

4.3.8. Hall measurements

The electrical resistivity of a semiconductor thin film can be written using Ohm's law, $\rho = 1/e(n\mu_n + p\mu_p)$ where ρ is the film resistivity, e is the electronic charge, n and p are the number density of carriers, electrons and holes, respectively. μ_n and μ_p are the carrier mobility for electrons and holes respectively. According to Ohm's law, low resistivity can be achieved by increasing the carrier concentration or mobility or both. Increasing the carrier concentration is somewhat self-limiting because at some point the increased number of free carriers decreases the mobility of the film due to carrier-carrier scattering. Hence there is a tradeoff between the carrier density and carrier mobility for achieving low resistivity. For our work samples were cut into 5 mm x 5 mm to 1 cm x 1 cm squares and contacts were made on the corners using 10 nm of sputtered titanium followed by 100 nm of gold, with each contact area less than 10% of total sample area. The four contacts were then wire bonded (using West Bond 7476E wedge-wedge bonder,

using 1% Si/Al wire 38 um in diameter) to a chuck used inside the Hall measurement system, composed of a Quantum Design Model 6000 PPMS control rack for temperature and field control with a liquid helium cooled vacuum chamber, a Keithley 220 current source, and a Keithley 2182 voltmeter. The chamber was sealed and pumped to a pressure around 0.8 mTorr.

The Hall signal was measured between two ends while passing the current through the other two ends. The Hall mobility is related to the change in resistance due to magnetic field, which was applied to measure Hall voltage (*59*). The Hall mobility is assumed to be the mobility for materials in the case of band transport. The carrier concentration can be extracted by knowing the mobility and resistivity.

4.3.9. X-Ray Diffraction Studies

A given substance always produces a characteristic X-ray diffraction pattern (XRD) whether that substance is present in the pure state or as one constituent of a mixture of substances, as long as the substance has sufficient long-range order to be detected. This fact is the basis for the diffraction method of chemical analysis. X-ray diffraction analysis thus provides structural rather than chemical information. As such it can distinguish between different phases of the same material if there is sufficient difference in the structure. Compared with ordinary chemical analysis the diffraction method has the advantage that it is much faster, requires only a very small sample and is nondestructive. The basic law involved in the diffraction method is Bragg's law (*367*). X-ray diffraction studies gives a whole range of information about the crystal structure, orientation,

average crystalline size and stress in the films. Experimentally obtained diffraction patterns of the sample are compared with the standard powder diffraction files published by the International Centre for Diffraction Data (ICDD).

XRD measurements of the films in the present studies were done using a Bruker-AXS microdiffractometer. A 2.2 kW Sealed Cu X-ray source was used for recording the diffraction pattern. The data was processed using JADE software.

4.3.10. Scanning Electron Microscope (imaging, EDX)

The Scanning Electron Microscope (SEM) uses electrons rather than light to form an image (*368*). The combination of higher magnification, larger depth of focus, greater resolution, and ease of sample observation makes the SEM one of the most heavily used instruments in current research and development. The electron beam comes from a filament, made of various types of materials.

The streams of electrons that are attracted through the anode are made to pass through a condenser lens, and are focused to very fine point on the sample by the objective lens. The electron beam hits the sample, producing secondary electrons from the sample. These electrons are collected by a secondary detector or a backscatter detector, converted to a voltage, and amplified to form an image.

Energy dispersive x-ray (EDX) analysis is a technique used for identifying the elemental composition of the specimen, or an area of interest thereof (*368*). During EDX Analysis, the specimen is bombarded with an electron beam inside the scanning electron microscope. The bombarding electrons collide with the specimen atom's own electrons,

knocking some of them off in the process. A higher-energy electron from an outer shell eventually occupies a position vacated by an ejected inner shell electron. To be able to do so, however, the outer electron must give up some of its energy by emitting an x-ray. By measuring the energy of the x-rays emitted by a specimen during electron beam bombardment, the identity of the atom from which the x-ray was emitted can be established. This allows for composition analysis of a sample.

For the SEM and EDX analysis, a JOEL 6700 with a Thermo-Noran Vantage system and Oxford MonoCL 2 system was used.

4.3.11. Optical absorption and band gap

Intrinsic optical absorption of a single photon across the band gap is the dominant optical absorption process in a semiconductor. It happens when the energy of the incident photon (hν) is larger than the band gap energy the excitation of electrons from the valence band to the empty states of the conduction band occurs. The light passing through the material is then absorbed and the number of electron hole pairs generated depends on the number of incident photons. The frequency ν is related to the wavelength λ by the relation, $\lambda = c/\nu$, where c is the velocity of light. The photon flux decreases exponentially inside the crystal,related to the absorption coefficient , which is determined by the absorption process in semiconductors and the extinction coefficient. For semiconductors with a parabolic band structure (i.e. free electron like), the relation between the absorption coefficient (α) and the band gap of the material is dependant on the allowed direct/indirect, and forbidden direct/indirect transitions. In the case of direct

transition, a plot of $(\alpha h\nu)^2$ as a function of $h\nu$ will be a straight line and the intercept on the energy axis ($(\alpha h\nu)^2$ equal to zero) will give the band gap energy. The transmissions of the thin films were recorded using an Ocean Optics Inc. HR2000 spectrophotometer in the present studies.

Chapter 5: Experimental

5.1 The n-type layer

Zinc stannate was deposited on silicon and glass (Thermo scientific gold seal slides 3010 unless stated otherwise) by RF magnetron sputtering in an AJA ATC 2000 sputtering system within a reactive oxygen environment using a ceramic target made of 50 atomic % ZnO and 50 atomic % SnO_2. The target-substrate distance was varied between 6.5 cm and 12.5 cm to control the influence of adatom energy and plasma radiation on the film. The oxygen concentration in the sputtering gas was varied between 2 % and 20 % to control the film stoichiometry. The chamber pressure and substrate temperature were varied between 2 mTorr (0.267 Pa) and 20 mTorr (2.67 Pa) and between room temperature and 250 ^oC, respectively, while the sputtering power was maintained at 125 W. The substrate was biased with RF power, which was varied between 0 and 75 W. The deposition temperature is constrained to below 300 ^oC by Cd

diffusion from the CdS buffer layer into the CIGS film (*369*). We limited the sputtering temperature to 250 ^{o}C and used post-deposition Rapid Thermal Annealing (RTA) between 200 ^{o}C and 600 ^{o}C for 1 to 10 min either in O_2 or in N_2 to investigate the effects of thermal cycles on the broken gap junction performance. This was done to simulate the thermal cycle required to deposit the upper device in a tandem stack.

The band gap and the work function of the films were measured using optical absorption on glass substrates and Kelvin Probe Force Microscopy (KPFM) on tin doped indium oxide (ITO)-coated glass (Delta Technologies produced ITO on boro-aluminosilicate glasses) substrates, respectively. We chose ITO as the substrate since it was conductive enough to use as a bottom contact for KPFM and it, along with AZO, is commonly used in the CIGS device stack where is would serve as a substrate for the broken gap junction. Carrier concentration and mobility were determined from Hall effect measurements on glass substrates. Composition and chemical bonding were examined using X-ray photoelectron and Auger electron spectroscopies (XPS and AES) using films deposited on silicon substrates. Film structure and morphology were studied using x-ray diffraction (XRD) and atomic force microscopy (AFM) on silicon and glass substrates. Four point probe with Van Der Pauw geometry was used for determining the electrical resistivity of the films on glass substrates.

5.2 The p-type layer

Cu_2O (cuprous oxide) was chosen for the p-type layer and thin films of this material were deposited on silicon and glass using RF reactive, sputtering of a 99.99 % pure

copper target in an Ar/O_2 gas mixture. The target-substrate distance was similar to that used for zinc-stannate deposition and the oxygen concentration in the feed gas was varied between 1.1 % and 2.7 %. The total chamber pressure was varied between 1 mTorr (0.133 Pa) and 30 mTorr (4 Pa) and the sputtering power was varied between 71 W and 200 W. Substrate RF bias and the deposition temperature were varied between 0 and 50 W and between room temperature and 250 ^oC respectively. The films were annealed post-deposition using RTA, between 300 ^oC and 600 ^oC for 1 to 10 min in either O_2 or N_2. The characterization methods used were identical to those used for zinc-stannate.

Cuprous oxide was also deposited on silicon and glass using RF sputtering of a ceramic 99.99 % Cu_2O target in an Ar gas. The target-substrate distance was similar to previous. The total chamber pressure was varied between 1 mTorr (0.133 Pa) and 30 mTorr (4 Pa) and the sputtering power was varied between 71 W and 220 W. Substrate RF bias and the deposition temperature were varied between 0 and 50 W and between room temperature and 250 ^oC, respectively. The films were annealed post-deposition using RTA, between 300 ^oC and 500 ^oC for 1 to 5 min in either O_2 or N_2. The characterization methods used were identical to those used for

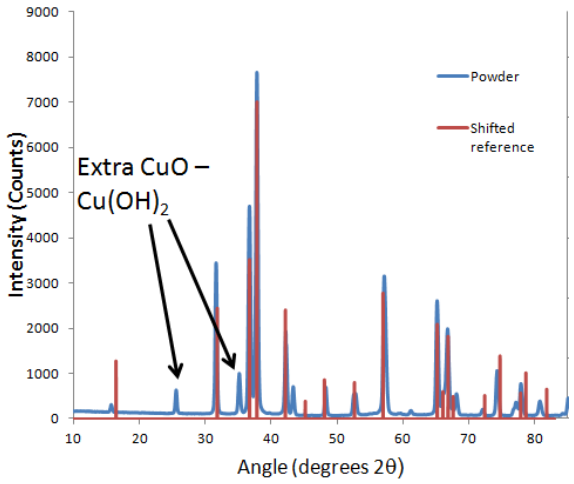

Figure 5.1. XRD plot of powder prior to pressing and sintering to form the sputter target used. The reference XRD spectra is from a computer model of $CuAlO_2$, which had to be shifted and compressed slightly to match our data.

zinc-stannate.

An alternative p-type TCO, $CuAlO_2$, was deposited from a custom ceramic sputter target. Copper oxide powder (99.99% Cu_2O, >10 μm particle size, Sigma Aldrich) was ground down to an average under 1 μm using a ball mill. Aluminum oxide powder (Al_2O_3 – alpha phase, 99.99% purity, ~100 nm avg. particle size, Inframat Advanced Materials) was mixed with the copper oxide powder in equal portions by atomic percent. The mixture was heated at 1100 ^oC overnight and reground the next day. This process was repeated until there were very little (visually identifiable) white and red particles left. The powder had a light bluish white appearance. We used SEM/EDS to confirm that the vast majority of the powder was stoichiometric and XRD to verify the $CuAlO_2$ phase (see figure 5.1). The powder was pressed at 2000 psi for 1 hr to form a 3" diameter by 0.125" thick disc, this was then sintered at 1160 ^oC for 16 hrs. The final target was bonded to a copper plate and a 5 hr burn-in of the target at 100W RF was performed. The target was subsequently stored in a dessicator when not in use to slow possible further oxidation as reported for $CuAlO_2$ particles in the 1μm-10 μm range (*344*).

Films were sputtered using 100W RF for 5 hrs to get 10 nm films. The argon flow was set at 50 sccm while oxygen flow was set at 5 sccm, with a chamber pressure of 5 mTorr. The substrate to target distance was 12.5 cm. The characterization methods used were identical to those used for zinc-stannate.

5.3 BGJ Fabrication

Devices were constructed on ITO-coated glass because the surface roughness of the ITO approximates the surface of a typical CdS-coated CIGS film. Film deposition conditions were chosen for $ZnSnO_3$ as 1 hr at 125 W with pure argon at 5 mTorr (0.67 Pa), no heat or RF bias applied to substrate, and target-substrate separation at 12.5 cm. Deposition conditions were chosen for Cu_2O as: 20 min at 71W, with 1.6 % oxygen at 3.3 mTorr (0.44 Pa), no heat or RF bias applied to the substrate. Devices were patterned in the substrate using a two-step photolithography process with rapid thermal annealing before the top metal contacts were deposited. This was done to avoid heating the stack with the top contact in place, which increases the likelihood of metal contact diffusion (*370*). A 110nm thick aluminum doped ZnO (AZO) layer was deposited first onto the ITO-coated glass substrate using atomic layer deposition (ALD). The AZO was used as the bottom layer to better approximate the window-layer (*371*) and to provide lateral conduction from the device stack to the common electrode (Figure 5.2). The $ZnSnO_3$ and Cu_2O layers were deposited sequentially and the stack was defined using photolithography and liftoff. After each photoresist developing step, samples were subjected to a 1 min oxygen plasma ashing to remove any remaining resist residue in the patterned region. In between each layer deposition, the samples were heated above 100 ^oC in a vacuum to remove hydroxides and water adsorbed onto the surface during air exposure. The samples were allowed to cool to below 45 ^oC *in situ* prior to deposition. After the Cu_2O was deposited, the samples were diced to produce multiple devices for each subsequent anneal.

Electrical measurements were conducted using the 3-terminal method (see figure 5.2a) where the voltage is applied to the top of the BGJ device stack (electrode 1), and

electrode 2 is held at ground. An additional voltage is measured from the 3rd electrode, also on the AZO in order to extract the lateral voltage drop through the AZO. In some cases two probes were placed on electrode 1 to make a 4-terminal measurement whereby potential drops from the probe on electrode 1 could be extracted. Device sizes ranged from 3×3 mm^2 to 5×5 mm^2. Due to sample realignment from the previous RTA steps, the mask for the top metal contact (electrode 1) was smaller than the junction oxide stack by 200 μm, with a total alignment tolerance of ±100 μm. Gold was used for the top metal contact because it provided a low resistance path to the BGJ and a reliable work function of 5 to 5.3 eV, making a low resistance contact to Cu_2O. To test for possible Au reaction with Cu_2O nickel top contacts were also used, but no difference was observed between measurements with Au and Ni contacts.

To measure the voltage drop from the gold to p-type material, a second gold electrode was created next to electrode 1 (figure 5.2b). The resistance through the device stack can be described by the diagram in figure 5.3. If the resistance of the bulk p and n type materials is much less than the resistance at their interface, then the current spreads between the electrodes and the potential gradient is consistent throughout the stack (figure 5.3a). If the bulk resistances are much greater resistance than the interface resistance then the potential gradient in figure 5.3b is observed, whereby the potential measured at electrode 4 will be erroneously lower. To account for this, a different type of device was patterned in figure 5.2c which uses an outer half-ring electrode to drive the current down to a lower ring electrode 2, while the potential is measured with two inner pin geometries for the top and bottom. This produces the equivalent circuit shown in figure 5.3c and allows both Au/p-layer and n-layer/AZO interface losses to be extracted.

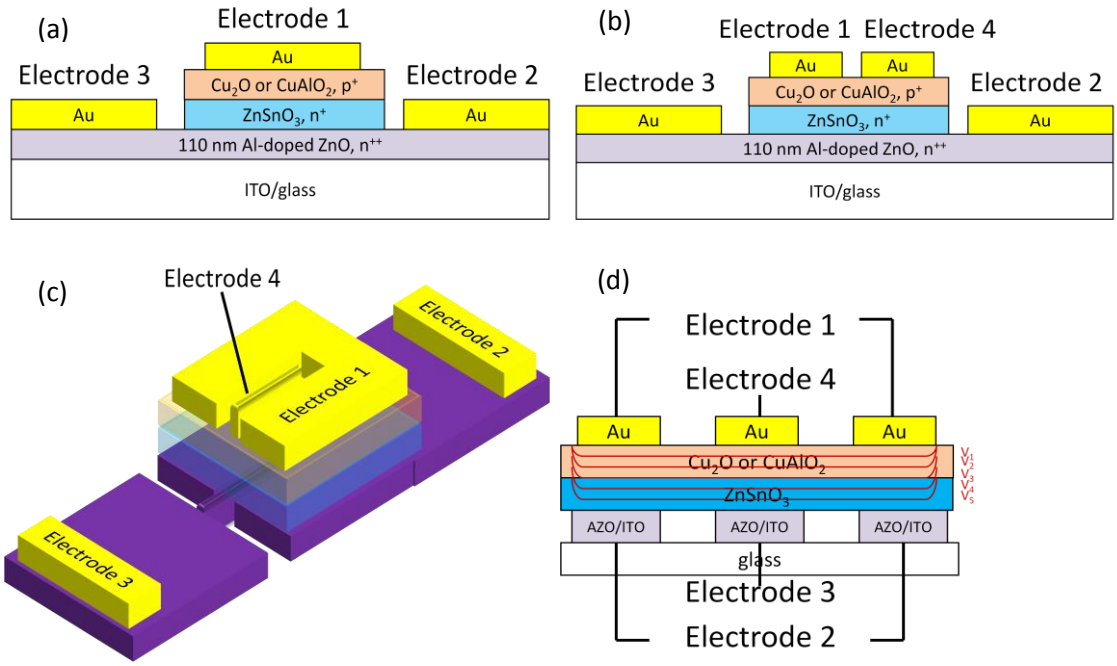

Figure 5.2. Measurement setup: Schematic of the devices used to measure the resistance of the tunnel junction stack. The potential between electrodes 1 and 2 are swept between -2 V and +2 V while the current flowing between electrodes 1 and 2 is measured. In setup (a) the potential between electrodes 1 and 3 is measured, while in setup (b) and (c) a second electrode was placed on the top of the stack and the potential between electrodes 4 and 3 are measured. Electrode 1 is cut away in this figure. Electrodes 1 and 4 are contacted using a thin gold wire spring or two metal whisker probes, while electrodes 2 and 3 are contacted using a tungsten tip probe. The outer half-ring and inner pin design of setup (c) produces a potential gradient, shown in (d).

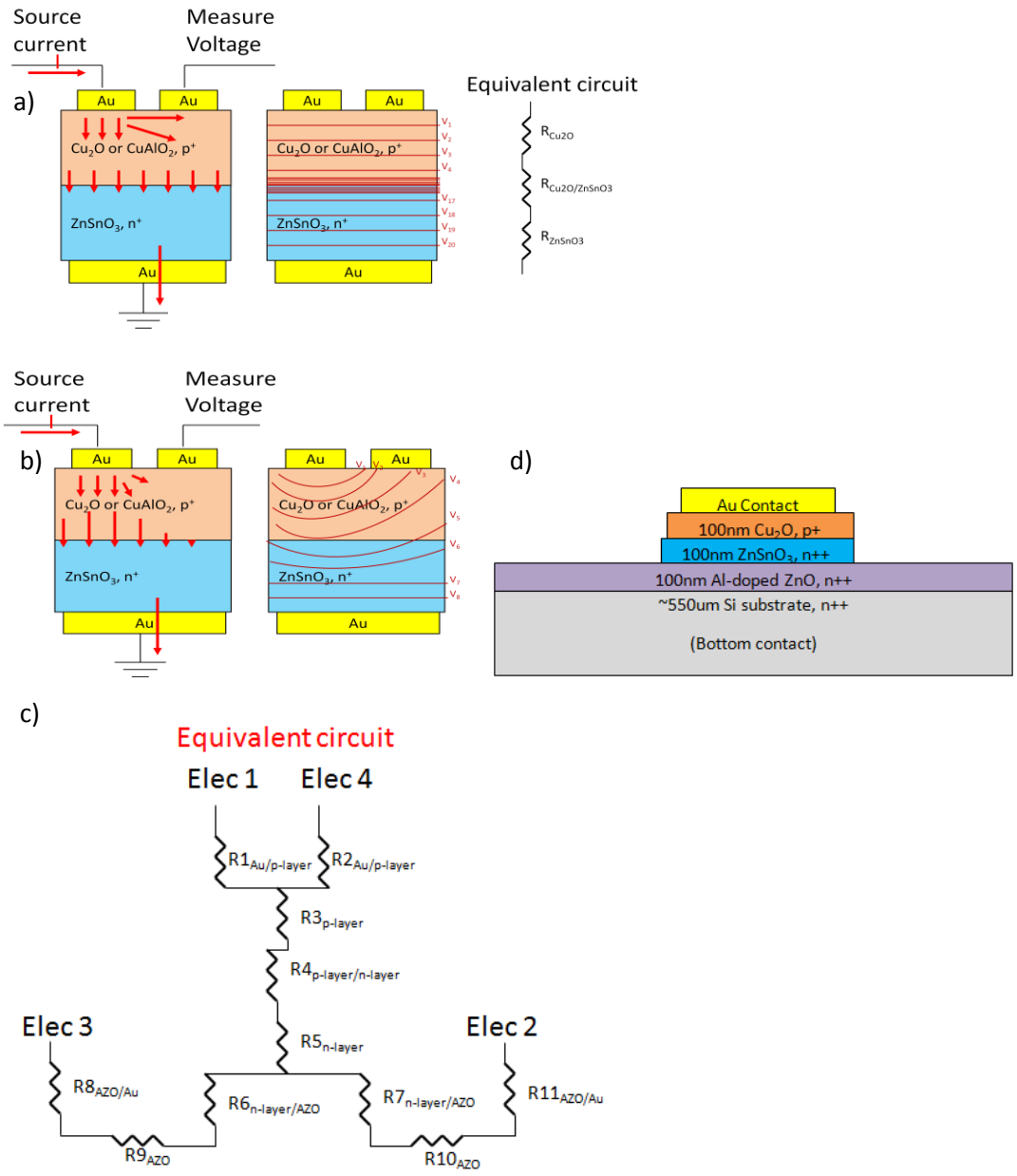

Figure 5.3: Models of device operation are shown. In (a) the p/n junction resistance is much greater than the bulk resistances of the p and n layers, causing a laterally uniform vertical potential gradient. In (b) the p/n junction resistance is much less than the bulk resistances of the p and n layers, producing a laterally non-uniform vertical potential gradient. The four terminal connection in (c) represents the equivalent circuit of the outer half-ring and inner pin design. In (d) is shown alternate 2-probe thru-wafer setup for some devices made on heavily doped silicon substrates.

For 4-probe measurements made using setup c, a Stanford Research Systems SR830 DSP Lockin amplifier was used. The internal function generator was used with a 1 V rms signal at 190 Hz. The signal output was applied to both the oscilloscope and the center of the BNC connection to electrode 1, while the shield was the ground and was connected to electrode 2. The input voltage measurement was set to differential mode. A time constant of 300msec was used, with the F and 2F line filters enabled along with a 24 db 'sync' filter. The reserve was set to low noise, with input AC-coupled and floating. The two input signals were connected sequentially to electrodes 1 and 2, 4 and 3, 1 and 3, and 4 and 2 for measuring each device. During each measurement the final differential voltage was taken after X/Y-error converged on a value.

Devices were also deposited in configurations to test the influence of substrate type. Devices were made in setup (a) using silicon instead of the ITO/glass, while additionally in some cases the AZO layer was replaced with $ZnSnO_3$. Devices were made on glass without the ITO layer. Another set of devices were made on heavily doped Si utilizing through-wafer two terminal I-V measurement (figure 5.3c). The voltage sweep during I-V measurements were typically limited to ±2 V (unless stated otherwise) to prevent damage to the metal oxides, which is known to occur primarily at the metal-oxide interface (*372*).

After each process step a piece of the sample was stored for future reference and characterization. For each film deposition, an additional witness substrate (soda lime glass and silicon) was included for characterization of the film properties. The spatial

variation of the composition in the BGJ films and vertical variation through the BGJ device was examined using depth profiling by Auger electron spectroscopy.

Chapter 6: Results

6.1 The n-type layer

Films were sputtered with a deposition rate of 1.33nm/min for films sputtered at 125W used for BGJ applications, which was in line with the rates seen for other metal

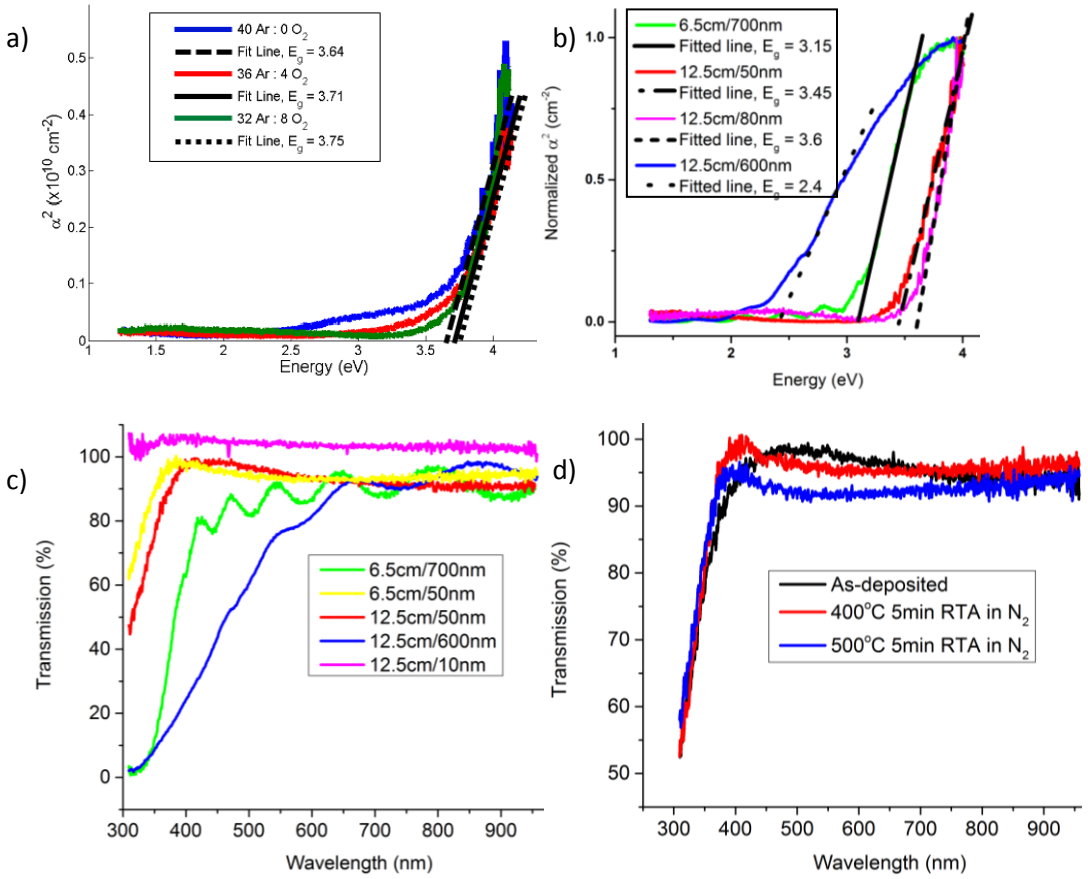

Figure 6.1: $ZnSnO_3$ results at 5 mTorr total pressure. (a) Tauc plots for films as a function of oxygen content for 150 W power, no intentional heating, and 1 hr deposition. The thickness varied from 152 nm at 0 % O_2 to 93 nm at 20 % O_2. (b) Tauc plot as a function of thickness and substrate-target distance for films sputtered at 125 W for 1 hr in pure Ar. 10 nm Films could not be fit. 6.5 cm / 50 nm and 12.5 cm / 80 nm data were nearly identical giving the same band gap. 12.5 cm / 80 nm Films annealed for 5 min up to 500 ^oC in N_2 were unchanged from the as-deposited samples. (c) Optical transmission for films made with different thicknesses and substrate-target distance. (d) 80 nm Films used for BGJ devices as a function of post-deposition temperature.

oxides of similar sputtering power. A band gap of 3.6 eV was measured for as-deposited zinc-stannate. As described below, on the band gap increases with increasing oxygen partial pressure in agreement with the literature (*181*). In most cases, the optical transmission of the films were over 90 % between 400 nm and 900nm. We also found that the film properties were sensitive to the target, even when bought from the same vendor. When sputtered under the same conditions, the band gap increased by 0.1 eV, the nominal optical transmission dropped from 95 % to 92 %, and the resistivity decreased by about 250 Ω-cm. Adjusting the process parameters allowed us to replicate the original results.

The direct band gap TAUC plots are shown in figure 6.1 for different deposition conditions and film properties. The sputtering rate decreased from 2.5nm/min to 1.55nm/min with increasing oxygen from 0 % to 20 %. Since it is unlikely that the transport efficiency from the target to the substrate would change this much, it is likely that even though we are sputtering from a stable metal oxide target there is a mechanism driving further oxidation of the target surface. The oxygen increases the direct gap slightly, as well as decreasing the band tail states, while minimally influencing overall transmission. This differs from previous reports by Ma (*13*), who saw a change in transmission from ~50 % to 90 % going from 0 % to 0.01 % oxygen partial pressure. Other films deposited at substrate temperatures up to 250 ^{o}C show direct gaps around 3.8 eV with no dependence on oxygen partial pressure and almost no change in thickness. This confirms a trend seen by Minami (*181*), in that it is easier for oxygen to be incorporated into metal films at higher substrate temperatures, possibly due to enhancement of the sticking coefficient (*373*). The large band gaps seen with all of our

films are substantially higher than the single crystal form of 3.35 eV (*180*), however a recent DFT study (*17*) indicates that a lowering of the mass density of an amorphous ZTO sample leads to an increase of the conduction band edge, which may explain why our amorphous films have a higher band gap than thicker crystalline films.

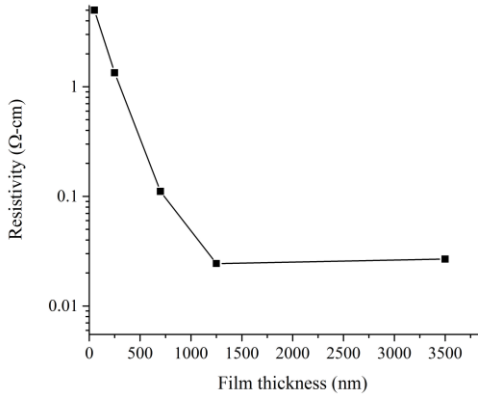

Figure 6.2: The resistivity of $ZnSnO_3$ films as a function of film thickness using substrate-to-target spacing of 6.5 cm and no surface passivation layer.

In figures 6.1b and 6.1c, film optical properties as a function of thickness and substrate-target separation are shown. Films sputtered at 12.5 cm and 6.5 cm substrate-target separation with thickness under 100 nm had similar band gap and transmission, however with increasing film thickness the band gap drops for both, but substantially more for the 12.5 cm-separation films. Zhu et al. (*374*) studied this effect in AZO with different target-substrate distances and found the opposite trend with increasing thickness. Films used for BGJ device fabrication were 80 nm and 10 nm with as-deposited band gaps of 3.6 eV.

The electrical resistivity was in the range of 10^{-2} to 10^{2} Ω–cm, depending on the film thickness (Figure 6.2), and substrate temperature and oxygen partial pressure (*177, 181*), as reported previously. RF biasing of the substrate during film deposition led to much higher resistivity.

Resistivity data vs. thickness for substrate-target distance of 6.5 cm is shown in figure 6.2. The two orders of magnitude change in resistivity with thickness cannot be explained

by mobility alone, despite AFM measurements which show that thicker films have much bigger grains. Hall measurements done on films with a resistivity of ~10^{-2} Ω–cm give carrier concentrations in the mid 10^{18} cm^{-3}. It is possible that rapidly decreasing resistivity with thicker films is minimizing the influence of surface depletion discussed further later. Similar large changes in resistivity with thickness have been observed in aluminum-doped zinc oxide (*374*) with the increase effect split approximately evenly between both mobility and carrier concentration. This was attributed to both improved crystallinity and increased crystallite size that weakens intercrystallite boundary scattering and increases the carrier lifetime. 80 nm and 10 nm films were made for BGJ applications using a 12.5 cm substrate-target separation. These had as-deposited resistivities of 1.2x10^3 Ω–cm and 1.05x10^3 Ω–cm, respectively. This dropped to ~6x10^2 Ω–cm after surface passivation.

In general, films sputtered at 12.5 cm displayed optical transmission and electrical conductivity near the best of the reports in the literature, while films sputtered at 6.5 cm were much lower quality, suggesting that ion impingement plays a role in degrading the films.

AFM measurements for 80 nm films used for BGJ applications were deposited on ITO/glass. The surface roughness of the 3.6 eV band gap films did not change significantly after post-deposition anneal (Figure 6.4a) in agreement with previous work by *Choi et al.* (*184*). Films were also grown on silicon with 3 nm thermal oxides and 6 nm thermal oxides to observe their roughness independent from the influence of ITO. The former are shown in shown in figure 6.3. Results show a surface roughness around

0.5 nm as-deposited. The RTA increased roughness by increasing a few large grains but most of the smaller grains stayed the same size. A similar trend was observed for the

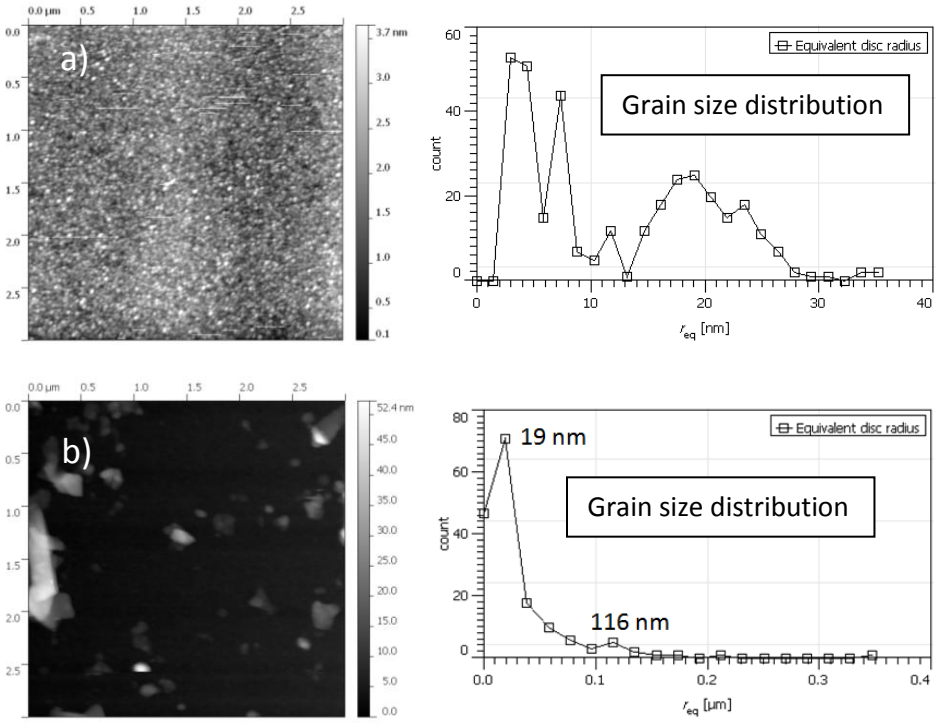

Figure 6.3: zinc-stannate films on (a) 3 nm SiO_2 before annealing, with an RMS roughness of 0.50 nm and excess area = 0.13 %. (b) 3 nm SiO_2 after RTA at 500 ^oC for 5 min in N_2. Some large grains grow with annealing, RMS roughness of 5.95 nm with excess area = 0.68 %.

films on 6 nm.

Selected 80 nm BGJ-application films deposited on ITO-coated glass substrates were examined using KPFM (see figure 6.4) using multiple platinum probe tips calibrated with pyrolytic graphite and gold films. The work function, measured using KPFM, were 4.6±0.25 eV for as-deposited films. The work function increased to 4.93±0.33 eV after post-deposition RTA in 1 atm of N_2 at 500 ^oC for 5 min. As can be seen in figure 6.4c,

the work function distribution broadens with increasing RTA temperature, suggesting annealing affects the film heterogeneously.

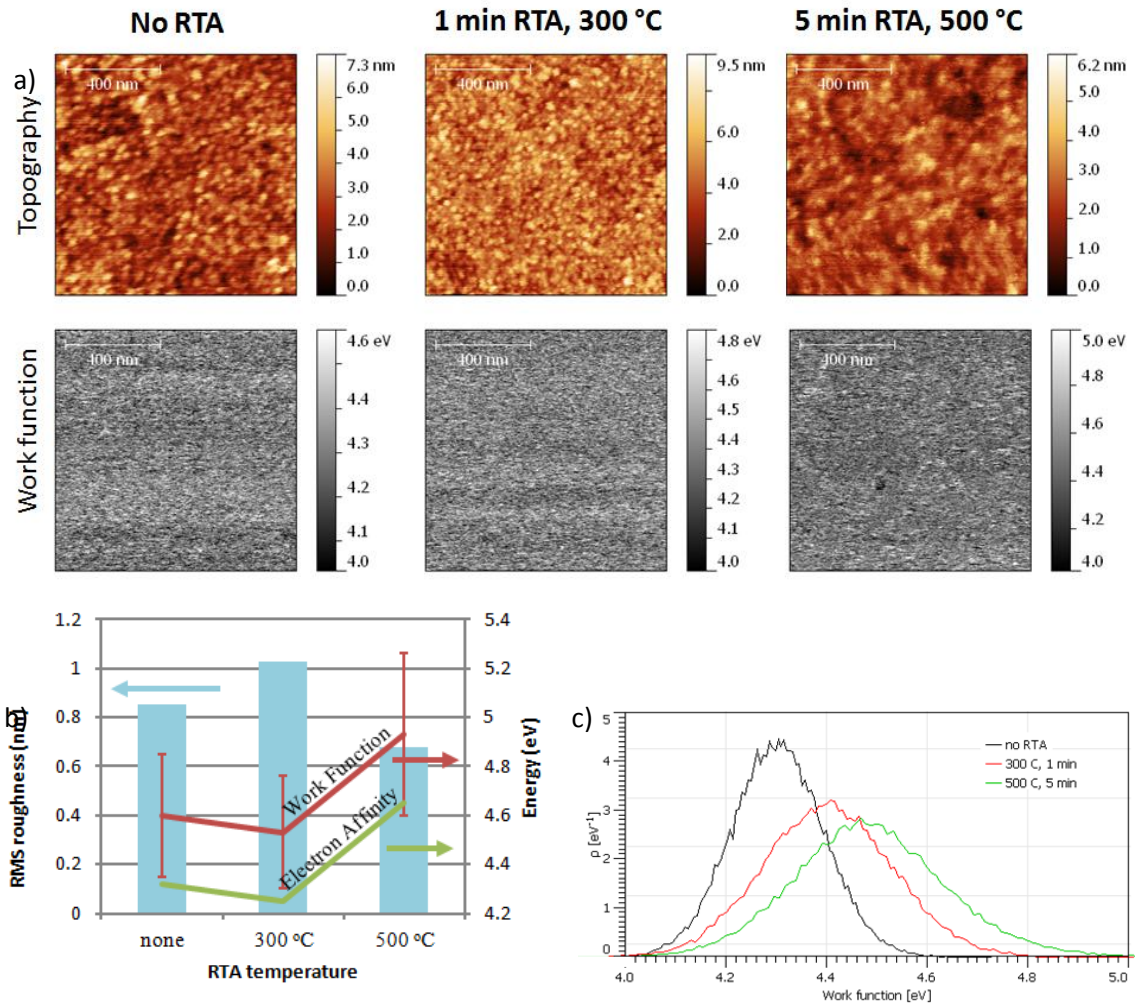

Figure 6.4: AFM and KFM images of 1x1 um region of zinc stannate films on ITO/glass substrates (a). Film roughness & band alignment: The RMS roughness, work function, and electron affinity for (b) different RTA conditions. Work function values are given as averages plus/minus the half-width at half-maximum of the distribution of values shown in similar (c) over the image (a), represented as error bars, which directly correlates to the electron affinity's minimum error (not shown). In (c) is not actually the same data represented by (a) and (b) but a similar measurement with an offset error.

UPS measurements were done by NREL on the 80 nm BGJ-application films. The samples were made by depositing ZTO onto a cleaned ITO/glass substrate and exposed for up to 30 min in air before sealing in an ampoule under vacuum down to 10^{-6} Torr. Prior to UPS analysis the ampoules were opened in a glove box. Samples were heated in a vacuum in an attempt to remove surface contamination without preferential sputtering or damaging the surface. The data is shown in figure 6.5. The results show Ef-Ev shifts from 3.56 eV to 3.42 eV respectively, however the latter XPS data show a substantial drop in the tin/zinc ratio to 0.56. Initially the valence band is around 7.46 eV, and increases to 7.64 eV at 210 ^{o}C sample temperature and most of the carbon is gone. At 348 ^{o}C the amount of zinc drops substantially and we don't believe the respective valence band measurement of 7.96 eV can be considered accurate. It is known that certain carbon-hydrogen-bonded zinc-oxides become volatile at temperatures over 250^{o}C (*375*). On our film's surface we have carbon contamination, thus resulting in our observed loss of zinc at 348 ^{o}C. Also these measurements assume the band gap is fixed at 3.6 eV for all temperatures, which may not be true for the higher temperature measurements. The increase of 0.5 eV with heating up to 348^{o}C almost exactly matches the increase seen by *Choi et al.* of 0.5 – 0.51 eV (*184*) with pre-UPS analysis heating over a similar temperature range. They didn't report the composition for the heated films. Our findings suggest that there is good reason to believe their 500 ^{o}C annealed data is not accurate for $ZnSnO_3$. Focusing on the data for films heated up to 210 ^{o}C we see that an electron affinity of 4.04 eV is predicted, which is ~1 eV or more below the expected value of 5 to 5.3 eV.

The UPS E_f-E_V data point to a heavy doping level in the films which we tried to confirm by C-V measurements using platinum contacts, however we were unable to attain a good capacitance transition point. This likely confirms the doping level of the ZTO films is high enough to cause a low resistance contact with platinum and makes the measurement difficult, although another possibility is that the work function of platinum was too close to that of the ZTO because the work function of platinum is known to vary by as much as 0.8 eV (*376*).

Temp.	C	O	Zn	Sn	ϕ	Ef-Ev	V_b	E_A
RT	11.7	52.4	18.3	17.5	3.90	3.56	7.46	3.86
100°C	10.5	50.5	20.1	19.0	4.05	3.47	7.52	3.92
210°C	6.0	50.1	21.4	22.5	4.15	3.49	7.64	4.04
348°C	1.8	55.5	13.5	29.2	4.55	3.41	7.96	4.36

Table 5: XPS composition data and UPS energy level data for a single film on ITO heated in vacuum at sequentially higher temperatures prior to analysis.

UPS measurements were repeated using similar films by ThermoFisher Scientific on as-deposited films and results show an E_f-E_v of 3.32 eV and valence band of about 8.4 eV and an electron affinity of 4.8 eV. This is much closer to the expected 5 to 5.3 eV for zinc stannate and the doping level is more in line with that projected by the Hall measurements described next.

Hall measurements done on 80 nm films proved inconclusive due to high resistance (see figure 6.6a). Qualitatively, the results gave unrealistically low carrier concentration and high mobility. The trends after anneal were the opposite of those anticipated, all of which contradicted data from XRD and AFM measurements. It is known that surface states can deplete lightly doped thin films, greatly reducing the amount of free carriers available (*377*). We therefore deposited a ~100 nm layer of SiO_2 by PECVD at 100 ^oC on top of the zinc-stannate to provide surface passivation. The resultant structures were far more conductive than the corresponding unpassivated films (3.28 Ω-cm vs. 372 Ω-cm for films with post-deposition 300 ^oC RTA). Surface passivated films annealed at 500 ^oC for 5 min showed a decrease in resistivity from 3.28 Ω-cm to 0.58 Ω-cm. Hall measurements after surface passivation (figure 6.6b) showed a mobility of ~1 cm^2 / Vs and a carrier concentration of about 10^{18} cm^{-3} for films with a 300 ^oC RTA. Films annealed at 500 ^oC for 5 min had a Hall mobility of ~10 cm^2 / Vs and similar carrier concentration in contrast with similar films by Choi (*184*) where carrier concentration increased one to two orders

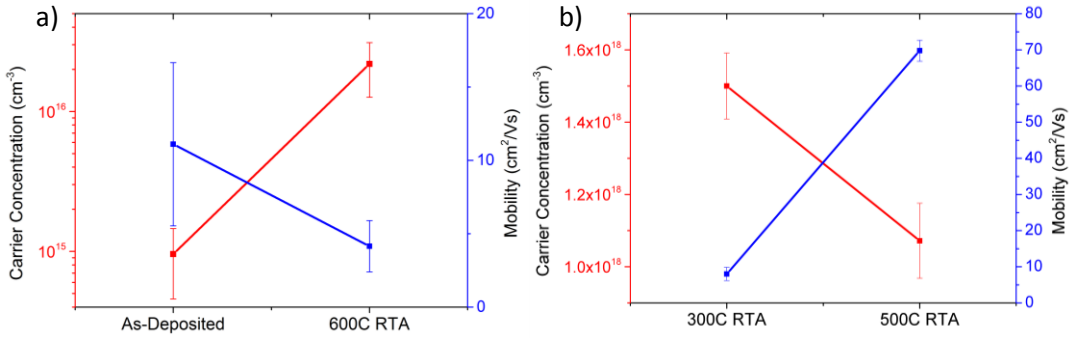

Figure 6.6: The carrier concentration and mobility of $ZnSnO_3$ films before (a) and after (b) surface passivation. In (a) the applied current was 0.1 uA and 1 uA for the as-deposited and annealed samples, respectively. The field was swept +/- 2 Tesla. In (b) the applied current and field were 5 μA and +/- 6 Tesla for the 300 C RTA samples and 10 μA and +/- 2 Tesla for the 500 ^oC RTA samples. The error bars correspond to one standard deviation in several measurements on the same sample.

of magnitude at 500 ^{o}C 10 min RTA in a vacuum, while mobility increased by less than a factor of two. These measurements used a fixed voltage while varying the field. The Hall voltage was not perfectly linear with field. As a result the measured values should be

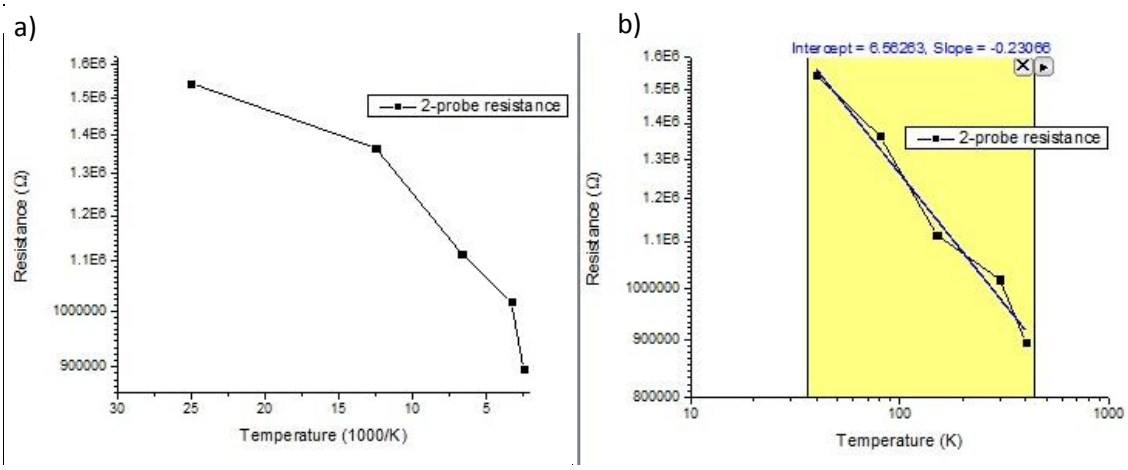

Figure 6.7: The 2-probe resistance vs. temperature of zinc stannate samples plotted in semi-log (a), and log-log (b) with a linear curve fit, showing variable range hopping. The sample had two titanium electrodes. Measurements were done using tungsten probes. The sample was attached to a glass slide using double sided tape. The slide rested on a thermoelectrically cooled copper plate. The system was pumped down to below 0.1 mTorr and the sample was cooled to 40 K overnight and measured. The sample was heated for subsequent measurements. All samples were allowed to sit at the target temperature for at least 1 hr prior to measurement.

considered an approximation (*378*).

Temperature dependent conductivity measurements (see figure 6.7) were performed between 30 K and 400 K to determine the carrier transport method. The data showed $T^{-1/4}$ dependence consistent with variable range hopping (VRH). Hopping is known to be the primary conduction mechanism in nonstoichiometric amorphous oxides and a source of nonlinearities in Hall measurements (*379, 380*). Despite this we needed this data in order to compute band structure in conjunction with KPFM data.

The electron affinity was computed using the KPFM work function data plus density of states (DOS) simulation data from Körner and Elsässer (*176*). The latter used the self-interaction correction-based LDA on the basis of density functional theory using the computational mixed-basis pseudopotential method. A 60 atom super cell of crystalline $ZnSnO_3$ was used, giving an integrated total of 36 states in the conduction band (above 3.03 eV). Using the hexagonal Bravis lattice (space group R3c) with a unit cell volume of 342 $Å^3$ and formula units per cell of 6 (*3*), we calculated the total number of conduction band states at 3.6 per unit cell. This results in a DOS (N_c) total of 6.32×10^{22} cm^{-3} conduction band states. Using the equations below

$$\left(E_f - E_c\right) = ln(n/N_c)kT \tag{6.1}$$

$$E_{vac} - E_c = W - \left(E_c - E_f\right) \tag{6.2}$$

with the non-degenerate doping level n of 1×10^{18} cm^{-3} gives a conduction band edge (E_c) 0.28 eV above the Fermi level (E_f) at room temperature (kT = 0.0256 eV). Using the KPFM measurements as W (Figure 6.4a) puts the final average electron affinity ($E_{vac} - E_c$) varying from 4.32 eV for the as-deposited films, to 4.65 eV for the post-deposition rapid thermal annealed films at 500 ^oC for 5 min. This compares to the experimental affinity of around 5.3 eV as measured by ultraviolet photoelectron spectroscopy (*381*). This discrepancy could be due to inaccuracies in the extraction method used or differences in the electronic structure of zinc-stannate films used in the experiments.

Auger depth profiles for $ZnSnO_3$ are shown in figure 6.8. The films shows oxygen deficiency below the stoichiometric 60 %, with most measurements giving between 50

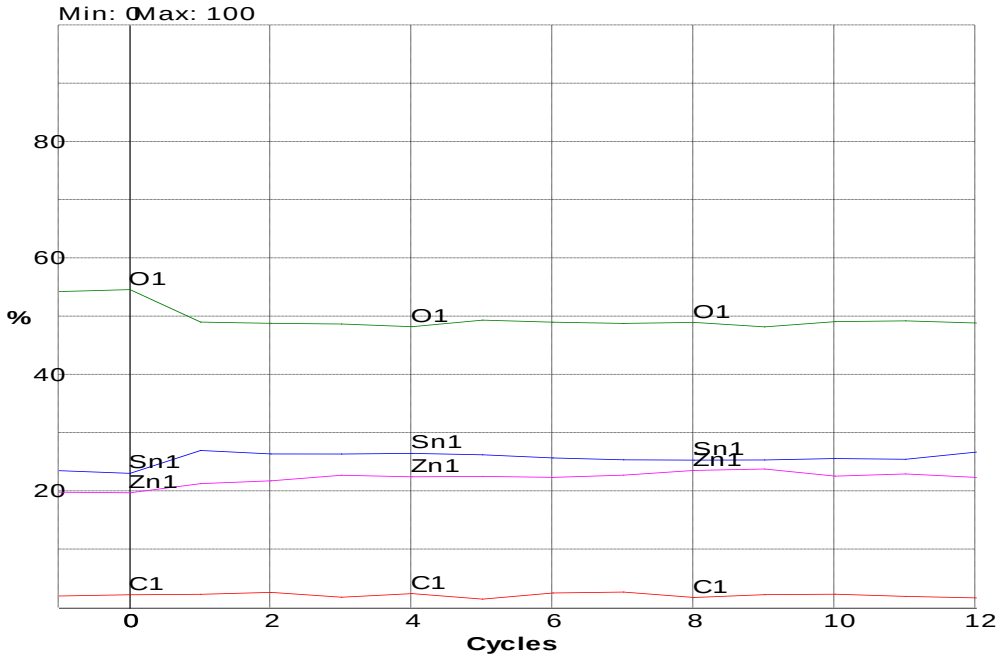

Figure 6.8: Auger depth profile with a depth resolution of approximately 10 nm/cycle. The noise contribution is around 3 %.

and 55 % after sputtering the surface. Sputter-cleaning samples, however, is known to preferentially remove oxygen over other elements (*382*). Waiting for 5 min after sputter cleaning results in higher levels of oxygen, typically gaining 3 %, however this cannot be relied on as an accurate measurement of oxygen because excess oxygen is typically absorbed from the chamber over time even in ultra high vacuum conditions. The samples also typically show 20 to 53 % zinc deficiency relative to tin prior to sputtering, which is supported by NREL's XPS measurements. Once steady state profiling is reached, there is consistently a 10 to 20 % excess of tin relative to zinc, which could be due to preferential sputtering.

In figure 6.9 the XPS results of zinc-stannate film's O1s binding energies are examined and compared to individual zinc oxide and tin oxide films sputtered from ZnO

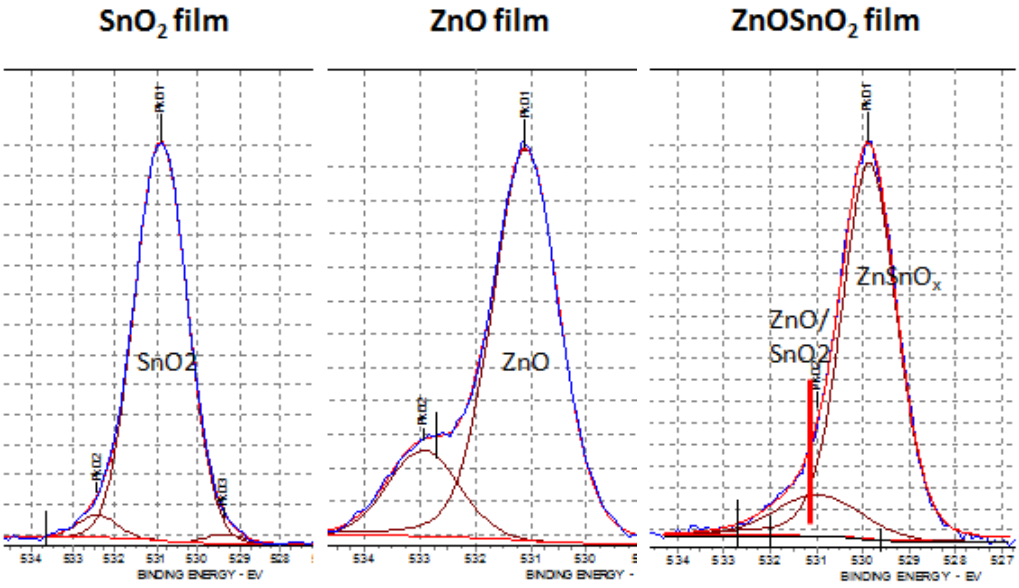

Figure 6.9: XPS data for SnO_2, ZnO, and $ZnSnO_3$ films after a 1 min sputter cleaning of the surface at about 2 nm/min, with Chi-squared fit error less than 2.

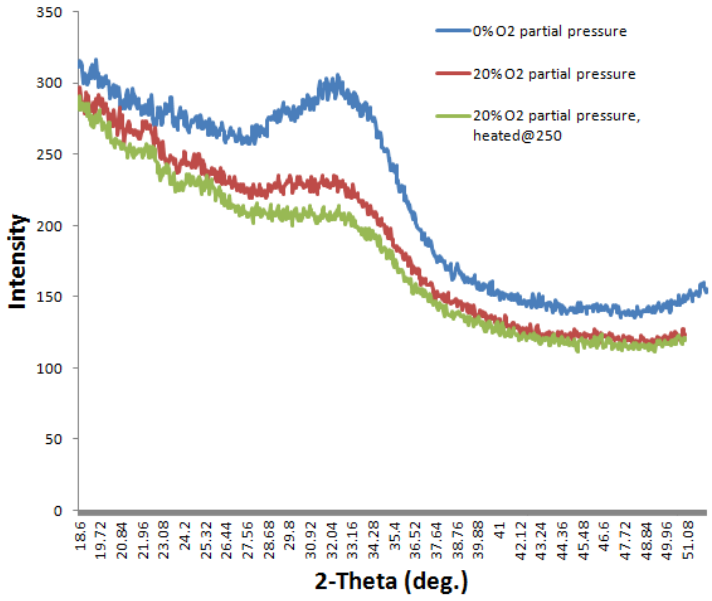

Figure 6.10: The XRD spectra of zinc stannate films deposited on silicon as a function of oxygen partial pressure.

and SnO_2 targets. The results show we have mostly $ZnSnO_3$, with a minor amount of individual oxides. These results were confirmed by XPS measurements done by NREL on similar films.

XRD measurements for as-deposited films on silicon matched that of literature, revealing amorphous material with a hump around 33^o 2-theta (figure 6.10), representative of the dominant peak value for zinc-tin-oxide compounds. This was true for all sputter conditions with a substrate-target distance of 12.5 cm. In an attempt to get crystalline films to check the phase, films were annealed on silicon substrates at 700 ^{o}C in nitrogen for 4 hours. The results, shown in figure 6.11, produced crystalline material with peaks matching that of Zn_2SnO_4, confirming Kovacheva's work (5) showing zinc stannate is not stable in the $ZnSnO_3$ phase above 600-700 ^{o}C.

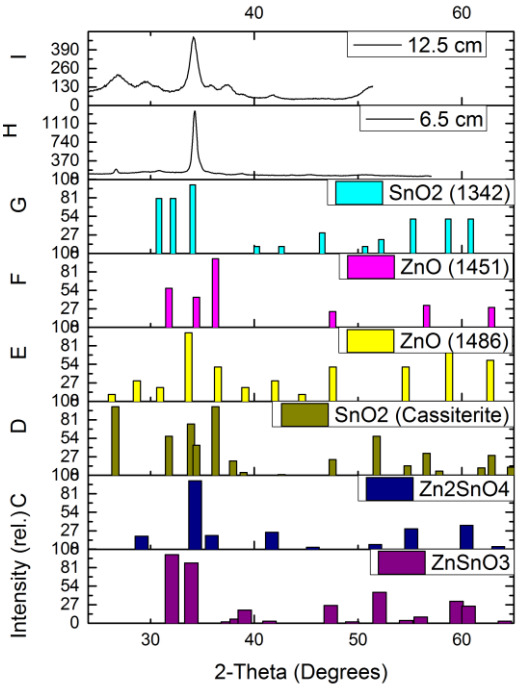

Figure 6.11: Comparison of XRD for zinc-stannate deposited at a substrate-to-target distance of 12.5 cm and 6.5 cm followed by a N_2 post-anneal done at 700 ^{o}C for 4 hrs.

6.2 The p-type layer Cu_2O –metal-sputtered

The electrical and optical properties of copper oxide are known to depend strongly on the deposition and annealing temperatures (*16, 216, 238, 247*). By maintaining the sputtering parameters within a narrow (~2 %) range around 71 W (1.56 W/cm^2) and 5.4x10^{-5} Torr (7.2 mPa) O_2 partial pressure we achieved films with 2.5 eV band gap, a peak optical transmission of 75 %, and an as-deposited (and surface passivated) resistivity of 351 Ω–cm which were used for BGJ device fabrication. These films had a deposition rate of 3nm/min, which is very low relative to those who reported rates for metal-sputtered films, however most of them use much closer substrate-target spacing. A minimum resistivity of 30 Ω–cm was achieved after post-deposition anneal in N_2 at 500 ^{o}C for 5 min.

Hall measurements were attempted on 50 to 70 nm thick Cu_2O films but the sheet resistance was too high to get reproducible results. After surface passivation using the same process as $ZnSnO_3$, the Hall effect showed that the as-deposited films had a mobility of ~0.5 cm^2/Vs and carrier

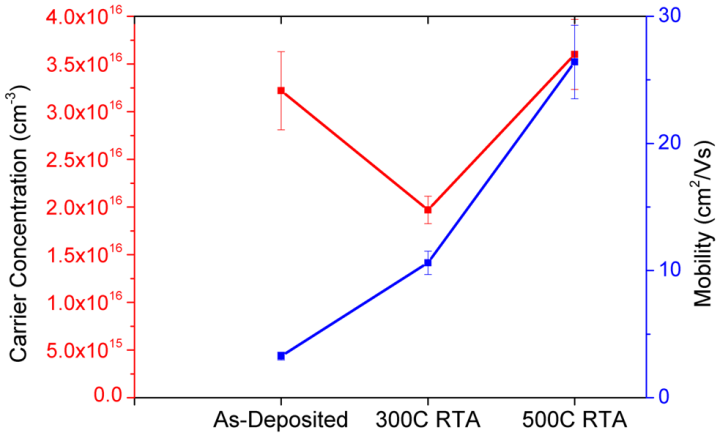

Figure 6.12: The carrier concentration and mobility of metal-sputtered Cu_2O films after surface passivation. The applied current was fixed at 0.1 uA for the as-deposited film, 0.7 uA for the 300^{o}C samples and at 1 uA for the 500 ^{o}C samples. In all cases the magnetic field was swept up/down +/-6 Tesla. The error bars correspond to the standard deviation in measurements on the same sample.

concentrations of 10^{16} cm^{-3} (figure 6.12). Five minute RTA at 500 ^{o}C increased the mobility to ~26 cm^2/Vs while leaving the carrier concentration unchanged. These mobilities are in line with those observed by Reddy (*241*) although they applied heat during deposition instead of post-deposition. From as-deposited to 300 ^{o}C RTA the carrier concentration drops by about a factor of two. This also matches Reddy's results, however at 500 ^{o}C RTA we see a rebound that has not been observed at higher temperatures by others (*216, 242, 252*).

Higher substrate deposition temperatures promoted grain growth, in agreement with previous work (*216, 242*). However deposition at a substrate temperature of 200 ^{o}C resulted in the formation of films with bandgaps below 2.5 eV. This may be due to the tight tolerance of sputter parameters necessary to produce films with the desired properties combined with an effective increase in oxygen flux vs. copper for higher substrate temperature due to increasing gas-phase collisions. For the tandem cell application we were focusing on higher band gaps therefore we concentrated on room-temperature deposition. Under these conditions grain sizes increased an average of 45 nm from as-deposited to 500 ^{o}C annealed films as identified by AFM (figure 5a – d), although roughness data (figure 6b) reveals most of the change is coming at temperatures above 300 ^{o}C, in agreement with previous findings (*252*).

As-deposited films on glass contained ~70 nm copper-rich inclusions observable in AFM (figure 5). The composition was confirmed using SEM-EDS scans of particles (figure 6.13) on silicon substrates using samples that had undergone elevated an RTA, in agreement with the literature (*228*). These could potentially penetrate the Cu_2O film. After the films were annealed at 300 ^oC for 5 min in N_2 the copper features aggregate (figure 5b, 5e). Between 300 ^oC and 500 ^oC, these structures cease growing, indicating they are kinetically limited with the surroundings. As explained in Section 3.3b these inclusions form natural Schottky diodes within the

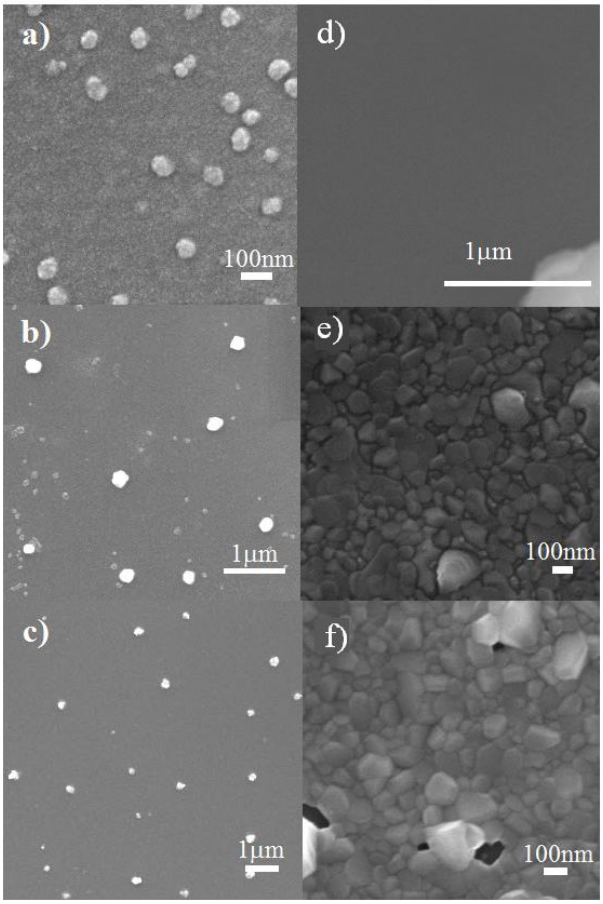

Figure 6.13: SEM images of Cu_2O films as-deposited on glass (**a**), after a 300^oC RTA for 5min in N_2 (**b**), after a 500^oC RTA for 5min in N_2 (**c**), and as-deposited on silicon substrates (**d**), after a 300^oC RTA for 5min in N_2 (**e**), after a 500^oC RTA for 5min in N_2 (**f**). The films in (**d**) have a foreign particle in the bottom right, and films in (**f**) appear to have cracks forming alongside the larger inclusions.

material, depleting carriers within the film and raising the resistivity, however their formation assists in creating copper vacancies which help dope the material p-type. The aggregation of these features should reduce their overall depletion region volume in the material due to a reduction of total precipitate surface area-to-volume ratio, however our measurements suggest a decrease in carrier concentration at 300 ^{o}C when most of the aggregation seems to occur. It may be that the separate phases are forming at higher anneal temperatures, as found by Yang in XRD data giving small amounts of copper and CuO peaks (*237*). Similar Cu_2O films were also subjected to 5min RTA in oxygen at 300^{o}C and 500^{o}C, and AFM results show a reduction and maybe elimination of copper inclusions after 300^{o}C, but conversion to CuO at 500^{o}C. This suggests an anneal with a mixed ratio of nitrogen and oxygen could result in a reduction of inclusions while maintaining the right film composition, as found by Pierson (*238*), who demonstrates that annealing in air up to 300 ^{o}C for 4hrs maintains stable Cu_2O.

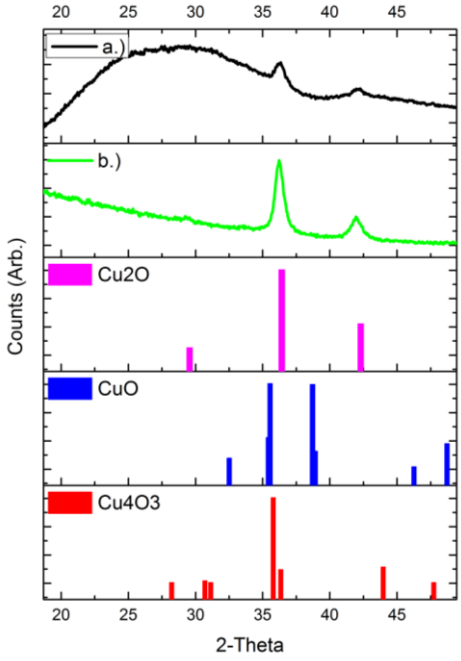

Figure 6.14: A comparison of XRD-spectra for metal-sputtered 50nm Cu_2O films deposited on **a**) glass (density 6.06 g/cm^3), **b**) silicon (density 5.92 g/cm^3). The referenced density for Cu_2O is 6.1078 g/cm^3 (*2*). The grain size for (111) and (200) orientations are (a) 12nm and 12.3nm and (b) 14.8nm and 9.5nm respectively.

Films deposited on glass substrates preferred grain orientations in the (111) and (200) directions identified by XRD whereas films deposited on silicon are predominantly orientated in the (111) direction and exhibit more crystallinity (see figure

6.14a and 6.14b). The relative mix of orientations may be related to the substrate lattice matching on silicon, while the smaller peaks on glass may be due to the influence of film heating on glass versus silicon. Substrate heating has been found to lead to a weaker texture and increase of polycrystalline domains in Cu_2O (*16*). No detection of copper or other copper oxide phases were observed.

Auger depth profiles (see figure 6.15) on silicon revealed a consistently lower ratio of

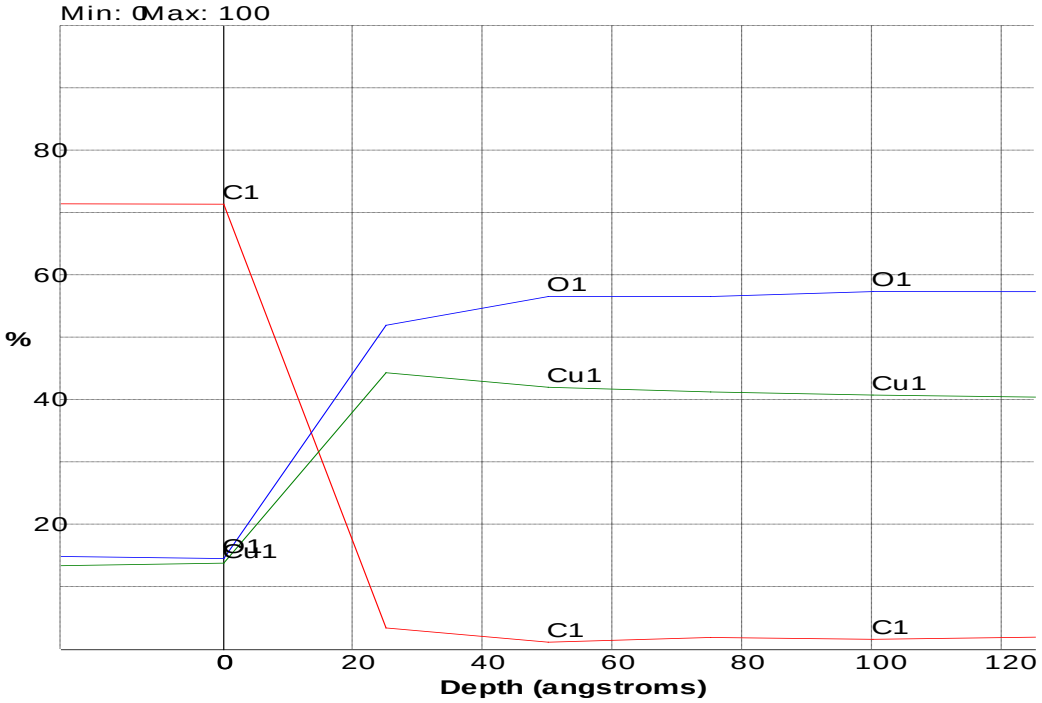

Figure 6.15: The auger depth profile for ~50nm films (c) with a sputtering rate of ~3nm/cycle.

copper to oxygen as would be expected for Cu_2O films, and more closely matches Cu_4O_3, however since the XRD measurements support Cu_2O, the excess oxygen may represent interstitial oxygen, peroxide inclusions, or most likely oxygen in a lattice with some copper vacancies, which provide the dominant form of p-type doping in these materials. It could also be from preferential sputtering.

Cu_2O films deposited on ITO-coated glass substrates were examined using KPFM and the data was analyzed in a similar manner as the $ZnSnO_3$ (see figure 6.16f). As-

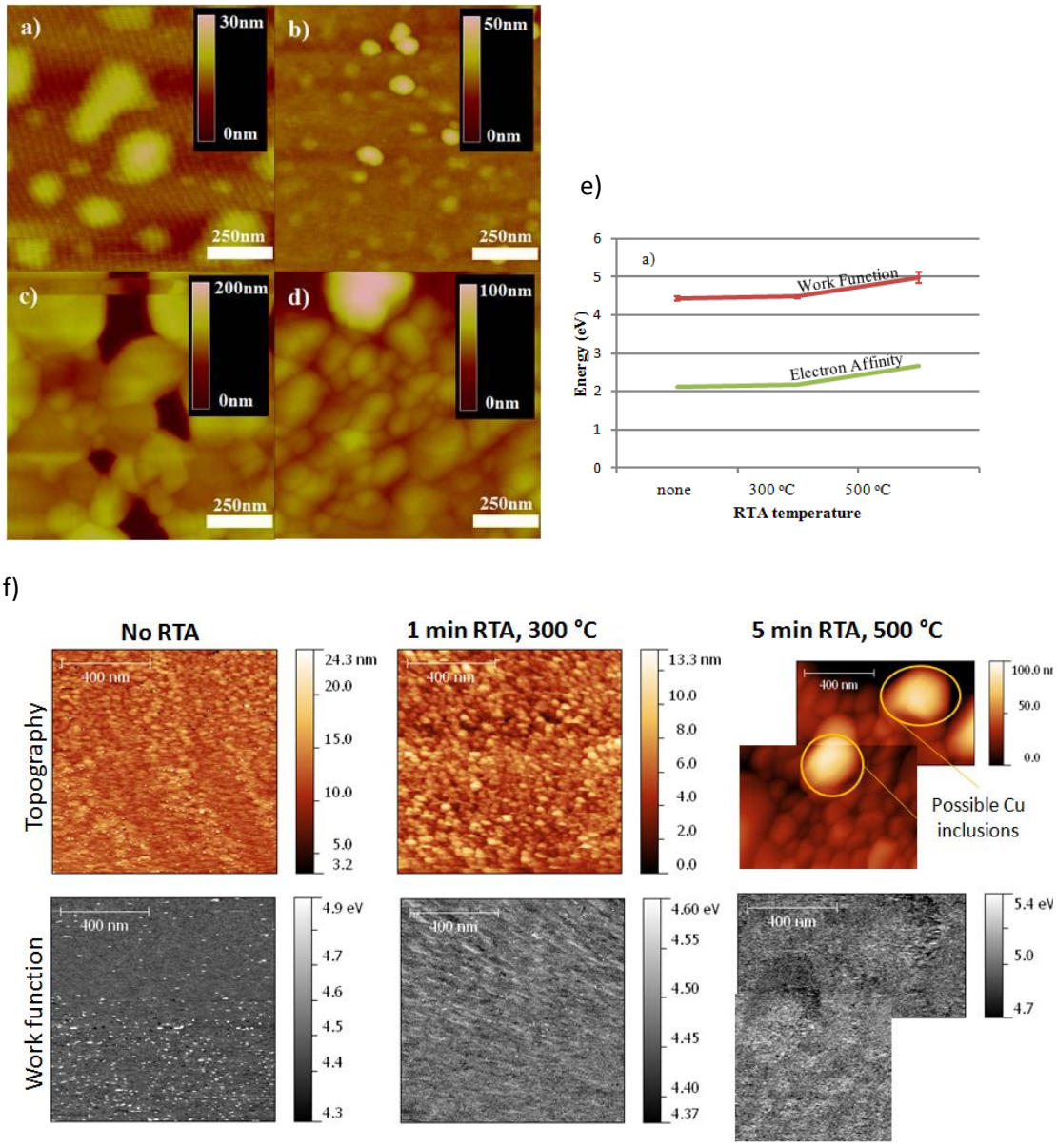

Figure 6.16: AFM and KFM measurements over a 1x1um region of Cu_2O films deposited on silicon (**a** & **c**) and glass (**b** & **d**) substrates. Image (**a**) and (**b**) are as-deposited and (**c**) and (**d**) are after 500^{O}C RTA for 5min in N_2. Note that the vertical lines in image (**a**) are instrument artifacts. In (e) is the work function and electron affinity for Cu_2O films for different RTA conditions on ITO/glass substrates shown in (f). Work function values are given as averages plus/minus the half-width at half-maximum of the distribution of values over the image (figure 6.17a), represented as error bars, which directly correlates to the electron affinity's minimum error (not shown).

deposited films have a relatively low work function, ~4.44±0.05 eV, in reasonable agreement with the reported value of 4.84 eV (*383*). This increases to 4.98±0.14 eV after post-deposition rapid thermal annealing at 500 ^{o}C for 5 min in 1 atm of N_2 (figure 6.16e). The overall work function distribution (figure 6.17a) is substantially less than that observed in $ZnSnO_3$ measurements. The copper inclusions exhibit higher work functions from the rest of the film by an average of +0.35 eV once 1 min anneals at 500 ^{o}C are performed (figure 6.17c), however they do not show a marked difference from the rest of the material after 5min anneals due to the rest of the material gaining in potential. Literature suggests that variations in carrier concentration can shift the work function from 4.3 to 4.7 eV (*384*). Reduction (under N_2 only) could increase O vacancies and shift the work function to a lower value (*286*) while decreasing conductivity unless it was over compensated for by grain growth and precipitate formation. However, our Hall measurements revealed carrier concentration shifting by only 9 %, which is not enough to account for the .5eV shift.

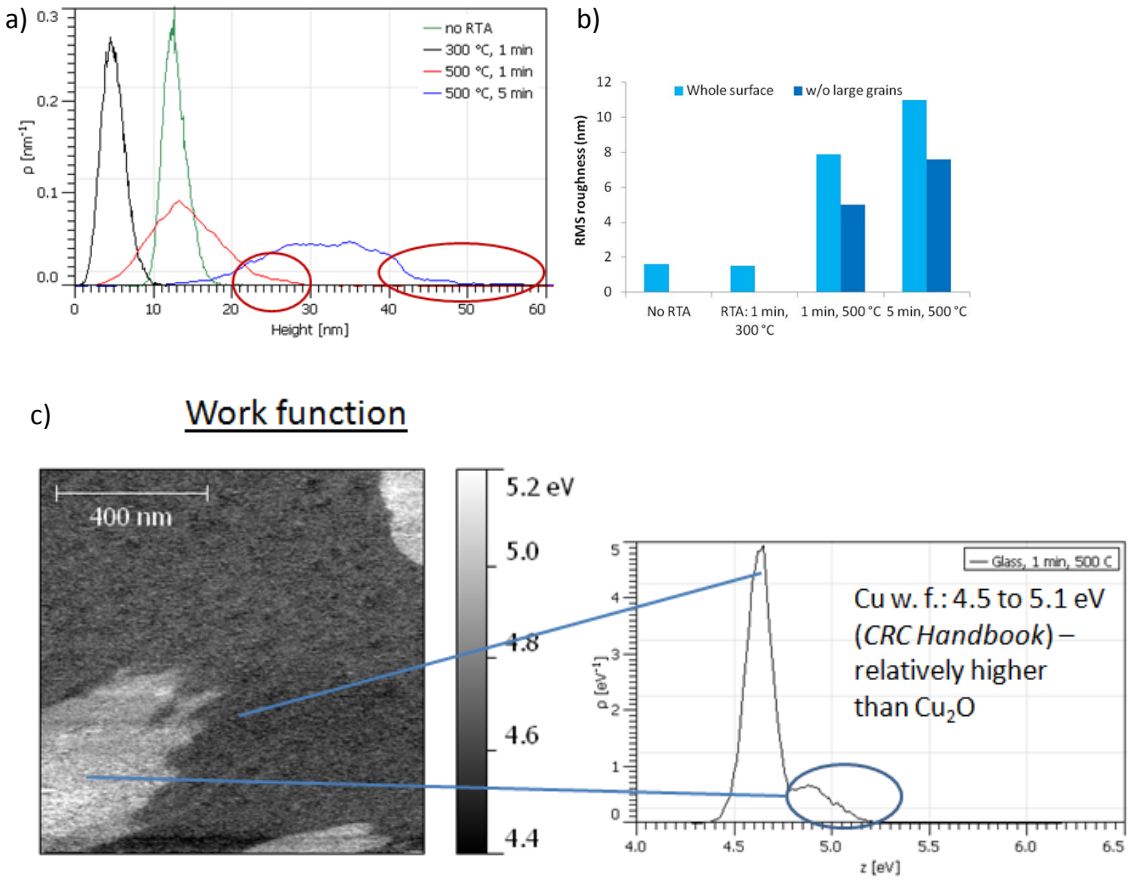

Figure 6.17: Work function distributions over the mapped imaged from figure 6.16f. (a), Cu_2O height distributions become bimodal with longer, hotter anneals – Cu inclusions). The RMS roughness (b) for the scanned regions in figure 6.16f. In (c) is the work function of image after 1min at 500°C in N_2 showing likely copper inclusions with a higher work function compared to the surrounding material.

Note that the calculation of the Cu_2O RMS roughness takes into account the copper inclusions, whose feature size differs substantially from the rest of the film.

To calculate the conduction and valence band position for Cu_2O we used effective mass data calculated by Nie *et al.* (*270*). The data was provided by the authors who carried out first-principles study of transparent p-type conductive materials such as $SrCu_2O_2$ and related compounds by LDA as implemented by the general potential

linearized augmented plane wave method on the basis of density functional theory. We used:

$$N_{lh,hh} = 2\left(\frac{^{*}m_{lh,hh}\, kT}{2\pi\hbar^2}\right)^{3/2} \tag{6.3}$$

$$E_v - E_f = \ln\left(\frac{p}{(N_{lh} + N_{hh})}\right) kT \tag{6.4}$$

$$(E_{vac} - E_v) = W + (E_f - E_v) \tag{6.5}$$

The effective masses provided were 0.36 and 1.49 for the light ($^{*}m_{lh}$) and heavy holes ($^{*}m_{hh}$), respectively, giving the total DOS N_{lh} and N_{hh}. Using the measured carrier concentration p of $3\text{x}10^{16}$ cm^{-3}, these equations give a valence band edge (E_v) positioned 0.19 eV below the Fermi level (E_f) at room temperature (kT = 0.0256 eV). Using the KPFM data for W (figure 6.16e) we get the valence band position calculated to be at 4.63 eV for the as-deposited film, increasing to 5.17 eV after RTA for 5 min at 500 ^{o}C. Using the optically measured 2.5 eV band gap this gives an electron affinity (E_v - 2.5) of 2.13 eV for as-deposited films increasing to 2.67 eV for 500 ^{o}C annealed films. The as-deposited material shows an affinity less than both the theoretical value of ~3.1 eV (*16*), and the measurements by XPS (3.2 to 3.3 eV)(*82*) (2.9 eV for thin films (*385*)). However,

the wider band gap of the material places the valence band edge near the expected ~5 eV after RTA at 500 ^{o}C.

The optical properties of the films were studied as a function of post-deposition anneal temperature and thickness (figure 6.18). For films around 50nm thick, a band gap

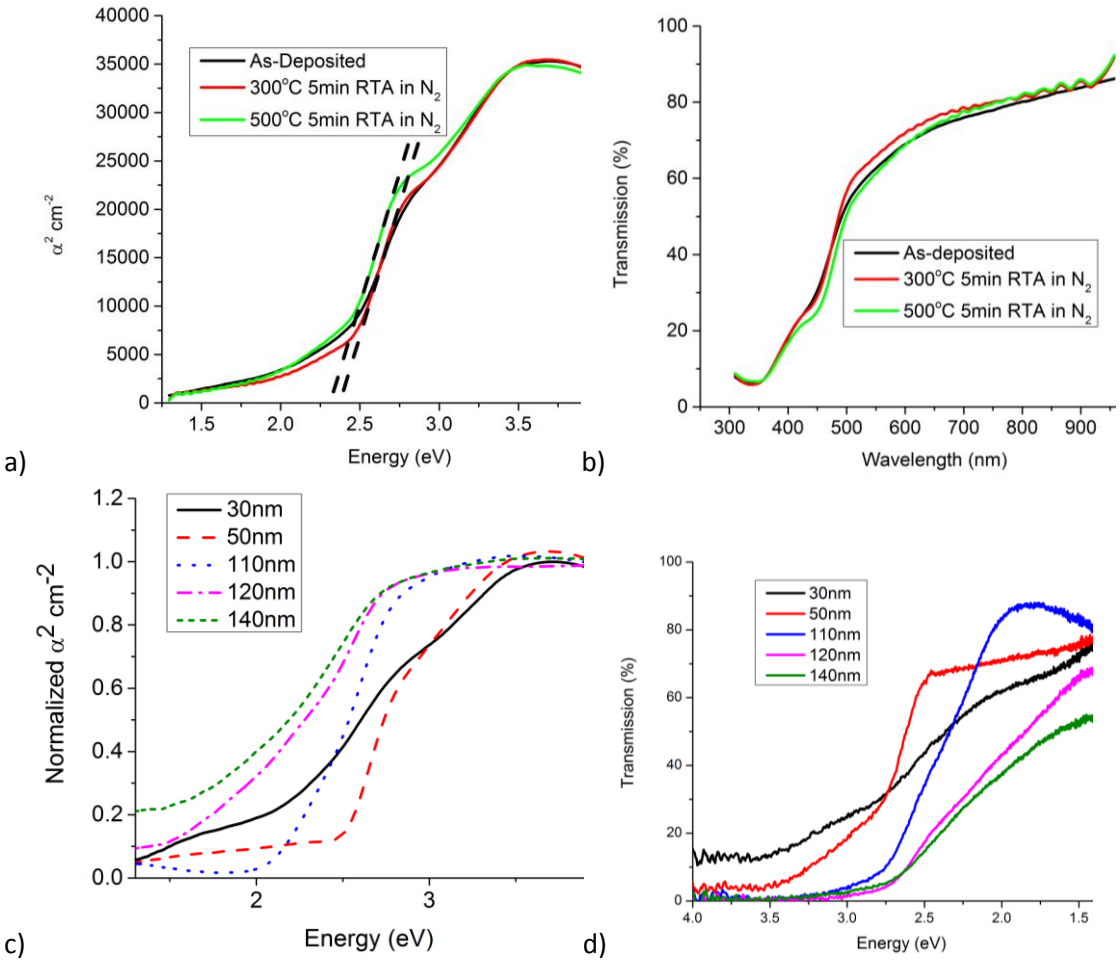

Figure 6.18: The direct band gap and optical transmission is shown in (a) and (b) for ~50nm films with different post-deposition anneal conditions, and depending upon film thickness in (c) and (d). (a), (b), and (c) were smoothed with 147-point savitzky-golay filters and 57-point for (d).

of 2.4 to 2.5 eV was obtained for as-deposited films up to 300^{o}C RTA in N_2 for 5min, but decreased to 2.3 eV after 500^{o}C RTA in N_2 for 5min. Transmission between 600nm and

1000nm was over 70 % as-deposited, increasing marginally with anneal. This is better than reported results for films with similar wide band gaps (*16, 238, 249*). A dependence of the band gap was also observed depending upon film thickness (see figure 6.18c). This was studied (*289*) and correlated to stress (*290*) recently, but only for sub-11nm films using a psuedomorphic growth method verses thin film deposition we use here.

In an attempt to better understand the band gap dependence on thickness, stress measurements were performed for Cu_2O films at thicknesses of 30, 50, 100, and 125 nm. Films were deposited under previously described conditions onto glass substrates (see figure 6.20), and on (100) silicon wafers (see figure 6.19). The back side of the glass was coated with 75nm of aluminum deposited by sputtering to facilitate stress measurements by determining changes in the wafer curvature. The temperature was ramped at 1 ^oC/min in a vacuum with a base pressure of $5x10^{-5}$ torr and with nitrogen at $1x10^{-4}$ torr. The ramp was done from room temperature to 500^oC. The sample was cooled back to room temperature, ramping at the same rate. Preliminary analysis of the results on silicon show stress relaxation mechanisms beginning around 150-170 ^oC that taper off sharply by about 300^oC (identified by shaded blue regions in the figure). This region is likely where the majority of Cu_2O grain growth and copper migration are occurring. Films have built in compressive stress at 30nm and 50nm. Films transition to built-in tensile stress at 100nm, however for all thicknesses films gain tensile stress with thermal cycling. It is likely that stress-relaxation occurs in the higher temperature portion of the cycle above the shaded blue regions. The unreasonably high built-in compressive stress for the 30nm films and downward trend with increasing temperature is unexpected and may represent some kind of instrument or setup error in the data. For all other thicknesses, the stress

relaxation follows the predicted trend from the higher thermal expansion coefficient of the silicon substrate compared to that of Cu_2O over the given temperature range. For the films on glass, we observed that all of the data show strong oscillations of a similar frequency with higher amplitude at lower temperatures. We believe these are related to an error in the measurement process. Smoothing trends were generated from the data using a 30-point 3^{rd} order Savitzky-Golay filter. Between ~150^{o}C and ~300^{o}C for 100nm and 125nm films there is still a 1^{st} and 2^{nd} order derivative trend matching that observed on silicon, and likely also exists for the other films but the level of noise would make it difficult to extract. Interestingly 30nm and 125nm films have built-in compressive stress while 50nm and 100nm films have built-in tensile stress, however all films gain more compressive stress after thermal cycling. It is important to point out that we don't know yet whether stress causes copper-rich precipitates to form, or if the copper precipitation is responsible for the change observed in the stress state.

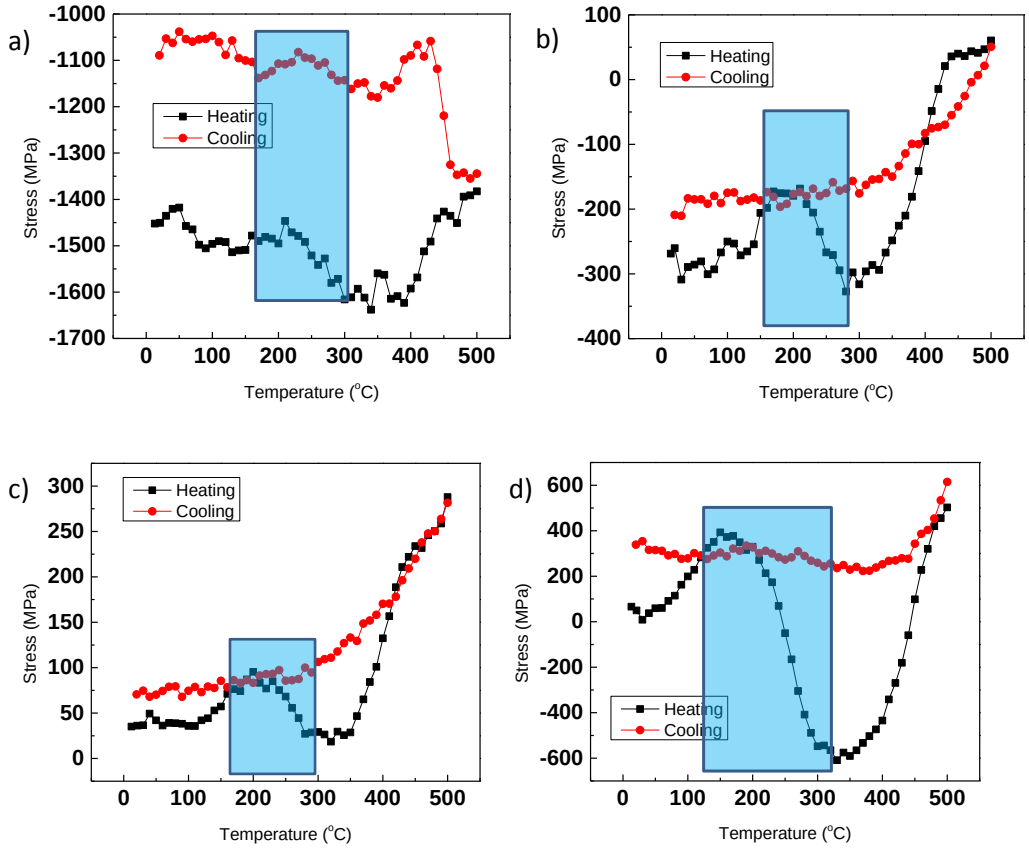

Figure 6.19: Metal-sputtered Cu_2O film stress vs. temperature for film thickness of (a) 30nm, (b) 50nm, (c) 100nm, and (d) 125nm on silicon substrates. (Si lattice: 0.543 nm, Cu_2O lattice: 0.427 nm, Si thermal expansion coefficient at RT: 2.6μm/m-K, Cu thermal expansion coefficient at RT: 16.5μm/m-K, Cu_2O thermal expansion coefficient: ~0 μm/m-K @ RT to 1.6μm/m-K @ 630K)**.** The rate of change of stress per thickness during the shaded-region of the heating cycle is -5MPa/nm at 30nm, -2.6MPa/nm at 50nm, -.55MPa/nm at 100nm, and -7.68MPa/nm at 125nm. The approx. changes in cooling cycle stress from 0°C to 500°C are -250MPa for (a), 250MPa for (b), 200MPa for (c), and 250MPa for (d).

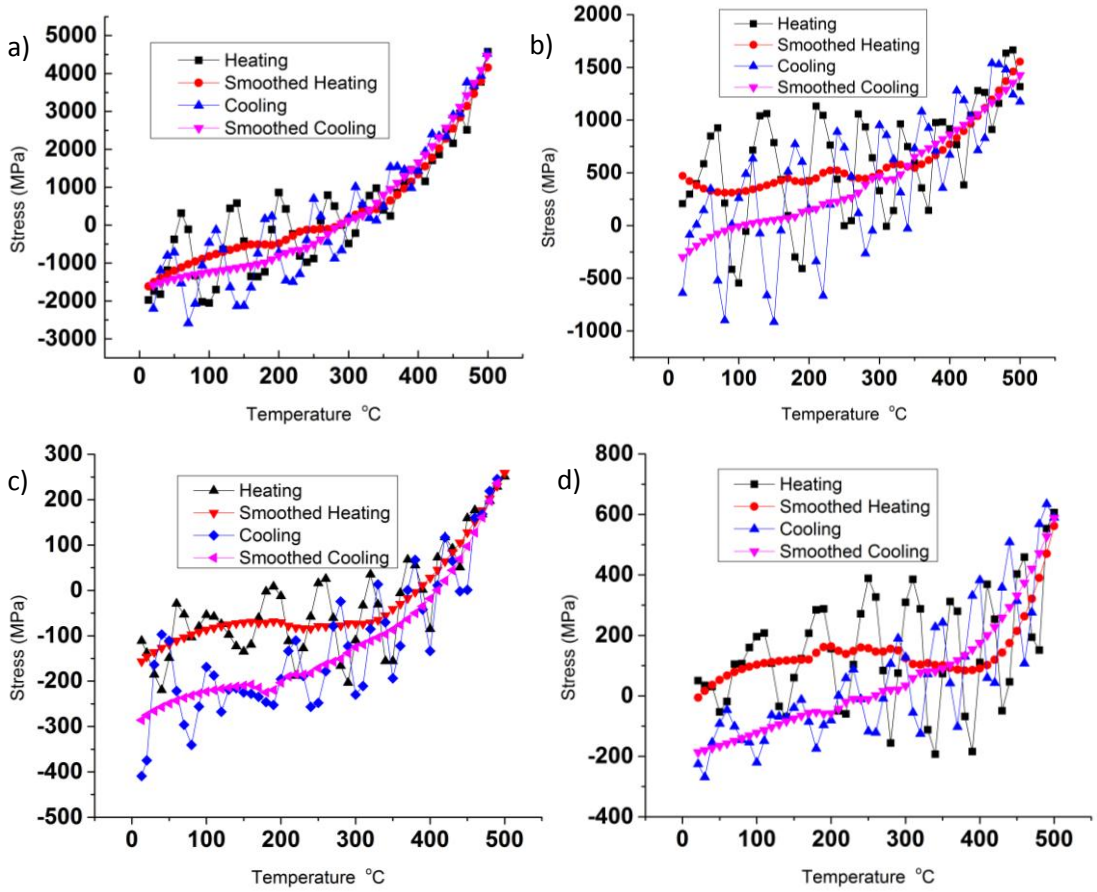

Figure 6.20: Reactive-sputtered Cu_2O film stress vs. temperature for film thickness of (a) 30nm, (b) 50nm, (c) 100nm, and (d) 125nm on glass substrates (Valley Design Corp soda lime flat float glass) with a thermal expansion coefficient of 8.6 μm/m-K. Given that the thermal expansion coefficient for the substrates is about 4 times higher than silicon, it is no surprise that the stress relaxation produces approximate changes in cooling cycle stress from 0°C to 500°C of 6050MPa for (a), 1730MPa for (b),

6.3 The p-type layer: Cu_2O –ceramic-sputtered

Films used for BGJ applications with the same deposition parameters except sputter time were measured by profiliometer to have a thickness of 220nm and 10nm. These films had a deposition rate of 3.67nm/min, a little faster than that observed by our 71W metal-sputtered Cu_2O films but still low relative to reported rates for ceramic-sputtered Cu_2O films (*237*). For the former, 220nm thick as-deposited films had resistivity of $2.7x10^3$ Ω-cm with post-deposition anneals in nitrogen at 500 ^oC for 5 min decreasing it to $1.3x10^2$ Ω-cm. The carrier concentration and mobility for 220nm thick surface-passivated films is shown in figure 6.21. The carrier concentration for as-deposited films is at $3x10^{14}$ cm^{-3}, rising to 10^{15} cm^{-3} after 5min at 500^oC, while over the same range mobility increases from 2 to 18 cm^2/Vs. Both values are lower than those observed for the metal-sputtered films and may point to the electrical benefits of the copper inclusions at the cost of some optical transmission. An anomaly is observed for films

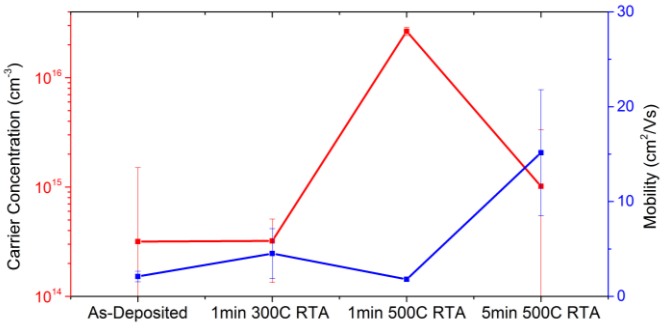

Figure 6.21: The carrier concentration and mobility of 200 W ceramic-sputtered Cu_2O films after surface passivation. The applied current was fixed at 0.1 uA for the as-deposited film, and at 1 uA for the films annealed at 500 ^oC for 1min and 5min, and 50 nA for films annealed at 300^oC. In all cases the applied magnetic field was swept up/down +/-6 Tesla. The error bars correspond to one standard deviation in measurements on the same sample.

annealed for 1min at 500°C whereby the carrier concentration appears to increase substantially while mobility drops. This was not observed in our metal-sputtered films nor in literature and may be an anomaly. Electrical measurements were not done on films with 10nm thickness.

Optical transmission was over 83% as-deposited (above 600 nm), with a band gap of 2.1 to 2.3eV depending upon the deposition temperature (figure 6.22). The transmission

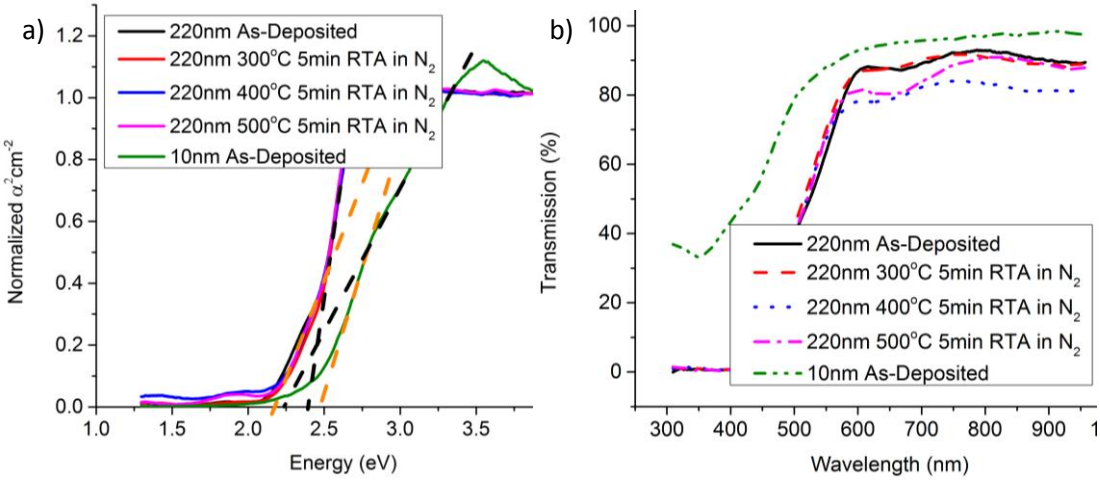

Figure 6.22: The direct band gaps and optical transmission of 200W ceramic-sputtered Cu_2O films are given in (a) and (b) respectively using a 147 point-window Savitzky–Golay filter.

is unchanged for anneals up to 300°C, then decreasing with higher temperature anneals. However, the overall transmission is superior to that observed from the metal-sputtered Cu_2O films, and much better than almost all published results to date (*247-249*). The direct gap remains very steady after anneal for the thick films, but the 10nm films show a substantial change in direct gap depending upon how the intercept is drawn. If the black dotted line corresponds to the direct gap, we actually see a decrease from 2.4 eV to 2.25 eV as we move from thicker to thinner films, however if one assumes the orange dotted line then the gap increases from 2.15 eV to ~2.5 eV.

The 220nm thick films were studied by SEM for copper inclusions (see figure 6.23). None were observed for as-deposited films up to 500 ^{o}C anneals for films deposited on glass substrates, however some particles were observed after 500 ^{o}C anneals on silicon substrates. The large particles could not be identified by SEM-EDS as being of any different than the bulk Cu_2O films. However, since the films were over 200nm thick, if the particles were copper rich, we likely would not be able to detect this given the small size of the particles relative to the bulk film thickness.

A second target was used to make these films after the first target cracked. XRD measurements were done for 220nm films shown in figure 6.24 for the first target used, and for the second target the sputtering power was adjusted, as well as deposition temperature to attempt to get similar crystallinity. Data revealed phase-pure Cu_2O with strong (111) orientation as well as an increased density of 6.025 g/cm^3 on silicon compared to

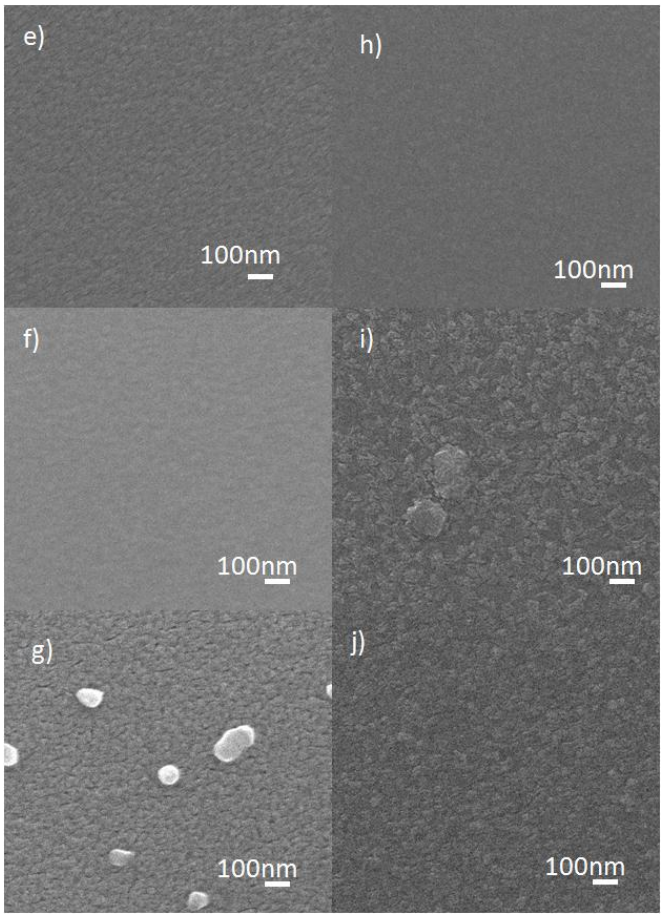

Figure 6.23: SEM images of 200 W Cu_2O films as-deposited on silicon (**e**), after a 300^{o}C RTA for 5min in N_2 (**f**), after a 500^{o}C RTA for 5min in N_2 (**g**), and as-deposited on glass (**h**), after a 300^{o}C RTA for 5min in N_2 (**i**), after a 500^{o}C RTA for 5min in N_2 (**j**).

the metal-sputtered Cu_2O on silicon. The higher density may be due to better crystal packing, and may lead to a more stable film at higher annealing temperatures. All films except (d) show dominant (111)-grain orientation with increased power from 100W to 220W giving reduced (200) peaks, however films deposited at 250W show a conversion to a multi-phase copper oxide. In terms of the (200)/(111) peak ratio: (a) has 2%, (b) has 13%, (c) has 6% (f) has 4.5%. For grain size, (a): 15.6 nm-(111), 9.8 nm-(200), (b): 11.9 nm-(111), 5.2 nm-(200), (c): 26.7 nm-(111), 10.2 nm-(200), (f): 31.6 nm-(111), 10.2 nm-(200). Overall the grain size varied by at most a few nm for (200) grains, and at best a factor of 3 for (111) grains. The relative grain sizes of the (111) and (200) orientations on silicon (a) are very similar to our 50 nm metal-sputtered films on silicon, despite a difference of a factor of ~4 in thickness and ~3 in sputter power. The reason for the multiphase formation seen in (e) is unknown and is not predicted in the phase diagram but could be due a change in the level of oxygen incorporated into the film. Adding a very small amount of oxygen to the process could compensate for this. As discussed in section 3.3, the common parameters used to achieve highly textured films are likely to include minimizing the substrate temperature and providing a high adatom energy through a combination of higher sputtering power (observed by Reddy (*249*)) and sufficiently low chamber pressure. This is confirmed by our results, however we did not attempt to obtain single 200 oriented grains but only 111 oriented grains as this was the dominant grains first observed with our initial deposition parameters.

AFM & KFM measurements are shown in figure 6.25. They show little or no change in roughness until the 5min 500^{0}C anneals, which helps explain the lack of mobility increase seen at lower temperatures. No obvious potential difference is observed in the KFM data until the 5min anneal at 500^{o}C, however the features have a somewhat lower potential than the rest of the material, in contrast with metal-sputtered Cu_2O films. This is

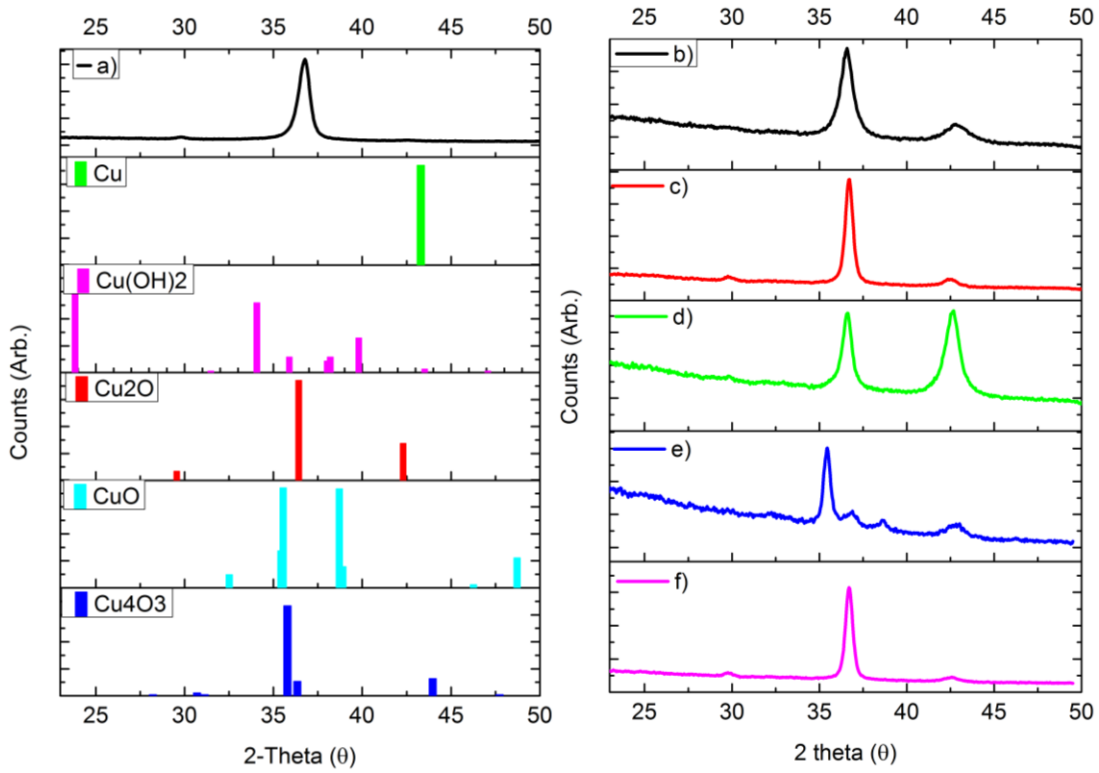

Figure 6.24: XRD of films produced on silicon substrates with a pure argon atmosphere of 40 sccm at a 5 mTorr chamber pressure. Sample (a) was sputtered at 200 W using sputter target one. Samples (b-f) used the second target with a power of (b) 100 W, (c) 200 W, (d) 100 W (e) 250 W, (f) 220 W. Sample d was heated to 200 ^{o}C during deposition. All other samples were not heated intentionally.

further evidence of the stability of this material over the metal-sputtered films. The as-deposited work function is somewhat higher than as-deposited metal-sputtered films, however this increases to a similar ~5 eV work function for both films after a 5min 500 ^{o}C RTA. Assuming a band gap of 2.15 eV this gives a projected as-deposited valence

band and electron affinity of 4.75 eV and 2.60 eV respectively, and 5.26 eV and 3.1 eV for films after 5min 500 ^{o}C RTA. This is larger than the values observed for the metal-sputtered films, however they are in line with the high end of the expected values for this film.

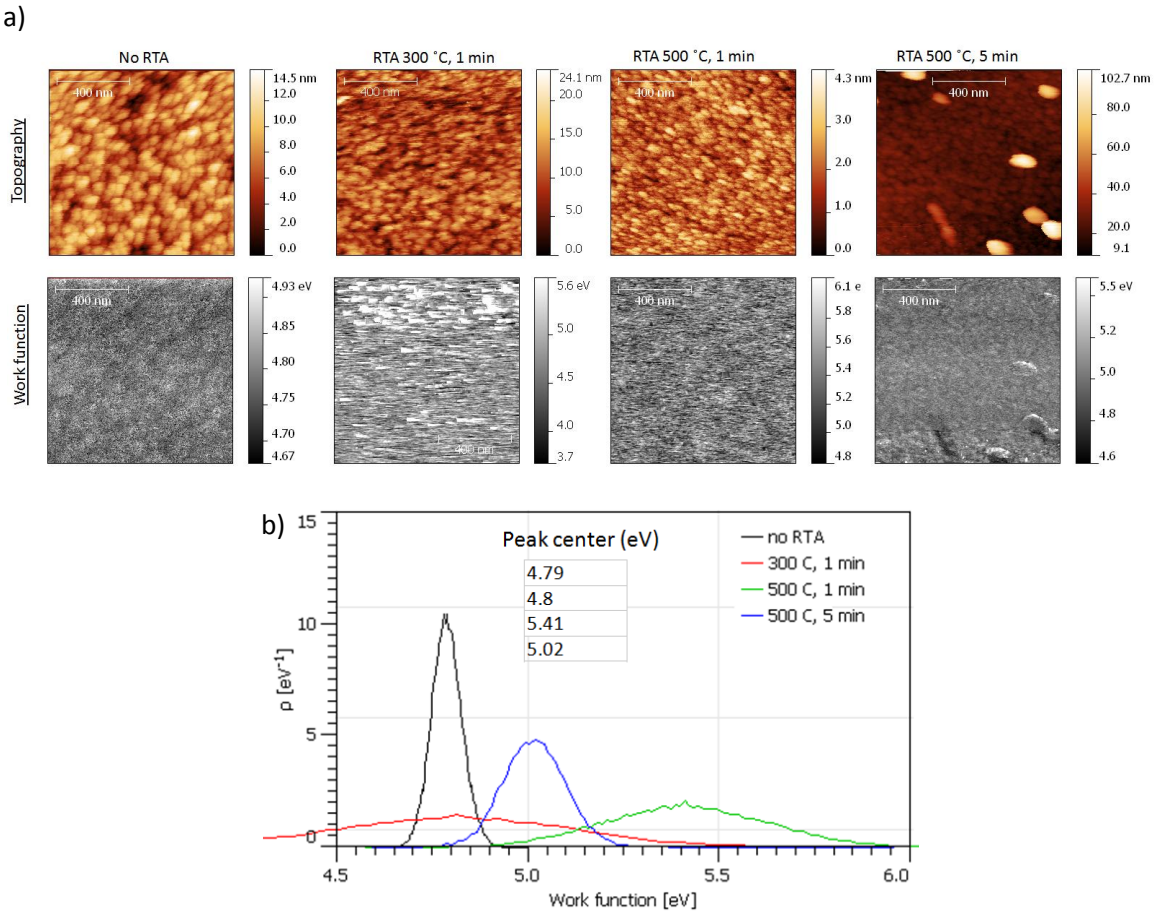

Figure 6.25: Topography and work function measurements over a 1x1um region of 200 W ceramic-sputtered Cu_2O films deposited on ITO/glass substrates with various post-deposition RTAs in N_2. Note that the horizontal white lines at 300^{o}C are an instrument artifact. In (b) the work function distribution data is shown. Samples at 300^{o}C and 500^{o}C for 1mins have broad distribution due to scanning probe noise issues, while the latter sample also has a feedback loop problem giving a contact potential difference locked in at -1.2 V instead of ~0 V. Therefore this data is not reliable.

6.4 The p-type layer $CuAlO_2$

Films were made for BGJ applications using a single recipe and measured by both ellipsometry and profilometer to be 10nm, giving a growth rate of about 0.042nm/min, which is nearly an order of magnitude lower than the lowest recorded (*323*). We think this may be explained by the somewhat low power density we used (2.19 W/cm^2) compared to other groups who sputtered from ceramic targets although many don't report the growth rate and power density.

Optical absorption measurements reveal as-deposited films with transmission over 90% for photon energies below the band gap of 2.7 eV (figure 6.27a, b). This band gap is substantially below the theoretical direct gap value of 3.5 eV (*299*), and may be explained by a large amount of defects in the material and possibly due to mixed phase material. A 5min RTA anneal at 500^oC in N_2 increases the transmission to near 100% and shifts the band gap to 3.6eV in line with similar work found by Lan (*312*). The films were found to be very stable optically even after a 600 ^oC anneal for 1+ hours. Some of the films showed over 100 % transmission which may be due to a change in reflective properties or sample measurement error. In figure 6.27c and 6.27d are similar films which reveal the amount of variation we observed in these films from sample to sample and deposition iteration, with as-deposited band-gaps varying by .25 eV but converging on 3.6 eV at higher temperature anneals. This may possibly be due to a change in the sputter target oxygen concentration while not in use due to excess absorption of sintered particles as alluded to by Kumekawa (*344*).

Four-point DC electrical measurements were unsuccessful at obtaining any repeatable

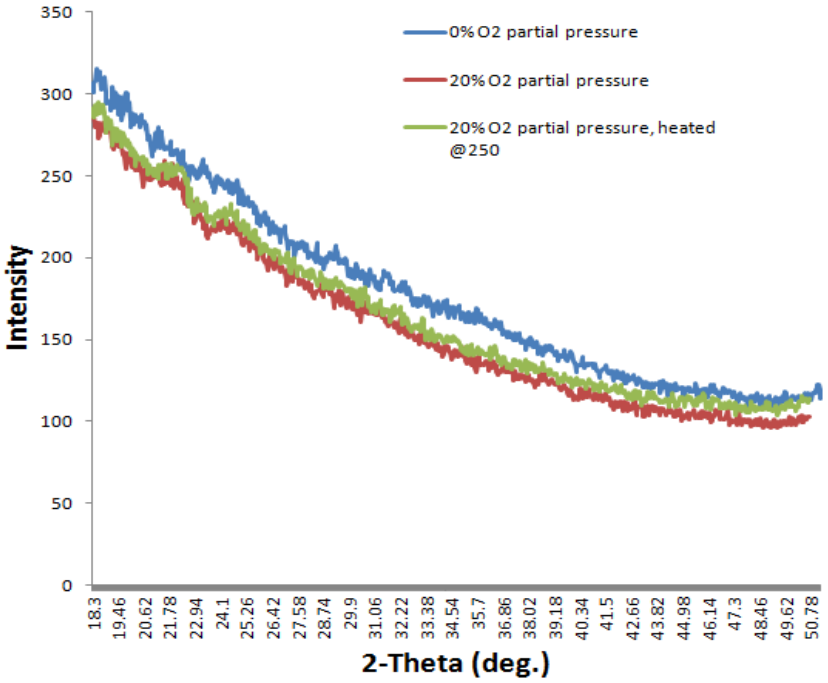

Figure 6.26: The XRD for films on silicon.

resistivity value. We believe this is from a combination of surface states depleting the film, along with a very thin film, large device area, and low carrier concentration, but could also be related to preferential surface segregation of the aluminum oxide, known to occur in multi-metal films where one metal has a much higher oxygen affinity (*386*), as well as in doped metal oxides (*387*).

AFM measurements reveal .3 nm to .5 nm rms roughness as-deposited with no meaningful change after the performed anneals. This is unsurprising given the reported lack of grain growth in $CuAlO_2$ up until 800^{o}C (*312*). XRD revealed completely amorphous films for all sputter conditions (see figure 6.26).

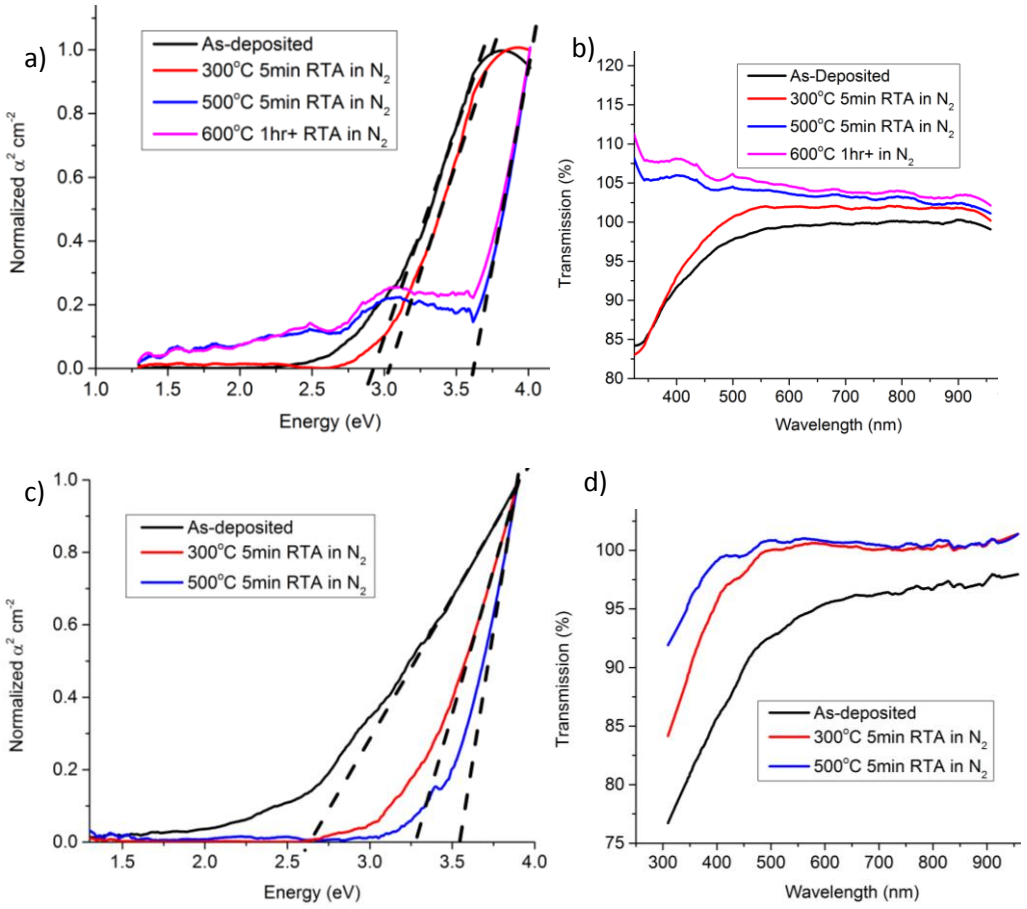

Figure 6.27: Optical bandgap (a) and transmission (b) of $CuAlO_2$ films. In (c) and (d) are similar films made a few months earlier using the same sputtering conditions. Because of the higher transmission level and wide band gap in these films, a larger 147-point Savitzky-Golay filter was used instead of the usual 57-point. Using the 57-point filter resulted in a ~3.75 eV band gap for the 500°C and 600°C anneals in (a). The transmission of films annealed at 300°C were within the instruments ~3% margin of error while films annealed at 500°C and 600°C showed over 100% indicating more light detected. This may be due to a change in the film's properties causing more reflectance as we found this data repeatable.

Composition measurements were attempted using Auger depth profile however the results consistently gave a copper to aluminum ratio of between ½ and $^1/_4$ depending upon deposition run and sample analyzed (see figure 6.28b). In figure 6.28a, 200nm thick

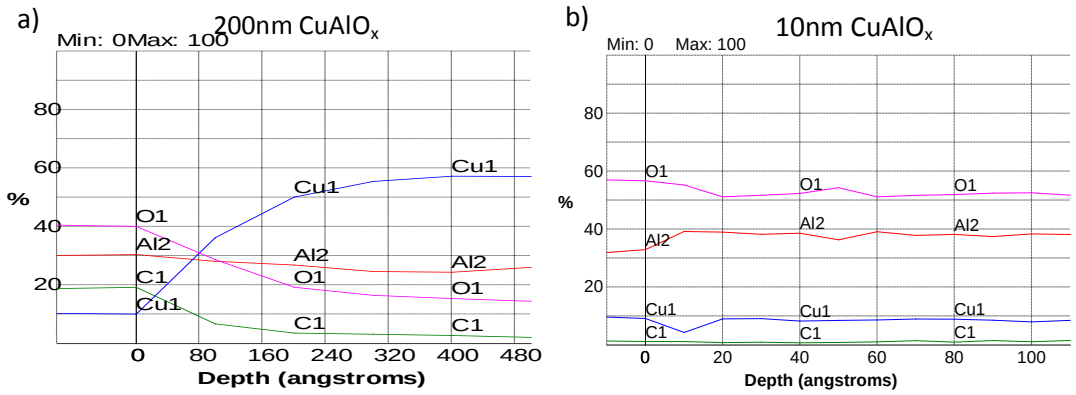

Figure 6.28: In (a) is the Auger depth profile of oxygen-deficient $CuAlO_x$ films deposited by argon sputtering poisoned CuAl target known to have ~50/50 copper/aluminum. In (b) is the depth profile of $CuAlO_x$ films made in oxygen-intensive sputtering conditions from a ceramic $CuAlO_2$ target.

films were sputtered from a poisoned alloy CuAl target using pure argon. The results show a copper to aluminum ratio of 3, however the composition by SEM-EDS measurements indicated a ratio near 1. Initially RBS measurements of sub-10nm $CuAlO_x$ films on silicon pointed to a copper deficiency validating the Auger data from (figure 6.28b), however due to the nature of aluminum and silicon having atomic masses so close to each other the accuracy was questionable. Therefore, RBS measurements were repeated with a tantalum layer between the $CuAlO_2$ and silicon substrate. The results, shown in figure 6.30 show a good fit for a model with a copper/aluminum ratio of ~5/4. Apart from verifying that we likely have a stoichiometry close to the desired $CuAlO_2$, we believe these RBS results demonstrate preferential knock-on of the copper atoms during sputter-depth profiling when the films are severely oxygen deficient, and preferential sputtering of the copper atoms when the films are close to or above the stoichiometric level of oxygen for $CuAlO_2$.

XPS results done by NREL (shown in figure 6.29 and Table 6) were performed on

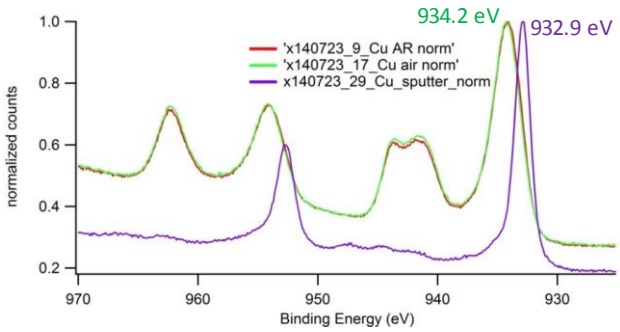

Sample	C	N	O	Al	Cu	In
As-received	11.6	0.5	52.1	13.9	21.9	-
15 min air	12.0	0.3	51.9	14.3	21.6	-
6 min sputter	-	-	60.0	30.8	9.5	0.2

Figure 6.29/Table 6: XPS binding energy for copper Cu2p (3/2) and composition for $CuAlO_2$ films on ITO/glass.

ITO/glass substrates that had only been exposed to room air for under 30min between sample creation and subsequent vacuum sealing in ampule. Upon entry of the sample into the analysis chamber, the sample was analyzed (red line, x140723_9_Cu AR norm) exposed to air for 15minutes however subsequent analysis there was basically no change (green line, x140723_17_Cu air norm). Sputtering removes adventitious carbon and the trace amount of nitrogen, as well as drastically changing the copper to aluminum ratio in agreement with the preferential sputtering observed in our Auger measurements, and begins to reveal Indium from substrate ITO. As received Cu 2p spectrum resembles spectrum for Cu(II) compounds. This is not consistent with Cu(I) in the delafossite structure $Cu^{(+1)}Al^{(+3)}O_2^{(-2)}$. Sputtering appears to reduce Cu^{+2} and uncover a mixed oxide structure, however this could be due to damage of the surface bonds from the sputter

process itself. The Cu2p (3/2) satellite features seen around 940eV-950 eV have been shown by Yao (*331*) to enhance the electrical conductivity and widen the band gap.

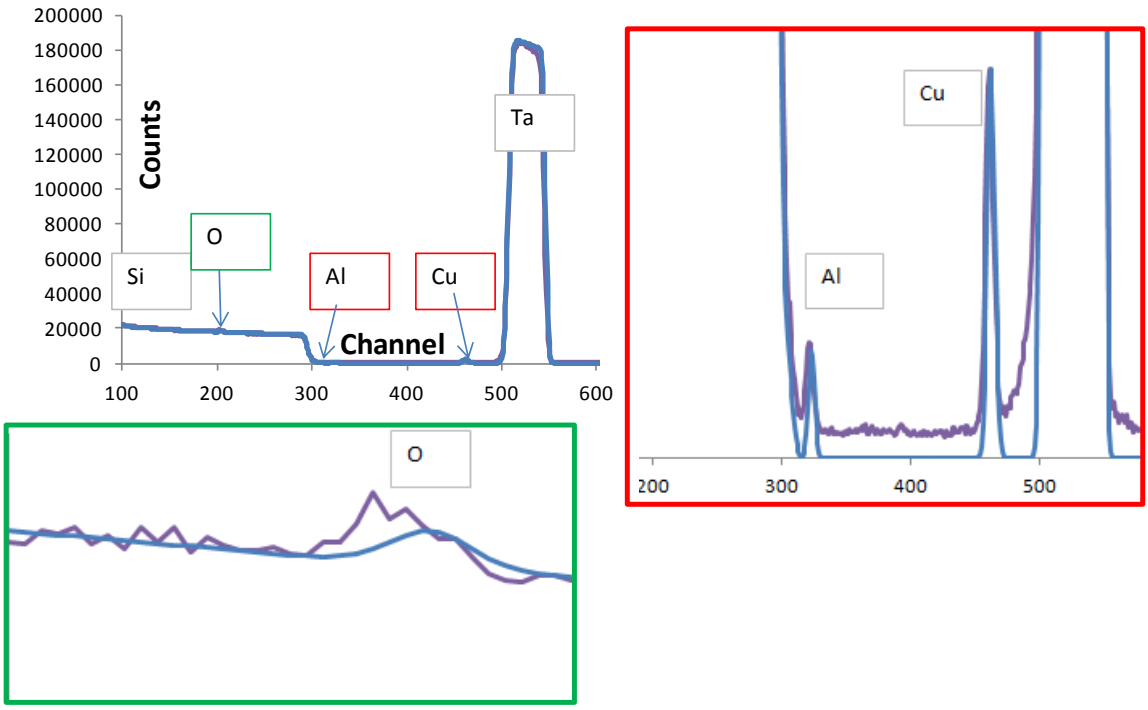

Figure 6.30: RBS data (purple line) from a ~10nm copper aluminum oxide film sputtered onto 110nm tantalum film to shift the spectra from the silicon substrate so that the aluminum peak no longer overlaps it. The blue line is a manual curve fit using QUARK with approximately $CuAlO_2$ composition. The slight shift in oxygen signal may be due to an unaccounted for layer of oxygen in the silicon substrate.

6.5 BGJ Devices-metal sputtered Cu_2O

BGJ devices in configuration (a) were made from copper oxide and zinc-stannate with the previously specified behavior on ITO-coated glass substrates. Figure 6.31 (a)

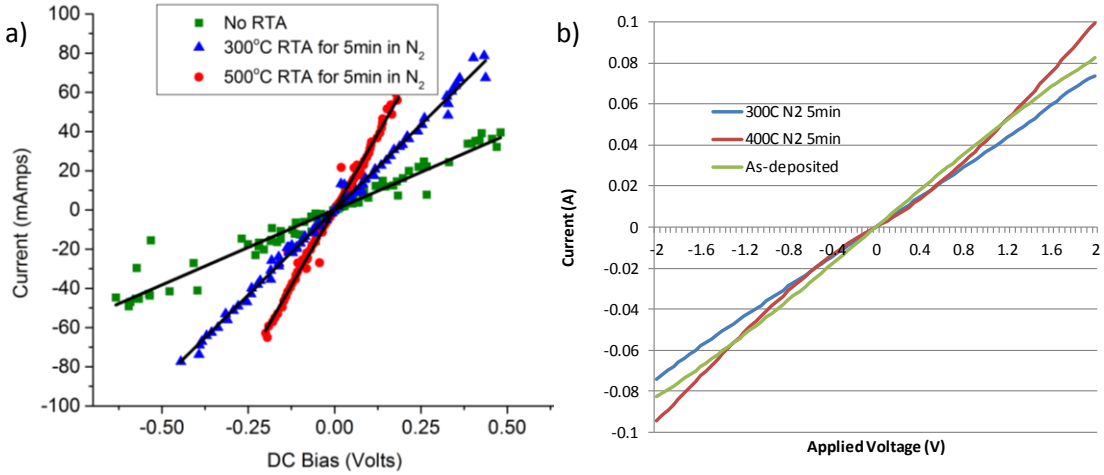

Sample	Processing Conditions				Results:
	Top Contact	Measurement Temp	RTA after $ZnSnO_3$	RTA after Cu_2O	R_c (Ω-cm^2)[a]
1	Au	Room temp	600 °C @10 min in O_2	300 °C @ 5 min in O_2	4.2
2	Au	Room temp	none	none	1.02
3	Au	Room temp	none	300 °C @ 1 min in N_2	$1.31\pm7.7\times10^{-1}$
4	Au	Room temp	none	500 °C @ 1 min in N_2	$9.11\times10^{-1}\pm2.03\times10^{-2}$
5	Au	Room temp	none	300 °C @ 5 min in N_2	$8.87\times10^{-1}\pm7.99\times10^{-2}$
6	Au	Room temp	none	500 °C @ 5 min in N_2	$3.74\times10^{-1}\pm1.33\times10^{-1}$
7	Ni	Room temp	none	none	$1.59\pm6.15\times10^{-1}$
8	Ni	Room temp	none	500 °C @ 1 min in N_2	$1.32\pm1.23\times10^{-1}$
9	Au	38 K	none	none	<3[b]
10	Au	35 K	none	300 °C @ 1 min in N_2	<4[b]

[a] The specific resistivity is measured as the slope of the J-V plot. The average and standard deviation is obtained by testing multiple samples.

[b] Since these were 2-probe measurements, the voltage drop through the AZO is not subtracted, so the true specific resistivity is less than stated.

Figure 6.31/Table 7. (a) Four probe I-V characteristics of $ZnSnO_3$-Cu_2O broken gap junctions deposited on ITO-coated glass substrates: Current noise is due to use of metal whisker probes. This data and others is summarized in Table 7. (b) Low-temperature I-V characteristics: the sample had electrode's 1 and 2 wire bonded to an external gold plated package which was contacted with tungsten probes. The sample was attached to the package using double sided tape. The package rested on top of a thermoelectrically cooled copper plate, and also contains a thermocouple for temperature measurement. The system was pumped down to 13mTorr and allowed to reach the lowest possible temperature overnight (typically 30 K temperature measured at the stage is reached within a couple hours). Because these were 2-probe measurements the lower current/voltage slope is likely due to the effect of the lateral voltage drop through the AZO layer.

shows that the room temperature I-V characteristics are ohmic . This is consistent with expected broken gap band alignment between the $ZnSnO_3$ and Cu_2O films. Table 7 shows specific junction resistivities for devices operated under forward and reverse bias. A minimum average specific resistivity of 0.37 Ω-cm^2 was measured for junctions made from films annealed using RTA at 500 ^oC for 5 min in N_2. Negligible hysteresis was detected during the I-V measurements. Generally higher temperature and a longer duration RTA of films in N_2 improved the electrical performance while anneals in oxygen tended to reduce it. Low temperature I-V measurements were also done (Figure 6.31 b). The results are very similar to room-temperature measurements, albeit scaled because of the use of 2 probes. This confirms a lack of conduction across the junction by traps, such is that seen in amorphous silicon reverse biased junctions, since this mechanism would be disabled at lower temperatures. The sample annealed at 400^oC shows a slight Schottky, however this was also observed in the device prior to cooling (not shown).

Similar devices produced on heavily doped silicon substrates utilizing configuration (d) (Figure 6.32a) gave inconsistent I-V profiles between deposition runs and with post-deposition RTA. This may have been related to the possible reaction of AZO and silicon although depth profiles revealed no measurable amount of diffusion. Another factor may be the influence of surface morphology on $Cu_2O/ZnSnO_3$ interface states. Devices made

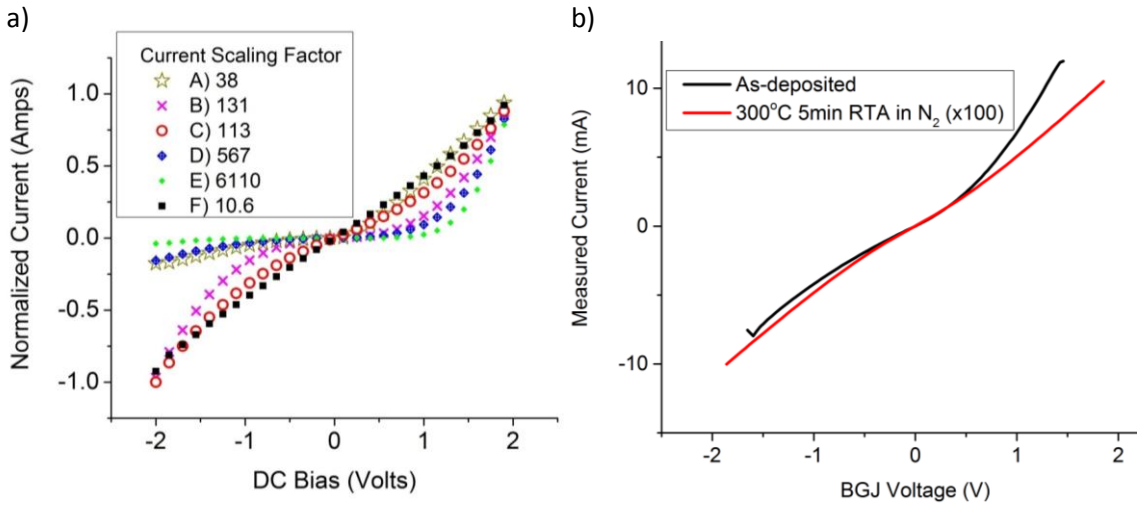

Sample	Processing Conditions	
	RTA after $ZnSnO_3$	RTA after Cu_2O
A	none	none
B	600°C@10min in O_2	none
C	none	300°C@5min in O_2
D	600°C@10min in O_2	300°C@5min in O_2
E	600°C@10min in O_2	600°C@10min in O_2
F	none	600°C@10min in O_2

Figure 6.32/Table 8: (a) The reactive-$Cu_2O/ZnSnO_3$ devices on silicon using a thru-wafer device stack in a two probe configuration: Samples were ohmic only after an RTA. (Note: divide by the current scaling factor to get the actual current for a given plot.) Results were not reproducible between device fabrication (repeating a second set of devices caused ohmic/Schottky behavior to be observed at different post-deposition anneals). (b) I-V profiles for 3-probe laterally-configured BGJ devices on glass without the ITO layer.

on glass substrates (in configuration (a)) without the ITO layer are shown in Figure 6.32b

and show a substantial increase in contact resistances. Moderate Schottky profiles are introduced for the as-deposited films and contact resistances were in the 10-20 Ω–cm^2 range, while profiles for films after 300^oC anneal become more linear but contact resistances jump into the 2k to 3k Ω–cm^2 range.

We tried heated measurements of films deposited on silicon utilizing 3-probe lateral conduction (configuration a) in an attempt to see if any interface states which could be

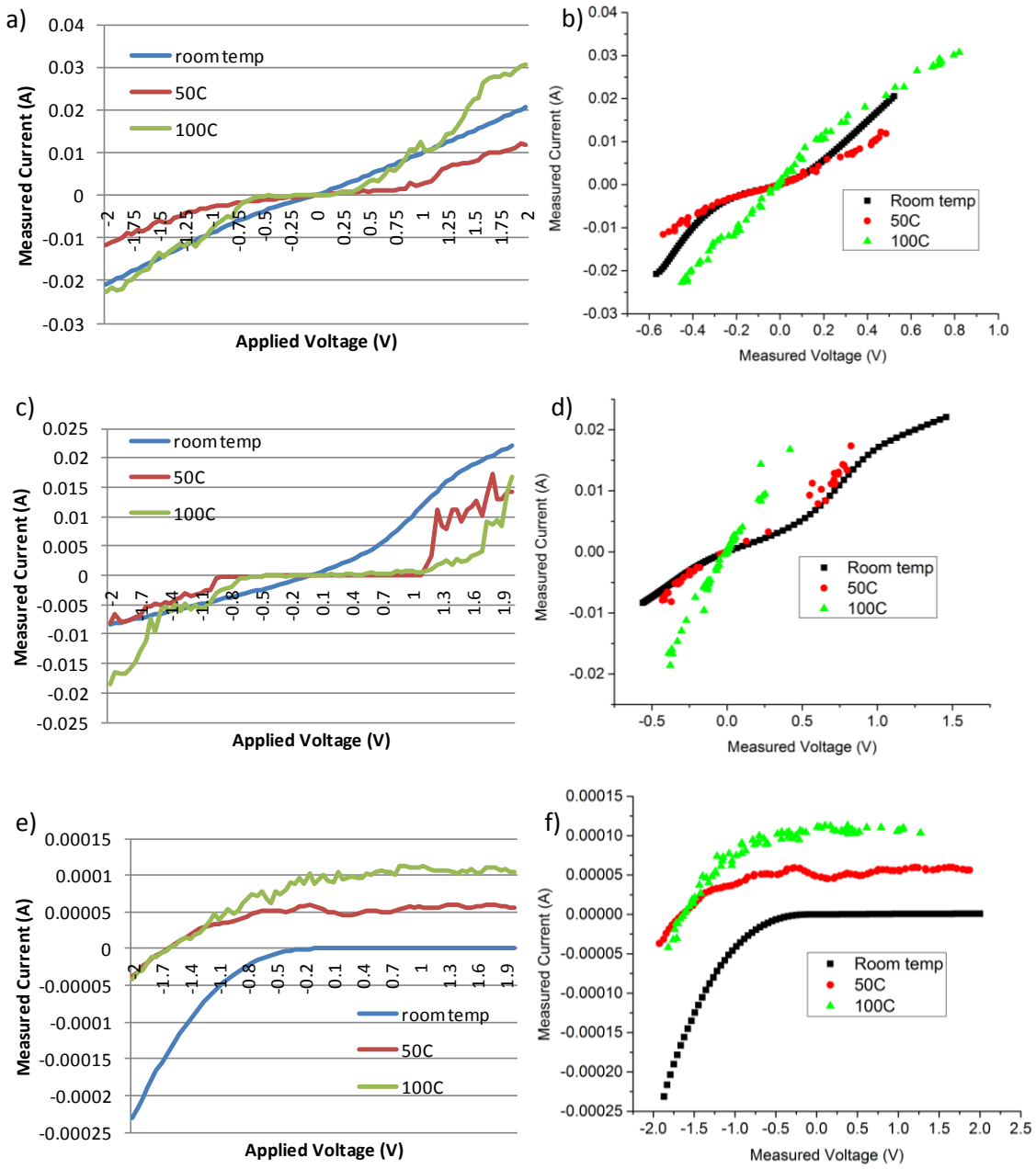

Figure 6.33: 3-contact BGJ devices on silicon at various measurement temperatures. (a) and (b) are as-deposited films; (c) and (d) are films after a 1min RTA at 300^{o}C in N_2; (e) and (f) are films after 5min RTA at 500^{o}C in N_2. (a), (c), and (e) take into account the lateral voltage drop through the AZO and AZO/Au losses.

overcome with higher temperature were preventing ohmic conduction . The results are shown in Figure 6.33, with (a), (c), and (e) showing applied voltage, and (b), (d), and (f) giving only the voltage across the Au/Cu_2O/$ZnSnO_3$/AZO interface. From this we see that the lateral AZO and/or AZO/Au contact have a substantial influence on the overall I-V profile of the devices, with generally more linear responses for I-V data when looking only at the Au/Cu_2O/$ZnSnO_3$/AZO. Increases in measurement temperature also show some improvement towards a linear I-V profile for Au/Cu_2O/$ZnSnO_3$/AZO up until 500^{o}C annealed films, which are universally nonohmic. When the lateral AZO + AZO/Au is taken into account, the increase in measurement temperature actually makes the profile worse. This clearly demonstrates that the AZO material properties substantially influence our overall device stack performance and there is a link with the substrate material. In addition there is a possible link between the substrate surface morphology and the copper oxide bulk or interface properties on the BGJ junction and/or the Cu_2O/Au interface.

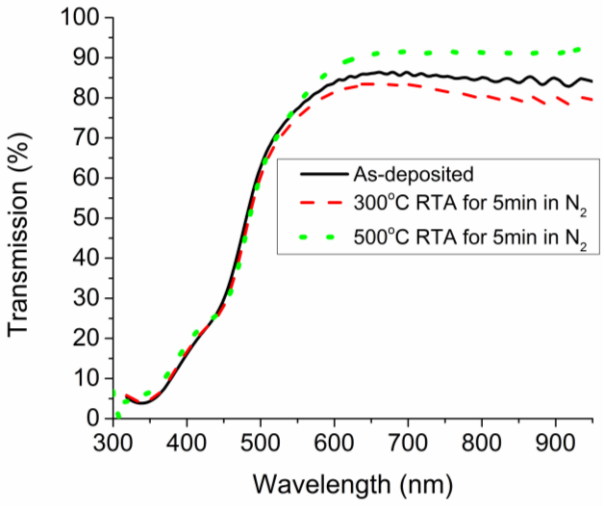

Figure 6.34: Optical transmission for Cu_2O/$ZnSnO_3$/glass devices under different annealing conditions in N_2. The data was smoothed with a 2nd order 147 point-window Savitzky–Golay filter to remove measurement system noise.

The as-deposited junctions had a minimum transmission of 78 % below 2.4 eV (Figure 6.34) which corresponds to the measured band gap of the copper oxide layer.

Post-deposition RTA processing of the junction revealed optical transmission increasing up to as much as 90 % with a 5 min 500 ^{o}C RTA in N_2.

Concentration depth profile measurements using Auger electron spectroscopy of the device stack are shown in Figure 6.35. Films annealed at 300 ^{o}C for 5 min revealed

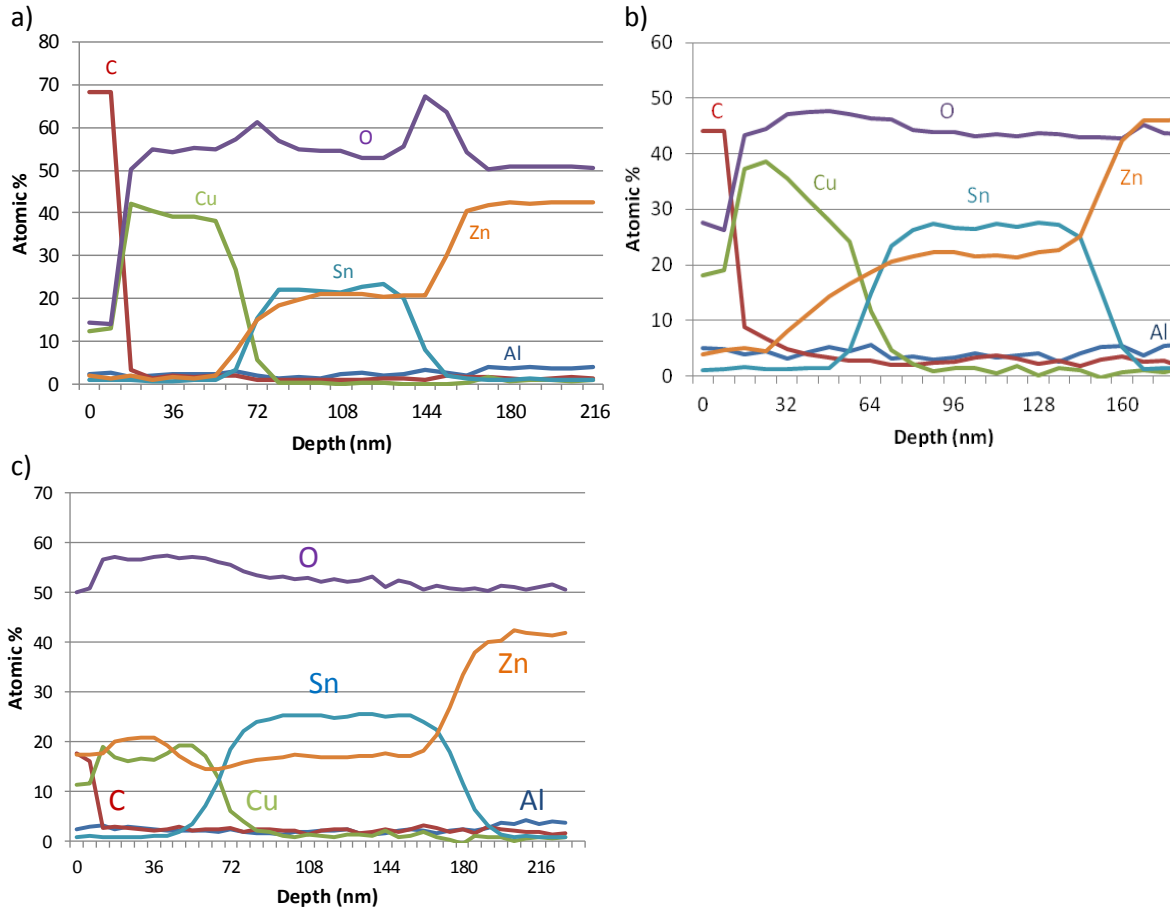

Figure 6.35: Auger depth profiles for samples annealed up to 300^{o}C, 500^{o}C, and 600^{o}C are shown in (a), (b), and (c), respectively.

abrupt transitions at both the $Cu_2O/ZnSnO_3$ and $ZnSnO_3$/AZO interfaces (Figure 6.35b). The spikes of oxygen near the interface of $Cu_2O/ZnSnO_3$ and $ZnSnO_3$/AZO is likely due to the difference in the oxygen sputter yield for the two oxides and may be considered an artifact. At 500^{o}C (Figure 6.35b), partial diffusion of zinc into the copper oxide was

apparent, and complete zinc diffusion is seen at 600^{o}C (Figure 6.35c). No indication of aluminum diffusion from the AZO into the $ZnSnO_3$ was observed. All devices showed a large presence of oxygen in the Cu_2O layer suggesting a composition of CuO or Cu_2O with a large amount of excess oxygen that is not observed in depth profiles of stand-alone films.

If the copper-rich inclusions present in these films penetrate to $ZnSnO_3$, they could form an ohmic contact given the 4.3-4.7 eV work function of copper and our projected work function range of 4-4.9 eV for $ZnSnO_3$. In addition, the inclusions would lead to degrading the optical transmission. A metal-semiconductor Au/AZO/$ZnSnO_3$/Cu/Au device stack revealed ohmic conduction with specific resistivity ranging from 1.5 Ω-cm^2 to as low as 0.07 Ω-cm^2. However, this does not rule out ohmic current conduction through the $ZnSnO_3$/Cu_2O interface. To check for preferential conduction through the inclusions conductive AFM measurements were made on an as-deposited Au/AZO/$ZnSnO_3$/Cu_2O stack using a platinum coated probe. As shown in Figure 6.36, the current flow is uniform to within ~10 % (11 pA rms variation out of 110 pA). This is despite the fact that identically processed stand alone films showed copper inclusions on SEM. No regions with sharply higher current than the average were observed as would be expected if conduction was primarily through the $ZnSnO_3$/Cu interface. However, likely copper inclusions are identified by the lower spots in friction (Figure 6.36c). A clear correlation between conducting regions and Cu_2O grain structure was seen in the deflection image (Figure 6.36d). The probe deflection image gives first derivative-like data of the topography, which is more useful in revealing the surface roughness of the top

Cu_2O layer. Grain regions conducted more than grain boundaries. In Figure 6.37 are films

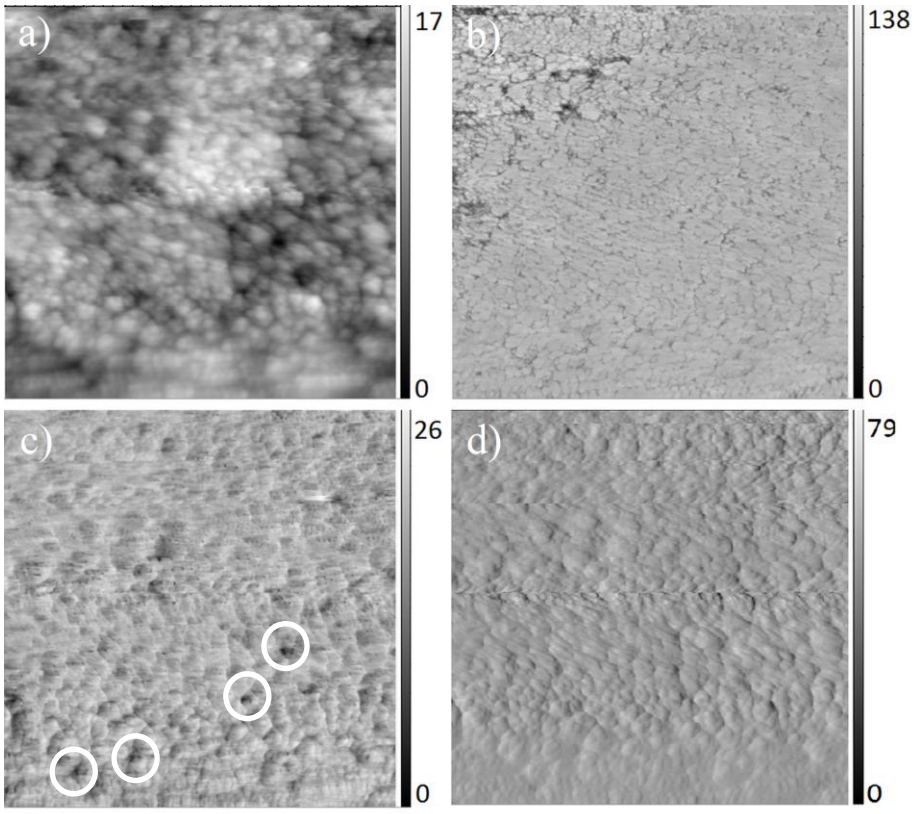

Figure 6.36. Contact mode (single trace direction) conductive AFM images of 1x1 um^2 region of $Cu_2O/ZnSnO_3$/AZO/ITO/glass stack (as-deposited) without top metal contact: (a) shows topography in nm; (b) shows current in pA; (c) shows friction in mV with possible copper inclusions highlighted due to lower coefficient of friction; and (d) shows probe deflection in mV.

after 300^oC RTA for 5min in N_2. The friction data confirms the large protruding regions of the film are likely the copper-rich inclusions identified previously due to copper metals lower coefficient of friction. Current data reveals that dominant current conduction is not through these Cu-rich regions but through the bulk of the material. This could mean that either these regions are not pure copper, or that they do not connect to the $ZnSnO_3$ interface and form diodes to the material around them, as suggested by Weichman (*228*). Also, high concentrations of large Cu regions were not observed in previous AFM

measurements on glass or Si, and point to the possible influence of underlying roughness on their generation. There were also devices annealed at 500^{o}C (not shown), and these reveal likely copper inclusions starting to conduct more relative to the bulk but are still small. A consistent specific resistivity was also observed between devices produced in the same processing run with different levels of lateral area which means that even if there are pin holes conducting through layers, they are not the dominant form of conduction across the junction.

The electrical measurements point clearly to a broken gap alignment. Not only does one observe ohmic behavior, but measurements at low temperature (down to 38 K) are

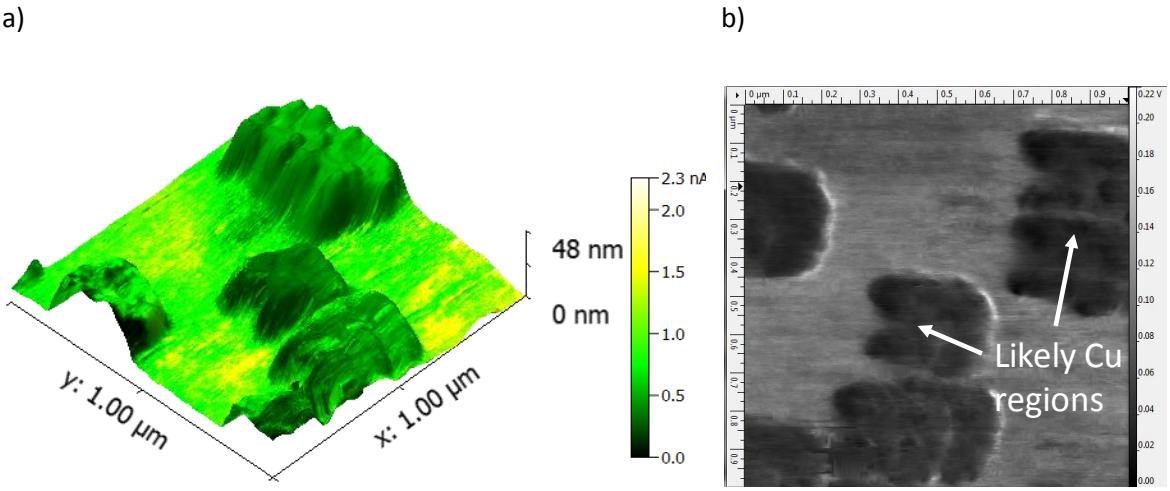

Figure 6.37: Contact mode (single trace direction) conductive AFM images of 1x1 um^2 region of $Cu_2O/ZnSnO_3$/AZO/ITO/glass stack (after 300^{o}C RTA for 5min in N_2) without top metal contact: (a) A 3D of topography overlaid by color-coded current in nA, and (b) the friction in volts.

unchanged suggesting both a lack of hopping between localized states at different energies and a lack of freeze-out in the constituent oxides. This is consistent with autodoping by the band alignment as discussed in Section 2. However, the resistance

achieved is much higher than the 10^{-7} Ω-cm^2 observed in epitaxial junctions (*78*). This may be due to defects at the interface in our devices or additional losses at the Au/Cu_2O interface or $ZnSnO_3$/AZO interface. Furthermore, the electron affinities extracted from KPFM measurements suggest an overlap of the p-material valence band and n-material conduction band of about 0.3 eV in the as deposited junction increasing to 0.5 eV after rapid thermal annealing at 500 ^oC RTA (figure 6.38) if one assumes the simple and commonly used Anderson model of band alignment (*388*). Utilizing the UPS measurements for $ZnSnO_3$ from NREL gives a band overlap of 0.77 to 0.59 eV depending upon carbon removal heating, which is even worse. This large of an overlap should interfere with broken gap behavior. There are multiple possible explanations for this discrepancy. First, the Anderson model is often inaccurate; discrepancies of the order observed here are not uncommon (*389*). Often this is due to interfacial charge or dipoles. Second there is considerable uncertainty (~0.3 eV) in the KPFM measurements, the density of states calculations used to extract the affinity from the work function, and the estimated error in the carrier concentrations from the Hall measurements. In addition, the use of ITO as an underlying conductive grounding layer for KPFM measurements may have resulted in a probe potential offset. Furthermore, the KFM measurements of Cu_2O were done on films deposited directly on ITO. Films deposited on $ZnSnO_3$ may have a slightly different affinity. In the case of UPS data there are uncertainties in the preparation and carbon decontamination in UPS results, as well as the method to clean the sample prior to analysis. If we look at the UPS measurements for $ZnSnO_3$ from ThermoFisher Scientific combined with Cu_2O KPFM data we get a band overlap of -0.17

eV, which is substantially different. The reasons for the differences in the two sets of UPS data remains unknown.

Another interesting note is the influence post-deposition RTA on the band alignment of the p-n materials with respect to one another and overall. The interface overlap increases with anneal temperature, however the electron affinities of the materials shift down also, potentially giving a benefit of fine tuning the overall device band structure to align better to adjacent solar material.

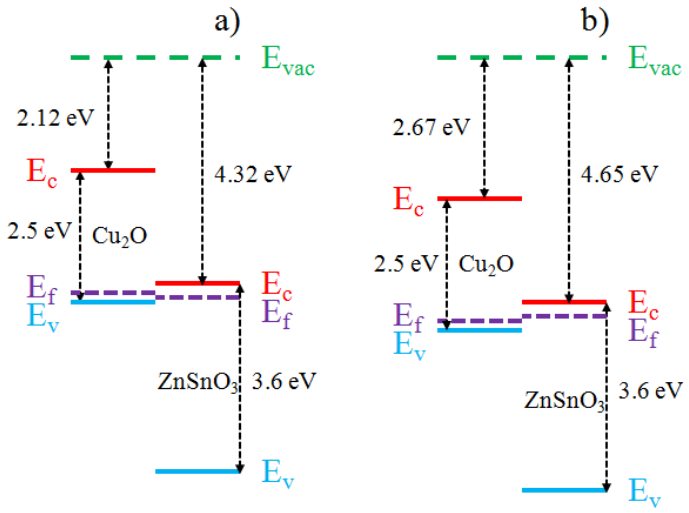

Figure 6.38: Band alignment prior to putting the films in contact for Cu_2O and $ZnSnO_3$ using KPFM and Hall data for as-deposited (a) and 5min 500 ^oC RTA in N_2 (b).

6.6 BGJ Devices-ceramic sputtered $Cu_2O/ZnSnO_3$

BGJ devices have been produced using ceramic sputtered Cu_2O films with the previously described properties in configuration (a) configuration, and the I-V results (see Figure 6.39a) show ohmic conduction with contact resistance down to 0.4 Ω-cm^2. Interestingly the lowest resistance was observed for a 400 ^{o}C RTA.

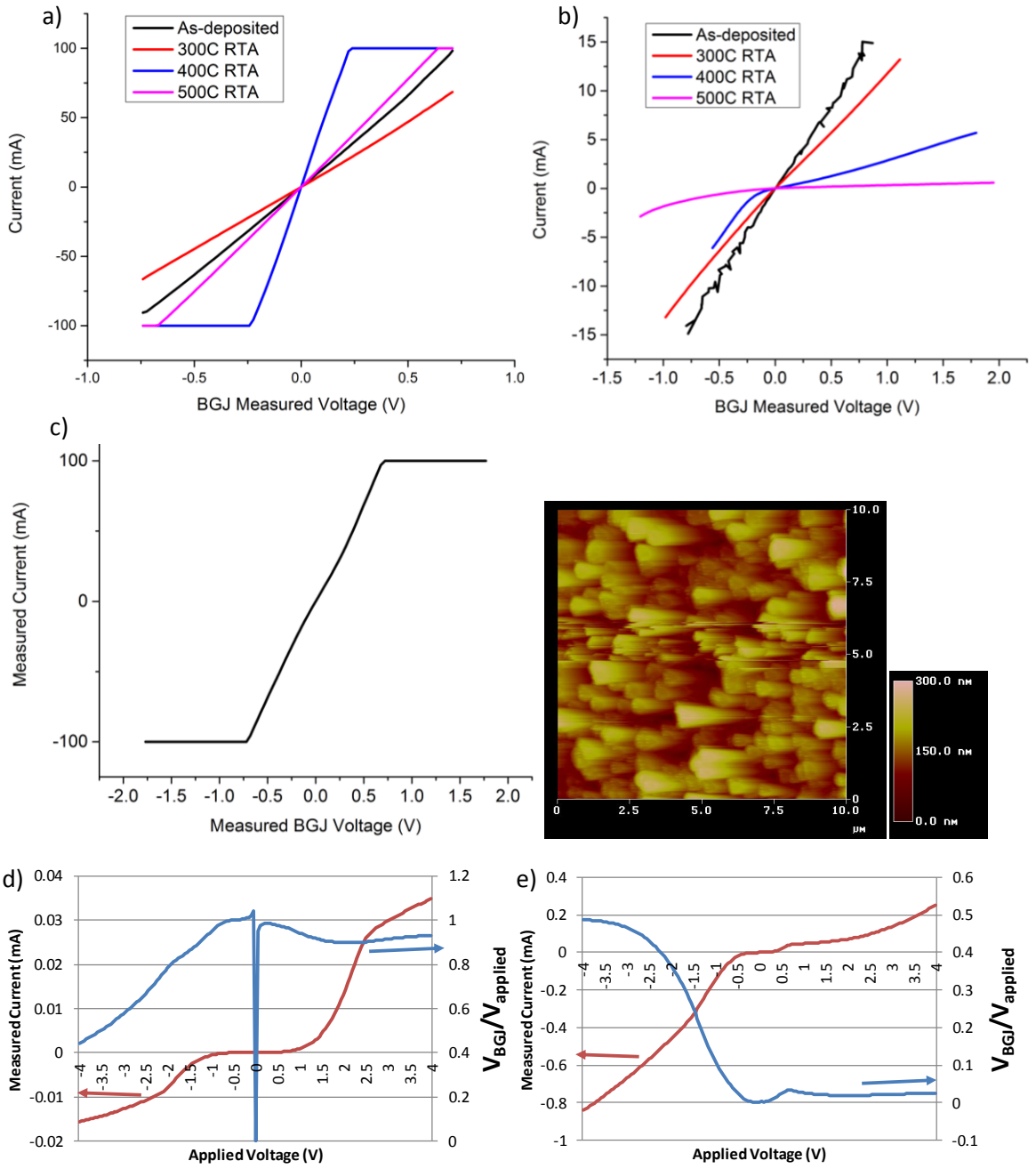

Figure 6.39: The I-V profiles of ceramic-sputtered-Cu_2O-based BGJ devices deposited on: (a) ITO/glass, and (b) silicon, followed by RTA in N_2 for 5min, and on (c) CIGS with the corresponding AFM image of the CIGS surface before deposition. (d) and (e) show the behavior of devices on silicon without AZO, where $ZnSnO_3$ was used as the lateral conductor for the as-deposited and 500°C 5min RTA in N_2, respectively.

The performance degraded at higher temperatures. This trend was also seen in the

electrical properties of individual ceramic sputtered Cu_2O films. BGJ devices with the same configuration were also made on a rough CIAGS surface (Figure 6.39c). As-deposited I-V measurements showed mostly ohmic profiles and a contact resistance of ~1 Ω–cm^2. Devices were also made on silicon (Figure 6.39b) and reveal ohmic conduction for as-deposited and 300 ^oC RTA films, however the contact resistance went up by a large amount, and at 400 ^oC or higher the films become non-ohmic. This reinforces our findings on metal-sputtered Cu_2O-BGJ devices about the influence of the copper oxide and AZO material properties on different substrates.

To eliminate the issues with AZO affecting device behavior, new configuration (a) devices were also made on silicon without AZO, where $ZnSnO_3$ was used as the lateral current conductor in addition to the vertical junction with Cu_2O. If the $ZnSnO_3$ is close to its theoretical electron affinity, gold contacts should be ohmic. Results (Figure 6.39d & e) show highly non-ohmic performance. The plot giving the ratio $V_{BGJ}/V_{applied}$ should

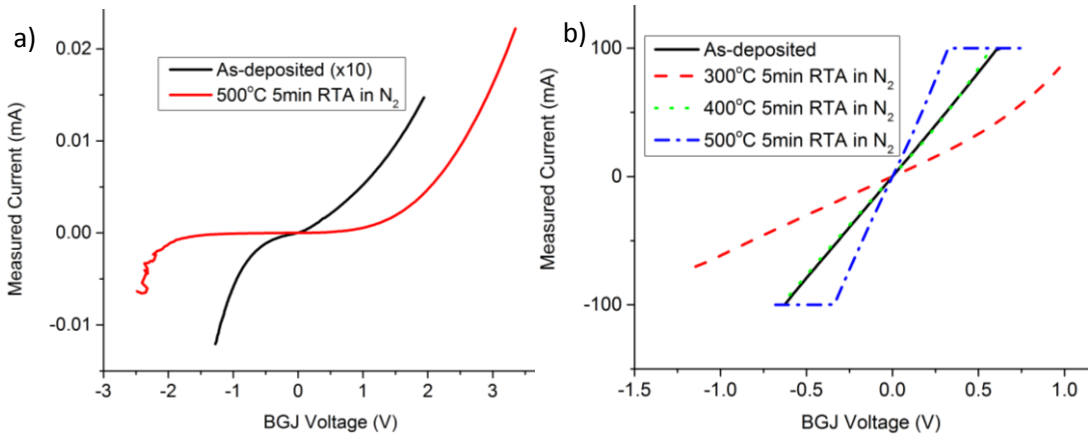

Figure 6.40: (a) Devices identical to those produced in Figure 9 (d & e) with a 1hr 700^oC anneal in N_2 done on the $ZnSnO_3$ layer prior to Cu_2O deposition. (b) The I-V profile for Au/AZO/$ZnSnO_3$/Cu_2O/Au on ITO/glass BGJ devices using the same processing as devices in Figure 6.39(a), but with deposition time limited to produce 20nm versions.

ideally be a flat line if all junctions in the stack are ohmic. For as-deposited devices (Figure 6.39d) it starts out close to 1 at a low applied voltage, which means almost all the potential is dropped across the $Cu_2O/ZnSnO_3$ junction. At higher applied voltages the ratio decreases indicating more and more potential is dropped across the $ZnSnO_3$/Au junction, pointing to Schottky behavior in the $Cu_2O/ZnSnO_3$ junction. For the 500 ^oC annealed films (Figure 6.39e) devices biased with a positive voltage show a mostly flat line (ohmic), however for negative applied voltages there is a sharp rise pointing to Schottky behavior in the $ZnSnO_3$/Au junction. Overall the measured currents are much lower, however this is expected because the AZO and ITO layers previously used greatly reduced the lateral voltage drop underneath the BGJ stack to the side electrodes.

In an attempt to see if the crystallinity of the underlying films affects the I-V profile of the BGJ devices, devices identical to those produced in Figure 6.39 (d & e) were run through a 1hr 700^oC anneal (prior to deposition of Cu_2O/Au layers) in nitrogen where the films are known to crystallize. The results are shown in (Figure 6.40a) for as-deposited and 500^oC 5min RTA in N_2 films. Other properties of the films were not characterized (although we had prior confirmed crystallinity at this temperature), but as-deposited films show better-although still schottky behavior, and films with post-Cu_2O deposition RTA got substantially more schottky-like.

Devices were also made with two top contacts in configuration B configuration to check for losses at the Cu_2O/Au junction, and results (not shown) give ohmic profiles with contact resistance down to ~.04 Ω–cm^2. This is much less than any of the devices in configuration (a) and it suggests that the Cu_2O/Au junction is responsible for the vast majority of losses across the stack at minimum for all cases where good ohmic conduction is observed, excluding the lateral losses through the AZO layer. It brings up another issue suggested in Section 5.3, which is that depending upon the bulk p/n-type resistances vs. their junction resistance the additional 4th contact on the top of the stack may or may not accurately represent the bulk potential just inside the p-layer. Another revelation from the low contact resistance is that it is close to the limit observed for the Au/AZO/$ZnSnO_3$/Cu/Au devices pointing to the $ZnSnO_3$/AZO junction resistance being the second highest voltage drop region after the Cu_2O/Au junction. No further investigation on the influence of underlying substrate on BGJ performance was done because it was determined ITO/glass morphology approximates CIGS/CIAGS surface better.

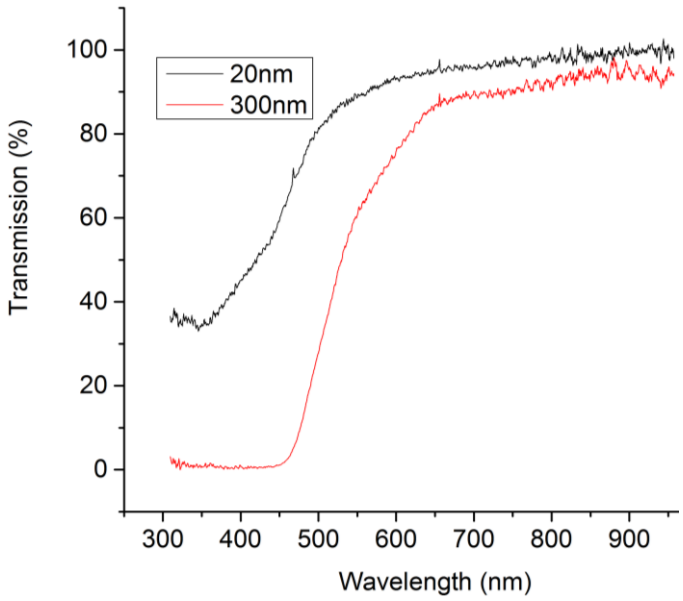

Figure 6.41: The optical transmission profile for 20nm and 300nm devices is shown in (d).

To see if we could get higher performing films, thinner 20nm (10nm $ZnSnO_3$, 10nm Cu_2O) devices were made for ceramic-sputtered Cu_2O-based configuration (a) BGJ devices utilizing the same processing with deposition time limited. In (Figure 6.40b) is the resulting I-V profiles. In these films we see that the contact resistance starts at 0.9 Ω–cm^2 for as-deposited films, increasing to 2.3 Ω–cm^2 after 300^{o}C anneal, and then back to .95 Ω–cm^2 after 400^{o}C anneal, decreasing down to 0.5 Ω–cm^2.

To attempt and extract the actual BGJ voltage drop, that is, the value excluding the Au/Cu_2O and $ZnSnO_3$/AZO voltage drops, 4-probe 20nm thick BGJ devices (10nm Cu_2O and 10 nm $ZnSnO_3$ in configuration c) were made using the same processing sequence. Results show an approximate junction resistance of -> $9x10^{-3}$ Ω–cm^2, dropping about 0.01% of the applied voltage. This resistance is much closer to the observed levels of 10^{-4} to 10^{-5} Ω-cm^2 (*72, 73*).

The optical transmission profile was measured for as-deposited 20nm and 300nm BGJ devices on glass (Figure 6.41d). The 300nm thick devices show substantially greater transmission below the gap compared to the metal-sputtered Cu_2O-based BGJ devices, despite being roughly twice as thick. The improvement is probably due to reduced copper inclusions and copper vacancies which both scatter optically. Predictably the 20nm devices have even better transmission.

Depth profiles were performed on devices after anneals to check for interdiffusion (Figures 6.42a, b, c). In (a) and (c) the level of oxygen in the copper oxide layer more

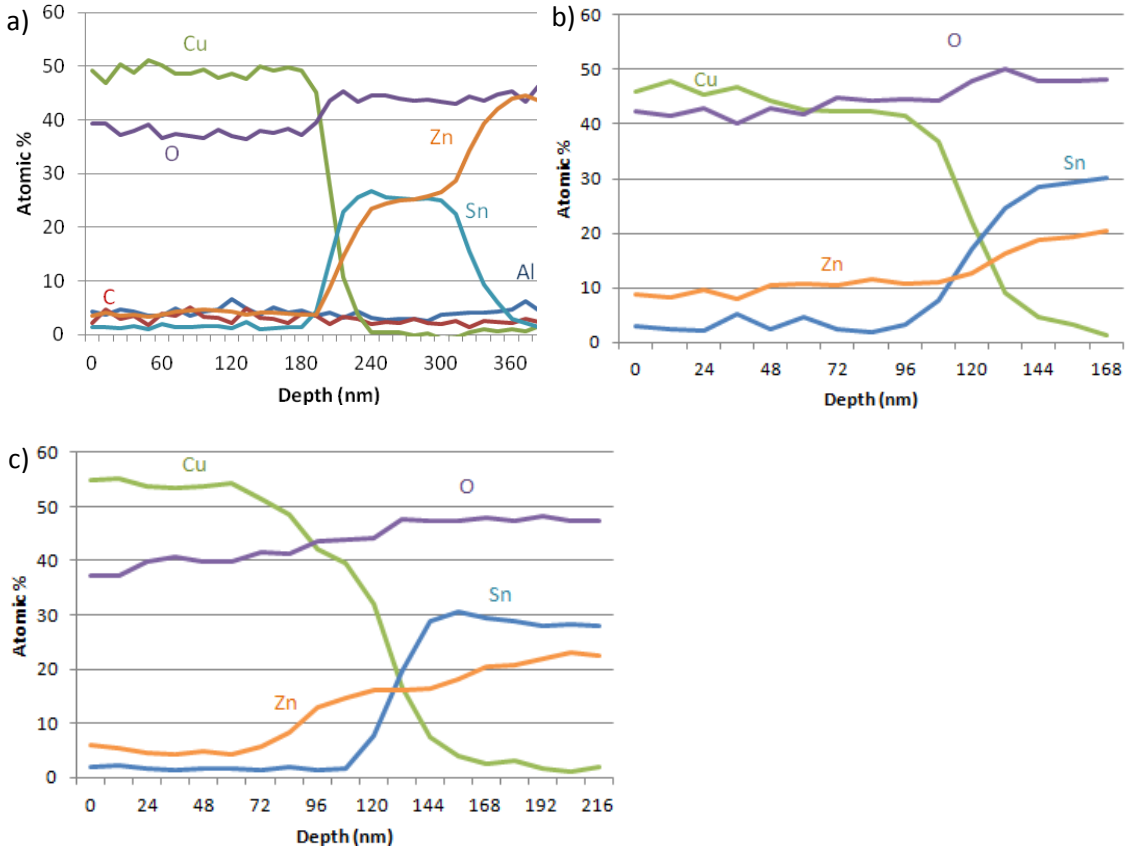

Figure 6.42: In (a) the auger depth profile of 200W 220nm ceramic-sputtered-Cu_2O (with (200)/(111) peak ratio of 2%)-based BGJ devices on ITO/glass annealed at 500^oC for 5min in N_2. In (b) is for similar Cu_2O films (but half as thick) on $ZnSnO_3$ using sputter power of 100W (with (200)/(111) peak ratio of 13%), and in (c) is using sputter power 220W (with (200)/(111) peak ratio of 4.5%).

closely matches that observed for independently deposited Cu_2O films, and stands in contrast to the level of oxygen seen in the metal-sputtered devices. Profile (b) shows both zinc diffusion and the incorporation of more oxygen in the copper oxide layer. The deposition conditions associated with the Cu_2O used in (a) clearly point to a more stable BGJ device at higher annealing temperatures, which may be due to an increased density from a single orientated grain structure along with a lack of copper inclusions. Smaller

grain films tend to have higher effective diffusion coefficients due to the increased density of grain boundaries. However from XRD data in Section 5.3 indicates little difference in grain size between the films. Device (c) has minor zinc-diffusion yet has larger (111) grains than device (a) which showed no diffusion. Another possibility is that the defect concentration (other than grain boundaries) could be different, and these promote diffusion. This has some support for 200W sputtered films from the electrical measurements giving reduced carrier concentration in ceramic sputtered Cu_2O as well as the optical transmission being quite high.

If we use the KPFM measured work function and Hall values for this material from Section 5.3 and $ZnSnO_3$ from 5.1 we get an overlap at the junction of 0.43 eV for as-deposited devices, increasing to 0.61 eV for devices after 5min 500 ^oC anneals. These values are larger than those observed for metal-sputtered Cu_2O-based BGJ devices and yet they show better overall electrical and optical properties. This contradicts the simulations discussed in section 2.6. In these devices no copper inclusions have been observed that could provide a short, and the thicker 220nm copper films make conduction by pinholes unlikely. We believe these junctions make a better overall device for tandem CIGS cells due to their better overall optical, electrical, and thermal properties – except for a reduced band gap which is unnecessary for a tandem solar cell where the top cell will almost certainly have a bandgap less than 2.1 eV and so will absorb most of the light in this part of the spectrum before it reaches the tunnel junction.

6.7 BGJ Devices-$CuAlO_2/ZnSnO_3$

I-V measurements were performed on $CuAlO_2/ZnSnO_3$ BGJ devices in (a) configurations (Figure 6.43a) and showed ohmic profiles with 2-4 Ω-cm^2 as-deposited with a slight Schottky, which is virtually eliminated after anneals and resistance is found increasing up to 3-8 Ω-cm^2 after 5min 300^{o}C RTA and 3-9 Ω-cm^2 after 5min 500^{o}C RTA. The increased variation in contact resistance was a consistent feature producing devices utilizing $CuAlO_2$ films. The justification for the higher contact resistance of the device compared to the copper oxide-based devices may be due increases in the $Au/CuAlO_2$ and/or $ZnSnO_3$/AZO junctions because 4-probe devices in configuration c configuration revealed much lower (see table 9 below) values. The data show a small amount of potential is dropped across the probe/Au contacts but the voltage across the BGJ layers is about $1.9x10^{-5}$, and showing little change with anneal conditions. This is less than .01 % of the applied voltage and shows device performance closer to those observed by Kristijonas et al. (*78*). Another interesting point is the negative phase observed for some of the data, which indicates reactive components in the measurement and may reveal that we are measuring the impedance of the connecting cables and our actual junction impedance is lower.

Devices in (a) configuration were also made on silicon substrates and the data in

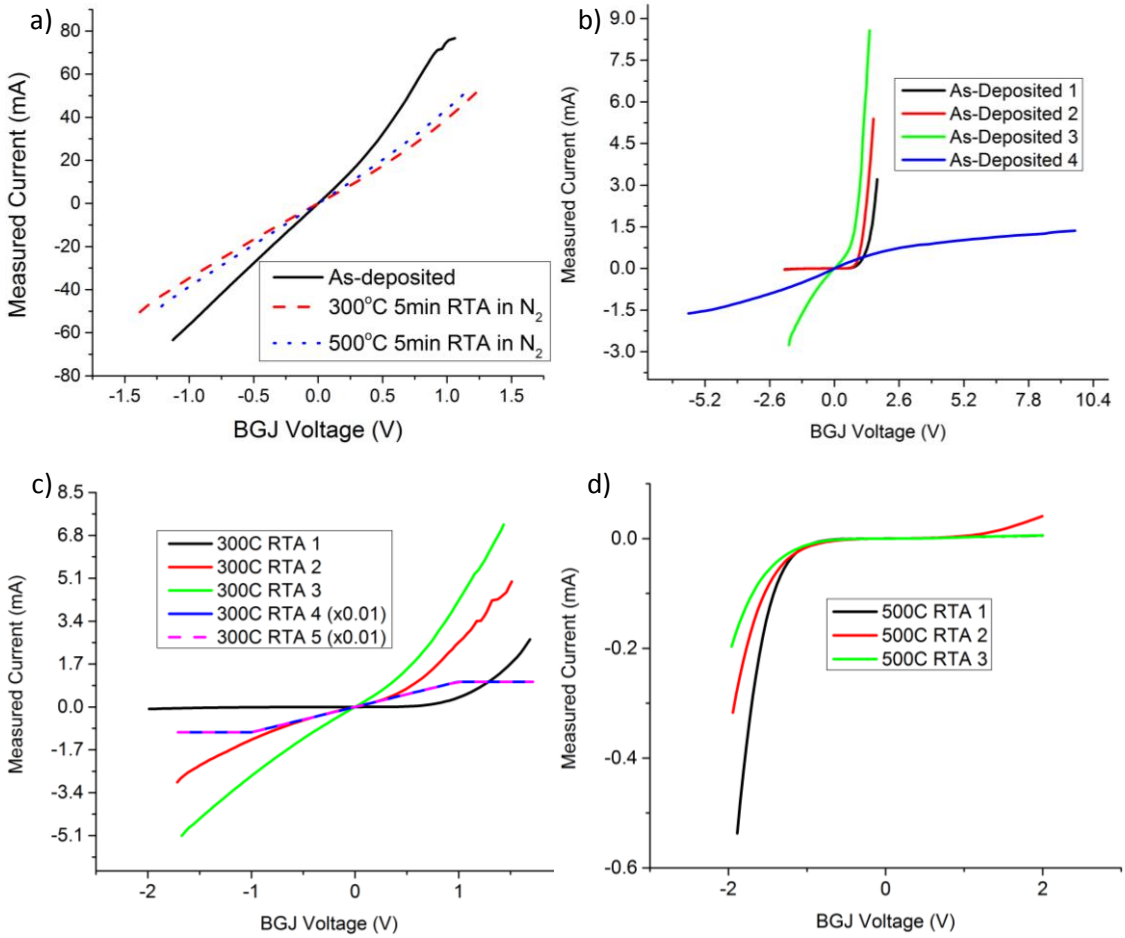

Figure 6.43: (a) The I-V 3-probe results of 80nm ZTO/10nm $CuAlO_2$ devices on ITO/glass. (b), (c), and (d) are the I-V 3-probe results for similar devices on silicon substrates as-deposited, after 300°C, and after 500°C RTA, respectively. Multiple device measurements are shown individually to demonstrate the amount of fluctuation in performance observed for devices using $CuAlO_2$.

(Figure 6.43a, b, and c) show a wide variation in performance.

All devices showed high optical transmission as-deposited (see Figure 6.44) above 90% for 90nm thick as-deposited films rising to near 100% for 20nm thick films at higher post-deposition anneals.

Sample	Applied voltage (V_{rms})	Measured Voltage (V_{rms})			
		Magnitude	Phase	Magnitude	Phase
Probe position	1 & 2	1 & 2	1 & 2	4 & 3	4 & 3
as-deposited	0.3945	0.351+/-.038	-163.450+/-.071	1.92E-05+/-5.27E-06	-2.500+/-115.683
300C 5min	0.47233333	0.463+/-.006	-163.500+/-.000	1.55E-05+/-2.64E-06	145.800+/-18.185
500C 5min	0.3605	0.340+/-.013	16.550+/-.000	1.41E-05+/-1.97E-05	34.950+/-32.598
600C 1+ hrs	0.42075	0.357+/-.028	-73.413+/-103.909	1.75E-04+/-1.75E-04	-14.275+/-107.631

Table 9: 4-probe results in configuration c. The first value is the average among devices of the same sample tested, and the second value is the standard deviation. The amount of error due to lock-in signal measurement in all cases was less than 1%. The measurements from 1 or 2 to 3, and 1 or 2 to 4 did not give meaningful data due to the high lateral resistance through the inner electrode to outer electrode which was found to be in the GΩ range by separate measurements.

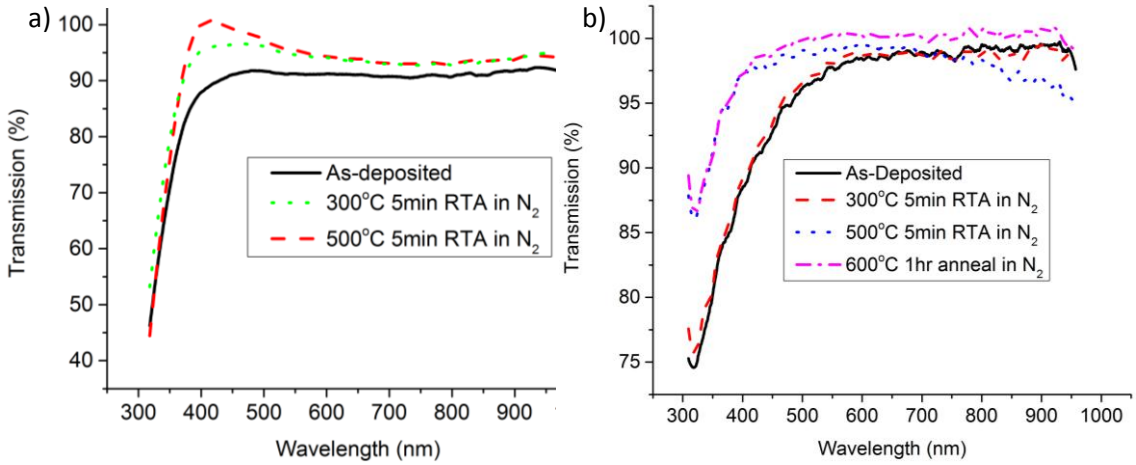

Figure 6.44: (a) Optical transmission for 80nm $ZnSnO_3$/10nm $CuAlO_2$ devices on ITO/glass, and (b) 10nm $ZnSnO_3$/10nm $CuAlO_2$ devices. The data was processed through a 57-point Savitzky–Golay filter. The longer wavelength drop-off in transmission for the 500°C anneal sample in (b) was not observed before and may be due to post-deposition contamination of the sample surface.

Chapter 7: Conclusions

A set of n-type zinc-tin-oxide films has been sputtered. Their properties are consistent with the literature on $ZnSnO_3$, however the band structure measurements have been inconsistent with most showing substantially lower-than-expected electron affinity. The material has shown a wide band gap with low absorption in the visible spectrum, and is amorphous for annealing temperatures up to 600 ^oC. Thus it would be an excellent diffusion barrier for tandem CIGS. The electrical conductivity is on the high end of that observed in literature, likely due to the low mobility as evidenced by the observed VRH. The material has proved very stable in air; however surface passivation is required for accurate electrical measurements. New properties of exceptionally large changes in conductivity were observed as a function of thickness.

A set of p-type films has been reactively sputtered from pure copper with properties consistent with literature on Cu_2O and a valence band as measured by KPFM close to the predicted value of 5 – 5.3 eV. The material shows a small range of sputtering conditions in which a wider-band gap form can be produced with a small sacrifice in optical transmission due to the presence of copper inclusions. A new observation of band gap shift with thickness has been observed but was not investigated further. The material deposits with low crystallinity, but shows grain growth at 300 ^oC, while also showing an increase in valence band position with annealing, which would be useful for band alignment adjustment in a tandem solar cell. Short anneal times in an oxidizing atmosphere had a large influence on the properties.

A version of Cu_2O material sputtered from a ceramic target has also been formed with properties in line with literature on Cu_2O with a valence band similar to metal-sputtered films. The material is on the high end of reported resistivities, however the band gap is close to the theoretical value of 2.1 eV and the optical transmission is near the highest reported. In addition, no copper inclusions could be observed in annealing temperatures up to 500 ^oC for short periods of time. Grain orientation was confirmed to be tied to sputtering power and may help with diffusion resistance of the material.

A second p-type material has been reactively sputtered from a custom $CuAlO_2$ ceramic target with properties consistent with literature on $CuAlO_2$ although it is difficult to confirm the composition. The material deposition rate is very slow and morphology is amorphous. The films' electrical properties vary considerably between depositions and area analyzed but is probably near the high end of those reported with a likely large amount of traps. The material has found to have a wide band gap with very low absorption in the visible spectrum, and is amorphous for annealing temperatures up to 600 ^oC –an excellent diffusion barrier for tandem CIGS.

BGJ devices have been developed by sputtering using the above thin film TCO materials, all of which are abundant and easy-to-manufacture. The band alignment of the n-type and p-type materials is appropriate for a tandem CIGS solar cell, however between the layers our band structure characterization methods project an overlapped interface of as much as 1 eV, depending on anneal conditions. However low-temperature I-V measurements rule out conduction by interface states and conducting AFM measurements show conduction is through most of the material and not through shorts. Furthermore thick devices using 220 nm small-grain Cu_2O make it highly unlikely we have pin-holes

for the top contact metal to deposit into, and depth profile measurements verify no presence of the top contact. We believe we have ample evidence that explains the inaccuracy of our individual material's band structure and that its values are incorrect.

The optimized deposition and post-deposition RTA processing gives a series specific resistivity for all $ZnSnO_3/Cu_2O$ as-deposited devices using gold contacts and ITO/glass substrate below 1 Ω-cm^2 and transmission suitable for solar cells, while further 4-probe measurements revealed specific resistivity in the 10^{-2} Ω-cm^2 range for devices using Cu_2O and around 10^{-4} Ω-cm^2 for devices using $CuAlO_2$ with transmission in the visible spectrum over 95 %. Thinning the devices down to 20 nm lead to transmission increases within the margin of error of our instruments.

Devices showed a strong ohmic I-V profile dependence on the substrate type, with nearly all devices made on ITO/glass giving ohmic profiles. $ZnSnO_3/Cu_2O$ devices deposited on a CIAGS sample showed similar electrical properties. Devices on plain glass were also ohmic but the specific resistivity appeared to be higher. Devices made on silicon showed nonreproducible profiles that were usually Schottky. The influence of substrate morphology may be behind the change in device behavior due to BGJ interface change.

The BGJ devices made using pure copper-sputtered Cu_2O demonstrated stability up to 500 ^oC for short periods of time with minor interdiffusion, while ceramic-sputtered Cu_2O demonstrated increased stability with no detectable interdiffusion. BGJ devices using $ZnSnO_3/CuAO_2$ were stable up to 600 ^oC for over 1 hr as confirmed by optical and electrical measurements.

7.1 Future work

There are other things that could be investigated for the improvement of BGJ devices for tandem solar cells. The first would be to identify the reasons for the drastic change in electrical properties caused by the change in underlying substrate. It may be that unintentional doping occurs of the zinc-stannate layer from the underlying AZO or that the band structure of the n- and/or p-type layers near their interface are influenced by the underlying layer morphology. A second topic would be identifying the cause and effect relating to the stress in copper oxide films and the change in band gap with thickness. A third topic would be attempting to make BGJ devices in reverse order to see if some reaction is occurring during deposition of the p-layer on top of the n-layer which alters the chemical makeup near the interface to produce the necessary band structure. Finally, a study on the influence of the sputter plasma on the BGJ interface could provide some valuable insight.

Bibliography

1. Mindat directory, *Cuprite*, http://www.mindat.org/min-1172.html., Accessed November 2014
2. R. Restori, D. Schwarzenbach, *Acta Cryst* **B**, (1986).
3. Y. Inaguma, M. Yoshida, T. Katsumata, A Polar Oxide ZnSnO3 with a LiNbO3-Type Structure. *J. Am. Chem. Soc.* **130**, 6704 (05/01/2008).
4. A. F. Wells, *Structural Inorganic Chemistry*. (Clarendon Press, Oxford, ed. 3, 1984).
5. D. Kovacheva, K. Petrov, Preparation of crystalline ZnSnO3 from Li2SnO3 by low-temperature ion exchange. *Solid State Ionics* **109**, 327 (6/2/1998).
6. E. A. S. Song, S. Campbell, Metal-oxide broken-gap tunnel junction for copper indium gallium diselenide tandem solar cells. *Sol. Energy Mater. Sol. Cells* **133**, 133 (2/1/2015).
7. F. Biccari, PhD, Sapienza – University of Rome (2009).
8. T. Minami, New n-Type Transparent Conducting Oxides. *MRS Bulletin* **25**, 38 (8/1/2000).
9. Webmineral, *Cuprite*, http://www.webmineral.com/data/Cuprite.shtml., Accessed November 2014
10. J. Robertson, S. J. Clark, Limits to doping in oxides. *Phys. Rev. B: Condens. Matter* **83**, 075205 (02/28/2011).
11. M. Neumann-Spallart, R. Pinto, Growth conditions of CuAlO2 films — Thermodynamic considerations. *Thin Solid Films* **520**, 1299 (12/1/2011).
12. A. Sivasankar Reddy, P. Sreedhara Reddy, S. Uthanna, G. Mohan Rao, Characterization of CuAlO2 films prepared by dc reactive magnetron sputtering. *J. Mater. Sci.: Mater. Electron.* **17**, 615 (08/012006).
13. J. Ma, S. Huang, H. Ma, L. Gai, Preparation and characterization of transparent conducting Zn−Sn−O films deposited on organic substrates at low temperature. *Sci China Ser G: Phy & Ast* **46**, 619 (12/012003).
14. J. H. Ko *et al.*, Transparent and conducting Zn-Sn-O thin films prepared by combinatorial approach. *Appl. Surf. Sci.* **253**, 7398 (7/15/2007).
15. H. Gou *et al.*, Energetic stability, structural transition, and thermodynamic properties of ZnSnO3. *Appl. Phys. Lett.* **98**, 091914 (2011).
16. B. K. Meyer *et al.*, Binary copper oxide semiconductors: From materials towards devices. *Phys. Status Solidi (b)* **249**, 1487 (2012).
17. W. Körner, C. Elsässer, Density-functional theory study of stability and subgap states of crystalline and amorphous Zn–Sn–O. *Thin Solid Films* **555**, 81 (3/31/2014).
18. J. W. Hodby, T. E. Jenkins, C. Schwab, H. Tamura, D. Trivich, Cyclotron resonance of electrons and of holes in cuprous oxide, Cu 2 O. *Journal of Physics C: Solid State Physics* **9**, 1429 (1976).

19. T. Ohyama, T. Ogawa, H. Nakata, Determination of deformation-potential constants of Cu2O by microwave cyclotron resonance. *Phys. Rev. B: Condens. Matter* **56**, 3871 (08/15/1997).
20. U. S. E. I. Administration, *International Energy Outlook*, 2013, http://www.eia.gov/forecasts/ieo/world.cfm, Accessed September 14
21. U. S. D. o. Energy, *U.S. EIA 2013 data report*, 2013, http://www.eia.gov/electricity/data, Accessed September 14
22. B. J. M. De Vries, D. P. Van Vuuren, M. M. Hoogwijk, in *Energy Policy*. (http://www.journals.elsevier.com/energy-policy, 2007), vol. 35, pp. 2590.
23. G. Masson, S. Orlandi, M. Rekinger, "Global Market Outlook for Photovoltaics 2014-2018" (European Photovaltaic Industry Association, http://www.epia.org/news/publications/, 2014).
24. D. Feldman *et al.* (U.S. Department of Engergy, Sunshot, 2013).
25. W. Shockley, H. J. Queisser, Detailed Balance Limit of Efficiency of p-n Junction Solar Cells. *J. Appl. Phys.* **32**, 510 (1961).
26. *Best Research-Cell Efficiencies*, 2014, http://www.nrel.gov/ncpv/images/efficiency_chart.jpg, Accessed October 2014
27. D. Rudmann *et al.*, Sodium incorporation strategies for CIGS growth at different temperatures. *Thin Solid Films* **480–481**, 55 (6/1/2005).
28. A. M. Gabor *et al.*, Band-gap engineering in Cu(In,Ga) Se2 thin films grown from (In,Ga)2Se3 precursors. *Sol. Energy Mater. Sol. Cells* **41–42**, 247 (6/1996).
29. D. Tarrant, J. Ermer, in *Photovoltaic Specialists Conference, 1993., Conference Record of the Twenty Third IEEE*. (1993), pp. 372-378.
30. P. Jackson *et al.*, High quality baseline for high efficiency, Cu(In1−x,Gax)Se2 solar cells. *Progress in Photovoltaics: Research and Applications* **15**, 507 (2007).
31. T. J. Vink, M. A. J. Somers, J. L. C. Daams, A. G. Dirks, Stress, strain, and microstructure of sputter-deposited Mo thin films. *J. Appl. Phys.* **70**, 4301 (1991).
32. A. Chirilă *et al.*, Highly efficient Cu(In,Ga)Se2 solar cells grown on flexible polymer films. *Nat. Mater.* **10**, 857 (9/18/2011).
33. R. R. Potter, Enhanced photocurrent ZnO/CdS/CuInSe2 solar cells. *Solar Cells* **16**, 521 (1/1986).
34. J. Hedstrom *et al.*, in *Photovoltaic Specialists Conference, 1993., Conference Record of the Twenty Third IEEE*. (1993), pp. 364-371.
35. M. Powalla *et al.*, High-efficiency Cu(In,Ga)Se2 cells and modules. *Sol. Energy Mater. Sol. Cells* **119**, 51 (6/13/2013).
36. M. A. Green, K. Emery, Y. Hishikawa, W. Warta, E. D. Dunlop, Solar cell efficiency tables (version 42). *Progress in Photovoltaics: Research and Applications* **21**, 827 (2013).
37. P. Jackson *et al.*, New world record efficiency for Cu(In,Ga)Se2 thin-film solar cells beyond 20%. *Progress in Photovoltaics: Research and Applications* **19**, 894 (2011).
38. I. Repins *et al.*, 19·9%-efficient ZnO/CdS/CuInGaSe2 solar cell with 81·2% fill factor. *Progress in Photovoltaics: Research and Applications* **16**, 235 (2008).
39. M. Nakamura *et al.*, in *Photovoltaic Specialists Conference (PVSC), 2013 IEEE 39th*. (2013), pp. 0849-0852.

40. D. N. Congreve *et al.*, External Quantum Efficiency Above 100% in a Singlet-Exciton-Fission–Based Organic Photovoltaic Cell. *Science* **340**, 334 (4/19/2013).
41. A. S. Brown, M. A. Green, Impurity photovoltaic effect: Fundamental energy conversion efficiency limits. *J. Appl. Phys.* **92**, 1329 (2002).
42. M. Haase, H. Schäfer, Upconverting Nanoparticles. *Angewandte Chemie International Edition* **50**, 5808 (2011).
43. S. V. Boriskina, G. Chen, Exceeding the solar cell Shockley–Queisser limit via thermal up-conversion of low-energy photons. *Opt. Commun.* **314**, 71 (3/1/2014).
44. W. A. Tisdale *et al.*, Hot-Electron Transfer from Semiconductor Nanocrystals. *Science* **328**, 1543 (6/18/2010).
45. M. A. Green, Third generation photovoltaics: Ultra-high conversion efficiency at low cost. *Progress in Photovoltaics: Research and Applications* **9**, 123 (2001).
46. A. Martí, G. L. Araújo, Limiting efficiencies for photovoltaic energy conversion in multigap systems. *Sol. Energy Mater. Sol. Cells* **43**, 203 (1996).
47. H. Lee, M. V. Klein, J. M. Olson, K. C. Hsieh, CuPt-type ordering and dopant effect of In0.5Ga0.5P/GaAs using spectroscopic ellipsometry. *Phys. Rev. B: Condens. Matter* **53**, 4015 (02/15/1996).
48. J. M. Olson, A. Kibbler, S. Kurtz, in *19th IEEE Photovoltaic Specialists Conference*. (1987), pp. 285-288-A.
49. B. K. Tanner, S. J. Miles, G. G. Peterson, R. N. Sacks, Measurement of aluminium concentration in GaAlAs epitaxial layers by double-axis X-ray diffraction. *Mater. Lett.* **7**, 239 (11/1988).
50. D. Jung, C. A. Parker, J. Ramdani, S. M. Bedair, AlGaAs/GaInP heterojunction tunnel diode for cascade solar cell application. *J. Appl. Phys.* **74**, 2090 (1993).
51. S. Hideo, A. Chikao, Y. Akio, Y. Masafumi, Double Heterostructure GaAs Tunnel Junction for a AlGaAs/GaAs Tandem Solar Cell. *Jpn. J. Appl. Phy.* **27**, 269 (1988).
52. B. A. Andersson, Materials availability for large-scale thin-film photovoltaics. *Progress in Photovoltaics: Research and Applications* **8**, 61 (2000).
53. S. Kim *et al.*, Remarkable progress in thin-film silicon solar cells using high-efficiency triple-junction technology. *Sol. Energy Mater. Sol. Cells* **119**, 26 (12/2013).
54. A. Shah *et al.*, Microcrystalline silicon and 'micromorph' tandem solar cells. *Thin Solid Films* **403–404**, 179 (2/1/2002).
55. Y.-T. Lin, C.-H. Chou, F.-C. Chen, C.-W. Chu, C.-S. Hsu, Reduced optical loss in mechanically stacked multi-junction organic solar cells exhibiting complementary absorptions. *Opt. Express* **22**, A481 (3/10/2014).
56. T. Ameri, N. Li, C. J. Brabec, Highly efficient organic tandem solar cells: a follow up review. *Energy & Environmental Science* **6**, 2390 (2013).
57. Stion, *Stion Demonstrates 23.2% Efficiency Thin Film With Simply Better Tandem Technology*, February 27, 2014, http://www.stion.com/stion-demonstrates-23-2-efficiency-thin-film-with-simply-better-tandem-technology, Accessed 8/19/2014
58. G. I. Koleilat, X. Wang, E. H. Sargent, Graded Recombination Layers for Multijunction Photovoltaics. *Nano Lett.* **12**, 3043 (6/13/2012).
59. S. M. Sze, K. K. Ng, *Physics of Semiconductor Devices*. (2007).

60. L. Esaki, New Phenomenon in Narrow Germanium p-n Junctions. *Physical Review* **109**, 603 (01/15/1958).
61. L. D. Landau, E. M. Lifshitz, *Quantum Mechanics*. (Addison-Wesley, Reading, Massichusets, 1958).
62. K. K. Thornber, T. C. McGill, C. A. Mead, The Tunneling Time of an Electron. *J. Appl. Phys.* **38**, 2384 (1967).
63. M. Ohring, *Materials Science of Thin Films: Deposition & Structure*. (Academic Press, ed. 2nd, 2002).
64. T. I. Kamins, J. Manoliu, R. N. Tucker, Diffusion of Impurities in Polycrystalline Silicon. *J. Appl. Phys.* **43**, 83 (1/1972).
65. K. Mochizuki, T. Nakamura, Comparison of Be and C diffusion in heavily doped polycrystalline GaAs. *Appl. Phys. Lett.* **65**, 2066 (10/17/1994).
66. Y.-J. Zhao, C. Persson, S. Lany, A. Zunger, Why can CuInSe2 be readily equilibrium-doped n-type but the wider-gap CuGaSe2 cannot? *Appl. Phys. Lett.* **85**, 5860 (2004).
67. S. B. Zhang, S.-H. Wei, A. Zunger, A phenomenological model for systematization and prediction of doping limits in II–VI and I–III–VI2 compounds. *J. Appl. Phys.* **83**, 3192 (1998).
68. A. Banerjee, J. Yang, T. Glatfelter, K. Hoffman, S. Guha, Experimental study of p layers in ‘‘tunnel’’ junctions for high efficiency amorphous silicon alloy multijunction solar cells and modules. *Appl. Phys. Lett.* **64**, 1517 (1994).
69. J. Löffler *et al.*, Amorphous and ‘micromorph’ silicon tandem cells with high open-circuit voltage. *Sol. Energy Mater. Sol. Cells* **87**, 251 (5/2005).
70. M. P. Mikhailova, A. N. Titkov, Type II heterojunctions in the GaInAsSb/GaSb system. *Semicond. Sci. Technol.* **9**, 1279 (1994).
71. T. Tomizawa, *Numerical simulation of submicron semiconductor devices,*. (Artech house, Boston, 1993).
72. H. Sakaki *et al.*, In1−xGaxAs-GaSb1−yAsy heterojunctions by molecular beam epitaxy. *Appl. Phys. Lett.* **31**, 211 (1977).
73. A. K. Srivastava, J. L. Zyskind, R. M. Lum, B. V. Dutt, J. K. Klingert, Electrical characteristics of InAsSb/GaSb heterojunctions. *Appl. Phys. Lett.* **49**, 41 (1986).
74. G. J. Gualtieri, G. P. Schwartz, R. G. Nuzzo, R. J. Malik, J. F. Walker, Determination of the (100) InAs/GaSb heterojunction valence-band discontinuity by x-ray photoemission core level spectroscopy. *J. Appl. Phys.* **61**, 5337 (1987).
75. D. A. Collins *et al.*, Experimental observation of negative differential resistance from an InAs/GaSb interface. *Appl. Phys. Lett.* **57**, 683 (1990).
76. M. P. Mikhailova, K. D. Moiseev, Y. P. Yakovlev, Interface-induced optical and transport phenomena in type II broken-gap single heterojunctions. *Semicond. Sci. Technol.* **19**, R109 (2004).
77. B. Mattias Borg *et al.*, Diameter reduction of nanowire tunnel heterojunctions using in situ annealing. *Appl. Phys. Lett.* **99**, (2011).
78. V. Kristijonas, T. Marcel, A. Shamsul, A. Markus-Christian, Ultra-low resistive GaSb/InAs tunnel junctions. *Semicond. Sci. Technol.* **26**, 075021 (2011).

79. H. Tanaka, T. Shimakawa, T. Miyata, H. Sato, T. Minami, Electrical and optical properties of TCO–Cu2O heterojunction devices. *Thin Solid Films* **469–470**, 80 (12/22/2004).
80. A. Facchetti, T. J. Marks, *Transparent Electronics: From Synthesis to Applications*. (Wiley, New York, 2010).
81. A. Walsh *et al.*, Nature of the Band Gap of In2O3 Revealed by First-Principles Calculations and X-Ray Spectroscopy. *Phys. Rev. Lett.* **100**, 167402 (04/25/2008).
82. B. Kramm *et al.*, The band alignment of Cu2O/ZnO and Cu2O/GaN heterostructures. *Appl. Phys. Lett.* **100**, (2012).
83. S. O. Koswatta, S. J. Koester, W. Haensch, On the Possibility of Obtaining MOSFET-Like Performance and Sub-60-mV/dec Swing in 1-D Broken-Gap Tunnel Transistors. *Electron Devices, IEEE Transactions on* **57**, 3222 (2010).
84. J. Knoch, J. Appenzeller, Modeling of High-Performance p-Type III-V Heterojunction Tunnel FETs. *Electron Device Letters, IEEE* **31**, 305 (2010).
85. *ISE DESSIS*, Vers. 9.5, 2004, Manual Release, Synopsys, Mountain View
86. C. N. R. Rao, B. Raveau, in *Transition Metal Oxides*. (John Wiley & Sons, Inc., 1998), pp. 4-27.
87. C. N. R. Rao, B. Raveau, in *Transition Metal Oxides*. (John Wiley & Sons, Inc., 1998), pp. 208-213.
88. C. N. R. R. (ed.), *Chemistry of advanced materials*. (Blackwell, Oxford, 1992).
89. C. Kittel, *Introduction to Solid State Physics*. (Wiley, New York, 1977).
90. A. R. West, *Solid State Chemistry and Its Applications*. (Wiley, Chichester, 1985).
91. *Oxide Semiconductors*. Semiconductors and Semimetals (Academic Press, ed. 1, 2013), vol. 88.
92. T. Minami, S. Suzuki, T. Miyata, Transparent conducting impurity-co-doped ZnO:Al thin films prepared by magnetron sputtering. *Thin Solid Films* **398–399**, 53 (11/2001).
93. T. Minami, T. Miyata, Y. Ohtani, T. Kuboi, Effect of thickness on the stability of transparent conducting impurity-doped ZnO thin films in a high humidity environment. *physica status solidi (RRL) – Rapid Research Letters* **1**, R31 (2007).
94. H. Lida, T. Mishuku, A. Ito, K. Kato, Y. Hayashi, Characteristics of SnO2: F films by CMD (chemical mist deposition) method. *Electrical Engineering in Japan* **19**, (1989).
95. H. Kim *et al.*, Effect of film thickness on the properties of indium tin oxide thin films. *J. Appl. Phys.* **88**, 6021 (2000).
96. R. G. Gordon, Criteria for Choosing Transparent Conductors. *MRS Bulletin* **25**, 52 (2000).
97. K. Nomura *et al.*, Thin-Film Transistor Fabricated in Single-Crystalline Transparent Oxide Semiconductor. *Science* **300**, 1269 (5/23/2003).
98. P. Irvin *et al.*, Rewritable nanoscale oxide photodetector. *Nat Photon* **4**, 849 (12/2010).
99. H. Peelaers, E. Kioupakis, C. G. Van de Walle, Fundamental limits on optical transparency of transparent conducting oxides: Free-carrier absorption in SnO2. *Appl. Phys. Lett.* **100**, (2012).

100. M. D. McCluskey, S. J. Jokela, Sources of n-type conductivity in ZnO. *Physica B: Condensed Matter* **401–402**, 355 (12/15/2007).
101. S. E. Harrison, Conductivity and Hall Effect of ZnO at Low Temperatures. *Physical Review* **93**, 52 (01/01/1954).
102. A. R. Hutson, Hall Effect Studies of Doped Zinc Oxide Single Crystals. *Physical Review* **108**, 222 (10/15/1957).
103. S. B. Zhang, S. H. Wei, A. Zunger, Intrinsic n-type versus p-type doping asymmetry and the defect physics of ZnO. *Phys. Rev. B: Condens. Matter* **63**, 075205 (01/31/2001).
104. D. Taïnoff *et al.*, Residual and nitrogen doping of homoepitaxial nonpolar m-plane ZnO films grown by molecular beam epitaxy. *Appl. Phys. Lett.* **98**, (2011).
105. B. G. Svensson *et al.*, Hydrothermally Grown Single-Crystalline Zinc Oxide; Characterization and Modification. *MRS Online Proceedings Library* **1035**, null (2007).
106. I. Hamberg, C. G. Granqvist, K. F. Berggren, B. E. Sernelius, L. Engström, Band-gap widening in heavily Sn-doped In2O3. *Phys. Rev. B: Condens. Matter* **30**, 3240 (09/15/1984).
107. B. E. Sernelius, K. F. Berggren, Z. C. Jin, I. Hamberg, C. G. Granqvist, Band-gap tailoring of ZnO by means of heavy Al doping. *Phys. Rev. B: Condens. Matter* **37**, 10244 (06/15/1988).
108. H. Hosono, Y. Ogo, H. Yanagi, T. Kamiya, Bipolar Conduction in SnO Thin Films. *Electrochem. Solid-State Lett.* **14**, H13 (01/01/2011).
109. B. J. Ingram, G. B. Gonzalez, D. R. Kammler, M. I. Bertoni, T. O. Mason, Chemical and Structural Factors Governing Transparent Conductivity in Oxides. *J Electroceram* **13**, 167 (07/01/2004).
110. H. Kawazoe, H. Yanagi, K. Ueda, H. Hosono, Transparent p-Type Conducting Oxides: Design and Fabrication of p-n Heterojunctions. *MRS Bulletin* **25**, 28 (2000).
111. C. N. R. Rao, B. Raveau, in *Transition Metal Oxides*. (John Wiley & Sons, Inc., 1998), pp. 251.
112. J. B. Varley, A. Janotti, C. Franchini, C. G. Van de Walle, Role of self-trapping in luminescence and p-type conductivity of wide-band-gap oxides. *Phys. Rev. B: Condens. Matter* **85**, 081109 (02/27/2012).
113. H. Hartnagel, A. Dawar, A. Jain, C. Jagadish, Semiconducting transparent thin films, 1995. *Institute of Physics Publishing*, (1995).
114. T. Minami, H. Nanto, S. Takata, Highly conductive and transparent zinc oxide films prepared by rf magnetron sputtering under an applied external magnetic field. *Appl. Phys. Lett.* **41**, 958 (1982).
115. T. Minami, H. Nanto, S. Shooji, S. Takata, The stability of zinc oxide transparent electrodes fabricated by R.F. magnetron sputtering. *Thin Solid Films* **111**, 167 (1/13/1984).
116. S. Takata, T. Minami, H. Nanto, The stability of aluminium-doped ZnO transparent electrodes fabricated by sputtering. *Thin Solid Films* **135**, 183 (1/15/1986).
117. P. Hohenberg, W. Kohn, Inhomogeneous Electron Gas. *Physical Review* **136**, B864 (11/09/1964).

118. W. Kohn, L. J. Sham, Self-Consistent Equations Including Exchange and Correlation Effects. *Physical Review* **140**, A1133 (11/15/1965).
119. A. Janotti, C. G. V. d. Walle, Fundamentals of zinc oxide as a semiconductor. *Reports on Progress in Physics* **72**, 126501 (2009).
120. C. G. Van de Walle, J. Neugebauer, First-principles calculations for defects and impurities: Applications to III-nitrides. *J. Appl. Phys.* **95**, 3851 (2004).
121. R. J. Needs, in *Theory of Defects in Semiconductors*, D. Drabold, S. Estreicher, Eds. (Springer Berlin Heidelberg, 2007), vol. 104, pp. 141-164.
122. A. Janotti, C. G. Van de Walle, LDA + U and hybrid functional calculations for defects in ZnO, SnO2, and TiO2. *Phys. Status Solidi (b)* **248**, 799 (2011).
123. P. Rinke, A. Janotti, M. Scheffler, C. G. Van de Walle, Defect Formation Energies without the Band-Gap Problem: Combining Density-Functional Theory and the GW Approach for the Silicon Self-Interstitial. *Phys. Rev. Lett.* **102**, 026402 (01/14/2009).
124. P. Rinke *et al.*, First-Principles Optical Spectra for F Centers in MgO. *Phys. Rev. Lett.* **108**, 126404 (03/20/2012).
125. A. D. Becke, A new mixing of Hartree–Fock and local density-functional theories. *The Journal of Chemical Physics* **98**, 1372 (1993).
126. A. Alkauskas, P. Broqvist, A. Pasquarello, Defect Energy Levels in Density Functional Calculations: Alignment and Band Gap Problem. *Phys. Rev. Lett.* **101**, 046405 (07/25/2008).
127. P. Deák, B. Aradi, T. Frauenheim, E. Janzén, A. Gali, Accurate defect levels obtained from the HSE06 range-separated hybrid functional. *Phys. Rev. B: Condens. Matter* **81**, 153203 (04/12/2010).
128. H.-P. Komsa, A. Pasquarello, Assessing the accuracy of hybrid functionals in the determination of defect levels: Application to the As antisite in GaAs. *Phys. Rev. B: Condens. Matter* **84**, 075207 (08/11/2011).
129. J. Lægsgaard, K. Stokbro, Hole Trapping at Al impurities in Silica: A Challenge for Density Functional Theories. *Phys. Rev. Lett.* **86**, 2834 (03/26/2001).
130. J. Heyd, G. E. Scuseria, M. Ernzerhof, Hybrid functionals based on a screened Coulomb potential. *The Journal of Chemical Physics* **118**, 8207 (2003).
131. A. V. Krukau, O. A. Vydrov, A. F. Izmaylov, G. E. Scuseria, Influence of the exchange screening parameter on the performance of screened hybrid functionals. *The Journal of chemical physics* **125**, 224106 (12/2006).
132. R. Zallen, *the physics of amorphous solids*. (Wiley-VCH, 1998), pp. 318.
133. M. H. Cohen, D. Turnbull, Metastability of Amorphous Structures. *Nat.* **203**, 964 (08/29/1964).
134. G. S. Cargill, *J. Appl. Phys.* **41**, (1970).
135. G. S. Cargill Iii, in *Solid State Physics*, F. S. Henry Ehrenreich, T. David, Eds. (Academic Press, 1975), vol. 30, pp. 227-320.
136. P. Chaudhari, D. Turnbull, Structure and Properties of Metallic Glasses. *Science* **199**, 11 (01/06/1978).
137. W. H. Zachariasen, THE ATOMIC ARRANGEMENT IN GLASS. *J. Am. Chem. Soc.* **54**, 3841 (10/01/1932).
138. D. A. Drabold, Topics in the theory of amorphous materials. *The European Physical Journal B* **68**, 1 (03/01/2009).

139. H.-L. Chen, Y.-M. Lu, W.-S. Hwang, Characterization of sputtered NiO thin films. *Surf. Coat. Technol.* **198**, 138 (8/1/2005).
140. M. T. Greiner, M. G. Helander, Z.-B. Wang, W.-M. Tang, Z.-H. Lu, Effects of Processing Conditions on the Work Function and Energy-Level Alignment of NiO Thin Films. *The Journal of Physical Chemistry C* **114**, 19777 (11/25/2010).
141. V. Varadarajan, D. P. Norton, J. D. Budai, Phase stability and orientation of SrCu2O2 films grown by pulsed laser deposition. *Thin Solid Films* **488**, 173 (9/22/2005).
142. K. Tonooka, N. Kikuchi, Preparation of transparent CuCrO2:Mg/ZnO p–n junctions by pulsed laser deposition. *Thin Solid Films* **515**, 2415 (12/5/2006).
143. D. J. Singh *et al.*, Optical Properties and Electronic Structure of Spinel ZnRh2O4. *Chem. Mater.* **18**, 2696 (05/01/2006).
144. R. E. Stauber, University of Colorado (2003).
145. K. I. Hagemark, Defect structure of Zn-doped ZnO. *J. Solid State Chem.* **16**, 293 (1/15/1976).
146. F. A. Kroger, *The Chemistry of imperfect Crystals*. (Masterdam, North Holland, 1974).
147. D. C. Look, J. W. Hemsky, J. R. Sizelove, Residual Native Shallow Donor in ZnO. *Phys. Rev. Lett.* **82**, 2552 (03/22/1999).
148. G. Neumann, *Current Topics in Materials Science*. (North Holland Publishing Co, North-Holland, Amsterdam, 1981), vol. 7.
149. A. F. Kohan, G. Ceder, D. Morgan, C. G. Van de Walle, First-principles study of native point defects in ZnO. *Phys. Rev. B: Condens. Matter* **61**, 15019 (06/01/2000).
150. A. Alkauskas, A. Pasquarello, Band-edge problem in the theoretical determination of defect energy levels: The O vacancy in ZnO as a benchmark case. *Phys. Rev. B: Condens. Matter* **84**, 125206 (09/12/2011).
151. S. J. Clark, J. Robertson, S. Lany, A. Zunger, Intrinsic defects in ZnO calculated by screened exchange and hybrid density functionals. *Phys. Rev. B: Condens. Matter* **81**, 115311 (03/10/2010).
152. Ç. Kılıç, A. Zunger, Origins of Coexistence of Conductivity and Transparency in SnO2. *Phys. Rev. Lett.* **88**, 095501 (02/12/2002).
153. J. Robertson, P. W. Peacock, Doping and hydrogen in wide gap oxides. *Thin Solid Films* **445**, 155 (12/15/2003).
154. A. L. Dawar, A. K. Jain, C. Jagadish, *Semiconducting Transparent Thin Films*. (Institute of Physics, London, 1995).
155. S. Major, S. Kumar, M. Bhatnagar, K. L. Chopra, Effect of hydrogen plasma treatment on transparent conducting oxides. *Appl. Phys. Lett.* **49**, 394 (1986).
156. T. Minami, H. Sato, H. Nanto, S. Takata, Heat treatment in hydrogen gas and plasma for transparent conducting oxide films such as ZnO, SnO2 and indium tin oxide. *Thin Solid Films* **176**, 277 (9/15/1989).
157. N. Ogawa, T. Mouri, T. Iwamoto, T. Minami, in *S. Takata Society of Vacuum Coaters 33rd Annual Technical Conf. Proc.* . (1990), vol. 257.
158. O. Kuboi, Degradation of ITO Film in Glow-Discharge Plasma. *Jpn. J. Appl. Phy.* **20**, L783 (1981).

159. J. H. Thomas III, X-ray photoelectron spectroscopy study of hydrogen plasma interactions with a tin oxide surface. *Appl. Phys. Lett.* **42**, 794 (1983).
160. T. Minami, T. Miyata, A. Iwamoto, S. Takata, H. Nanto, Reactive Ion Etching of Transparent Conducting Tin Oxide Films Using Electron Cyclotron Resonance Hydrogen Plasma. *Jpn. J. Appl. Phy.* **27**, L1753 (1988).
161. T. Minami, H. Nanto, S. Takata, Highly Conducting and Transparent SnO 2 Thin Films Prepared by RF Magnetron Sputtering on Low-Temperature Substrates. *Jpn. J. Appl. Phy.* **27**, L287 (1988).
162. L. HL, W. XH., *Functional Materials* **30**, 549 (1999).
163. S. Yu-Sheng, Z. Tian-Shu, Preparation, structure and gas-sensing properties of ultramicro ZnSnO3 powder. *Sensors and Actuators B: Chemical* **12**, 5 (3/15/1993).
164. T. Zhang, Y. Shen, R. Zhang, Ilmenite structure-type β-CdSnO3 used as an ethanol sensing material. *Mater. Lett.* **23**, 69 (4/1995).
165. W. ZC, L. TM, Y. L., *Journal of Chinese Ceramic Society* **32**, 1555 (2004).
166. X.-H. Wu *et al.*, Study on ZnSnO3 sensitive material based on combustible gases. *Solid-State Electron.* **46**, 715 (5/2002).
167. M. D. Aguas, L. Morris, I. P. Parkin, Self-propagating solid state routes to BaSnO3; investigation of gas sensing properties. *J. Mater. Sci.* **37**, 375 (01/01/2002).
168. I. Stambolova, K. Konstantinov, D. Kovacheva, P. Peshev, T. Donchev, Spray Pyrolysis Preparation and Humidity Sensing Characteristics of Spinel Zinc Stannate Thin Films. *J. Solid State Chem.* **128**, 305 (2/1/1997).
169. J. Xu, X. Jia, X. Lou, J. Shen, One-step hydrothermal synthesis and gas sensing property of ZnSnO3 microparticles. *Solid-State Electron.* **50**, 504 (3/2006).
170. B. Geng, C. Fang, F. Zhan, N. Yu, Synthesis of Polyhedral ZnSnO3 Microcrystals with Controlled Exposed Facets and Their Selective Gas-Sensing Properties. *Small* **4**, 1337 (2008).
171. Z. Wang *et al.*, Size-Controlled Synthesis of ZnSnO3 Cubic Crystallites at Low Temperatures and Their HCHO-Sensing Properties. *The Journal of Physical Chemistry C* **114**, 13577 (08/19/2010).
172. M. Inagaki, T. Kuroishi, Y. Yamashita, M. Urata, Syntheses of MSn(OH)6 by coprecipitation and of MSnO3 by thermal decomposition (M = Mg, Co, Zn, Mn, Cd, Ca, Sr, Ba). *Z. Anorg. Allg. Chem.* **527**, 193 (1985).
173. R. Shannon, Revised effective ionic radii and systematic studies of interatomic distances in halides and chalcogenides. *Acta Crystallographica Section A* **32**, 751 (1976).
174. K. S. Valeev, E. I. Medvedovskaya, S. D. Notkina, T. Gosudarst, *Issledovatel. Elektrokeram. Inst.* **4**, (1960).
175. P. Ramamurthy, E. A. Secco, Studies on Metal Hydroxy Compounds. XIII. Thermal Analyses and Decomposition Kinetics of Hydroxystannates of Bivalent Metals. *Can. J. Chem.* **49**, 2813 (09/01/1971).
176. W. Körner, C. Elsässer, Density-functional theory study of stability and subgap states of crystalline and amorphous Zn–Sn–O. *Thin Solid Films*, 6 (2013).

177. T. Minami, H. Sonohara, S. Takata, H. Sato, Highly Transparent and Conductive Zinc-Stannate Thin Films Prepared by RF Magnetron Sputtering. *Jpn. J. Appl. Phy.* **33**, L1693 (1994).
178. T. Minami, S. Tsukada, Y. Minamino, T. Miyata, *Journal of Vacuum Science Technology A* **23**, (2005).
179. Y. Hayashi *et al.*, ZnO–SnO2 transparent conductive films deposited by opposed target sputtering system of ZnO and SnO2 targets. *Vacuum* **74**, 607 (6/7/2004).
180. C.-H. Wang, S.-W. Chen, J.-M. Wu, C.-N. Wei, H.-Y. Bor, Effect of Postdeposition Oxidation and Subsequent Reduction Annealing on Electric and Optical Properties of Amorphous ZnO – SnO2 Transparent Conducting Films. *Electrochem. Solid-State Lett.* **14**, P5 (03/01/2011).
181. T. Minami, S. Takata, H. Sato, H. Sonohara, Properties of transparent zinc-stannate conducting films prepared by radio frequency magnetron sputtering. *J. Vac. Sci. Technol., A* **13**, 1095 (1995).
182. T. Moriga *et al.*, Transparent conducting amorphous Zn-Sn-O films deposited by simultaneous dc sputtering. *J. Vac. Sci. Technol., A* **22**, 1705 (2004).
183. D. Hong, H. Q. Chiang, J. F. Wager, Zinc tin oxide thin-film transistors via reactive sputtering using a metal target. *Journal of Vacuum Science & Technology B* **24**, L23 (2006).
184. Y.-Y. Choi, S. J. Kang, H.-K. Kim, Rapid thermal annealing effect on the characteristics of ZnSnO3 films prepared by RF magnetron sputtering. *Curr. Appl. Phys.* **12, Supplement 4**, S104 (12/20/2012).
185. B. V. Crist, in *Handbook of the Elements and Native Oxides*. (XPS International, Inc., Ames, Iowa, USA, 1999), vol. 1, pp. 658.
186. J. H. Ko *et al.*, Effects of ZnO addition on electrical and structural properties of amorphous SnO2 thin films. *Thin Solid Films* **494**, 42 (1/3/2006).
187. K. Nomura *et al.*, Carrier transport in transparent oxide semiconductor with intrinsic structural randomness probed using single-crystalline InGaO3(ZnO)5 films. *Appl. Phys. Lett.* **85**, 1993 (2004).
188. W. J. Moon, J. H. Yu, G. M. Choi, The CO and H2 gas selectivity of CuO-doped SnO2–ZnO composite gas sensor. *Sensors and Actuators B: Chemical* **87**, 464 (12/20/2002).
189. H.-R. Kim *et al.*, Effects of Hydrogen Doping on the Electrical Properties of Zinc–Tin–Oxide Thin Films. *Jpn. J. Appl. Phy.* **49**, (2010).
190. J. Kulczyk-Malecka, P. J. Kelly, G. West, G. C. B. Clarke, J. A. Ridealgh, Investigations of diffusion behaviour in Al-doped zinc oxide and zinc stannate coatings. *Thin Solid Films* **520**, 1368 (12/30/2011).
191. H. Wang, H. Huang, B. Wang, First-principles study of structural, electronic, and optical properties of ZnSnO3. *Solid State Commun.* **149**, 1849 (11/2009).
192. J. Zhang *et al.*, First-principles study of the ferroelectric and nonlinear optical properties of the LiNbO3-type ZnSnO3. *Phys. Chem. Chem. Phys.* **12**, 9197 (2010).
193. M. Nakayama, M. Nogami, M. Yoshida, T. Katsumata, Y. Inaguma, First-Principles Studies on Novel Polar Oxide ZnSnO3; Pressure-Induced Phase Transition and Electric Properties. *Adv. Mater. (Weinheim, Ger.)* **22**, 2579 (2010).

194. M. K. Jayaraj, K. J. Saji, K. Nomura, T. Kamiya, H. Hosono, Optical and electrical properties of amorphous zinc tin oxide thin films examined for thin film transistor application. *Journal of Vacuum Science & Technology B* **26**, 495 (2008).
195. H. Mizoguchi, P. M. Woodward, Electronic Structure Studies of Main Group Oxides Possessing Edge-Sharing Octahedra: Implications for the Design of Transparent Conducting Oxides. *Chem. Mater.* **16**, 5233 (12/01/2004).
196. M. Miyauchi, Z. Liu, Z.-G. Zhao, S. Anandan, K. Hara, Single crystalline zinc stannate nanoparticles for efficient photo-electrochemical devices. *Chem. Commun. (Cambridge, U. K.)* **46**, 1529 (2010).
197. D. E. Mencer *et al.*, On the surface analysis of copper oxides: the difficulty in detecting Cu3O2. *Vacuum* **77**, 27 (12/17/2004).
198. Mindat directory, *Cuprite*, 2010, Available from: http://www.mindat.org/min-1172.html., Accessed November 2014
199. Webmineral *Cuprite*, 2010, Available from: http://www.webmineral.com/data/Cuprite.shtml, Accessed November 2014
200. J. I. C. f. D. Data., Ed. (1996).
201. A. Werner, H. D. Hochheimer, High-pressure x-ray study of Cu2O and Ag2O. *Phys. Rev. B: Condens. Matter* **25**, 5929 (05/01/1982).
202. R. Mittal, S. L. Chaplot, S. K. Mishra, P. P. Bose, Inelastic neutron scattering and lattice dynamical calculation of negative thermal expansion compounds Cu_{2}O and Ag_{2}O. *Phys. Rev. B: Condens. Matter* **75**, 174303 (05/21/2007).
203. H. Timm, J. Janek, On the Soret effect in binary nonstoichiometric oxides—kinetic demixing of cuprite in a temperature gradient. *Solid State Ionics* **176**, 1131 (3/31/2005).
204. R. Elliott, Symmetry of excitons in Cu2O. *Physical Review* **124**, (1961).
205. J. B. Grun, M. Sieskind, S. É. Nikitine, Spectrophotométrique des spectres continus de Cu2O a diverses temperatures. *J. Phys. Chem. Solids* **19**, (1961).
206. A. Daunois, J. L. Deiss, B. É. Meyer, Spectrophotométrique de l'absorption bleue et violette de Cu2O. *Journal de Physique* **27**, (1966).
207. W. H. Brattain, The Copper Oxide Rectifier. *Reviews of Modern Physics* **23**, 203 (07/01/1951).
208. D. Wu, Q. Zhang, M. Tao, LSDA+U study of cupric oxide: Electronic structure and native point defects. *Phys. Rev. B: Condens. Matter* **73**, 235206 (06/15/2006).
209. H. Raebiger, S. Lany, A. Zunger, Origins of the p-type nature and cation deficiency in Cu2O and related materials. *Phys. Rev. B: Condens. Matter* **76**, 045209 (07/16/2007).
210. A. F. Wright, J. S. Nelson, Theory of the copper vacancy in cuprous oxide. *J. Appl. Phys.* **92**, 5849 (2002).
211. M. Nolan, S. D. Elliott, The p-type conduction mechanism in Cu2O: a first principles study. *Phys. Chem. Chem. Phys.* **8**, 5350 (2006).
212. D. O. Scanlon, G. W. Watson, Understanding the p-type defect chemistry of CuCrO2. *J. Mater. Chem.* **21**, 3655 (2011).
213. M. A. Meki-Jeskari, Density functional study of antiferromagnetic copper oxide. *Modelling And Simulation In Materials Science And Engineering* **14**, (2006).

214. D. O. Scanlon, B. J. Morgan, G. W. Watson, A. Walsh, Acceptor Levels in p-Type Cu2O: Rationalizing Theory and Experiment. *Phys. Rev. Lett.* **103**, 096405 (08/28/2009).
215. C. Carel, M. Mouallem-Bahout, J. Gaudé, Re-examination of the non-stoichiometry and defect structure of copper(II) oxide or tenorite, Cu1±zO or CuO1±ϵ: A short review. *Solid State Ionics* **117**, 47 (2/1/1999).
216. Y. S. Lee, M. T. Winkler, S. C. Siah, R. Brandt, T. Buonassisi, Hall mobility of cuprous oxide thin films deposited by reactive direct-current magnetron sputtering. *Appl. Phys. Lett.* **98**, 192115 (2011).
217. H. L. MicKinzie, M. O'Keeffe, High Temperature Hall Effect in Cuprous Oxide. *Physics letters. A* **24A**, (1967).
218. G. P. Pollack, D. Trivich, Photoelectric properties of cuprous oxide. *J. Appl. Phys.* **46**, 163 (1975).
219. M. Zouaghi, M. Tapiero, J. P. Zielinger, R. Burgraf, Hall mobility and hole density in photoactivated Cu2O single crystals. *Solid State Commun.* **8**, 1823 (11/15/1970).
220. H. Shimada, T. Masumi, Hall Mobility of Positive Holes in Cu2O. *J. Phys. Soc. Jpn.* **58**, 1717 (05/15/1989).
221. D. O. Scanlon, G. W. Watson, Undoped n-Type Cu2O: Fact or Fiction? *The Journal of Physical Chemistry Letters* **1**, 2582 (09/02/2010).
222. F. Biccari, C. Malerba, A. Mittiga, Chlorine doping of Cu2O. *Sol. Energy Mater. Sol. Cells* **94**, 1947 (11/2010).
223. K. Akimoto *et al.*, Thin film deposition of Cu2O and application for solar cells. *Solar Energy* **80**, 715 (6/2006).
224. S. Ishizuka, S. Kato, T. Maruyama, K. Akimoto, Nitrogen Doping into Cu 2 O Thin Films Deposited by Reactive Radio-Frequency Magnetron Sputtering. *Jpn. J. Appl. Phy.* **40**, 2765 (2001).
225. S. Ishizuka, S. Kato, Y. Okamoto, K. Akimoto, Hydrogen treatment for polycrystalline nitrogen-doped Cu2O thin film. *J. Cryst. Growth* **237–239, Part 1**, 616 (4/2002).
226. D. O. Scanlon, G. W. Watson, Uncovering the Complex Behavior of Hydrogen in Cu2O. *Phys. Rev. Lett.* **106**, 186403 (05/03/2011).
227. F. L. Weichman, Some Rationale for the Unusual Behavior of the Dielectric Constant of Cu2O. *Can. J. Phys.* **51**, 680 (03/15/1973).
228. F. L. Weichman, J. M. Reyes, Optical absorption of Cu2O in the near infrared and the role of metallic inclusions. *Can. J. Phys.* **58**, 325 (03/01/1980).
229. A. A. Berezin, F. L. Weichman, Photovoltaic effect in cuprous oxide-copper junctions in relation to the optical absorption spectrum of cuprous oxide. *Solid State Commun.* **37**, 157 (1/1981).
230. F. L. Weichman, Internal Schottky barriers in semiconductors. *Can. J. Phys.* **60**, 269 (03/01/1982).
231. G. J. Wang, F. L. Weichman, The temperature dependence of the electrical conductivity and switching phenomena in Cu2O single crystals. *Can. J. Phys.* **60**, 1648 (11/01/1982).

232. C. K. Teh, F. L. Weichman, Photoluminescence and optical absorption studies of the effects of heat treatment on cuprous oxide. *Can. J. Phys.* **61**, 1423 (10/01/1983).
233. D. G. Hughes, S. Mohanty, L. Pandey, F. L. Weichman, Detection of copper precipitates in Cu2O by NMR. *Can. J. Phys.* **63**, 397 (03/01/1985).
234. R. Kuzel, C. D. Cann, S. S. Sheinin, F. L. Weichman, Hole mobility in Cu2O. II. Scattering by defects. *Canadian journal of physics Revue canadienne de physique* **48**, (1970).
235. T. Ito, H. Yamaguchi, K. Okabe, T. Masumi, Single-crystal growth and characterization of Cu2O and CuO. *J. Mater. Sci.* **33**, 3555 (07/01/1998).
236. P. E. d. Jong, D. Vanmaekelbergh, J. J. Kelly, Cu2O: Electrodeposition and Characterization. *Chem. Mater.* **11**, (1999).
237. W.-Y. Yang, W.-G. Kim, S.-W. Rhee, Radio frequency sputter deposition of single phase cuprous oxide using Cu2O as a target material and its resistive switching properties. *Thin Solid Films* **517**, 967 (11/28/2008).
238. J. F. Pierson, A. Thobor-Keck, A. Billard, Cuprite, paramelaconite and tenorite films deposited by reactive magnetron sputtering. *Appl. Surf. Sci.* **210**, 359 (4/15/2003).
239. A. v. Richthofen, R. Domnick, R. Cremer, Preparation of cuprite (Cu2O), paramelaconite (Cu32+Cu21+O4) and tenorite (CuO) with magnetron sputtering ion plating: characterization by EPMA, XRD, HEED and SEM. *Fresenius. J. Anal. Chem.* **358**, 312 (05/01/1997).
240. Z. G. Yin *et al.*, Two-dimensional growth of continuous Cu2O thin films by magnetron sputtering. *Appl. Phys. Lett.* **86**, 061901 (2005).
241. A. Sivasankar Reddy, P. Sreedhara Reddy, S. Uthanna, G. Venkata Rao, A. Klein, Effect of substrate temperature on the physical properties of dc magnetron sputtered Cu2O films. *phys. status solidi (a)* **203**, 844 (2006).
242. T. M. Shogo Ishizuka, Katsuhiro Akimoto, Thin-Film Deposition of Cu2O by Reactive Radio-Frequency Magnetron Sputtering. *Jpn. J. Appl. Phy.* **39**, (2000).
243. C. L. Azanza Ricardo *et al.*, Structural properties of RF-magnetron sputtered Cu2O thin films. *Thin Solid Films* **520**, 280 (10/31/2011).
244. H. Zhu *et al.*, Cu2O thin films deposited by reactive direct current magnetron sputtering. *Thin Solid Films* **517**, 5700 (8/3/2009).
245. F. M. Li *et al.*, Low temperature (<100°C) deposited P-type cuprous oxide thin films: Importance of controlled oxygen and deposition energy. *Thin Solid Films* **520**, 1278 (12/1/2011).
246. H.-C. Lu, C.-L. Chu, C.-Y. Lai, Y.-H. Wang, Property variations of direct-current reactive magnetron sputtered copper oxide thin films deposited at different oxygen partial pressures. *Thin Solid Films* **517**, 4408 (6/1/2009).
247. B.-b. Li, J.-x. Zhu, Z.-f. Chen, H.-l. Shen, J. Luo, Effect of oxygen content on structural and optical properties of single Cu2O film by reactive magnetron sputtering method. *J. Shanghai Jiaotong Univ. (Sci.)* **17**, 523 (10/01/2012).
248. A. S. Reddy, S. Uthanna, P. S. Reddy, Properties of dc magnetron sputtered Cu2O films prepared at different sputtering pressures. *Appl. Surf. Sci.* **253**, 5287 (4/15/2007).

249. A. S. Reddy *et al.*, Effect of sputtering power on the physical properties of dc magnetron sputtered copper oxide thin films. *Mater. Chem. Phys.* **110**, 397 (8/15/2008).
250. A. Parretta *et al.*, Electrical and Optical Properties of Copper Oxide Films Prepared by Reactive RF Magnetron Sputtering. *phys. status solidi (a)* **155**, 399 (1996).
251. T. Ohwaki, Y. Taga, Changes in composition and deposition rates in the reactive sputtering of copper, titanium, and yttrium exposed to oxygen. *Appl. Phys. Lett.* **54**, 1664 (1989).
252. S. Noda, H. Shima, H. Akinaga, Cu 2 O/ZnO Heterojunction Solar Cells Fabricated by Magnetron-Sputter Deposition Method Films Using Sintered Ceramics Targets. *Journal of Physics: Conference Series* **433**, 012027 (2013).
253. K. Matsuzaki *et al.*, Effects of post-annealing on (110) Cu2O epitaxial films and origin of low mobility in Cu2O thin-film transistor. *phys. status solidi (a)* **206**, 2192 (2009).
254. K. Borgohain, N. Murase, S. Mahamuni, Synthesis and properties of Cu2O quantum particles. *J. Appl. Phys.* **92**, 1292 (2002).
255. M. T. Clavaguera-Mora, J. L. Touron, J. Rodríguez-Viejo, N. Clavaguera, Thermodynamic description of the Cu・O system. *J. Alloys Compd.* **377**, 8 (9/8/2004).
256. M. Hansen, K. Anderko, *Constitution of Binary alloys*. (Genium Publishing Corporation, ed. 2, 1988).
257. L. Schramm, G. Behr, W. Löser, K. Wetzig, Thermodynamic reassessment of the Cu-O phase diagram. *J. Phase Equilib. Diffus.* **26**, 605 (12/01/2005).
258. J. Xue, R. Dieckmann, The high-temperature phase diagram of the Cu–O system in stability region of cuprous oxide (Cu2−_O). *High Temperatures–High Pressures* **24**, (1992).
259. L. Tertian, D. Hokim, J. P. Rivière, Transformations in thin foils of cuprous oxide as observed in an electron microscope. *J. Phys. France* **39**, 1135 (1978).
260. R. A. Yund, G. Kullerud, Stable mineral assemblages of anhydrous copper and iron oxides. *The American Mineralogist* **49** (1964).
261. N. L. Peterson, C. L. Wiley, Diffusion and point defects in Cu2O. *J. Phys. Chem. Solids* **45**, (1984).
262. W. J. Moore, Y. Ebisuzaki, J. A. Sluss, Exchange and Diffusion of Oxygen in Crystalline Cuprous Oxide. *The Journal of Physical Chemistry* **62**, 1438 (11/01/1958).
263. W. J. Moore, B. Selikson, The Diffusion of Copper in Cuprous Oxide. *The Journal of Chemical Physics* **19**, 1539 (1951).
264. F. Perinet, S. Barbezat, C. Monty, TRANSPORT IN OXIDES New investigation of oxygen self-diffusion in Cu2O. *J. Phys. Colloques* **41**, C6 (1980).
265. F. Perinet, S. Barbezat, J. Philibert, Mechanism of Oxygen Self-Diffusion in Cu2O. *Synthetic Materials for Electronics (Materials Science Monographs)* **10**, (1982).
266. F. Perinet, J. Le Duigou, C. Monty, *Oxygen diffusion in volume and in grain-boundaries of Cu2−xO" in Non Stoichiometric Compounds: Surface, Grain*

Boundaries and Structural Defects. NATO Science Series C (Kluwer Academic Publishers (Springer), 1989).
267. N. L. Peterson, C. L. Wiley, Diffusion and point defects in Cu2O. *J. Phys. Chem. Solids* **45**, 281 (1984).
268. Z. Grzesik, M. Migdalska, S. Mrowec, Chemical diffusion in non-stoichiometric cuprous oxide. *J. Phys. Chem. Solids* **69**, 928 (4/2008).
269. L.-C. Chen, C.-C. Wang, S.-W. Lu, Annealing Effects of Sputtered Cu2O Nanocolumns on ZnO-Coated Glass Substrate for Solar Cell Applications. *Journal of Nanomaterials* **2013**, 6 (2013).
270. X. Nie, S.-H. Wei, S. B. Zhang, First-principles study of transparent p-type conductive SrCu2O2 and related compounds. *Phys. Rev. B: Condens. Matter* **65**, 075111 (01/31/2002).
271. J. P. Hu *et al.*, On-site interband excitations in resonant inelastic x-ray scattering from Cu2O. *Phys. Rev. B: Condens. Matter* **77**, 155115 (04/15/2008).
272. A. Önsten *et al.*, Probing the valence band structure of Cu2O using high-energy angle-resolved photoelectron spectroscopy. *Phys. Rev. B: Condens. Matter* **76**, 115127 (09/26/2007).
273. L. Kleinman, K. Mednick, Self-consistent energy bands of Cu2O. *Phys. Rev. B: Condens. Matter* **21**, 1549 (02/15/1980).
274. L. C. Olsen, R. C. Bohara, M. W. Urie, Explanation for low-efficiency Cu2O Schottky-barrier solar cells. *Appl. Phys. Lett.* **34**, 47 (1979).
275. J. P. Dahl, A. C. Switendick, Energy bands in cuprous oxide. *J. Phys. Chem. Solids* **27**, 931 (6/1966).
276. D. O. Scanlon, B. J. Morgan, G. W. Watson, Modeling the polaronic nature of p-type defects in Cu2O: The failure of GGA and GGA+U. *The Journal of Chemical Physics* **131**, (2009).
277. R. Laskowski, P. Blaha, K. Schwarz, Charge distribution and chemical bonding in Cu2O. *Phys. Rev. B: Condens. Matter* **67**, 075102 (02/05/2003).
278. F. Tran, P. Blaha, Implementation of screened hybrid functionals based on the Yukawa potential within the LAPW basis set. *Phys. Rev. B: Condens. Matter* **83**, 235118 (06/09/2011).
279. A. Filippetti, V. Fiorentini, Coexistence of ionic and metallic bonding in noble-metal oxides. *Phys. Rev. B: Condens. Matter* **72**, 035128 (07/19/2005).
280. F. Bruneval *et al.*, Exchange and Correlation Effects in Electronic Excitations of Cu2O. *Phys. Rev. Lett.* **97**, 267601 (12/28/2006).
281. M. van Schilfgaarde, T. Kotani, S. Faleev, Quasiparticle Self-Consistent GW Theory. *Phys. Rev. Lett.* **96**, 226402 (06/06/2006).
282. T. Kotani, M. van Schilfgaarde, S. V. Faleev, Quasiparticle self-consistent GW method: A basis for the independent-particle approximation. *Phys. Rev. B: Condens. Matter* **76**, 165106 (10/03/2007).
283. J. Paier, M. Marsman, G. Kresse, Dielectric properties and excitons for extended systems from hybrid functionals. *Phys. Rev. B: Condens. Matter* **78**, 121201 (09/15/2008).
284. P. Cortona, M. Mebarki, Cu2O behavior under pressure: an ab initio study. *J. Phy. Codens. Mat.* **23**, 045502 (2011).

285. V. N. Dobrovol'skii, Y. I. Gritsenko, Use of the Hall current for investigation of carrier scattering in semiconductors. *Soviet Physics - Solid State* **4**, 2760 (1963).
286. M. T. Greiner, L. Chai, M. G. Helander, W.-M. Tang, Z.-H. Lu, Transition Metal Oxide Work Functions: The Influence of Cation Oxidation State and Oxygen Vacancies. *Adv. Funct. Mater.* **22**, 4557 (2012).
287. H. M. Wei, H. B. Gong, L. Chen, M. Zi, B. Q. Cao, Photovoltaic Efficiency Enhancement of Cu2O Solar Cells Achieved by Controlling Homojunction Orientation and Surface Microstructure. *The Journal of Physical Chemistry C* **116**, 10510 (05/17/2012).
288. C. M. McShane, W. P. Siripala, K.-S. Choi, Effect of Junction Morphology on the Performance of Polycrystalline Cu2O Homojunction Solar Cells. *The Journal of Physical Chemistry Letters* **1**, 2666 (09/16/2010).
289. P. Poulopoulos *et al.*, Intense Quantum Confinement Effects in Cu2O Thin Films. *The Journal of Physical Chemistry C* **115**, 14839 (08/04/2011).
290. Z. Zhu, A. Zhang, Y. He, G. Ouyang, G. Yang, Interface relaxation and band gap shift in epitaxial layers. *AIP Advances* **2**, (2012).
291. H. Kawazoe *et al.*, P-type electrical conduction in transparent thin films of CuAlO2. *Nat.* **389**, 939 (10/30/1997).
292. C. Friedel, Comptes Rendus. *Académie des Sciences Paris* **77**, (1873).
293. B. J. Ingram, T. O. Mason, R. Asahi, K. T. Park, A. J. Freeman, Electronic structure and small polaron hole transport of copper aluminate. *Phys. Rev. B: Condens. Matter* **64**, 155114 (09/28/2001).
294. A. Buljan, P. Alemany, E. Ruiz, Electronic Structure and Bonding in CuMO2 (M = Al, Ga, Y) Delafossite-Type Oxides: An Ab Initio Study. *The Journal of Physical Chemistry B* **103**, 8060 (09/01/1999).
295. J. Tate *et al.*, Origin of p-type conduction in single-crystal CuAlO2. *Phys. Rev. B: Condens. Matter* **80**, 165206 (10/16/2009).
296. J. Li, A. W. Sleight, C. Y. Jones, B. H. Toby, Trends in negative thermal expansion behavior for AMO2 (A=Cu or Ag; M=Al, Sc, In, or La) compounds with the delafossite structure. *J. Solid State Chem.* **178**, 285 (1/2005).
297. D. B. Rogers, R. D. Shannon, C. T. Prewitt, J. L. Gilson, Opto-electronic properties of Delafossites. *Inorg. Chem.* **10**, (1971).
298. T. Ishiguro, A. Kitazawa, N. Mizutani, M. Kato, Single-crystal growth and crystal structure refinement of CuAlO2. *J. Solid State Chem.* **40**, 170 (11/15/1981).
299. F. A. Benko, F. P. Koffyberg, Opto-electronic properties of CuAlO2. *J. Phys. Chem. Solids* **45**, 57 (1984).
300. Y.-C. Liou, U.-R. Lee, Non-calcining process for CuAlO2 and CuAl0.9Ca0.1O2 ceramics. *J. Alloys Compd.* **467**, 496 (1/7/2009).
301. Y. C. Liou, W. C. Tsai, W. Y. Lin, Y. R. Lee, Synthesis of Ca3Co4O9 and CuAlO2 Ceramics of the Thermoelectric Application Using A Reaction-Sintering Process. *Journal of The Australian Ceramics Society* **44**, 17 (2008).
302. S. K. Misra, A. C. D. Chaklader, The System Copper Oxide—Alumina. *J. Am. Ceram. Soc.* **46**, 509 (1963).
303. K. T. Jacob, C. B. Alcock, Thermodynamics of CuAlO2 and CuAl2O4 and Phase Equilibria in the System Cu2O-CuO-Al2O3. *J. Am. Ceram. Soc.* **58**, 192 (1975).

304. R. E. Stauber, J. D. Perkins, P. A. Parilla, D. S. Ginley, Thin Film Growth of Transparent p-type CuAlO2. *Electrochem. Solid-State Lett.* **2**, 654 (12/01/1999).
305. A. N. Banerjee, C. K. Ghosh, K. K. Chattopadhyay, Effect of excess oxygen on the electrical properties of transparent p-type conducting CuAlO2+x thin films. *Sol. Energy Mater. Sol. Cells* **89**, 75 (10/14/2005).
306. G. Thomas, Materials science: Invisible circuits. *Nat.* **389**, 907 (10/30/print1997).
307. M. S. Lee, T. Y. Kim, D. Kim, Anisotropic electrical conductivity of delafossite-type CuAlO2 laminar crystal. *Appl. Phys. Lett.* **79**, 2028 (2001).
308. R. Nagarajan *et al.*, p-Type conductivity in the delafossite structure. *International Journal of Inorganic Materials* **3**, 265 (6/2001).
309. H. Yanagi *et al.*, Electronic structure and optoelectronic properties of transparent p-type conducting CuAlO2. *J. Appl. Phys.* **88**, 4159 (2000).
310. H. F. Jiang *et al.*, Effects of Mg substitution on the structural, optical, and electrical properties of CuAlO2 thin films. *J. Alloys Compd.* **509**, 1768 (2/3/2011).
311. P. Dong, M. Zhangz, G. Dong, X. Zhao, H. Yan, The Optical and Electrical Properties of Zn-Doped CuAlO2 Thin Films Deposited by RF Magnetron Sputtering. *Journal of Electrochemical Society* **155**, H319 (2008).
312. W. Lan *et al.*, Annealing effect on the structural, optical, and electrical properties of CuAlO2 films deposited by magnetron sputtering. *J. Mater. Sci.* **44**, 1594 (03/01/2009).
313. W. Lan, M. Zhang, G. Dong, Y. Wang, H. Yan, Improvement of CuAlO2 thin film electrical conduction by the anisotropic conductivity. *J. Mater. Res.* **22**, 3338 (2007).
314. W. Lan *et al.*, The effect of oxygen on the properties of transparent conducting Cu–Al–O thin films deposited by rf magnetron sputtering. *Mater. Science and Engineering: B* **139**, 155 (5/15/2007).
315. N. Tsuboi *et al.*, Delafossite CuAlO2 films prepared by reactive sputtering using Cu and Al targets. *J. Phys. Chem. Solids* **64**, 1671 (9/2003).
316. N. Tsuboi *et al.*, Composition and Structure Control of Cu–Al–O Films Prepared by Reactive Sputtering and Annealing. *Jpn. J. Appl. Phy.* **46**, 351 (2007).
317. N. Tsuboi *et al.*, Characterization of CuAlO 2 Thin Films Prepared on Sapphire Substrates by Reactive Sputtering and Annealing. *Jpn. J. Appl. Phy.* **47**, 592 (2008).
318. A. S. Reddy, H.-H. Park, G. M. Rao, S. Uthanna, P. S. Reddy, Effect of substrate temperature on the physical properties of dc magnetron sputtered CuAlO2 films. *J. Alloys Compd.* **474**, 401 (4/17/2009).
319. A. N. Banerjee, S. Kundoo, K. K. Chattopadhyay, Synthesis and characterization of p-type transparent conducting CuAlO2 thin film by DC sputtering. *Thin Solid Films* **440**, 5 (9/1/2003).
320. A. N. Banerjee, R. Maity, K. K. Chattopadhyay, Preparation of p-type transparent conducting CuAlO2 thin films by reactive DC sputtering. *Mater. Lett.* **58**, 10 (1/2004).
321. A. N. Banerjee, K. K. Chattopadhyay, Size-dependent optical properties of sputter-deposited nanocrystalline p-type CuAlO2 thin films. *J. Appl. Phys.* **97**, 084308 (2005).

322. A. N. Banerjee, C. K. Ghosh, S. Das, K. K. Chattopadhyay, Electro-optical characteristics and field-emission properties of reactive DC-sputtered p-CuAlO2+x thin films. *Physica B: Condensed Matter* **370**, 264 (12/15/2005).
323. B. L. Stevens *et al.*, DC reactive magnetron sputtering, annealing, and characterization of CuAlO2 thin films. *J. Vac. Sci. Technol., A* **29**, 011018 (2011).
324. C.-T. Su, H.-Y. Lee, B.-K. Wu, M.-Y. Chern, Development of phase-pure CuAlO2 thin films grown on c-plane sapphire substrates prepared by RF sputtering. *J. Cryst. Growth* **328**, 25 (8/1/2011).
325. C. H. Ong, H. Gong, Effects of aluminum on the properties of p-type Cu–Al–O transparent oxide semiconductor prepared by reactive co-sputtering. *Thin Solid Films* **445**, 299 (12/15/2003).
326. P.-H. Hsieh, Y.-M. Lu, W.-S. Hwang, J.-J. Yeh, W.-L. Jang, Effect of Al content on electrical conductivity and transparency of P-type Cu-Al-O thin film. *Surf. Coat. Technol.* **205, Supplement 1**, S206 (12/25/2010).
327. Y. M. Lu *et al.*, RF reactive sputter deposition and characterization of transparent CuAlO2 thin films. *phys. status solidi (c)* **3**, 2895 (2006).
328. S. Takahata, T. Imao, H. Nakanishi, M. Sugiyama, S. F. Chichibu, Helicon-wave-excited plasma sputtering deposition of CuAlO2 thin films. *phys. status solidi (c)* **5**, 3101 (2008).
329. J. Li *et al.*, Optical and Wetting Properties of CuAlO2 Films Prepared by Radio Frequency Magnetron Sputtering. *J. Am. Ceram. Soc.* **95**, 431 (2012).
330. E. M. Alkoy, P. J. Kelly, The structure and properties of copper oxide and copper aluminium oxide coatings prepared by pulsed magnetron sputtering of powder targets. *Vacuum* **79**, 221 (8/19/2005).
331. Z. Q. Yao *et al.*, Energy band engineering and controlled p-type conductivity of CuAlO2 thin films by nonisovalent Cu-O alloying. *Appl. Phys. Lett.* **100**, (2012).
332. K. Sreenivas, M. Sayer, Characterization of Pb(Zr,Ti)O3 thin films deposited from multielement metal targets. *J. Appl. Phys.* **64**, 1484 (1988).
333. D. J. Aston *et al.*, High-resolution x-ray spectroscopic study of the electronic structure of the prototypical p-type transparent conducting oxide CuAlO2. *Phys. Rev. B: Condens. Matter* **72**, 195115 (11/28/2005).
334. J. Pellicer-Porres *et al.*, On the band gap of CuAlO2 delafossite. *Appl. Phys. Lett.* **88**, 181904 (2006).
335. J. Robertson, P. W. Peacock, M. D. Towler, R. Needs, Electronic structure of p-type conducting transparent oxides. *Thin Solid Films* **411**, 96 (5/22/2002).
336. M. Nolan, Defects in Cu2O, CuAlO2 and SrCu2O2 transparent conducting oxides. *Thin Solid Films* **516**, 8130 (9/30/2008).
337. R. Laskowski, N. E. Christensen, P. Blaha, B. Palanivel, Strong excitonic effects in CuAlO2 delafossite transparent conductive oxides. *Phys. Rev. B: Condens. Matter* **79**, 165209 (04/27/2009).
338. D. Huang, Y. Pan, First-principles calculations of intrinsic defects in the p-type semiconductor CuAlO2. *Can. J. Phys.* **88**, 927 (12/01/2010).
339. D. O. Scanlon, G. W. Watson, Conductivity Limits in CuAlO2 from Screened-Hybrid Density Functional Theory. *The Journal of Physical Chemistry Letters* **1**, 3195 (11/04/2010).

340. N. E. Christensen *et al.*, Electronic properties of 3R-CuAlO2 under pressure: Three theoretical approaches. *Phys. Rev. B: Condens. Matter* **81**, 045203 (01/14/2010).
341. Q.-J. Liu, Z.-T. Liu, L.-P. Feng, Theoretical calculations of mechanical, electronic, chemical bonding and optical properties of delafossite CuAlO2. *Physica B: Condensed Matter* **405**, 2028 (4/15/2010).
342. F. Trani, J. Vidal, S. Botti, M. A. L. Marques, Band structures of delafossite transparent conductive oxides from a self-consistent GW approach. *Phys. Rev. B: Condens. Matter* **82**, 085115 (08/19/2010).
343. P. Poopanya, A. Yangthaisong, C. Rattanapun, A. Wichainchai, Theoretical Study of Electronic Structure and Thermoelectric Properties of Doped CuAlO2. *J. Electron. Mater.* **40**, 987 (05/01/2011).
344. Y. Kumekawa *et al.*, Evaluation of thermodynamic and kinetic stability of CuAlO2 and CuGaO2. *J. Therm. Anal. Calorim.* **99**, 57 (01/01/2010).
345. R. Brahimi, Y. Bessekhouad, A. Bouguelia, M. Trari, CuAlO2/TiO2 heterojunction applied to visible light H2 production. *Journal of Photochemistry and Photobiology A: Chemistry* **186**, 242 (2/25/2007).
346. M. Fang *et al.*, Optical properties of p-type CuAlO2 thin film grown by rf magnetron sputtering. *Appl. Surf. Sci.* **257**, 8330 (8/1/2011).
347. C. J. Overbeck, Color in films of sputtered tin. *Journal of the Optical Society of America* **23**, (1933).
348. G.Glockler, *The Electrochemistry of Gases and other Dielectrics*. (John Wiley and Sons, Inc., New York, 1939).
349. N. S. J. Braithwaite, Introduction to gas discharges. *Plasma Sources Science and Technology* **9**, 517 (2000).
350. A. J. v. Roosmalen, J. A. G. Baggerman, S. J. H. Brader, *Dry etching for VLSI*. (Springer, ed. 1st, 1991).
351. J. Hisek, PhD Thesis, University of Salford (2005).
352. F. Paschen, Ueber die zum Funkenübergang in Luft, Wasserstoff und Kohlensäure bei verschiedenen Drucken erforderliche Potentialdifferenz. *Annalen der Physik* **273**, 69 (1889).
353. H. R. S. P. Carazzetti, *Journal of Micro/Nanolithography, MEMS, and MOEMS* **8**, (2009).
354. F. M. Penning, Die glimmentladung bei niedrigem druck zwischen koaxialen zylindern in einem axialen magnetfeld. *Physica* **3**, 873 (11/1936).
355. Q. Qingquan, L. Qingfu, S. Jingjing, J. Yu, J. Finley, Influence of Operating Parameters on Target Erosion of Rectangular Planar DC Magnetron. *Plasma Science, IEEE Transactions on* **36**, 1899 (2008).
356. D. M. Mattox, *Handbook of Physical Vapor Deposition (PVD) Processing*. (Noyes Publications, 1998).
357. P. J. Kelly, R. D. Arnell, Magnetron sputtering: a review of recent developments and applications. *Vacuum* **56**, 159 (3/2000).
358. P. J. Kelly, J. Hisek, Y. Zhou, R. D. Pilkington, R. D. Arnell, Advanced Coatings Through Pulsed Magnetron Sputtering. *Surf. Eng.* **20**, 157 (2004).

359. B. D. RATNER, D. G. CASTNER, in *Surface Analysis – The Principal Techniques*, J. C. Vickerman, I. S. Gilmore, Eds. (John Wiley & Sons, 2009), pp. 47-112.
360. J. W. Rabalais, *Principles of ultraviolet photoelectron spectroscopy*. Wiley-Interscience monographs in chemical physics (John Wiley & Sons Inc, 1977).
361. H. J. O. MATHIEU, in *Surface Analysis – The Principal Techniques*, J. C. Vickerman, I. S. Gilmore, Eds. (John Wiley & Sons, 2009), pp. 9-45.
362. E. TAGLAUER, in *Surface Analysis – The Principal Techniques*, J. C. Vickerman, I. S. Gilmore, Eds. (John Wiley & Sons, 2009), pp. 270-331.
363. *RUMP*, http://www.genplot.com/doc/rump.htm, Accessed 2/18/15
364. G. Haugstad, *Atomic Force Microscopy: Understanding Basic Modes and Advanced Applications*. (Wiley, 2012).
365. *Ellipsometry at the Nanoscale*. (Springer, Verlag Berlin Heidelberg, 2013).
366. L. J. v. d. PAUYV, A method of measuring specific resistivity and Hall effect of discs of arbitrary shape. *Philips Research Reports* **13**, 1 (1958).
367. C. A. LUCAS, in *Surface Analysis – The Principal Techniques*, J. C. Vickerman, I. S. Gilmore, Eds. (John Wiley & Sons, 2009), pp. 391-478.
368. J. Goldstein *et al.*, *Scanning Electron Microscopy and X-ray Microanalysis*. (Springer, ed. 3rd, 2007).
369. S. Kijima, T. Nakada, High-Temperature Degradation Mechanism of Cu(In,Ga)Se$_{2}$-Based Thin Film Solar Cells. *Appl. Phys. Express* **1**, 075002 (2008).
370. J. D. McBrayer, R. M. Swanson, T. W. Sigmon, Diffusion of Metals in Silicon Dioxide. *J. Electrochem. Soc.* **133**, 1242 (06/01/1986).
371. F. J. Pern *et al.*, in *Reliability of Photovoltaic Cells, Modules, Components, and Systems*. (Proceedings of SPIE, San Diego, CA, 2008), vol. 7048, pp. 70480P-70480P-14.
372. R. E. Hummel, Electromigration and related failure mechanisms in integrated circuit interconnects. *Int. Mater. Rev.* **39**, 97 (1994).
373. T. Engel, The interaction of molecular and atomic oxygen with Si(100) and Si(111). *Surf. Sci. Rep.* **18**, 93 (1993).
374. B. L. Zhu *et al.*, Thickness study of AZO films by RF sputtering in Ar + H2 atmosphere at room temperature. *phys. status solidi (a)* **209**, 1251 (2012).
375. S. Polarz *et al.*, Chemical Vapor Synthesis of Size-Selected Zinc Oxide Nanoparticles. *Small* **1**, 540 (2005).
376. *CRC Handbook of Chemistry and Physics*. (CRC Press, ed. 89th, 2008), pp. 12–114.
377. E. H. Nicollian, Surface Passivation of Semiconductors. *J. Vac. Sci. Technol., A* **8**, S39 (1971).
378. D. W. Koon, T. G. Castner, Variable-range hopping and the hall coefficient in Si:As. *Solid State Commun.* **64**, 11 (10/1987).
379. C. N. R. Rao, B. Raveau, *Transition Metal Oxides*. (Wiley-Interscience, ed. 2, 1998).
380. D. Ginley, H. Hosonol, D. C. Paine, *Handbook of transparent conductors*. (Springer, 2011).

381. T. Minami, T. Miyata, T. Yamamoto, Work function of transparent conducting multicomponent oxide thin films prepared by magnetron sputtering. *Surf. Coat. Technol.* **108–109**, 583 (10/10/1998).
382. J. B. Malherbe, S. Hofmann, J. M. Sanz, Preferential sputtering of oxides: A comparison of model predictions with experimental data. *Appl. Surf. Sci.* **27**, 355 (12/1986).
383. W.-Y. Yang, S.-W. Rhee, Effect of electrode material on the resistance switching of Cu2O film. *Appl. Phys. Lett.* **91**, (2007).
384. I. Pallecchi *et al.*, Cu2O as a nonmagnetic semiconductor for spin transport in crystalline oxide electronics. *Phys. Rev. B: Condens. Matter* **81**, 165311 (04/19/2010).
385. A. E. Rakhshani, Thermostimulated impurity conduction in characterization of electrodeposited Cu2O films. *J. Appl. Phys.* **69**, 2290 (1991).
386. J. Camra *et al.*, Role of Al segregation and high affinity to oxygen in formation of adhesive alumina layers on FeCr alloy support. *Catal. Today* **105**, 629 (8/15/2005).
387. R. G. Egdell, S. C. Parker, in *Material Science Monographs* J. Nowotny, Ed. (1991), vol. 75, pp. 41.
388. R. L. Anderson, Germanium-Gallium Arsenide Heterojunctions [Letter to the Editor]. *IBM J. Res. Development* **4**, 283 (1960).
389. C. G. V. d. Walle, J. Neugebauer, Universal alignment of hydrogen levels in semiconductors, insulators and solutions. *Nat.* **423**, 3 (2003).
390. J. Zhao, A. Wang, M. A. Green, in *Proceedings of the 2nd World Conference on Photovoltaic Energy Conversion*. (1998), pp. 1681–1684.
391. A. Rohatgi, S. Narasimha, in *Proceedings of the 9th International Photovoltaic Science and Engineering Conference*. (1996), pp. 187–197.
392. L. Mittelstädt, S. Dauwe, A. Metz, R. Hezel, C. Häßler, Front and rear silicon-nitride-passivated multicrystalline silicon solar cells with an efficiency of 18.1%. *Progress in Photovoltaics: Research and Applications* **10**, 35 (2002).
393. O. Schultz, S. W. Glunz, G. P. Willeke, Multicrystalline silicon solar cells exceeding 20% efficiency. *Progress in Photovoltaics: Research and Applications* **12**, 553 (2004).
394. S. Reber, T. Kieliba, S. Bau, *Thin film solar cells: fabrication, characterization and applications*. J. Poortmans, V. Arkhipov, Eds., Materials for Electronic & Optoelectronic Applications (Wiley, England, 2006).
395. R. Bergmann, J. Kohler, R. Dassow, C. Zaczek, J. Werner, Nucleation and growth of crystalline silicon films on glass for solar cells. *Physica Status Solidi A—Applied Research* **166**, 587 (1998).
396. M. Keevers, T. Young, U. Schubert, M. Green, in *22nd European Photovoltaic Solar Energy Conference*. (Milan, Italy, 2007), pp. 1783-1790.
397. Y. Qiu *et al.*, in *25th European Photovoltaic Solar Energy Conference and Exhibition / 5th World Conference on Photovoltaic Energy Conversion*. (Valencia, Spain, 2010), pp. 3633-3637.
398. C. Becker *et al.*, Microstructure and photovoltaic performance of polycrystalline silicon thin films on temperature-stable ZnO:Al layers. *J. Appl. Phys.* **106**, 1 (2009).

399. L. Carnel, I. Gordon, D. Van Gestel, G. Beaucarne, J. Poortmans, Efficient solar cells based on fine-grained polysilicon. *Thin Solid Films* **516**, 6839 (2008).
400. J. Dore *et al.*, Thin-film polycrystalline silicon solar cells formed by diode laser crystallisation. *Progress in Photovoltaics: Research and Applications* **21**, 1377 (2013).
401. T. Iwamoto, K. Mori, M. Mizuta, H. Kukimoto, Doped InGaP grown by MOVPE on GaAs. *J. Cryst. Growth* **68**, 27 (9/1/1984).
402. S. R. Kurtz, J. M. Olson, A. E. Kibbler, S. Asher, in *Indium Phosphide and Related Materials, 1992., Fourth International Conference on*. (1992), pp. 109-112.
403. L. J *et al.*, in *2nd World Conference on Photovoltaic Solar Energy Conversion, 15th European PV Solar Energy Conference, 27th US IEEE Photovoltaics Specialists Conference, 10th Asia/Pacific PV Science and Engineering Conference : proceedings of the International Conference*. (Vienna, Austria, 1998), vol. 3, pp. 3520-3523.
404. A. Gomyo *et al.*, Evidence for the existence of an ordered state in Ga0.5In0.5P grown by metalorganic vapor phase epitaxy and its relation to band-gap energy. *Appl. Phys. Lett.* **50**, 673 (1987).
405. A. Poruba *et al.*, Optical absorption and light scattering in microcrystalline silicon thin films and solar cells. *J. Appl. Phys.* **88**, 148 (2000).
406. A. V. Shah *et al.*, Thin-film silicon solar cell technology. *Progress in Photovoltaics: Research and Applications* **12**, 113 (2004).
407. D. L. Staebler, C. R. Wronski, Reversible conductivity changes in discharge-produced amorphous Si. *Appl. Phys. Lett.* **31**, 292 (1977).
408. M. Fukawa, S. Suzuki, L. Guo, M. Kondo, A. Matsuda, High rate growth of microcrystalline silicon using a high-pressure depletion method with VHF plasma. *Sol. Energy Mater. Sol. Cells* **66**, 217 (2001).
409. Y. Mai *et al.*, Microcrystalline silicon solar cells deposited at high rates. *J. Appl. Phys.* **97**, 1 (2005).
410. J. Rüdiger, H. Brechtel, A. Kottwitz, J. Kuske, U. Stephan, VHF plasma processing for in-line deposition systems. *Thin Solid Films* **427**, 16 (2003).
411. F. Solar, 2014, http://www.firstsolar.com/en/about-us, Accessed Aug 13
412. J. Schaffner *et al.*, 12% efficient CdTe/CdS thin film solar cells deposited by low-temperature close space sublimation. *J. Appl. Phys.* **110**, 1 (2011).
413. J. Britt, C. Ferekides, Thin-film CdS/CdTe solar cell with 15.8% efficiency. *Appl. Phys. Lett.* **62**, 2851 (1993).
414. J. M. Kestner *et al.*, An experimental and modeling analysis of vapor transport deposition of cadmium telluride. *Sol. Energy Mater. Sol. Cells* **83**, 55 (2004).
415. S.-H. Wei, S. B. Zhang, Chemical trends of defect formation and doping limit in II-VI semiconductors:The case of CdTe. *Phys. Rev. B: Condens. Matter* **66**, 155211 (10/31/2002).
416. S. Ahmed *et al.*, A High Efficiency Electrodeposited Cu2ZnSnS4 Solar Cell. *Advanced Energy Materials* **2**, 253 (2012).

417. B. Shin *et al.*, Thin film solar cell with 8.4% power conversion efficiency using an earth-abundant Cu2ZnSnS4 absorber. *Progress in Photovoltaics: Research and Applications* **21**, 72 (2013).
418. Z. Yang, Dalian University of Technology (2011).
419. D. A. R. Barkhouse, O. Gunawan, T. Gokmen, T. K. Todorov, D. B. Mitzi, Device characteristics of a 10.1% hydrazine-processed Cu2ZnSn(Se,S)4 solar cell. *Progress in Photovoltaics: Research and Applications* **20**, 6 (2012).
420. H. Katagiri, K. Jimbo, M. Tahara, H. Araki, K. Oishi, in *Thin-film compound semiconductor photovoltaics--2009 : Materials Research Society Symposium Proceedings*. (Materials Research Society, San Francisco, California, U.S.A, 2009), vol. 1165, pp. 125-136.
421. I. V. Dudchak, L. V. Piskach, Phase equilibria in the Cu2SnSe3-SnSe2-ZnSe system. *J. Alloys Compd.* **351**, 145 (2003).
422. W. Zhou, Y. Zhou, The preparation for flower-shaped CZTS nano-particle by solvo thermal method and representational structure. *Chemical Research*, 70 (2012).
423. N. Kaur, M. Singh, D. Pathak, T. Wagner, J. M. Nunzi, Organic materials for photovoltaic applications: Review and mechanism. *Synth. Met.* **190**, 20 (4/2014).
424. K. C. Djuristic A, in *Organic Photovoltaics: Mechanisms, Materials and Devices*, S.-S. Sun, N. S. Sariciftci, Eds. (CRC Press, Boca Raton, Florida, 2005).
425. M. C. Scharber *et al.*, Design Rules for Donors in Bulk-Heterojunction Solar Cells—Towards 10 % Energy-Conversion Efficiency. *Adv. Mater. (Weinheim, Ger.)* **18**, 789 (2006).
426. T.-W. Lee, O. O. Park, The Effect of Different Heat Treatments on the Luminescence Efficiency of Polymer Light-Emitting Diodes. *Adv. Mater. (Weinheim, Ger.)* **12**, 801 (2000).
427. K. L. Mutolo, E. I. Mayo, B. P. Rand, S. R. Forrest, M. E. Thompson, Enhanced Open-Circuit Voltage in Subphthalocyanine/C60 Organic Photovoltaic Cells. *J. Am. Chem. Soc.* **128**, 8108 (06/01/2006).
428. T. Oku, T. Noma, A. Suzuki, K. Kikuchi, S. Kikuchi, Fabrication and characterization of fullerene/porphyrin bulk heterojunction solar cells. *J. Phys. Chem. Solids* **71**, 551 (4/2010).
429. A. Kaniyoor, S. Ramaprabhu, Enhanced efficiency in dye sensitized solar cells with nanostructured Pt decorated multiwalled carbon nanotube based counter electrode. *Electrochim. Acta* **72**, 199 (6/30/2012).
430. P. Calandra, G. Calogero, A. Sinopoli, P. G. Gucciardi, Metal Nanoparticles and Carbon-Based Nanostructures as Advanced Materials for Cathode Application in Dye-Sensitized Solar Cells. *International Journal of Photoenergy* **2010**, 15 (2010).
431. N. K. McKinnon, D. C. Reeves, M. H. Akabas, 5-HT3 receptor ion size selectivity is a property of the transmembrane channel, not the cytoplasmic vestibule portals. *The Journal of General Physiology* **138**, 453 (10/1/2011).
432. P. Umari, E. Mosconi, F. De Angelis, Relativistic GW calculations on CH3NH3PbI3 and CH3NH3SnI3 Perovskites for Solar Cell Applications. *Sci. Rep.* **4**, (03/26/2014).

433. M. A. Green, A. Ho-Baillie, H. J. Snaith, The emergence of perovskite solar cells. *Nat Photon* **8**, 506 (07/2014).
434. J. Burschka *et al.*, Sequential deposition as a route to high-performance perovskite-sensitized solar cells. *Nat.* **499**, 316 (07/18/2013).
435. J. N. Freitas, A. S. Goncalves, A. F. Nogueira, A comprehensive review of the application of chalcogenide nanoparticles in polymer solar cells. *Nanoscale* **6**, 6371 (2014).
436. W. U. Huynh, J. J. Dittmer, W. C. Libby, G. L. Whiting, A. P. Alivisatos, Controlling the Morphology of Nanocrystal–Polymer Composites for Solar Cells. *Adv. Funct. Mater.* **13**, 73 (2003).
437. B. Sun, N. C. Greenham, Improved efficiency of photovoltaics based on CdSe nanorods and poly(3-hexylthiophene) nanofibers. *Phys. Chem. Chem. Phys.* **8**, 3557 (2006).
438. L. Wang, Y. Liu, X. Jiang, D. Qin, Y. Cao, Enhancement of Photovoltaic Characteristics Using a Suitable Solvent in Hybrid Polymer/Multiarmed CdS Nanorods Solar Cells. *The Journal of Physical Chemistry C* **111**, 9538 (07/01/2007).
439. H. Lili *et al.*, Synthesis of high quality zinc-blende CdSe nanocrystals and their application in hybrid solar cells. *Nanotechnology* **17**, 4736 (2006).

Appendix

a. Other Solar Technologies

Bulk Silicon: Crystalline silicon is a non-toxic material with high stability and durability, and possesses an energy gap of 1.12 eV which is well suited for maximum single-junction solar cell efficiencies. Furthermore, silicon is an abundant material and in principle is not subject to natural resource limitations in case a strong rise of the solar electricity demands in the future. However, it competes with the integrated circuit industry for and the price can vary with integrated circuit demand. Silicon-wafer based solar panels currently comprise the dominant portion of installed solar capacity throughout the world, with best lab efficiencies at 25% for unconcentrated single crystal cells (*26*). This has primarily been due to the prior extensive development of silicon-wafer based technology for integrated circuits. Due to the indirect band gap, optical absorption requires close to 100 μm of silicon, and since the wafers are cut from a boule, about half of the Si is lost to the kerf. The thickness is far larger than a depletion region. As a result, photogenerated carriers must diffuse to a contact for collection. This requires very low trap density material. As a result, crystalline silicon wafers have been relatively costly for PV, despite large volumes in production. Unless bulk multi-crystalline silicon wafers show a substantial improvement in performance or single crystalline wafers fall much farther in cost, they will likely not be the solar cells of the future.

Multicrystalline Silicon: To avoid the cost of the silicon wafer, developments were made in the last couple decades to produce thick-bulk multicrystalline silicon, with substantial progress in the early 2000s. This is now the basis of today's silicon

photovoltaic technology with the current record at 20.4 % (*26*). This silicon material can be produced more cheaply with only marginally reduced efficiencies. In the main techniques used today, silicon is melted within an induction-heated quartz crucible coated with silicon nitride it is allowed to solidify into an ingot using position sophisticated heating systems and maybe a second crucible. Crystallization starts at the bottom after the temperature is lowered. During this period the crystallisation front, that is, the liquid—solid interphase, moves in a vertical direction upwards through the crystallisation crucible resulting in columnar crystal growth and consequently adjacent wafers fabricated out of the ingots show nearly identical defect structures (grain boundaries and dislocations). Common crystallisation speeds are around 1.5 cm/h.

Multicrystalline silicon cells present new challenges vs. crystalline however, such as surface passivation of grain boundaries and extended crystal defects and impurities. It is important to have excellent light confinement and high-quality surface passivation in these cells. For front passivation, phosphorus is diffused into the silicon under high temperatures which also acts to getter impurities. For the rear, the most efficient cells so far use an oxide passivated rear surface with locally defined electrical contacts (*390*), however an aluminum back surface field (*391*) and silicon nitride (*392*) has also been used. Using masking oxidation and drive-in oxidation steps at 800^{o} C instead of the standard monocrystalline processing temperatures of 1050^{o} C maintain or enhance bulk carrier lifetime (*393*).

Despite the reductions in cost, this technology has not seen lab efficiency improvements in a decade and producing thick multicrystalline silicon material is seen as a barrier to long term competitiveness.

Recrystallized silicon: One route to reducing the cost of a silicon cell has been to reduce its thickness to the minimum necessary for optical absorption while minimizing the kerf losses. Efforts to do this by mechanically thinning the wafer don't really reduce costs since the removed silicon is lost. This has resulted in a series of techniques that attempt to produce as crystalline-as-possible silicon on foreign substrates. Polycrystalline silicon (poly-Si) thin-film solar cells deposited under vacuum in an amorphous state followed by solid phase crystallization (SPC) by thermal annealing is a popular technique only requiring temperatures of about 550 ^{o}C for a few hours on cheap substrates such as glass or ceramics (*394*). An impurity blocking barrier layer must be used on most flexible substrates such as stainless steel. Furthermore, thermal expansion matching must be done to prevent film flaking(*395*). One of the major current problems is the high concentration of deep level intragrain and grain-boundary defects which have limited open circuit voltage to about 500mV. The current record efficiency of 10.4% was set in 2007(*396*). The second poly-Si growth idea is the 'seed layer approach' where a very thin silicon seed layer with excellent crystallographic properties is first deposited as a template, and is then used for epitaxial growth of subsequent absorber layers leading to cell thickening with substantially larger grains and a higher crystalline quality compared to the previous method. Typical processing temperatures are far below 600 ^{o}C for shorter periods of time, however structural characteristics and electrical performance of this material are limited by defects inside the grains, rather than by grain boundaries, and have been limited to an efficiency of 8.5%(*397*).

The simplicity of direct growth of poly-Si thin films without further annealing steps is an appealing option, and has demonstrated highly crystalline films just over 350 ^{o}C at $1x10^{-7}$ mbar using electron beam evaporation(*398*). These films have grain sizes of 0.1 to 10um, although the crystallographic quality tends to be worse than other types of poly-Si growth methods with the best cells at 5%(*399*). A more recently successful poly-Si attempt has been using liquid phase crystallization, where silicon of 5–15 um thickness is deposited in the amorphous phase at a high rate, followed by a subsequent crystallization process whereby the silicon is selectively heated above the melting point of 1414 ^{o}C while attempting to limit the temperature of the substrate. This results in large grain widths up to hundreds of microns, with lengths up to the centimeter range, however careful selection of diffusion barriers and buffer layers is needed to minimize diffusion and thermo-mechanical mismatch between film and substrate. In addition to this very high dislocation densities have been observed in semi-monocrystalline parts of the material. Efficiencies are limited to 8.4%(*400*).

III-V Technologies: This solar cell technology defines the high-end of solar cells, with single unconcentrated thin film cells reaching 28.8% efficiency(*26*). The III-V terminology comes from the main cell elements being composed from groups 13 and 15 in the periodic table, of which up to this point has mainly been the usage of Ga, In, P, Al, and As. The key advantage of compound semiconductors is the ability to use epitaxial methods to form lattice-matched heterostructures and compositionally graded films with relatively low defect densities. Absorbers can be made n- or p-type, have radiation tolerance, and have high carrier mobilities and direct energy gaps, allowing for thin solar

films. Device stacks for a single cell typically consist of GaAs or Ge single-crystal substrate, followed by an Ag back contact, a p-type base, and moderately n-doped emitter layer, and a window layer and top Ag contact. For most of the layers, the elements Se and Si are commonly used *n*-type dopants in III–V materials(*401*) and for p-type Zn is most often used(*402*), although carbon and magnesium have been studied as well. Window layers are typically made of AlInP, which is closely latticed matched to the absorber to passivate the surface states associated with the emitter surface and reduce minority-carrier traps.

Generally devices are produced for mass production in sequential metal—organic chemical vapor deposition (MOCVD) processes, however they are more typically grown at the research level by other techniques such as molecular beam epitaxy (MBE)(*403*). For MOCVD processes, typical precursers are trimethylgallium, trimethylindium, arsine, and phosphine in a Pd-purified H_2 carrier gas. The dopants sources included H_2Se, Si_2H_6, diethylzinc, and CCl_4. This solar cell technology has been studied extensively, and some of the following are key improvements: the band gap shift of $Ga_xIn_{1-x}P$ is correlated with ordering of Ga and In on the group III sublattice(*404*), and is a function of the growth temperature and growth rate, phosphine partial pressure, substrate misorientation from (100), and doping level. The morphology of $Ga_xIn_{1-x}P$ grown on GaAs is an even more sensitive indicator of the quality of the original GaAs surface. III-V technology has matured to the point where pushing the efficiency higher to the S-Q limit requires unreasonably tight processing conditions. This has resulted in further cell efficiency improvement focusing on multi-junction fabrication, which is substantially easier for this technology than for all others at this point, and will be discussed next.

Although the efficiency of compound semiconductor cells is high, their cost is much higher than the other technologies. This is due to the need for single crystal substrates and epitaxial growth. The market for this technology, while important, is small. It is primarily limited to cost-insensitive applications such as aerospace.

b. Commercial Thin Film Technologies

A silicon-saving option that has been on the market for several decades is the use of hydrogenated amorphous silicon instead of crystalline Si wafers. With stable single cell efficiencies of 8% its main selling point is that it is much thinner due to the higher absorption coefficient (*405*). This change is due to the fact that a-Si:H is a direct gap material. It can be deposited at low temperatures onto flexible substrates. Silicon is deposited by plasma-enhanced chemical vapor deposition using mixtures of H_2 and SiH_4. Usually cells are constructed as *p-i-n* devices due to dopants increasing the density of recombination centers (*406*). These devices degrade substantially after light exposure, which has been identified as the Staebler–Wronski effect (*407*). Changing from amorphous silicon to nanocrystalline silicon helps to reduce the device degradation, however the deposition is much slower and the resulting film must be many times thicker due to the lower absorption coefficient (*405*). Recent improvements have focused on higher deposition rates by the use of very high frequency plasma sources, using higher pressures, and development of linear plasma sources (*408-410*). Despite the technology being in development since the 1980's, it struggles to compete in most markets at present. One exception to this is the use of an amorphous-Si/crystalline-Si heterojunction with a middle intrinsic thin layer for passivation. This device, called a HIT cell has resulted in

lab efficiencies up to 25.6 % (*26*), however, since it requires a silicon wafer, it should really be seen as an extension of the bulk technologies described above.

Besides the decrease in required light-absorbing material per solar cell, thin-film solar cells also offer the advantage of low-cost deposition on a large area. One of the most attractive features of flexible thin-film solar cells is the high potential to reduce production costs, because roll-to-roll manufacturing on flexible substrates enables use of compact high throughput deposition equipment. New application possibilities such as building integrated PV have emerged with the development of solar modules on flexible substrates.

CdTe: Of the thin film solar cell technologies, CdTe solar modules presently have the largest market share with approximately 20% of total installed world PV capacity (*411*). Unconcentrated lab efficiencies up to 21.0%(*26*) have been reported. CdTe is a compound semiconductor material with an absorption coefficient larger than 10^4 cm^{-1} for photons with energy above the band gap of 1.5 eV. The deposition methods to make it are numerous, but the top ones include concepts of condensation/reaction of Cd and Te_2 vapors on a surface, galvanic reduction of Cd and Te ions at a surface, and reaction of precursors at a surface with temperatures usually over 500^oC at some point during cell fabrication. Close space sublimation techniques have been developed to reduce sublimation from the substrate at such high temperatures (*412*). Close-space sublimation gives high performance cells (*413*), while very high deposition rates use convective vapor transport deposition (*414*). Peak efficiency CdTe solar cells are composed of

TCO/CdS/CdTe thin films as n-p heterojunctions sandwiched between front and back electrical contacts, typically fabricated as superstrate devices.

The annealing process can also promote recrystallization and grain growth. For low resistive ohmic electrical back contact formation, a chemical etching process for modification of the CdTe surface is commonly applied. The necessity of that surface treatment process prior to the metal back contact deposition is due to problems associated with the high electron affinity and energy band gap of CdTe. An on-going critical issue for CdTe solar cell processing has been obtaining acceptor concentrations greater than 10^{14} cm^{-3}. During thermal treatment steps the semiconductor system is pushed towards equilibrium. First-principles calculations have shown that a self-compensation mechanism occurs during *p*-type doping(*415*). High current densities have been achieved, but open-circuit voltage and fill factor have been limited by excessive forward-current recombination, low bulk lifetime and low carrier density. Due to the large use of Cadmium in these cells, this technology also has questionable long term use as some countries have banned solar modules containing cadmium.

c. Emerging Thin Film Technologies

The remaining solar technologies, all of which are less well developed, can be summarized in five categories: CZTS, Dye-sensitized, organic, perovskite, and quantum dot.

CZTS: Cu_2ZnSnS_4 (CZTS) is the main contender for thin film solar technologies competing for long term mass-usage due to its use of all earth- abundant nontoxic elements. The current record efficiency stands at 11.1%(*26*). CZTS suffers from very low defect formation energies and the difficulty of making it phase-pure. A much deeper understanding of the material is needed to progress further. Since CZTS was investigated as a derivative of CIGS development the device stack is usually made with the same accompanying layers. CZTS can be deposited by electrochemical deposition at 7.3%(*416*), vacuum-deposited coevaporation at 8.4%(*417*), electron-beam evaporation at 5.45%(*418*), and Sol-Gel at 10.1%(*419*) are among the highest efficiency achievements. CZTS can be formed in the Kesterite or Stannite crystal structure with a direct band gap of 1.5 eV. The substitution of selenium for sulfur can shift the band gap between 1.5 eV and 1 eV. The maximum efficiency cells are obtained in Zn-rich and Cu-poor material, with cells outside this range having a low efficiency(*420*). Many problems remain to be understood in the development of CZTS-based solar cells. Among them is a lack of understanding of the growth mechanism, which found that single-phase stannite Cu_2ZnSnS_4 or $Cu_2ZnSnSe_4$ is very hard to achieve, and the tolerance for element deviation was only 1-2% below 550^oC(*421*). The band structure is not understood, nor the nature of defects such as high series resistance, interface properties, and light induced degradation. The reproducibility and yield of high efficient cells is low and the relationship between material properties and device performance is severely lacking (*422*).

Organic: Organic and polymeric photovoltaic materials and technology is another attractive solar cell option due to the abundance of the elements and low manufacturing costs compared to other thin film deposition technologies and crystalline silicon. Current efficiencies reach 11.1%(*26*). The materials have easily tuned band gaps and work functions. For p-type materials this commonly includes C_{60}, $PC_{60}BM$, $PC_{70}BM$, ICMA, ICBA, and for n-type materials this includes PTPDDPP, PBDTT, P3HT, PCPDTBT, phthalocyanine, and subphthalocyanine(*423*). A standard organic-based solar stack typically has a TCO top contact and reflecting metal bottom contact with the organic active layer in between, along with a poly(ethylene dioxythiophene):polystyrene sulfonic acid layer, which enhances the hole transfer between the active layer and top contact(*424*). A thin LiF layer enhances electron transfer between the active layer and the metal electrode. The deposition methods for making these cells in a manufacturing environment are numerous, but the most widely used is currently ink-jet printing on a roll-to-roll process. These materials generate Frenkel-excitons (binding energy 0.1 eV to 1.0 eV) with short lifetimes. The electron hole pairs are typically separated by a hetero interface where the difference between the donor HOMO and acceptor LUMO material levels can be more effectively optimized to split the excitons. This gives a higher power conversion efficiency by increasing V_{oc} when the donor band gap energy is higher and tuning the donor LUMO level (*425*). There are currently three major reasons for the current performance limits. These are due to material energy structure variation/misalignment, poor material morphologies, and unoptimized cell structures and processes(*426*). In addition, the organic materials also have high sensitivity to moisture,

oxygen, atmospheric and particulate contamination, with constraints on drying time, uniformity of thickness and composition(*427*, *428*).

Dye-sensitized: Photoelectrochemical solar cells (PSCs), consisting of a photoelectrode, a redox electrolyte, and a counter electrode, have been studied extensively. These materials when used with a suitable redox electrolyte can produce solar light-to-electric power conversion efficiency up to 11.9%(*26*). Since the dye is a sensitive molecule, the deposition techniques are similar to organic cell processing. Several semiconductor materials, including single-crystal and poly-crystalline layers of n- and p-Si, and n- and p-GaAs have been used as photoelectrodes, however TiO_2 remains the most common material. Sometimes the counter electrode is a complex structured nanoparticle dispersion such as carbon nanotubes(*429*). Efficiency improvements have been made by optimizing the structure of what is usually nanoporous electrodes, that of Ru-complex dyes, and the composition of electrolytes. Platinum is used as the cathode to catalyze the reduction of the oxidized charge mediator(*430*). Current problems for this technology include frequent photocorrosion of the electrode under irradiation in the electrolyte solution, resulting in poor stability of the cell. Efforts have been made worldwide to develop more stable PSCs for real world environments. Also, the short circuit current must be increased, which means the near-IR region absorption must be improved. The open circuit voltage should be increased from the current ~.75V, which at present is limited by charge recombination.

Perovskite: A newcomer to the solar cell field is perovskite-based cells, which have grown quickly from less than 7% in 2011 to 17.9% efficiency in only a few years(*26*) by utilizing existing expertise in related dye-sensitized and organic PV. The main advantages of perovskites include ease of fabrication, strong solar absorption, a range of properties from different compatible compounds, high carrier mobility, low non-radiative carrier recombination rates, and ease of material preparation. Perovskites are materials described by the formula ABX_3, where X is an anion and A and B are cations of different sizes (A being larger than B). Typically A is an organic such as methylammonium(*431*) while B is inorganic. The highest efficiencies have been obtained when B is Pb(*432*). A solar cell stack consists of a glass substrate with a TCO layer (usually fluorine-doped tin oxide), followed by a TiO_2 layer and usually a perovskite scaffold, an optional perovskite electron transport material and some form of perovskite/organic hole transport layer, and lastly a gold contact(*433*). Deposition methods vary widely for depositing the perovskite-organic material, however they are all solution processed(*434*). Top performing cells use a mixed-halide resulting in higher carrier transport, coating nanoporous TiO_2 surfaces with thin perovskite layer, using an insulating Al_2O_3 scafolding in place of TiO_2, and improving morphology. Major disadvantages to the devices are currently the use of lead to achieve high performance, as well as fast degradation from UV and moisture exposure, and the processing variability observed with other solution-processed solar cells.

Quantum dot: Inorganic nanoparticle quantum dots (QDs) have been investigated for solar cells due to advantages in quantum confinement properties, as well as the fact that they can be easily synthesized in a wide variety of shapes (i.e. spheres, prisms, rods,

wires). Current maximum efficiencies are at 8.6%(*26*) but these have increased markedly over the last half decade. These types of cells are expected to provide other advantages over competing organic cells like efficient charge transfer between donor and acceptor materials, high electron mobility, and good stability while maintaining the cheap solution-based processing of organics and polymer cells(*435*). QDs function as the electron acceptor in the cell, are meshed with a conjugated polymer (hole transporter) or metal oxides/fullerenes (electron transporter). Many attributes influence the cells performance, among them the morphology (heavily influenced by the solvent used during deposition (*436-439*) and thermal or chemical treatments), acid-treatment which affects the interpenetrating nanoparticle network, changing QDs size and shape and metal, and controlling the interface and intermixing between the polymer and QDs phase. Challenges for this technology are numerous including the development of a controllable continuous percolation network, a well-defined interface between QDs and the polymer matrix, phase separation of inorganic nanoparticles from conjugated polymers, reducing surface traps, and better controlled energy level alignment.